CZECH TECHNICAL UNIVERSITY IN PRAGUE

Faculty of Civil Engineering
The Department of Landscape Water Conservation

Studying of dominant factors influencing a shallow runoff formation at a small catchment scale

Studium dominantních vlivů ovlivňujících formovaní mělkého podpovrchového odtoku na malých povodích

DOCTORAL THESIS

Ing. Jakub Jeřábek

Doctoral study program: Civil Engineering
Branch of study: Water Engineering and Water Management

Supervisor: Ing. David Zumr, Ph.D.
Co-supervisor: Ing. Petr Kavka, Ph.D.

Prague, 2022

CZECH TECHNICAL UNIVERSITY IN PRAGUE
Faculty of Civil Engineering
Thákurova 7, 166 29 Praha 6

DECLARATION

Ph.D. student’s name: Jakub Jeřábek, Ing.

Title of the doctoral thesis: Studying of dominant factors influencing a shallow runoff formation at a small catchment scale

I hereby declare that this doctoral thesis is my own work and effort written under the guidance of the tutor David Zumr, Ing., Ph.D..
All sources and other materials used have been quoted in the list of references.

The doctoral thesis was written in connection with research on the project:
- GP13-20388P Dynamics of water runoff generation and soil erosion as a result of temporary variable soil structure and soil properties on a cultivated catchment, 2013 - 2017
- Czech Ministry of Agriculture grant no. QJ1230056 - The impact of the expected climate changes on soils of the Czech Republic and the evaluation of their productive functions, 2012 - 2016
- TJ01000270 - Atlas HYDROLOGY - a modern tool for sediment and runoff calculating and anti-erosion measures dimensioning, 2018 - 2019
- LTC18030 - The effects of land use changes on soil erosion, sediment transport, water quality and runoff conditions, 2018 - 2020
- 773903 - Shui - Soil Hydrology research platform underpinning innovation to manage water scarcity in European and Chinese cropping systems, 2018 - 2022
- LTC20001 - Fire effects on soils, 2020 - 2023
- SGS20/156/OHK1/3T/11 - Monitoring, experimentální výzkum a matematické modelování srážko-odtokových a erozních procesů, 2020 - 2022
- SGS20/157/OHK1/3T/11 - Experimentání výzkum a modelování komplexních fyzikálních procesů v půdním prostřední, 2020 - 2022

In Prague on

signature

Poděkování

Děkuji svému školiteli Davidu Zumrovi za odborné vedení mým doktorským studiem. Děkuji svému školiteli specialistovi Petru Kavkovi za cenné praktické rady. Děkuji všem kolegům, kteří se podíleli na polních experimentech.

Děkuji svým rodičům za podporu při studiu. Děkuji Hance a Davidovi za podporu a vše ostatní.

Abstrakt

Na zemědělských povodích dochází vlivem agrotechnických operací k rychlým změnám hydraulických vlastností půd v ornici, vzniku kolejových řádků a zhutňování půdy v podorničí. Zatímco kolejové řádky ovlivňují směrování povrchového odtoku, zhutnělá vrstva, která je v porovnání s ornicí málo propustná, může přispívat k vzniku hypodermickému odtoku. Na základě předchozího výzkumu a existující literatury byl definován konceptuální model srážko-odtokové transformace na malých zemědělských povodích, který uvažuje rychlý transport srážkové vody ornicí k podorničí, kde dochází ke vzniku zavěšené mělké zvodně a rychlému hypodermickému odtoku. V rámci tohoto konceptu jsou velký rozdíl půdní struktury mezi ornicí a podorničím a přítomnost kolejových řádků hlavními faktory ovlivňujícími odtok z těchto území. K otestování platnosti tohoto modelu bylo provedeno měření mělké části půdního profilu pomocí odporové tomografie, pro stanovení mocnosti a variabilit podorničí a kolejové řádky. Dále byl proveden experiment s umělou srážkou k posouzení vlivu ornice, podorničí a kolejové řádky. Výsledky experimentu byly posouzeny prostřednictvím analýzy mikroreliéfu povrchu a numerického modelování infiltrace. Z měření vyplývá, že ornice je oproti podorničí relativně heterogenní. Při tvorbě povrchového odtoku hraje kolejový řádek významnou roli. V závislosti na jeho orientaci snižuje nebo zvyšuje množství povrchového odtoku a odteklého sedimentu. V průběhu srážky se povrch zplošťuje a stává se více propojený nehledě na přítomnosti či orientaci kolejové řádky. Z numerického experimentu vyplývá, že povrchový odtok vzniká nejdříve v kolejové řádce kvůli překročení infiltrační kapacity. Následně se do povrchového odtoku zapojuje zbytek povrchu kvůli nasycení ornice. K laterálnímu toku dochází pouze pokud je zanedbán vliv morfologie podorničí. Ta způsobuje, že voda při infiltraci směřuje do depresí v morfologii podorničí a nestéká laterálně po svahu. Výsledky naznačují, že kolejové řádky ovlivňují formování odtoku z povodí a je tedy třeba je zahrnovat do modelů například pomocí konceptu funkční konektivity. Zhutnělá vrstva a její morfologie ovlivňují transport vody pouze lokálně. Přesto může mít vliv na distribuci živin a vody v mělké části půdního profilu.

Klíčová slova: odtok z povodí; pramenné oblasti; zemědělská půda; prostorová variabilita; konektivita; numerické modelování, odporová tomografie

https://doi.org/10.14311/dis.fsv.2022.010

Abstract

Rapidly changing soil hydraulic properties, the presence of wheel tracks and the compacted layer in the shallow subsoil are phenomena formed in agricultural areas due to agrotechnical operations. While wheel tracks affect surface runoff routing, the compacted layer with its low permeability can contribute to hypodermic runoff formation. A conceptual model of the rainfall-runoff transformation was formulated based on previous research and a review of the literature. The model assumes fast passage of rainfall water through the topsoil to compacted subsoil where a shallow perched water table causes a rapid hypodermic runoff, while wheel tracks route the overland flow. Within this framework, the abrupt change in soil properties between the topsoil and subsoil and the wheel tracks are the first-order control of the runoff from such areas. Electrical resistivity tomography (ERT) measurements were performed to monitor the presence, heterogeneity and the thickness of shallow soil layers. Additionally, a simulated rainfall experiment was performed to study the effect of topsoil microtopography and wheel tracks. Analysis of the soil surface microrelief and numerical modeling were performed to explore the experimental data. ERT data showed that the topsoil is orders of magnitude more heterogeneous compared to the subsoil. Wheel tracks played an important role in surface runoff generation. A wheel track can increase or decrease surface runoff and sediment transport depending on its orientation. Furthermore, it was shown that rainfall and runoff flattened the soil surface microtopography regardless of the presence or orientation of the wheel track. Based on the numerical analysis, surface runoff is first generated on the wheel track due to infiltration excess followed by the saturation excess overland flow in the surrounding soil. Lateral subsurface flow occurred only if subsoil morphology was neglected. The subsoil morphology caused predominant flow in the depressions in the morphology, preventing the development of lateral flow. It was concluded that the wheel tracks affect the runoff from agricultural catchments and should be included in hydrological models, e.g. with the concept of functional connectivity. The compacted layers affect the subsurface runoff only locally; however, they can affect the distribution of nutrients and water in the shallow part of the soil profile.

Keywords: catchment runoff; headwater areas; agricultural soil; spatial variability; connectivity; numerical modeling; electrical resistivity tomography

Contents

Abstract **vii**

Introduction **1**
Objective . . . 2
Structure . . . 4

Theory and state of the art **9**

1 Governing equations **9**
1.1 Flow in variable saturated porous media . . . 9
1.1.1 Soil water retention curve . . . 10
1.1.2 Hydraulic conductivity . . . 11
1.2 Overland flow . . . 11

2 Hillslope and catchment scale hydrology **15**
2.1 Controlling factors of runoff generation at a hillslope scale . . . 15
2.2 Hillslope and catchment modeling . . . 16
2.2.1 Modeling approaches . . . 16
2.2.2 Controlling factors identification with models . . . 17

3 Tillage introduced changes to soil water dynamics **19**
3.1 Soil compaction . . . 19
3.2 Surface microtopography . . . 20
3.3 Influence of wheel tracks . . . 20
3.4 Soil hydraulic properties under various tillage practices . . . 21

4 Hydrological connectivity **23**

5 Electrical resistivity tomography **25**

Outcomes **29**

Field experiments and numerical modeling to study the runoff formation **33**

6 Topsoil and subsoil delineation **33**
6.1 Nučice site - deep structures . . . 34

6.2 Nučice site - depth of the compacted layer . . . 35
6.3 Řisuty site - delineation of a soil profile affected by wheel tracks . . . 36
  6.3.1 Study site . . . 36
  6.3.2 Artificial rainfall experiments . . . 36
  6.3.3 Experimental plots . . . 37
    6.3.3.1 Electrical resistivity tomography . . . 37
  6.3.4 Results & Discussion . . . 37
    6.3.4.1 Penetration resistance . . . 40
6.4 Key fingings . . . 41

7 Soil surface connectivity 43

7.1 Material & Methods . . . 44
  7.1.1 Microtopography observation . . . 44
  7.1.2 Random roughness . . . 44
  7.1.3 Structural connectivity . . . 44
  7.1.4 Functional connectivity . . . 45
    7.1.4.1 SMODERP2D model description . . . 46
    7.1.4.2 SMODERP2D model application . . . 47
  7.1.5 Runoff and sediment sampling . . . 47
  7.1.6 Tracer application . . . 47
7.2 Results & Discussion . . . 48
  7.2.1 Runoff and soil loss from soil with wheel tracks . . . 48
  7.2.2 Connectivity of the soil surface . . . 48
7.3 Surface water mixing . . . 50
7.4 Key findings . . . 51

8 Infiltration into tilled soil 53

8.1 Introduction . . . 53
8.2 Material & Methods . . . 54
  8.2.1 Experimental setup . . . 54
  8.2.2 Soil hydraulic characteristics . . . 55
  8.2.3 Modeling approach . . . 55
    8.2.3.1 One-dimension: inverse modeling . . . 56
    8.2.3.2 One-dimension: model setup . . . 57
    8.2.3.3 Two-dimension: soil layers morphology effect . . . 57
8.3 Results & Discussion . . . 58
  8.3.1 The soil structure . . . 58
  8.3.2 Infiltration front approach . . . 58
  8.3.3 Vertical flow . . . 60
  8.3.4 Measured soil hydraulic characteristics . . . 62
    8.3.4.1 Optimized soil hydraulic properties . . . 64
  8.3.5 Effect of soil layers morphology - 2D transects model . . . 64
    8.3.5.1 Influence of morphology on water dynamics in the soil . . . 64
    8.3.5.2 Influence of morphology on soil water pressure . . . 67
8.4 Key findings . . . 69

Conclusions **71**
8.5 Further advances 73

Bibliography **74**

List of author's publications **87**

Nomenclature **100**

A Collection of studies **101**

B Supplementary data for results section **169**

Introduction

Agricultural catchments are affected by unique factors. Tillage not only alters the soil hydraulic properties of the topsoil, but also creates a specific microrelief on a soil surface. The microtopography of the surface of freshly tilled soils is vulnerable to changes caused by rainfall and overland flow. Furthermore, wheel tracks are created on the soil surface due to multiple passages of agricultural machinery. The wheel track then affects the overland flow routing, surface connectivity, and wheel track compaction also propagates into the soil.

Soil compaction negatively affects the flow of water in soils. Typically, the compacted layer is less permeable to water. Therefore, a perched water table could be created on the compacted layer. This could lead to rapid hypodermic runoff and further reduction of recharge to deeper soil layers. However, the effect of the compacted layer is not clear, and it depends on the properties of the topsoil and subsoil, spatial heterogeneity of those properties, and properties of the delineation between topsoil and subsoil.

Headwater catchment research has been mainly focused on mountain forested areas. These areas often exhibit shallow, highly permeable soils, where runoff is controlled by the underlying bedrock. This concept can be adopted in agricultural soils where the shallow soil profile is represented by the tilled topsoil and the less permeable bedrock by the compacted subsoil. The accumulation of water in the subsoil layer can cause a saturation excess overland flow during intensive rainfall, leading to fast surface runoff and soil erosion. The difficulties of research in arable soils are, among others, rapidly changing soil properties and difficulty in measuring hydrological variables due to frequent agrooperations, fast crop growth, and changing crop type. However, tillage affects 14 millions km^2 of topsoil globally (Or et al., 2021) and it is therefore necessary to study the effect of agricultural operations on the hydrological circle.

The definition of the type of runoff process was systematically studied in Scherrer and Naef (2003). In this study, a decision diagram was defined that was used to define the dominant runoff process (both for surface and subsurface runoff). A single runoff process was defined by the mechanism of its origin and also by its time distribution using an artificial rainfall experiment on mountainous grasslands. In this thesis, a systematic analysis of the runoff process in agricultural soil is presented.

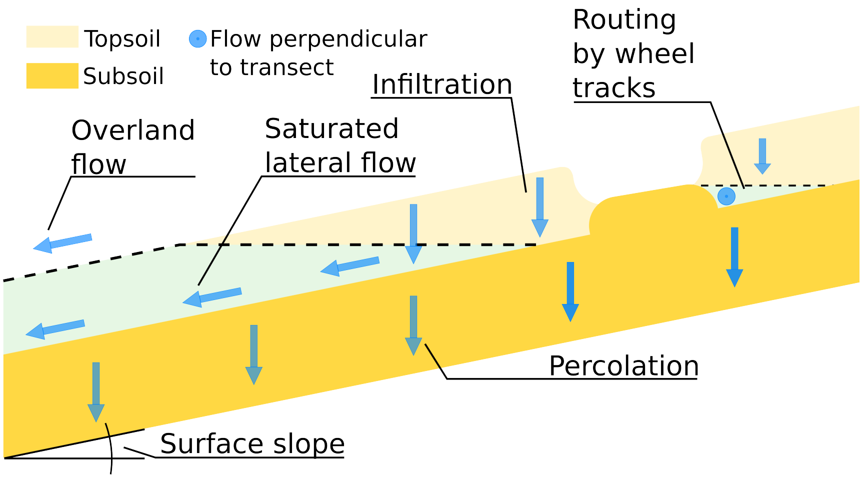

Figure 1: Conceptual model of runoff generation on tilled soil with the presence of wheel tracks

Objectives

In this dissertation, specific factors and their effect on runoff generation in small (agricultural) headwater catchment are investigated. The objectives of the thesis are to:

- investigate the effect of soil layering and surface topography on surface and subsurface runoff,
- investigate the position and soil physical properties of the compacted layer and the wheel track in agricultural soils,
- assess the effect of wheel tracks on the surface and shallow subsoil processes, and
- synthesize those findings to understand the formation of runoff on the small catchment scale.

A conceptual model of runoff generation on arable soil with the presence of wheel tracks is hypothesized in Figure 1. In this hypothesis, the lateral subsurface flow is formed on the compacted inclined subsoil. The percolation toward the deep soil horizon flow under gravitational flow and the ratio of lateral flow to percolation are controlled by the differences in soil physical properties. Overland flow is caused by the saturation excess mechanism and by spilling of the water accumulated on the wheels (Figure 1). Topsoil saturation during several rainfall events was observed in the experimental Nučice catchment in the middle and bottom part of a hillslope (Figure 2). Infiltration excess overland flow has not been observed much in mildly inclined agricultural areas such as the Nučice catchment (Zumr et al., 2015), except for the limited area of the wheel tracks.

Overland flow causes soil erosion and changes in soil surface microtopography. Overland flow is drained by wheel tracks in slope-wise direction or is stopped by contour line wheel tracks until it is spilled again (Figure 3). The influence of wheel tracks on the surface and subsurface runoff can be conceptualized in detail as shown in Figure 3. The process has been divided into three stages (excluding the dry state). In stage 1, the depression upslope

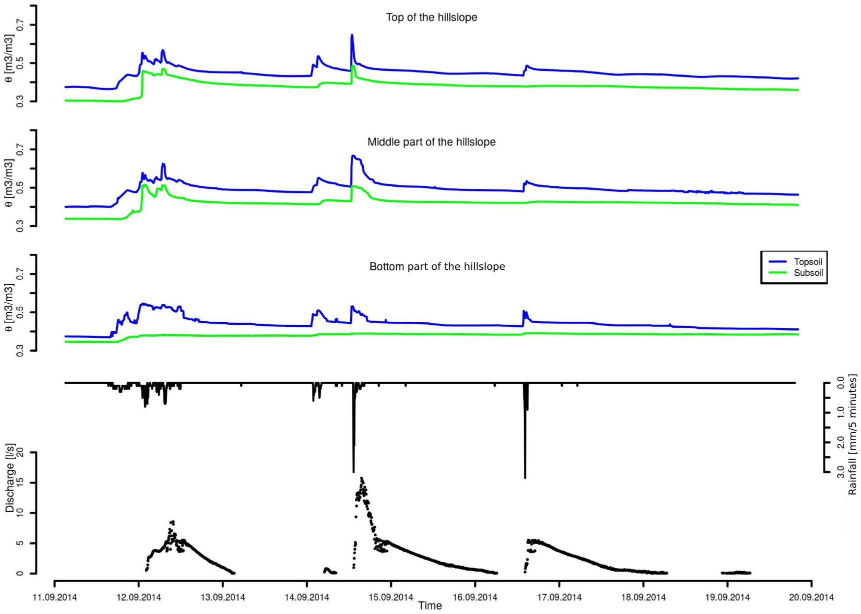

Figure 2: Topsoil and subsoil soil water content dynamics along the hillslope

of the wheel track is being filled (Figure 3a). This can cause a lateral flow of the ponded water, depending on the position of the wheel track on the hillslope. In stage two, the water level rises and fills the depression in the wheel track (Figure 3b). The ponded water

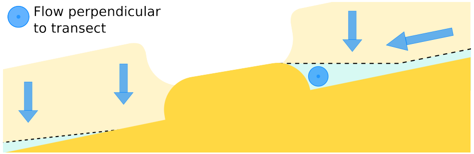

(a) Depression upslope the wheel track is being filled

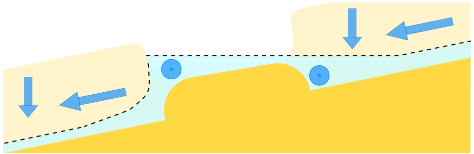

(b) Depression upslope the wheel track and the wheel track is being filled

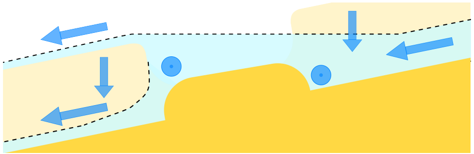

(c) Depression and wheel track are filled and contributes to the surface runoff

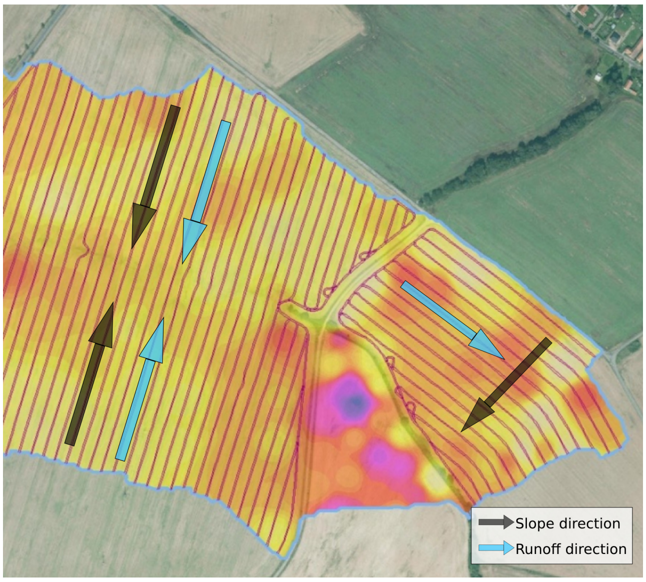

(d) Experimental catchment Nučice with identified wheel tracks. Arrows show the direction of the slope and direction of a flow affected by wheel tracks. The background color depict the depth of soil compaction.

Figure 3: Concept of wheel track influence on the runoff. Figures (a), (b) and (c) show the detail process. Figure (d) show the overall impact on the runoff at catchment scale.

in the depression can exceed the edge of the wheel track and start to contribute to surface runoff (Figure 3c). This effect on the catchment scale is depicted in Figure 3d where the water runs off either in the slope-wise or counter-slope-wise direction depending on the orientation of the wheel track on the slope.

Structure

This doctoral thesis consists of two main parts: Theory and state of the art, and Field experiments and numerical modeling to study the runoff formation. In Chapter 1 of the first part, I study and describe transport in variably saturated porous media, lateral saturated transport, or overland flow. In Chapter Chapter 2 I review the control factors of hillslope and small catchment scale hydrology. The agriculture dominated catchments are affected by specific processes such as soil compaction or rapidly changing soil hydraulic properties. Such processes are reviewed in Chapter 3. The connectivity concept is widely used in hydrology and erosion research and is briefly introduced in Chapter 4. Besides that, Chapter 5 also provides the basic theory and explanation of geophysical methods (used in the investigation).

The second part consists of three Chapters which study the factors affecting runoff at small agricultural sites. Chapter 6 is dedicated to geophysical investigation of the shallow and deep part of the soil profile. The heterogeneity and delineation of the topsoil and subsoil layers are given as well as a brief description of the wheel track effect. Chapter 7 shows the effect of tillage and wheel tracks on overland flow generation and on structural changes of the soil surface using several connectivity indices. The last Chapter 8 presents the numerical investigation of the water flow at the interface of topsoil and subsoil and the effect of the wheel track on the lateral.

Data and analysis presented in this thesis were partially published in:

- Jeřábek, J., Zumr, D., Laburda, T., Krása, J., and Dostál, T. (2022). Soil surface con- nectivity of tilled soil with wheel tracks and its development under simulated rainfall. Manuscript submitted for publication.
- Jeřábek, J. and Zumr, D. (2021). Geophysical survey as a tool to reveal subsurface stratification at within a small agricultural headwater catchment: a case study. The Civil Engineering Journal, 30(3). (60 %)
- Jeřábek, J., Zumr, D., Dostál, T., Tenreiro, T., Strauss, P., and M.D., V. (2021a). The effects of management practices and fires on soil water dynamics at three locations across Europe. In 2021 IEEE International Workshop on Metrology for Agriculture and Forestry, Como, IT. IEEE Instrumentation and Measurement Society. (60 %)
- Jeřábek, J., Zumr, D., Krása, J., and Dostál, T. (2018). Monitoring of runoff processes during an artificial rainfall on a freshly tilled soil. In TRANSPORT VODY, CHEMIKÁLIÍ A ENERGIE V SYSTéME PÔDA-RASTLINA-ATMOSFéRA, Bratislava, SK. Institute of Hydrology SAS.

- Jeřábek, J., Zumr, D., and Dostál, T. (2017). Identifying the plough pan position on cultivated soils by measurements of electrical resistivity and penetration resistance. Soil & Tillage Research, 174. (60 %, 8 citations)
- Li, T., Jeřábek, J., Noreika, N., Dostál, T., and Zumr, D. (2021a). An overview of hydrometeorological datasets from a small agricultural catchment (nučice) in the czech republic. Hydrological Processes, 35(2). (25 %)
- Tenreiro T.R., Jeřábek J., Gómez J.A., Zumr D., Martínez G., García-Vila M., and Fereres E. (2022). Simulating water lateral inflow and its contribution to spatial variations of rainfed wheat yields. European Journal of Agronomy, 137. (25 %)
- Zumr, D., Jeřábek, J., Klípa, V., Dohnal, M., and Sněhota, M. (2019b). Estimates of tillage and rainfall effects on unsaturated hydraulic conductivity in a small central European agricultural catchment. Water, 11(4). (15 %, 7 citations)

Project support

The research presented in this thesis was supported by following projects:

- GP13-20388P Dynamics of water runoff generation and soil erosion as a result of temporary variable soil structure and soil properties on a cultivated catchment, 2013 - 2017
- Czech Ministry of Agriculture grant no. QJ1230056 - The impact of the expected climate changes on soils of the Czech Republic and the evaluation of their productive functions, 2012 - 2016
- TJ01000270 - Atlas HYDROLOGY - a modern tool for sediment and runoff calculating and anti-erosion measures dimensioning, 2018 - 2019
- LTC18030 - The effects of land use changes on soil erosion, sediment transport, water quality and runoff conditions, 2018 - 2020
- 773903 - Shui - Soil Hydrology research platform underpinning innovation to manage water scarcity in European and Chinese cropping systems, 2018 - 2022
- LTC20001 - Fire effects on soils, 2020 - 2023
- SGS20/156/OHK1/3T/11 - Monitoring, experimentální výzkum a matematické modelování srážko-odtokových a erozních procesů, 2020 - 2022
- SGS20/157/OHK1/3T/11 - Experimentání výzkum a modelování komplexních fyzikálních procesů v půdním prostřední, 2020 - 2022

Theory and state of the art

Chapter 1

Governing equations

Runoff formation in small headwater catchments is a complicated process. The most important topics from the perspective of this thesis are: infiltration, water flow in variably saturated porous media, and overland flow. Related topics of soil physics and overland flow routing are discussed in the following chapters. Furthermore, the theory of geophysical measurement is also given, since those methods were used in this work.

1.1 Flow in variable saturated porous media

To calculate a transient flow in a variable saturated porous media, the Darcy-Buckingham law (Darcy, 1856; Buckingham, 1907) $q = -K(\psi)\nabla\Psi$, where q stands for Darcian flow (L.t^{-1}), K for unsaturated hydraulic conductivity (L.t^{-1}), ψ for suction pressure (L) and Ψ for total water potential can be inserted into the mass conservation equation (for incompressible fluid) $\partial_t\theta + \nabla \cdot \overrightarrow{q} = 0$ which becomes the well-known Richards equation (Richards, 1931). Three forms of the Richards equation were derived (Celia et al., 1990):

h-based:

$$C(h)\frac{\partial\psi}{\partial t} = \nabla \cdot K(\psi)\nabla\psi + \frac{\partial K}{\partial z}$$

θ-based:

$$\frac{\partial\theta}{\partial t} = \nabla \cdot D(\theta)\nabla\theta + \frac{\partial K}{\partial z}$$

mixed-form:

$$\frac{\partial\theta}{\partial t} = \nabla \cdot K(\psi)\nabla\psi + \frac{\partial K}{\partial z}.$$

Where the $C(h)$ stands for water capacity (L^{-1}) and $D(\theta)$ soil water diffusivity ($L^2.t^{-1}$). The most widely used forms of the Richards equation are the h- or mixed form. The advantage is that, unlike θ, the pressure potential ψ is always continuous, which favors numerical convergence (Roth, 2006). The θ-based form was used to derive some semi-analytical solution of Richards equation (Philip, 1957a).

Richards equation has several limitations. In theory, Darcy's law holds under conditions of laminar flow; for low flows and RE < 10. The law has to be altered for flows with higher velocity (Hassanizadeh and Gray, 1987). Germann (1990) argues that preferential paths (macropores flow) play an important role in transporting water through a soil during an infiltration process. However, the Richards equation assumes that infiltrating water fills smaller pores before the larger ones and that equilibrium between the pressure head and water content is always established. This is not the case under the macropores flow. Hassanizadeh and Gray (1987) also argue that simultaneous instant redistribution of porous pressure and water (which is assumed in the retention curve theory) applies only under steady state or quasi steady state conditions[1]. In addition, the Richards equation fails to describe the fingering effect overcome with semi-continuum model (e.g Kmec et al., 2019) and also it is unable to incorporate the pressure of the vapour phase and hence the effect of entrapped air in the porous system.

1.1.1 Soil water retention curve

The soil water retention curve (SWRC) is a relationship between the volumetric water content and the pressure potential. A mathematical parametrization is needed for computational purposes. The most common parametrizations of SWRC are van Genuchten (1980), Brooks and Corey (1964) parameterizations. Alternatively, a composite of two functions (with only two parameters) Hutson and Cass (1987) or the so-called flexible functions which are more versatile in terms of patterns in measured data (Prunty and Casey, 2002) can be used.

van Genuchten SRWC is widely used because of its reasonable amount of parameters and because the function (and its derivation) is continuous. The expression is as follows:

$$\theta_e(h) = \begin{cases} \frac{1}{(1+(\alpha|\psi|)^n)^m} & \text{for } \psi < 0, \\ 1 & \text{for } \psi \geq 0. \end{cases} \tag{1.1}$$

Where α, n, and m stand for the fitting parameters $(L^{-1}, -, -)$. The parameter α is an approximation of the bubbling pressure $h_b = 1/\alpha$ also called the air entry value. This approximation however holds only for larger values of n parameters. To reduce the number of parameters, the parameter m can be estimated (for common soils) as $m = 1 - 1/n$ (van Genuchten and Nielsen, 1985). The effective volumetric water content is defined as $\theta_e = (\theta - \theta_r)/(\theta_s - \theta_r)$. Finally, the product mn defines the equivalent pore-size distribution (van Genuchten et al., 1991).

SWRC curve was subjected to discussions. Hassanizadeh and Gray (1993) argue that the functional relation $\theta = f(\psi)$ aggregates many phenomena in porous space such as: phases immiscibility, surface tension, interfaces between fluids and soil, viscosity, soil surface wettability, particle size distribution, macro- and micro-scale heterogeneities, soil matrix deformations, soil fluid composition and others. These processes are usually not incorporated into empirically or heuristically inferred SWRCs. According to Hassanizadeh and Gray (1993), widely used definition of capillary pressure, which states that $P_c = P_n$ - P_w, where P_c is capillary pressure, and P_n and P_w is pressure of non wetting and wetting phase,

---

[1] Measurement of retention curve and unsaturated hydraulic conductivity is usually also done under these conditions.

describes capillary pressure only on a microscale (single meniscus scale) and only under equilibrium conditions. The change of external forcing on the capillary meniscus leads first to the change of capillary meniscus curvature and only if the force exceeds a certain value, the water is set into motion. Therefore, even a contact angle is not unique for certain P_c. Another problem of defining a macroscopic SWRC is hysteresis. Hysteresis is attributed to contact angle hysteresis, entrapped air effect, swelling/shrinking processes or aging of soil and to so called "ink-bottle effect"[2] (Hassanizadeh and Gray, 1993).

1.1.2 Hydraulic conductivity

The saturated hydraulic conductivity K_s controls the relation between the potential gradient and Darcian flux in the Darcy's law. If the soil is not fully saturated the flow is controlled by unsaturated hydraulic conductivity $K(\psi)$ (or $K(\theta)$). K deceases substantially since the flow is performed through a small cross section in the soil because only a small pores are filled and are more sparsely distributed in the porous space. Interestingly, the hysteresis in the unsaturated hydraulic conductivity is almost negligible if K derived from θ instead of ψ (Topp and Miller, 1966).

The models parametrizing the K are most often based on the capillary model theory approach, where the soil is represented by a set of "tubes" (the capillaries) the diameter of which is controlled by the pore size distribution function (Childs and Collis-George, 1950). Based on this approach, Mualem Mualem (1976) defined the relative unsaturated hydraulic conductivity K_r as

$$K_r\theta = \theta_e^l \left(\frac{\int_0^\theta d\theta/\psi}{\int_0^{\theta_s} d\theta/\psi} \right)^2 . \tag{1.2}$$

Where l express tortuosity and is commonly set to 0.5.

The expression (1.2) can be combined with any kind of SWRC parameterization to obtain an exact mathematical expression. Most commonly, it is combined with the van Genuchten's SWRC (1.1). The resulting formula for K_r is van Genuchten (1980)

$$K_r(\psi) = \begin{cases} \frac{(1-(-\alpha\psi)^{mn}(1+(-\alpha\psi)^n)^{-m})^2}{(1+(-\alpha\psi)^n)^{m/2}} & \text{if } \psi < 0, \\ 1 & \text{if } \psi \geq 0. \end{cases}$$

Finally, the relative unsaturated hydraulic conductivity is scaled with the saturated hydraulic conductivity to obtain the unsaturated hydraulic conductivity:

$$K(\psi) = K_s K_r(\psi).$$

1.2 Overland flow

The overland flow equation is derived from the Saint-Venant (SV) equations. SV equations are typically solved for 1D channel flow (Te Chow et al., 1988). A set of 3 equations for the

---

[2] This effect however showed only small changes in SWRC curve compared to total displacement of main drainage and imbibition curve (Morrow (1970) from Hassanizadeh and Gray (1993)).

2D flow can be given to describe the overland flow. Conservation of mass equation (Anderson and Burt, 1990):

$$w\frac{\partial h}{\partial t} + \frac{\partial (uA)}{\partial x} + \frac{\partial (vA)}{\partial y} = 0, \text{ and} \tag{1.3}$$

two momentum conservation equations:

$$\frac{\partial u}{\partial t} + u\frac{\partial u}{\partial x} + v\frac{\partial u}{\partial y} + g\frac{\partial h}{\partial x} = g(S_{ox} - S_{fx}) \tag{1.4}$$

$$\frac{\partial v}{\partial t} + u\frac{\partial v}{\partial x} + v\frac{\partial v}{\partial y} + g\frac{\partial h}{\partial y} = g(S_{oy} - S_{fy}) \tag{1.5}$$

In the equations 1.3, 1.4, 1.5, u and v stand for depth averaged velocity in the direction x and y, A stands for the cross section area normal to the flow, h stands for mean depth of the flow, w is the width of the flow section, S_{ox} and S_{oy} are surface slope in the direction x and y, S_{fx} and S_{fy} are the friction slope in x and y directions. Equations (1.3) to (1.5) do not show the lateral inflow term, wind shear, and eddy losses (Anderson and Burt, 1990; Te Chow et al., 1988).

The first three terms in the momentum equations express the inertia forces. The first term in the equations 1.4 and 1.5 expresses the local acceleration term (change of momentum due to change of local velocity in time). The second and third terms express the convective acceleration term (change in momentum due to changes in velocity in length). The last term on the left-hand side expresses the pressure term (change in water level in length) (Te Chow et al., 1988).

The momentum equations (1.4 and 1.5) are often simplified by neglecting some of the terms. If the local and convective acceleration components are small compared to the other forces, the first three terms can be neglected. This type of equation is called the diffusion wave approximation. In overland flow studies, the change in pressure term is also often neglected, and friction S_f may be set equal to the slope S_o. This simplification is called the kinematic wave approximation (Anderson and Burt, 1990; Te Chow et al., 1988).

In the kinematic wave approximation, it is assumed that the slope of the soil surface is parallel to the surface of the water. A shallow overland flow can be expressed in terms of normal flow depth h as (Te Chow et al., 1988)

$$q = uh = ah^m, \tag{1.6}$$

where q is the discharge per unit width and a and m the power law parameters. Equation 1.6 can be expressed in terms of Manning's formula under the assumption that the hydraulic radius R is similar to the height of the water level $R = h$, which holds for a very shallow and wide flow cross section area. The coefficient a can be expressed as $a = 1/ns^{1/2}$ (where n is the Manning's roughness and s is the surface slope), and the coefficient m as $m = 5/3$.

The clear advantage of the kinematic wave is its simplicity. The diffusion wave approximation is, however, more suitable in some cases since it allows for the backwater effect. Singh (1994) developed a dimensionless number γ (accounting for initial flow depth, surface slope, surface roughness, and acceleration due to gravity) from the spatially independent kinematic and diffusion wave approximation. He showed that for $5 > \gamma$ both approximations are acceptable. Another way to assess the justification of the kinematic wave approximation is the kinematic wave number K. In Moramarco and Singh (2002) it was shown that for spatially variable rainfall kinematic, the number is a good way to assess the feasibility of using kinematic wave approximation and that it is significantly dependent on the height of the downslope water level.

To solve the overland flow equations numerically, the choice of spatial and temporal discretization is crucial. To preserve numerical stability due to time step length Courant–Friedrichs–Lewiho criterion (CFL) is deployed. The theoretical value of CFL to preserve numerical stability is 1. The theoretical value of 1 is not satisfactory for shallow water flow calculations due to small surface water level compared to the size of the raster cell, roughness coefficient, or abrupt slope changes of adjacent calls (Zhang and Cundy, 1989; Esteves et al., 2000) The spatial discretization does not affect the overall performance of a model if parameters of the model were calibration for corresponding spatial discretization (Molnar and Julien, 2000). A larger raster cell size causes larger areas of surface runoff and larger calibrated roughness of a stream reaches in the model (Molnar and Julien, 2000).

Chapter 2

Hillslope and catchment scale hydrology

Headwater catchments are areas that transform rainfall into water in streams. The current findings of the key control factors of the water flow within the hillslope and small catchment are reviewed in this Chapter.

2.1 Controlling factors of runoff generation at a hillslope scale

Preferential flow is a mechanism that contributes to rapid infiltration and runoff generation. Preferential flow and the effect of various rainfall patterns on hillslope runoff with emphasis on land use and land cover type were investigated by using a dye tracer Bachmair et al. (2009). The microtopography characteristics of the top soil and subsoil were shown to be the controlling factors for the passage of the dye tracer through the soil profile, especially in farmland soils. More homogeneous soil physical properties led to an increase in the depth of infiltration with increasing rainfall amount especially in grasslands. Activation of preferential pathways depended more on the topsoil mircotopography than on the rainfall amount (Bachmair et al., 2009). In Flury et al. (1994), structural soils exhibited deeper dye tracer infiltration compared to unstructured soil and antecedent water content conditions played a minor role compared to soil structure. Also, ponding on the soil surface enhanced the passage of water through the preferential pathways Flury et al. (1994).

Hillslope-scale groundwater dynamics may control the subsurface runoff. Dynamics of groundwater level in the subsurface runoff of the hillslope was studied in relation to land use, hillslope, and soil physical characteristics (Bachmair and Weiler, 2012; Bachmair et al., 2012). Bachmair and Weiler (2012) showed with partial correlation analysis and Random Forest machine learning approach that groundwater level dynamics on a hillslope did not have single predictor variable, although soil structure and topography were the strongest ones. High-intensity rainfall under relatively dry soil conditions reduced the explanatory strength of all variables. Grassland soils exhibited a lower frequency of wells activation and a smaller increase in water level compared to forest soils with the same rainfall. During wet conditions, the ground water level increased more in the lower part of the hillslope (Bachmair et al., 2012). During dry conditions, the water level was usually activated on whole hillslope; the response was, however, more spatially heterogeneous. This behaviour coincides with soil moisture patterns that are controlled by hill slope topography under wet conditions, while under dry conditions it is controlled by local characteristics (such as vegetation or surface depressions) Grayson et al. (1997).

Topography of the subsurface layers was also identified as an important factor in runoff generation. An analysis of 147 storm events was performed on a hillslope with a distinct soil surface and bedrock topography Tromp-van Meerveld and McDonnell (2006a). Authors showed that there was a clear precipitation threshold that triggered the runoff. They concluded that subsurface runoff was controlled by soil depth during dry periods, soil depth and bedrock topography under low intensity storms during wet periods, and bedrock topography under heavy storms during wet periods of the year. The causes of the phenomena were studied by Tromp-van Meerveld and McDonnell (2006b). An increase in water level in adjacent wells was observed for a given rainfall depth, suggesting the connection of water between those wells. Such wells connectivity was shown to be persistent even for distinct rainfalls patterns with similar rainfall depths. This threshold behavior when bedrock depressions are being filled before the water is spilled over the edge of the depression was called fill and spill hypothesis.

Low permeable soil surface layers may have an effect similar to that of bedrock. The spill and fill hypothesis was studied in terms of the effect of a low-permeability soil layer on runoff in Du et al. (2016). The low-permeability argillic layer had a more heterogeneous topography than the ground surface. The groundwater perching began in the argillic layer, followed by the perching in the topsoil layer. Piezometric response was spatially heterogeneous and did not always lead to a runoff generation. A clear rainfall threshold for subsurface runoff initiation was observed for 60 mm of the amount of rain. Only a lateral flow was observed in the soil matrix during the events. Part of the perched water was lost via anomalies (cracks) in the argillic layer. Detailed description of groundwater perching on the of low-permeable soil layer was also observed by Ali et al. (2011). Depressions in the low-permeable layer and the boundaries of those depressions were determined, and various storage-discharge relations were defined and studied through properties of the perched GWL. The saturation deficit and water elevation above the low-permeable soil layer exhibited a different storage-discharge relation close to and far from the stream, suggesting a spatially heterogeneous runoff formation mechanism (Ali et al., 2011).

2.2 Hillslope and catchment modeling

2.2.1 Modeling approaches

The modeling of hillslope processes is challenging, and many approaches have been published. One of the first 3D physically based models for the unsaturated and saturated zone was developed and used by Freeze (1971, 1972). However, the 3D solution is not always necessary considering its demands for computation power and input parameters. For instance, the linked 1D Richards equation for vertical unsaturated flow and Boussinesq equation of lateral saturated flow was proposed by Pikul et al. (1974). This approach showed good performance for small slopes where no lateral unsaturated flow is expected and the Dupuit-Forchheimer assumptions are valid. Yakirevich et al. (1998) used similar modeling scheme with an explicit calculation of the water table position. They compared quasi two-dimensional model with two full 2D Richards equation based models. Although the quasi 2D model showed instabilities for larger time steps, the calculation was 16 to 22 times faster compared to the fully 2D models. In Dušek et al. (2012), 1D dual-continuum Richards equation and diffusion wave equation were coupled to study the saturated lateral water transport on the forested hillslope and compare it with the 2D model. The coupled approach exhibited larger peaks in the hydrograph compared to the full 2D model. The 2D model computed a larger total runoff volume and more realistically simulated measured suction pressures. However, none of these models represented the threshold behavior of the observed data in the field (Dusek and Vogel, 2014).

Four physically based models were compared with the 2D Richards equation model and the data measured on the slope transect in the benchmark paper of Sloan and Moore (1984). Some models calculated satisfactorily the hillslope discharge (kinematic model and Boussinesq discharge-storage model [1]) and some the water table position (kinematic wave and kinematic storage model) compared to more sophisticated Richards equation models. The problem of models was in the unsaturated input flow formulation. Sloan and Moore (1984) concluded that the kinematic wave model simulated the hillslope discharge with similar accuracy as the 1D and 2D models based on the Richards equation with less computational costs.

At large-scale models, the soil zone may be neglected. Seong et al. (2015) showed that the distributed physically based model was not able to match soil moisture data even with available high resolution topography. However, in large-scale modeling with low spatial resolution, the vertical infiltration component can be neglected Seong et al. (2015). Similarly, (Du et al., 2007) showed a good fit with the measured data in a setup where the rainfall water bypassed the soil profile and reached the bedrock immediately. The authors argue that this approach is valid for large-scale models in areas where only saturation excess overland flow can be anticipated (Du et al., 2007).

2.2.2 Controlling factors identification with models

The modeling exercise can be used to study the controlling factors of runoff (Weiler and McDonnell, 2007). Experimental watershed Panola (Georgia, USA) (Tromp-van Meerveld and McDonnell, 2006a,b) was subjected to a modeling experiment made in Hopp and McDonnell (2009). The model exhibited significant subsurface stormflow when rainfall exceeded 54 mm, which corresponded to field measurements (Tromp-van Meerveld and

---

[1] Discharge-storage (DS) model used in Sloan and Moore (1984) is a bulk model of the hillslope based on a mass balance equation. Kinematic DS model assumes that the water table has constant angle along the hillslope and the hydraulic gradient is equal to the bedrock slope. Boussinesq DS model assumes that the water table has constant angle along the hillslope and hydraulic gradient is equal to this slope.

McDonnell, 2006a). Additionally, the model was subjected to varying slope, soil depth, storm size, and bedrock permeability. Results suggested the importance of slope for the runoff coefficient, the duration of subsurface storm flow, and the variability of the saturation zones. The drainable porosity [2] and soil profile depth were identified as a first-order control for hillslope runoff (Weiler and McDonnell, 2004). The virtual hillslope was also able to reproduce the high portion of pre-event water in the runoff.

As was shown, the topography plays an important role in the runoff formation and hydrological connectivity. Surface runoff generation is affected by micro- and meso-scale surface topography, whereas meso-scale topography is mainly important at mild sloping hillslopes. Infiltration is affected by small-scale topography. Subsurface runoff is affected by both surface and subsurface layer topography. Subsurface topography is considered as the topography of an interface between distinctly permeable soil layers or bedrock topography (which may be different from surface topography) and plays a different role depending on the slope or depth of the soil profile.

---

[2] Pores which can freely drain up to potential of -100 cm.

Chapter 3

Tillage introduced changes to soil water dynamics

The subsoil layers morphology, depth of the soil profile, or soil microtopography are the key factors affecting the hydrology of the headwater catchments, as shown in previous Chapters. In agricultural soils, these factors may be represented by a compacted layer, the presence of a wheel track, and abrupt changes of the topsoil soil hydraulic properties due to tillage.

3.1 Soil compaction

Soil compaction is one of the negative effects of agricultural operations. For example, the length of the roots or the biomass in the topsoil are reduced due to soil compaction (Lipiec et al., 2012; Colombi et al., 2016). Climatic or weather conditions, tillage system (Pagliai et al., 2004), soil condition during harvest (Boizard et al., 2002), and used machinery (Pagliai et al., 2003) can lead to an increase or reduction in soil compaction.

Soil compaction affects the soil structure and the soil physical properties (Lal, 1999; Lindstrom et al., 1981). The compacted layer may exhibit smaller and less connected pores compared to soil subjected to minimum tillage under the conventional tillage system (Bertolino et al., 2010). The macroporosity and hydraulic conductivity decreased by up to 74% under direct compaction compared to non-compacted soil in the upper soil horizons (Kim et al., 2010). The compacted soil also exhibits reduced near-saturated hydraulic conductivity due to reduction in water-conducting pores (Ankeny et al., 1990; Seehusen et al., 2019; Pagliai et al., 2003; Daraghmeh et al., 2008). Tillage also has an effect on the isotropy / anisotropy of hydraulic conductivity. Conventional tillage introduced anisotropy into seedbed (dominant vertical direction) and the plow pan (mainstream horizontal direction), whereas conservation tillage caused insignificant anisotropy (Dörner and Horn, 2009).

Passage of a machinery had the largest impact in the first 10 *cm* of the soil profile where porosity decreased rapidly (Pagliai et al., 2003). Pagliai et al. (2003) also observed a reduction in elongated pores. Increase of penetration resistance of a soil was significant even at a depth of 35 - 40 *cm* (Pagliai et al., 2003).

Soil compaction caused various effects on different soil types. Clay loam exhibited a reduction in preferential flow (by reducing pores connectivity) with a higher compaction rate, while preferential flow was enhanced in sandy soil due to compaction (Mooney and Nipattasuk, 2003).

On the contrary, Roulier et al. (2002) observed an increase in hydraulic conductivity in the compacted layer due to the formation of bioporosity and due to the longer-term shrinking and swelling. Boizard et al. (2002) showed with long-term measurements that the formation of compacted zones at silt loam fields in France was reversible within a period of approx. 2 years.

Field observation of water flow through the soil with a developed plough pan was studied in Coquet et al. (2005a). Authors showed that the infiltration front propagated fast through the topsoil but became slower below the plough pan. Wheel tracks did not let through almost none of the infiltration water. Related numerical study simulated well the velocity of the infiltration front, however the values of the absolute water content and the lateral flow were not well represented by the numerical simulation (Coquet et al., 2005b).

3.2 Surface microtopography

The micro- to meso surface topography plays an important role in the surface runoff dynamics (Frei et al., 2010; Appels et al., 2016a). Surface runoff exhibited fill and spill behavior, especially on low inclined slopes with the presence of a shallow groundwater level. Surface flow dynamics and the mixing of surface and subsurface water depend on the configuration of the surface relief (Frei et al., 2010) and the type of surface runoff origin (Appels et al., 2016a). The microtopography of the soil surface is also important for soil loss and rill erosion (e.g. Jester and Klik, 2005).

Surface roughness (Taconet and Ciarletti, 2007) as microtopography characteristics can be used to estimate surface depression storage (Onstad et al., 1984), to partition rainfall water between infiltration and surface runoff (Zhao et al., 2018), or to estimate runoff and soil loss rates (Luo et al., 2018). Furthermore, temporal changes in surface roughness have been observed due to the impact of raindrops (Zobeck and Onstad, 1987; Bauer et al., 2015), surface runoff (Zobeck and Onstad, 1987), or during infiltration (Onstad et al., 1984). However, in some cases, the random roughness cannot explain the surface runoff dynamics and has to be replaced with more sophisticated indices, as will be shown in Chapter 4.

3.3 Influence of wheel tracks

Agricultural machinery traffic can cause permanent wheel track formation, which affects runoff processes. GPS tracking showed that most parts of an agricultural field are crossed by a tractor at least once during a single season (Augustin et al., 2020; Kroulík et al., 2011). These wheels may preferentially drain surface runoff and soil particles if oriented in the slope direction (Heathwaite et al., 2005; Silgram et al., 2010; Ryken et al., 2018b). Furthermore, the tillage and traffic direction may change the flow direction that would otherwise be oriented with the surface slope on more than 50% of the catchment area (Takken et al., 2001; Souchere et al., 1998; Couturier et al., 2013).

Wheel tracks affect surface runoff and erosion. Ryken et al. (2018a) conducted an experiment on two differently tilled fields with and without wheel tracks. Surface runoff was significantly higher on the plot with of wheel track. Sediment transport was also higher, even thought less significantly compared to runoff (Ryken et al., 2018a). In other studies, sediment transport increased as significantly as surface runoff with the presence of wheel tracks (Silgram et al., 2010). The loss of soil and nutrients can be reduced if the passage of agricultural machinery takes place under dry soil conditions (Withers et al., 2006) or if the wheel track is disturbed after the passage (Basher and Ross, 2001; Silgram et al., 2010).

The risk of rill erosion is increased in wheel tracks (Evans, 2017). The higher surface runoff velocity on wheel tracks lead to the initiation of rill erosion, especially on hillslopes with slope higher than 3° and on headlands (Evans, 2017). The origin of the eroded soil is on the wheel track and in the vicinity of the wheel track (Basher and Ross, 2001). The spatial variability of soil properties on the wheel track was lower compared to topsoil without wheel tracks. This in-wheel-track variability of soil properties depends on a number of machinery passages (Daraghmeh et al., 2008).

3.4 Soil hydraulic properties under various tillage practices

Soil structure is important for proper soil functioning. Soil organic carbon (SOC) was shown to be a good measure for healthy soil structure (Or et al., 2021), since high SOC can only develop in undisturbed soil structures where biological activity can produce and maintain SOC levels. However, SOC decreases under tillage conditions.

The tillage practice affects the soil hydraulic properties. The no-till often exhibits a decrease in the topsoil saturated hydraulic conductivity compared to conventional tillage (Haruna et al., 2018; Schwen et al., 2011; Sokolowski et al., 2020; Weninger et al., 2021). This decrease was generally contributed to soil surface sealing. In fields with minimum or reduced tillage, the hydraulic conductivity generally decreases as well (Katsvairo et al., 2002; Chang and Lindwall, 1992; Haruna et al., 2018). The extent of the decrease is, however, dependent on the crop rotation (Katsvairo et al., 2002).

The SWRC is also altered by tillage. For instance, the saturated volumetric water content generally decreases for non-tillage and conservation tillage systems compared to conventional tillage (Haruna et al., 2018; Schwen et al., 2011; Głab and Kulig, 2008; Castellini and Ventrella, 2012). The n parameter of van Genuchten's SWRC was shown to slightly decrease for silt loam soil texture (Haruna et al., 2018; Schwen et al., 2011; Głab and Kulig, 2008) or to slightly increase for sandy loam soil texture (Ren et al., 2019) under no till and conservation tillage practice. However, the effect of tillage was only restricted to larger pores (Ahuja et al., 1998). It was also shown that SWRC approaches its pretilled state due to natural soil reconsolidation (Ahuja et al., 1998).

Mulch is often used to reduce the negative effect of tillage. Soil cover such as mulch can reduce the negative impact of raindrops or reduce evaporation, and it can also increase the saturated hydraulic conductivity of the topsoil, the retention of soil water, or the activity of earthworms (Blanco-Canqui and Lal, 2007; Blanco-Canqui et al., 2007). On the contrary, the presence of mulch can increase soil water repellency and subsequently increase surface runoff in some cases (Blanco-Canqui and Lal, 2007). Mulch can also increase the hydraulic conductivity it fields with no tillage management where the hydraulic conductivity is typically reduced Głab and Kulig (2008).

Chapter 4

Hydrological connectivity

The focus on the water routing and pathways has recently been covered by the term hydrological connectivity. Hydrological connectivity is not yet precisely defined and is considered a concept or an approach to hydrological research with an emphasis on spatial and temporal (dis)connection of energies and masses in the landscape (Pringle, 2003). The term has its origin in ecology (Pringle, 2003).

To examine the hydrological connectivity of certain area, wide range of information is needed. In addition to records of hydrological quantities, such as discharge or precipitation, a geological and pedological survey has to be undertaken. Historical data about land-use changes and records of past management (in case of cultivated land) should be considered, as well as records of topography changes and data about the past and present vegetation cover or linear features such as roads, linear vegetation features, etc. (Lexartza-Artza and Wainwright, 2009).

Hydrological connectivity can be studied through components of the hydrological cycle, landscape features, spatial and temporal patterns, or through flow processes (Ali and Roy, 2009). Ali and Roy (2009) reported pros and cons of several study designs for hydrological connectivity research. Bracken and Croke (2007) debated the connectivity components and showed that the runoff generation process and the influence of the antecedent soil moisture strongly vary between humid and arid climates. Bracken et al. (2013) argued that hydrological connectivity needs to be studied not only through more and more dense measurement grids but also through processes which govern the connection of mass or energy in space and time. Approached Bracken et al. (2013) proposed were sometimes called structural[1] and functional[2] connectivity (e.g. Angermann et al., 2017; Jackisch et al., 2017). In Rinderer et al. (2018) structural, functional and effective connectivity was distinguished and analyzed with methods conventionally used in neuroscience. Graph theory was also

---

[1] Structural connectivity is related to static features of soil profile or hillslope such as soil texture and structure, voids or macropore connectivity or landscape features such as linear structures (roads, ditches) or land-use organization.

[2] Functional connectivity focuses to dynamic quantities such as soil water pressure, soil water content, water electrical conductivity or isotopic signature.

used to assess connectivity Zuecco et al. (2019).

Hillslope processes were studied using the concept of structural and functional connectivity by Angermann et al. (2017) and Jackisch et al. (2017). Their research was based on natural rainfall conditions and artificial rainfall experiments on the catchment and hillslope scale. They found the dominance of preferential transport in a few meters of depth on the hillslope with both approaches. This conclusion was drawn based on a poor piezometric response compared to fast water content changes in a large depth (Angermann et al., 2017). Double peak hillslope response also suggested a preferential flow activation (first peak had a larger portion of the pre-event water). Investigation of hillslope structures revealed a large fraction of inter-agregate voids that caused a rapid response despite the silty and cohesive nature of the soil on the hillslope (Jackisch et al., 2017).

Structural connectivity is often assessed via topography-based indices. One of the most popular indices used in the field of hydrology is the topography-wetness index (Beven and Kirkby, 1979). The spill and fill phenomena can be assessed with a combination of indices as shown in (Hopp and McDonnell, 2009). Furthermore, an index of connectivity (IC) was developed specifically to assess the connectivity of water flow and sediment transport within a landscape (Borselli et al., 2008). Although IC was developed with a focus on steep Alpine valleys and alluvial fans, it has been successfully used to identify sediment source areas at submeter scales with a DEM resolution of 1 cm (Prosdocimi et al., 2017).

Functional connectivity can be studied through observations of the temporal changes in inter-(dis)connection between soil surface depressions (Darboux et al., 2002b,a; Antoine et al., 2009). Antoine et al. (2009) introduced a relative surface connection function (RSCf) which is a relationship between the number of filled surface depressions and the area that contributes to runoff. This type of approach was used to observe the surface runoff connectivity of various surfaces (Antoine et al., 2011; Yang and Chu, 2013; Peñuela et al., 2016; Appels et al., 2011, 2016b). The change in soil surface due to natural rainfall and the subsequent response of surface runoff was well explained with the RSCf in (Peñuela et al., 2016). Moreover, RSCf can be used to improve the stepwise surface retention parameter of large-scale hydrological models, as runoff was observed before all deeressions are filled (Antoine et al., 2009, 2011; Peñuela et al., 2016).

Chapter 5

Electrical resistivity tomography

Geophysical methods are widely used to explore the earth subsurface. In principle, these methods indirectly monitor the electric, magnetic, or seismic properties of the subsurface layers. The most common geophysical methods are ground penetration radar, seismic refraction, magnetic methods, and electrical resistivity tomography (ERT) (Schrott and Sass, 2008). ERT has been shown to be promising for its versatility, low cost, and ease of use.

ERT has been widely used in research or practice for landslide investigation (e.g. Colangelo et al., 2008), delineation of contamination plume (e.g. Abudeif, 2015; Wang et al., 2015), studying the mixing of fresh and seawater in coastal areas (e.g. ?Satriani et al., 2012), or for archeological investigation (e.g. Haskins, 2010). ERT was also used to study the soil layers above the bedrock (Chambers et al., 2014; Jeřábek et al., 2017; Besson et al., 2004) or to delineate the geological layers (Zhou et al., 2000; Cheng et al., 2019; Jeřábek and Zumr, 2021).

In principle, ERT is used to obtain spatially distributed electrical resistivity (ρ_e) of the subsurface medium by sending an electrical pulse (current) in the subsurface medium and subsequent measuring of the resulting voltage (electric potential) at the surface. To obtain the spatially distributed ρ_e a numerical inversion must be carried out. The ρ_e correlates with several properties of the subsurface such as porosity (Archie law (Archie, 1942)), water content, bulk density or ions concentration (Samouëlian et al., 2005). Table 5.1 shows a typical ρ_e of some materials.

To obtain a 2D profile, current and potential electrode are placed in different configuration along the measured profile, and the measurement is repeated. Specific configuration of the electrodes during measurement is called the ERT array (5.1) and should be chosen according to the application since different arrays are sensitive to different structures (vertical, horizontal, smoothly delineated, sharply delineated) (Furman et al., 2003). For instance, dipole-dipole electrode array is more suitable for shallow vertical structures (Dahlin and Loke, 1997; Samouëlian et al., 2005), and was therefore used to characterize heterogeneity in the shallow soil profile in Jeřábek et al. (2017). Wenner-Schlumberger array have good

Table 5.1: Typical electrical resistivity ρ_e of the subsurface materials (Palacky, 1988)

		electrical resistivity Ωm	
origin	material	from	to
shield un-weathered rocks	massive sulfides, graphite	0.01	10
	igneous and metamorphic rocks	1000	100000
weathered layered		1	10000
glacial sediments	clays	3	100
	tills	30	3000
	gravel and sand	30	10000
sedimentary rocks	shales	50	300
	sandstone and conglomerate	50	10000
	lignite, coal	10	700
	dolomite, limestone	1000	100000
water, aquifers	salt water	0.3	1
	fresh water	2	100

vertical and horizontal sensitivity, depth of investigation, and signal strength (Samouëlian et al., 2005) and was therefore used to investigate the subsurface structures at the Nučice experimental catchment, as described in (Jeřábek and Zumr, 2021).

By this procedure, an apparent ρ_e is obtained; an aggregated information of the ρ_e in the subsurface. ρ_e is obtained with the formula $\rho_e = kV/I$, where k is a geometric factor (Figure 5.1), V is the voltage (measured with potential electrodes) and I the el. current (measured with el. current electrodes) To obtain the spatially distributed ρ_e a numerical

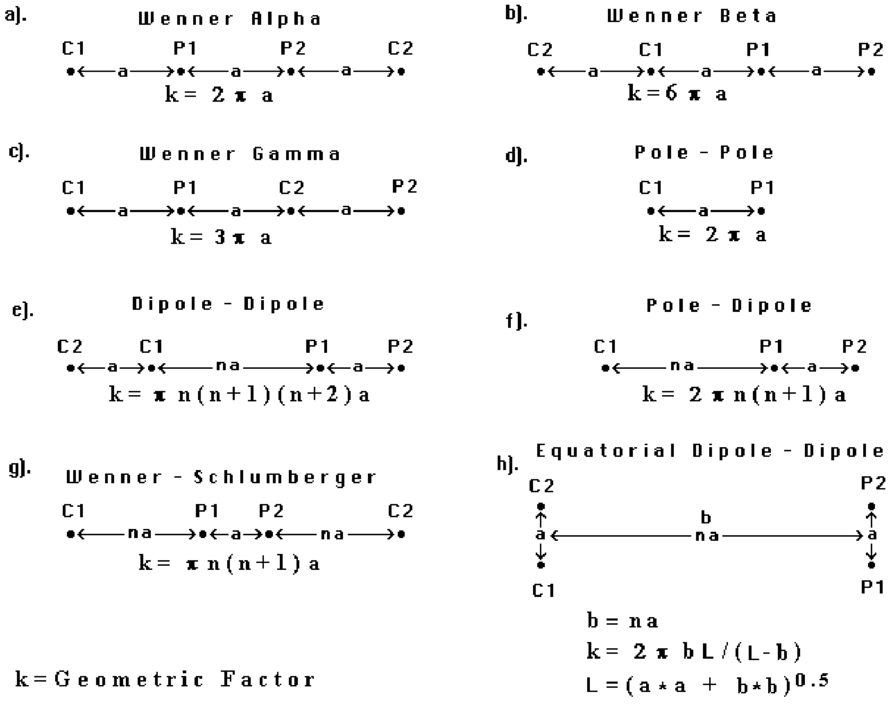

Figure 5.1: The example of electrode arrays for the ERT measurement (Loke, 1999)

inversion must be performed (Loke, 2004). In this procedure, the spatially distributed ρ_e are used as parameters to model the apparent ρ_e created by a given array. The goal is to find the best fit between the modeled and measured apparent ρ_e. The numerical inversion is complicated processes, since thousands of points of ρ_e may be optimized.

Outcomes

The most commonly reported factors affecting the runoff formation at headwater catchments are: the microtopography of the soil surface, morphology of the subsurface layers, depth of the soil profile and the soil hydraulic properties heterogeneity. All of which applies also for the agricultural catchments where the shallow soil profile is affected by frequent agricultural management and fast plant grow. Besides the vegetation, presence of compacted layer and wheel track formation are the key features affecting the runoff generation at agricultural sites. However a relevance and strength of such features on the runoff generation is not yet fully understood.

The most important findings of the literature review could be drawn as follows:

- The compacted layer plays an important role for the runoff formation at agricultural areas.
- Topsoil and subsoil on compacted fields have distinct properties due to agricultural activity.
- The soil surface topography or topography of low-permeable soil layers plays an important role in runoff formation.
- Engagement of macropores is dependent on the surface micro-topography or on the antecedent soil moisture conditions.
- Hydrologic connectivity is a versatile tool for hydrological research and can be used in various spatial scales.
- Geophysics is a suitable non-destructive tool for soil science investigation.

Field experiments and numerical modeling to study the runoff formation

Chapter 6

Topsoil and subsoil delineation - geophysical approach

Shallow profile soil hydraulic properties (SHP) play a key role in the runoff process at the small catchment scale. However, the spatial distribution of SHPs or delineation between the soil layers is still a challenge, as there are no direct methods to measure it. Additionally, the hydrogeological water divide is neither readily available nor easy to obtain in most cases. Geophysical methods are valuable tools for investigating subsurface structures, as described in Chapter 5.

Electrical resistivity is correlated with soil characteristics, and in many cases it is not easily distinguishable, which plays a key role. For this reason, additional information is commonly provided for a better interpretation of the electrical resistivity of the subsurface.

Geophysical investigation using the electrical resistivity tomography (ERT) method was performed in two localities on arable soils. The investigation shown in this chapter was also published in the following publications:

- Jeřábek, J. and Zumr, D. (2021). Geophysical survey as a tool to reveal subsurface stratification at within a small agricultural headwater catchment: a case study. The Civil Engineering Journal, 30(3). (60 %)

- Jeřábek, J., Zumr, D., Krása, J., and Dostál, T. (2018). Monitoring of runoff processes during an artificial rainfall on a freshly tilled soil. In TRANSPORT VODY, CHEMIKÁLIÍ A ENERGIE V SYSTéME PÔDA-RASTLINA-ATMOSFéRA, Bratislava, SK. Institute of Hydrology SAS. (60 %)

- Jeřábek, J., Zumr, D., and Dostál, T. (2017). Identifying the plough pan position on cultivated soils by measurements of electrical resistivity and penetration resistance. Soil & Tillage Research, 174. (60 %, 8 citations)

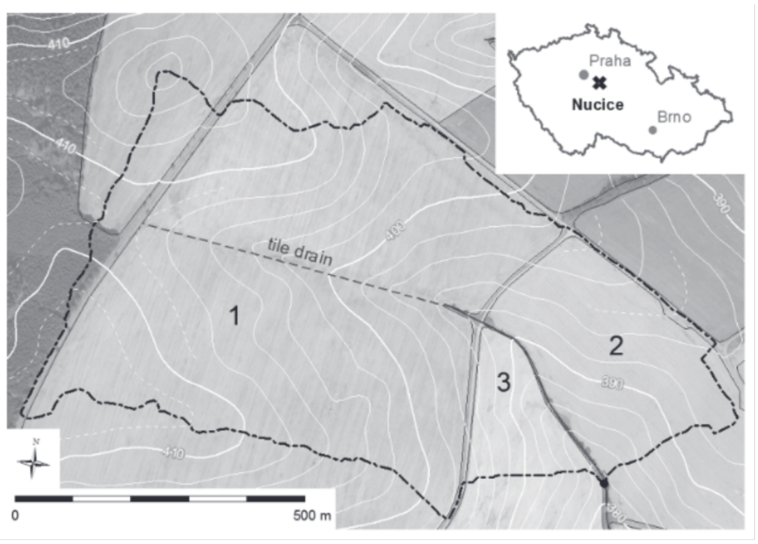

Figure 6.1: Nučice catchment. The numbers denote the three fields parcels (Zumr et al., 2015).

6.1 Nučice site - deep structures

An investigation of the deep structures of the experimental site Nučice was published in Jeřábek and Zumr (2021). Key findings of the study are summarized below. For more information, see the enclosed reprint of the original manuscript in Appendix A.

The Nučice site is an experimental catchment established to study shallow runoff processes and the rainfall-runoff response of typical agricultural land (Li et al., 2021) where shallow subsurface runoff was identified as predominant (Zumr et al., 2015). The topsoil and the compacted subsoil properties are the key soil layers affecting the runoff generation. However, limited information was known about the subsurface configuration of the catchment. Therefore, electrical resistivity tomography was used to identify those subsurface structures.

Experimental Nučice catchment is located at the central part of the Czech Republic (Figure 6.1). The catchment area is approximately 53 ha with a mean slope of 3.9%. The majority of the catchment is covered with arable land (96.4%). The bedrock consists of layers of sandstone, siltstone and conglomerate from the Carboniferous and Permian geological period.

A total of five ERT profiles were measured at the experimental site during the investigation. Two of the profiles were in the thalweg direction and three were perpendicular to the thalweg. Distribution of subsurface layers can be observed as shown in Figure 6.2. Two high electrical resistivity (ρ_e) layers were associated with low permeability. Shallow high ρ_e layer coincide with the soil surface, while the deeper high ρ_e layer had the same inclination throughout the catchment. It can be hypothesized that the water that percolates to the deeper layers may be transported via pathways with do not correspond to the soil surface topography. Also, the shape and declination of the deep layers were different in the upper and lower parts of the catchment, which indicated a heterogeneous geological setting even in a relatively small area. Although the indirect ERT method is hard to interpret quantitatively, the information presented in Jeřábek and Zumr (2021) improved the understanding of the water transport regime within the catchment and can be used for the modeling of the catchment scale.

6.2 Nučice site - depth of the compacted layer

Investigation of shallow soil layers and their heterogeneity using electrical resistivity tomography was published (Jeřábek et al., 2017). Reprint of the paper is enclosed in Appendix A for more details.

ERT was completed with mechanical penetration and measurements of soil physical properties. In addition, two electrode spacings of 0.1 and 0.2 m were tested. The measurements took place in two fields with slightly different development of the compacted layer. The objective of the study was to identify the feasibility of ERT to determine the position and spatial uniformity of the compacted layer.

The results of the study suggested that the ERT can be used to identify the position of the compacted layer. This finding was supported by mechanical penetration measurements and soil sampling, which exhibited a high correlation with electrical resistivity. The success was dependent on the electrode spacing, which should be chosen according to the anticipated depth of the compacted layer and also to the topsoil water saturation. The two differently tilled soils were identified even from the apparent el. resistivity values (values before numerical inversion). Semivariograms showed that the compacted layer exhibited one or two orders of magnitude smaller semivariance compared with the topsoil and that the scale of the topsoil semivariance was in orders of centimeters in topsoil while the compacted layer semivariance changed on the scale of several meters. ERT was shown to be a useful tool for topsoil delineation and for the evaluation of topsoil and subsoil spatial heterogeneity if combined with geostatistical methods. However, the morphology of the soil layers was not observed.

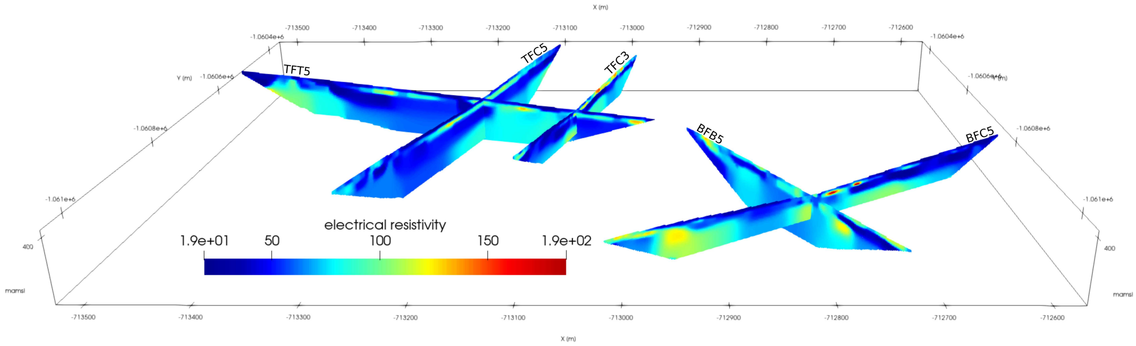

Figure 6.2: ERT profiles shown at its real positions at the Nučice catchment

6.3 Řisuty site - delineation of a soil profile affected by wheel tracks

Electrical resistivity tomography (ERT) measurement of the shallow soil profile affected by the presence of the wheel track was partially published in Jeřábek et al. (2018). The following text shows analysis based on published and unpublished data.

A series of ERT measurements were performed after artificial rainfall experiments (ARE). The aim of the geophysical measurement was to identify the effect of the compacted layer and the wheel tracks on infiltration and water redistribution. ERT profiles were measured slopewise along with the ARE plot or in the perpendicular direction to the longer edge of the ARE plot. ERT measurements were conducted several times after the rainfall experiment to capture the redistribution of the infiltrated water. The summary of all ERT measurements is shown in Table 6.1.

6.3.1 Study site

Experiments were carried out on experimental plots located on an agricultural site ca 30 km north-west of Prague, Czech Republic, at coordinates 50°13'2.0"N, 14°1'2.2"E (Figure 6.3). The site elevation is 310 – 315 m a.s.l. The annual mean temperature is 8°C and the mean annual precipitation is 500 mm. The climate is characterized as humid continental. The study site is located at the edge of a larger field in which ordinary agricultural production takes place. The topsoil is classified as loam with 18.3% of clay, 33.8% of silt and 47.9% of sand at the site. The soil type is Cambisol.

6.3.2 Artificial rainfall experiments

A total of five artificial rainfall experiments (AREs) were performed during two independent experimental campaigns. The first experimental campaign was conducted in September 2018 (hereafter referred to as campaign No. 1), and the second was conducted in June 2019 (hereafter referred to as campaign No. 2). Two wheel-track orientations were examined: slopewise direction (SWT) and contour line direction (CWT). The experimental setup was complemented with reference measurements on plots with no wheel tracks (NWT). A rainfall of 30 mm/hour intensity was applied, which is the rainfall of the 5-year return period at the location (Kašpar et al., 2021) was applied.

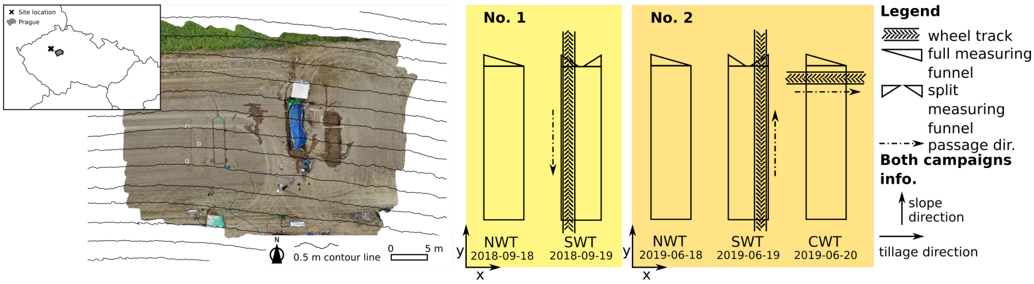

Figure 6.3: Location and orthophoto of the experimental Řisuty site on the left (orthophoto by Tomáš Laburda and Josef Krása). Experimental plot setting of campaign No. 1 and campaign No. 2 on the right (Jeřábek et al., 2022).

Table 6.1: Overview of ERT transects measurements performed after each artificial rainfall experiment. None to two repetitions were performed. ERT transect was either aligned along the plot (in downslope direction) or perpendicularly to the plot (in the contour line directions).

campaign	date time of the start	hours after the rainfall	WT orientation	ert transect orientation
No 1	19.9.2018 12:30	17.75	NWT	along the plot
No 1	19.9.2018 17:40	22.92	NWT	along the plot
No 1	20.9.2018 9:10	16.42	SWT	along the plot
No 1	20.9.2018 11:15	27.67	SWT	perpendicular to plot
No 2	18.6.2019 19:40	2.75	NWT	perpendicular to plot
No 2	19.6.2019 8:30	14.58	NWT	perpendicular to plot
No 2	19.6.2019 19:30	25.08	NWT	perpendicular to plot
No 2	19.6.2019 21:00	3.00	SWT	perpendicular to plot
No 2	20.6.2019 8:00	14.00	SWT	perpendicular to plot
No 2	20.6.2019 18:00	1.50	CWT	along the plot

6.3.3 Experimental plots

All experimental plots had an inclination of approximately 10% and were 8 m long and 2 m wide. Each experimental plot was delineated by metal plates inserted about 5 cm into the soil and equipped with a funnel for surface runoff and soil loss collection. The seedbed was prepared, and wheel tracks were created several days before the experiments. The tillage depth was 12 to 15 cm in both campaigns. In all cases, no natural rainfall occurred between the topsoil preparation and the experiments.

A tractor with trailed stubble cultivator was used to create wheel tracks during No. 1 campaign and tractor and water tank (with approximately 12 m^3 of water) was used to create the wheel tracks during campaign No. 2. The maximum static ground pressure of a single tire was estimated using the *soilphysics* R package (de Lima et al., 2021) at 201 kPa and 272 kPa for the tractor front and rear axle and 439 kPa for the stubble cultivator during the No. 1 campaign and to 206 kPa and 236 kPa for the front and rear wheels of the tractor and 455 kPa for the water tank's wheels during the No. 2 campaign. The bulk density of the tilled soil and soil on the wheel tracks was 1.31 ± 0.09 $g.cm^{-3}$ and 1.40 ± 0.1 $g.cm^{-3}$ during the No. 1 campaign, and 1.24 $g.cm^{-3}$ and 1.40 $g.cm^{-3}$ during the No. 2 campaign.

6.3.3.1 Electrical resistivity tomography

The electrical resistivity tomography (ERT) was used in a similar manner as in the case of the Nučice catchment measurements described in Jeřábek et al. (2017). The dipole-dipole array with an electrode spacing of 0.2 m was used in all measurements. ERT measurements are summarized in Table 6.1. In addition, a pit was excavated during the No. 1 campaign to compare the depth of the infiltration front with the ERT measurement.

6.3.4 Results & Discussion

The electrical resistivity (ρ_e) of the NWT plot of campaign No. 1 is shown in Figure 6.4. The wet topsoil is clearly visible to a depth of 20 cm in both profiles. The topsoil exhibited the lowest ρ_e values. The lower ρ_e was also observed deeper in the profile. Both profiles also exhibited areas of higher ρ_e which could indicate soil subjected to wheel track compaction

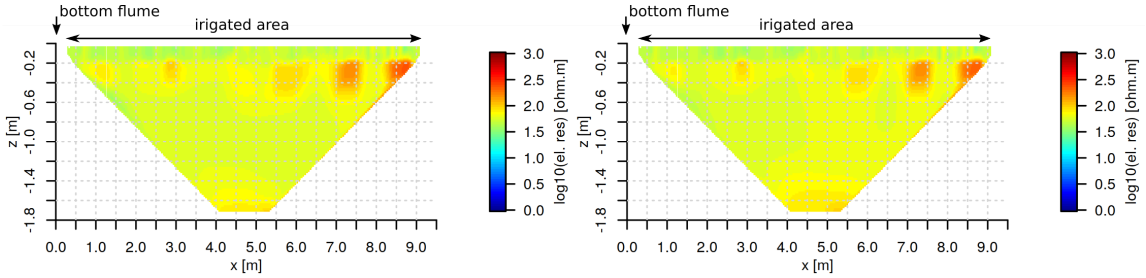

Figure 6.4: Transects measured at the NWT plot during the No. 1 campaign. Both transects were measured in the along the plot orientation. Left: electrical resistivity 17.75 hours after the rainfall. Right: electrical resistivity 22.92 hours after the rainfall.

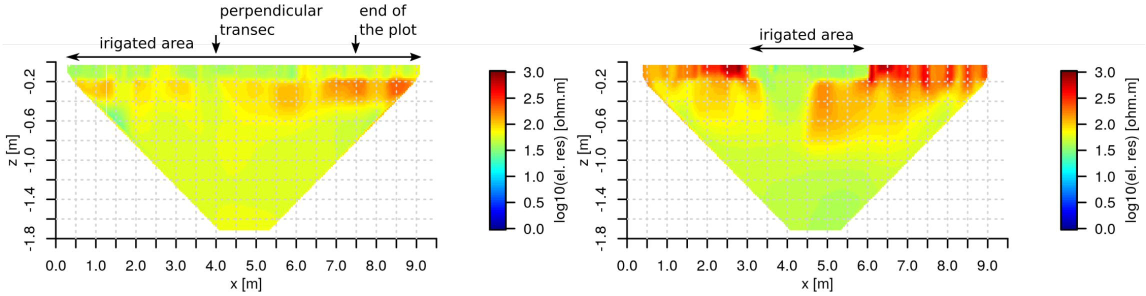

Figure 6.5: Transects measured at the SWT plot during the No. 1 campaign. Left: transect measured in the along the plot orientation 16.42 hours after the rainfall. Right: transect measured in the perpendicular direction to the plot 27.67 hours after the rainfall.

(as explained below). The two measurements took place relatively long after the end of the rainfall, but shortly after each other (see Table 6.1); therefore, no significant water redistribution was observed.

Two ERT transects were measured on the SWT plot during the No. 1 campaign (Table 6.1). In this case, one profile was measured in along-the-plot and one in a perpendicular-to-plot direction (Figure 6.5). The ρ_e exhibited patterns similar to the NWT plot shown for the along-the-plot measurement (Figure 6.4). However, the high ρ_e areas are more pronounced in this case. This could have been caused by the presence of a wheel track presented approximately 40 cm next to the ERT transect. The irrigated area is clearly visible at the perpendicular-to-plot measurement (Figure 6.5). The effect of irrigation resulting in lower topsoil ρ_e is clearly visible. The soil below the wheel track exhibited a relatively higher ρ_e compared to the soil without a wheel track.

A pit was excavated to investigate the ρ_e distribution below the plot on the SWT plot. As shown in Figure 6.6 the high ρ_e area corresponded to a drier soil below the wheel track. This is the evidence of wheel track effects on infiltration and could explain the presence of high ρ_e locations in the NWT profiles in Figure 6.4. Emerging bedrock was visible on the left side of the pit (Figure 6.6). The high ρ_e below the depth of 60 cm can indicate that the emerging bedrock was relatively permeable and that it allowed the water to percolate deeper through the soil.

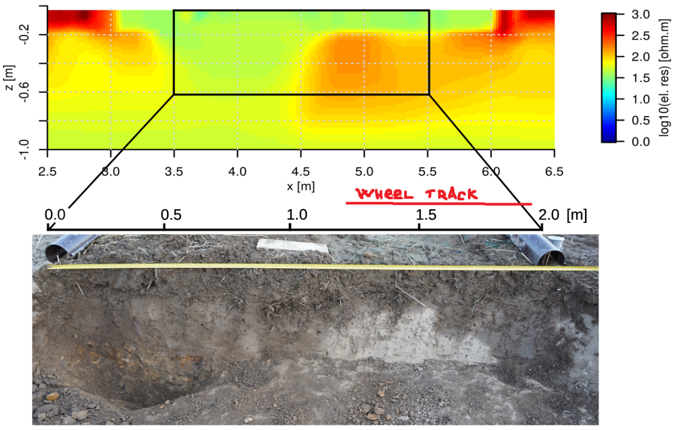

Figure 6.6: Detail of the ERT transect measured at the SWT plot during the No. 1 campaign and excavated pit along the transect.

All transects on NWT and SWT plots were oriented in the perpendicular-to-plot direction during the second campaign No. 2. In all cases, the irrigated area with lower ρ_e values, as well as the high ρ_e non irrigated topsoil were clearly presented as it is shown in Figures 6.7 and 6.8. In the case of the campaign No. 2, the first measurement in both plots was made shortly after the end of the rainfall experiment (2.75 and 3 hours, Table 6.1). The second set of measurements on the NWT and SWT plots was performed 12 and 11 hours after the first measurement, respectively. The decrease in ρ_e associated with an increase in volumetric water content was observed only in the irrigated area. The decrease in ρ_e continued at the third survey in the NWT plot which was performed another 12 hours later. Higher ρ_e values were observed in the irrigated area below the wheel track on the SWT plot. However, the contrast in ρ_e was less pronounced compared to the excavated pit plot.

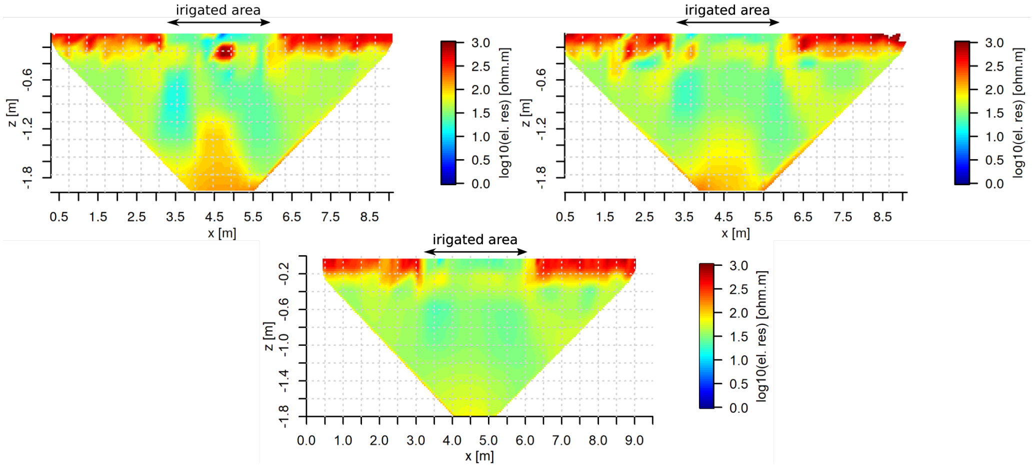

Figure 6.7: Transects measured at the NWT plot during the No. 2 campaign. All transects were measured in the perpendicular direction. Upper left: electrical resistivity measured 2.75 hours after the rainfall. Upper right: electrical resistivity measured 14.58 hours after the rainfall. Lower: electrical resistivity measured 25.08 hours after the rainfall.

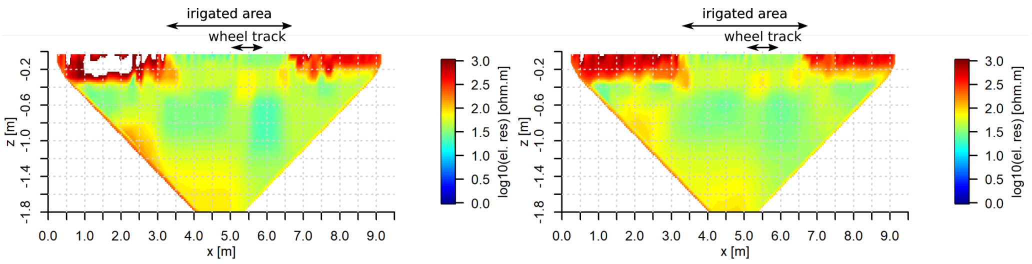

Figure 6.8: Transects measured at the sWT plot during the No. 2 campaign. All transects were measured in the perpendicular direction. Left: electrical resistivity measured 3 hours after the rainfall. Right: electrical resistivity measured 14 hours after the rainfall.

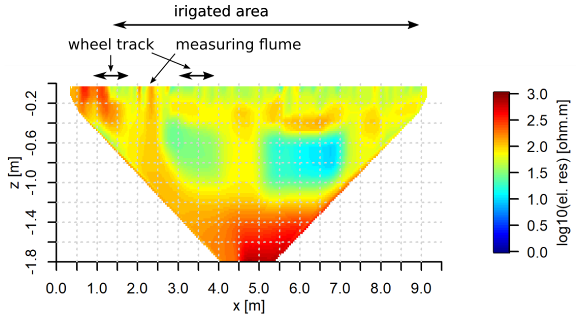

Figure 6.9: Transect measured at the CWT plot during the No. 2 campaign. Transect measured in the along the plot orientation. Electrical resistivity measured 1.5 after the rainfall.

A single measurement was made in the CWT plot during campaign No. 2 (Figure 6.9). The wheel track which was created before the experiment could not be distinguished from similar high ρ_e areas in the ERT measurement. However, a higher ρ_e layer was observed in depths of 20 to 60 cm. This layer could correspond to a compacted layer. Lower ρ_e was observed at depths between 60 and 120 cm.

The clear distinction between the high ρ_e tilled topsoil and the low ρ_e subsoil was reported in the literature (Besson et al., 2004; Basso et al., 2010). This correlation was attributed to the difference in bulk density between topsoil and subsoil. In Besson et al. (2004) the wheel tracks were also identified; however, in their case the wheel tracks only change ρ_e in the topsoil and not in the subsoil, unlike in the presented study where the wheel tracks were visible due to the low water content in the wheel track.

6.3.4.1 Penetration resistance

As was shown in (Jeřábek et al., 2017) for the case of the Nučice site experiments, mechanical penetration resistance correlates with the electrical resistivity. Mechanical resistance (p_{pr}) of the dry and wet soil (in and out of the wheel track) is shown in Figure 6.10 for campaign No. 1. The measurements took place in the vicinity of the ARE plots (Figure 6.10a) or in the SWC plot (Figure 6.10bc).

It was not possible to penetrate the device below ca. 20 cm during the dry soil and wet soil wheel track soil measurement (Figure 6.10ab) due to the high p_{pr}. ERT profiles only exhibited sharp degrease in ρ_e at a depth of ca. 20 cm, which corresponds to the results of

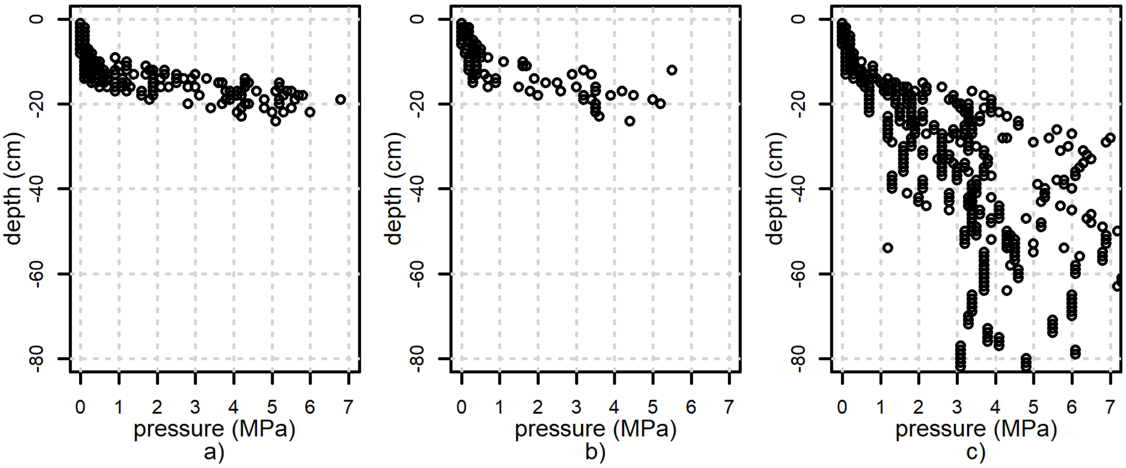

Figure 6.10: The mechanical penetration of the dry a), wet wheel track b) and wet non wheeled soil.

the Nučice site experiment. The p_{pr} was almost zero in the first 10 cm of the soil, which corresponded to the loose nature of the soil material created by the previous preparation of the seed bed. Only the measurement performed under wet conditions could penetrate below the depth of 20 cm (Figure 6.10c). The wet soil measurement exhibited the highest p_{pr} variability in the depth of around -35 cm. This variability may correspond to high ρ_e variability shown in ERT profiles (Figure 6.10c).

6.4 Key fingings

Measurements of electrical resistivity, mechanical penetration resistance, and soil physical properties were performed at two agricultural sites in order to

- assess the stratification of the subsoil layers of the catchment
- assess the presence and spatial uniformity of the compacted layer,
- assess the presence of wheel-track compaction and its effect on the infiltration and water redistribution, and

The measurements showed that the compacted layer is present in the soil profiles of both sites and that its position can be identified with the ERT. According to the semivariance, the compacted layer exhibits some spatial variability, but the spatial variability of the topsoil is higher by one or two orders of magnitude. This leads to the conclusion that the compacted layer is macroscopically uniform along a 2D transect.

The presence of wheel tracks clearly affected the water redistribution process. The results of the Řisuty site suggest that the wheel track compaction remains apparent in the subsoil even after topsoil is plowed. The soil under the wheel track stayed dry even after the substation rainfall amounts.

It was demonstrated that the ERT technique is a useful tool for making a qualitative assessment of the spatial characteristics of the compacted layer and the wheel tracks in

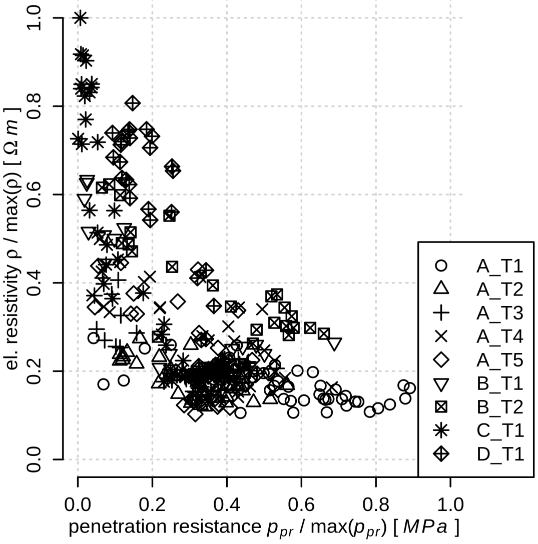

Figure 6.11: Correlation between normalized penetration resistance (p_{pr}) and electrical resistivity (ρ_e) (Jeřábek et al., 2017).

cultivated fields. However, the success of the approach depends on the current saturation state of the soil during the measurement and on the suitable electrode spacing selected according to the depth of the topsoil. The water saturation should not be lower than the field capacity. The electrode spacing is recommended to be approximately half the expected depth of the topsoil. This is inhered from the used ERT array. If all above recommendations are met, the ERT will show the topsoil layers delineation as shown in Figure 6.11.

Chapter 7

Soil surface connectivity of tilled soil with presence of wheel tracks

The work presented in this chapter was submitted to the Journal of Hydrology and was reviewed by two reviewers. The revised manuscript was submitted to the journal at the time of this thesis submission (Jeřábek et al., 2022). The reprint of the submitted paper is in Appendix A. Therefore, a summary of the work is given in this chapter. The deuterium tracer measurements and the description of the SMODERP2D model are presented in this chapter in addition to the results submitted in Jeřábek et al. (2022).

Ph.D. candidate was involved in the SMODERP2D model development. This work resulted in several publications where the candidate co-authored (software development, text reviewing) (Kavka et al., 2022; Landa et al., 2019) and in the version of the SMODERP2D model SMODERP Line where the candidate contributed to the code of the model (Kavka et al., 2020).

Series of artificial rainfall simulations (Kavka et al., 2018) were performed to study the effect of rainfall and runoff on soil surface microtopography in tilled soil with wheel tracks. During the investigation, surface runoff, sediment transport and soil surface microtopography were monitored at three plots of area 16 m^2 with slope wise oriented wheel tracks (SWT), contour line oriented wheel tracks (CWT) and a plot without wheel tracks (NWT).

The concepts of structural and functional hydrological connectivity were used for the investigation. Structural connectivity was investigated in terms of normalized downslope distance (NND) and flow accumulation algorithm. A simplification of the concept of relative surface connectivity function (Antoine et al., 2009) was used to assess functional connectivity. The investigation was completed with random roughness of the soil surfaces.

The digital elevation models (DEMs) needed for both connectivity metrics were obtained before and after the artificial rainfall experiments to see the temporal changes of the microtopography. The results obtained with the connectivity metrics were compared with direct measurement for validation.

The investigation presented below had two goals:

- Assess the effect of wheel tracks on surface runoff routing and
- to investigate the temporal changes of surface microrelief during a rainfall.

7.1 Material & Methods

The experiments were carried out at the experimental site Řisuty. The location and experimental plots were described in Sections 6.3.1 and 6.3.3.

7.1.1 Microtopography observation

The close-range Structure from Motion (SfM) method was used to obtain the high-resolution digital elevation model for each plot. Sony A6000 mirrorless camera with an APS-C size sensor with a resolution of 24 Mpx and equipped with a standard Sony 16-50 mm zoom lens fixed on 16 mm was used to obtain the DEMs before and after the rainfall. Photogrammetry reference targets were installed at the perimeter of each plot at a mutual distance of 1 to 2 meters. Agisoft Photoscan Professional 1.4.2 build 6205 software (Agisoft LLC) was used to reconstruct the images and obtain the DEMs (Laburda et al., 2021). The resolution of 1 cm was used for further analysis to keep high detail of the images and reduce the noise in the data. The DEMs were provided by my colleges Josef Krása and Tomáš Laburda.

7.1.2 Random roughness

Random roughness (RR) was calculated for plots before and after rainfall soil surface conditions, and for the in-the-wheel track and outside-the-wheel track soil. The formula was adopted from (Taconet and Ciarletti, 2007) as:

$$RR = \sqrt{\frac{1}{(n-1)(m-1)} \sum_{i}^{n} \sum_{j}^{m} (Z_{i,j} - \bar{Z})^2},$$

A manual detrending by plain was done prior the RR calculation to level all DEMs.

7.1.3 Structural connectivity

Normalized downslope distance (NDD) and flow accumulation raster were used to assess structural connectivity. NDD expresses the complexity of the surface topography from the perspective of a moving particle whose trajectory is begin tracked. Terrain analysis tool TauDEM (Tarboton, 2015) was used to calculate the downslope distance and flow accumulation raster for each of the plots. The downslope distance raster was further normalized by the shortest distance to the bottom of the plot to compensate for the relative position of each cell in the raster along with the plot. NDD is described in Figure 7.1 and was calculated with the formula

$$NDD = \frac{L_d}{L_s}, where \quad NDD = \{x \in \mathbb{R} \mid 1 \leq x < \infty\},$$

where L_d is the pathhway length of flowing particle to the bottom of the plot and L_s is the shortest length to the bottom of the plot.

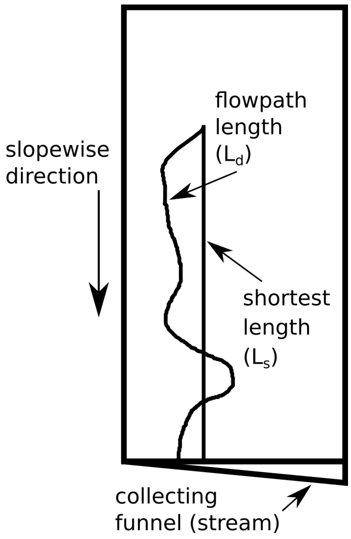

Figure 7.1: Diagram explaining the lengths of the normalized downslope distance index

7.1.4 Functional connectivity

Functional connectivity refers to a concept presented e.g. by Darboux et al. (2002a) or Antoine et al. (2009), where a surface runoff model is used to assess the connectivity of soil surface. SMODERP2D model was used for this investigation (Kavka et al., 2022). Detailed information on the model is given below.

Functional connectivity was expressed as a relationship between surface runoff coefficient and actually filled surface depression storage of the modeled surface. An example of this relationship is shown in Figure 7.2. The curve gradient expresses how fast surface runoff connects surface depressions. A low gradient expresses low connectivity because the soil depressions are being filled without any substantial increase in runoff. The high gradient indicates high connectivity since the soil surface depression connects to the runoff immediately.

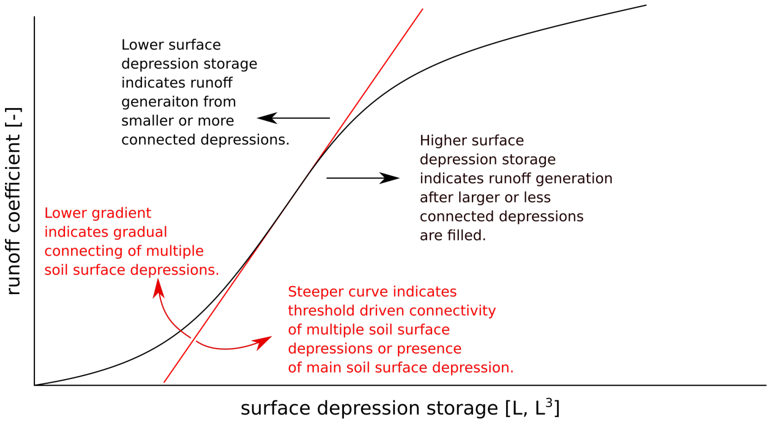

Figure 7.2: Diagram explaining the shape and shifts of the functional connectivity index

7.1.4.1 SMODERP2D model description

SMODERP2D model is a physically-based episodic model for hydrology and erosion applications. The model has been developed at the Department of Landscape Water Conservation (Dostál et al., 2000). Only a sheet flow calculation is shown below.

The model is based on the cell-by-cell evaluation of mass balance equation which can be written for each cell in the model as:

$$\frac{\mathrm{d}h}{\mathrm{d}t} = (q_{in} + ep) - (q_{out} + inf), \tag{7.1}$$

where h stands for the surface water level $[L]$, q_{in} and q_{out} for sheet overland inflow and outflow in and from a given raster cell $[L.t^{-1}]$, ep for an effective precipitation $[L.t^{-1}]$ and for inf for an infiltration rate $[L.t^{-1}]$.

The kinematic wave approach is used in the calculation. The momentum is therefore expressed in terms of the power law:

$$q = ah^b, \tag{7.2}$$

where a and b are power law parameters $(-)$. The equation (7.2) can by expressed in a form of the Manning-Strickler formula.

$$q = Xi^Y h^b, \tag{7.3}$$

where X and Y stand for empirical parameters $(-)$ and i for surface slope $(-)$.

The infiltration component of the mass balance equation (7.1) is calculated using Philip's infiltration equation (Philip, 1957b)

$$inf = 1/2St^{-1/2} + K_s, \tag{7.4}$$

where S stands for sorptivity $[L.t^{-1/2}]$ and K_s for saturation hydraulic conductivity $[L.t^{-1}]$.

Potential precipitation can be reduced due to interception (which is not considered in the presented study) and surface retention. Surface retention is defined as a single value for each cell. The value needs to be exceeded by actual precipitation before runoff can be produced. However, the infiltration capacity must be exceeded before the surface retention can begin to fill..

Surface runoff flow routing is based on the one-directional flow algorithm D_8 (O'Callaghan and Mark, 1984). The inflow to the cell i is defined as a sum of outflows from adjacent cells as

$$q_{in,i} = \sum_{j}^{m} q_{out,j} \tag{7.5}$$

where j stands for the index of adjacent up-slope cells identified by the D_8 flow algorithm and m is the set of the up-slope cells which flow in cell i.

Table 7.1: Soil hydraulic parameters of Loam soil used to calculate the functional connectivity with the SMODERP2D model (SMODERP2D development team, 2017)

parameter name	parameter value
saturated hydraulic conductivity K_s $[m.s^{-1}]$	1.67E-06
sorptivity S $[m.s^{-1/2}]$	1.39E-04
shallow water flow eq. parameter b [-]	1.73
shallow water flow eq. parameter X [-]	10.08
shallow water flow eq. parameter Y [-]	0.56

The time derivative in equation (7.1) is calculated using the explicit method. Therefore, the computation is sensitive to the time step size. The size of the time step is controlled with the Courant criterion, which must be kept below the theoretical maximum value 1 or in practice even lower (Zhang and Cundy, 1989; Esteves et al., 2000). The next time step $t+1$ of the equation (7.1) with incorporating eq. (7.5) is calculated for cell i as:

$$h_i^{t+1} = h_i^t + \mathrm{d}t \left(\sum_j^m q_{out,j}^t + ep_i^t - q_{out,i}^t - inf_i^t \right)$$

7.1.4.2 SMODERP2D model application

To account for soil surface depression storage, surface retention was calculated by subtracting DEM with its sinkless form. The soil parameters were assumed to be uniform and are shown in Table 7.1. All plots were exposed to a uniform rainfall intensity of 30 mm h^{-1}.

7.1.5 Runoff and sediment sampling

The runoff water with suspended sediment was sampled during the artificial rainfall experiment (ARE), see Section 6.3.2 for more details. The duration of the experiments ranged from 290 to 433 minutes. Collection funnels were installed at the bottom of each experimental plot to collect the surface runoff and the detached soil particles. On the SWT plot, two flumes were installed in order to separate water flowing through the wheel track and the water flowing through the adjacent tilled soil surface (Figure 6.3). The sampling interval had been prolonged with the duration of the experiment and reached 20 minutes when the runoff was approaching a steady state.

7.1.6 Tracer application

Deuterium was added to the rainfall water as a tracer during the No. 2 campaign in order to explore the mixing of the water on the soil surface with various connectivity. The hypothesis is that a more connected soil surface will exhibit faster mixing of the pulse and pre-pulse water compared to a less connected soil surface. The tracer of various concentrations was applied during each campaign after the runoff reached semi-steady-state conditions.

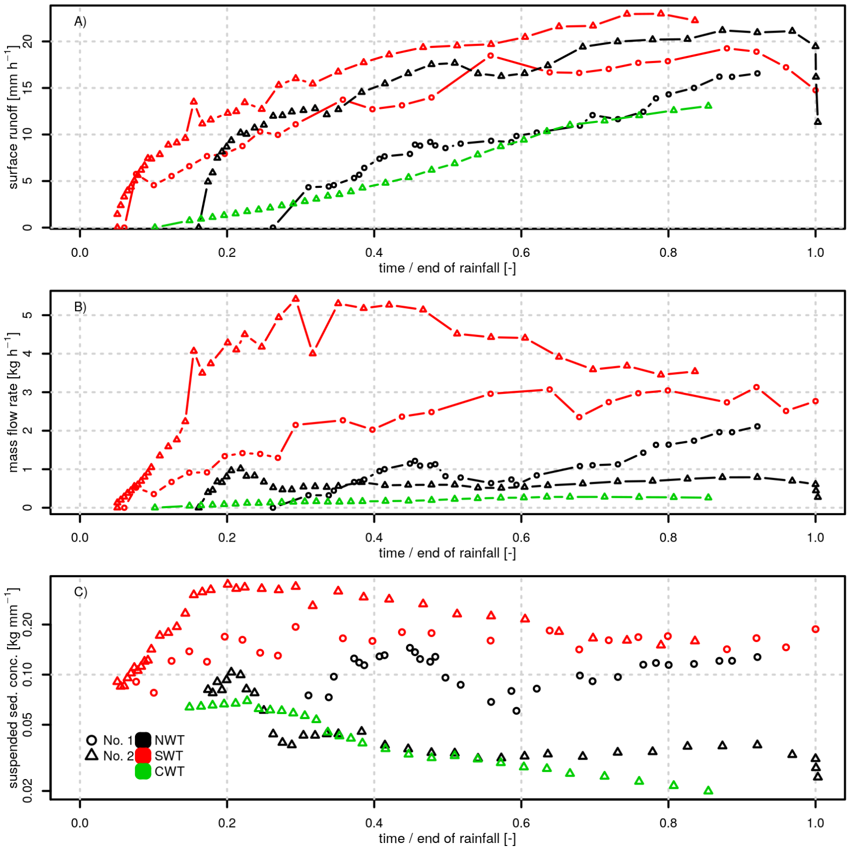

Figure 7.3: Development of: A) the surface runoff, B) the sediment flow rate and C) the concentration of the suspended solids in time. The time is normalized to the duration of the experiment.

7.2 Results & Discussion

7.2.1 Runoff and soil loss from soil with wheel tracks

The surface runoff and sediment transport are shown in Figure 7.3. SWT plots exhibited the shortest lag time before the runoff was initiated and the highest mass flow rate. The NWT plots exhibited a longer lag time than both SWT plots; however, the surface runoff reached similar values as the SWT plot during the No. 2 campaign, while the No. 1 NWT plot was similar to the CWT plot in terms of runoff.

The SWT plots were equipped with a split collecting flume in order to measure the runoff from the wheeled and unwheeled half of the plot separately. During the No. 1 campaign the runoff occurred only in the wheeled soil, while both halves of the plot — wheeled and unwheeled — contributed to the runoff at the SWT plot during the No. 2 campaign.

7.2.2 Connectivity of the soil surface

The random roughness of all plots is shown in Figure 7.4. The decrease was observed in all plots and also in the wheel track itself, suggesting the relocation of soil particles also in the wheel track. The decrease in roughness was attributed to the effect of surface runoff and rainfall in (Bauer et al., 2015; Zobeck and Onstad, 1987).

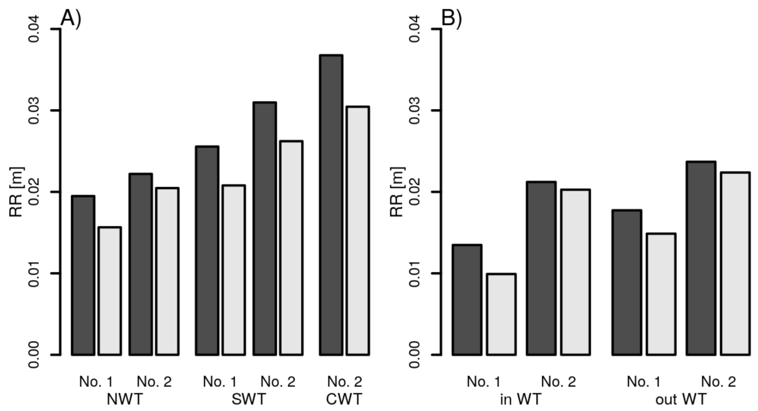

Figure 7.4: A) Bar plots of the random roughness for all wheel track configurations and for before- and after-rainfall soil surface conditions. B) Bar plots of the random roughness of the wheel track (in WT) and the surrounding soil surface (outside WT) on the SWT plot.

The structural connectivity is shown in terms of the NDD histograms in Figure 7.5. NWT and CWT plots exhibited the highest values of NDD for the before rainfall conditions, suggesting the lowest structural connectivity. The SWT plots exhibited bimodal histograms for the before rainfall conditions.

The flow accumulation rasters identified the main drainage pathways (Figure 7.5). Two main flow paths were observed in the SWT plots, which correspond to the bimodal histogram of NDD in the before-rainfall soil surface conditions. After the rainfall, the SWT during the No. 1 campaign changed to unimodal distributions of NDD. This corresponds to the change in the main flow paths shown in flow accumulation rasters where the whole plot surface was drained via the wheel track. The bimodal histogram remained unchanged for the after-rainfall soil surface conditions in the case of the No. 2 campaign which corresponded to the flow accumulation raster where the two main flow paths – on the wheel track and outside the wheel track — were indicated.

Interestingly, NDD increased in the NWT and CWT plots for the after-rainfall soil surface conditions. This effect was the most notable in the CWT plot, where the relocation of soil due to rainfall and runoff impact prolonged the main flow pathways as shown in the flow accumulation raster in Figure 7.5E.

The results of functional connectivity are shown in Figure 7.6. The before-rainfall soil surface conditions exhibited the highest connectivity in both SWT plots and the lowest connectivity in the CWT plot. The reference plot exhibited intermediate functional connectivity. The main cause of this was the different surface depression storage which was the highest in the CWT plot. SWT plots became connected almost immediately after the rainfall started which is indicated by an immediate increase in the runoff coefficient. The situation changed for the soil surface conditions after rainfall (Figure 7.6) where the NWT plot exhibited the lowest functional connectivity. In the case of all the other plots, the connectivity increased compared to before-rainfall soil surface conditions, which are indicated by steepening of the curve's gradient and reduction of the soil surface depression volume due to rainfall. The latter effect was also indicated by Darboux et al. (2002a) where the storage capacity of the soil surface decreased after rainfall. In Darboux et al. (2002a) the runoff was also triggered for smaller field soil surface storage suggesting a reorganization of the surface via a connection between surface depressions. The shape of the functional connectivity relationship may be further developed during successive rainfalls (Peñuela et al., 2016).

7.3 Surface water mixing

The pulse applied in the rainfall and the pulse response in the runoff are shown in Figure 7.7. The pulse consisted of two deuterium excess values on the NWT plot and a single deuterium excess value on the SWT and CWT plot. The pulse water started to flow in the runoff immediately after the deuterium application. All plots exhibited a similar increase in pulse water in the runoff, although the runoff was much smaller in the CWT plot compared to

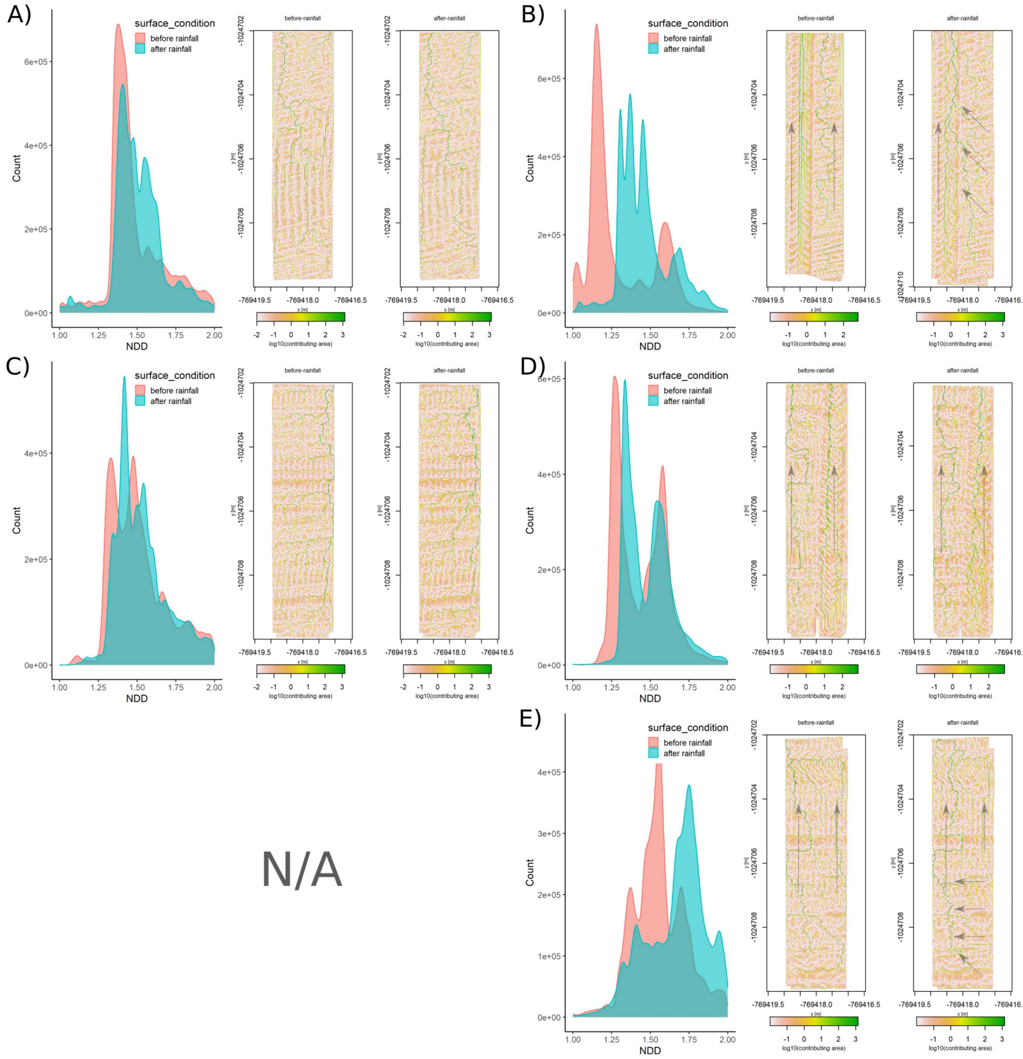

Figure 7.5: The histogram of NDD and the corresponding contribution area raster of the before-rainfall and after-rainfall surface conditions of: A) the NWT No. 1 plot, B) SWT No. 1 plot, C) NWT No. 2 plot, D) NWT No. 2 plot, and E) CWT No. 2 plot. Arrows in some of the flow accumulation rasters indicate the main flow direction.

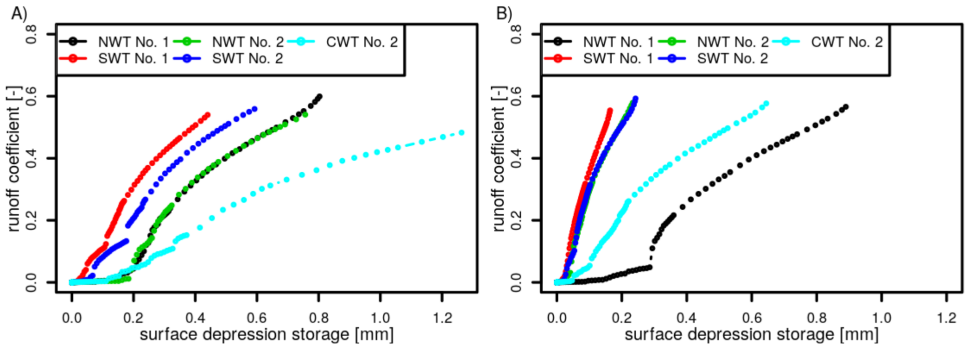

Figure 7.6: Functional connectivity of A) before-rainfall situation and B) after-rainfall soil surface conditions

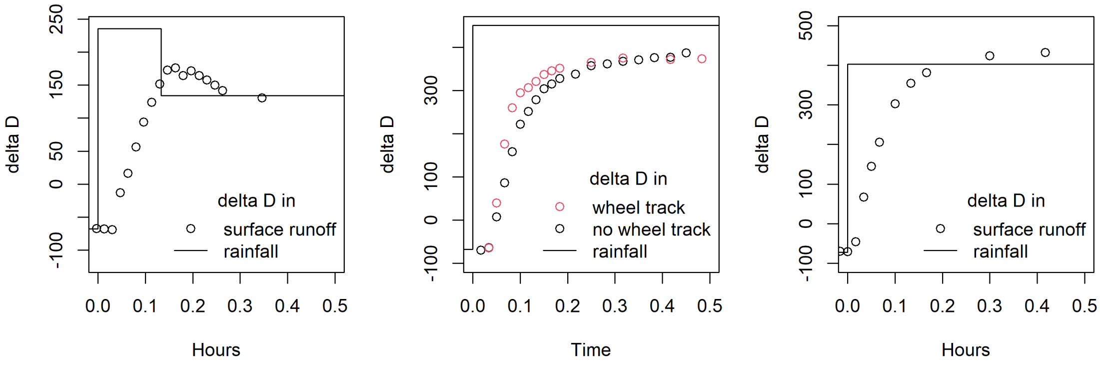

Figure 7.7: δD development in surface runoff and simulated rainfall on NWT plot (left), SWT plot (middle), and CWT plot (right)

the NWT and SWT plots, which exhibited similar runoff rates during campaign No. 2. The mixing was faster on the wheel track compared to the no wheel track soil on the SWT plot (Figure 7.7). The deuterium excess in the runoff exceeded the deuterium excess values in rainfall water in the CWT measurement probably due to the large amount of deuterium in the pulse water, which is not adequately measured.

Relative values of the deuterium excess are shown in Figure 7.8. The onset of the deuterium excess in runoff was very similar among the plots, as well as the time development. Only the wheel track of the SWT plot exhibited faster mixing. Neither connectivity nor runoff rate seem to have an effect on the mixing of the overland flow water. It is, however, not known, what part of the plot is actually drained to the collection flume.

7.4 Key findings

Direct measurement revealed that overland flow and sediment transport were the largest in the SWT plot. CWT plot exhibited the lowest values of both of those quantities. The reference NWT exhibited intermediate values (with one exception). Random roughness decreased due to rainfall, suggesting flattening of the surface. This flattening was observed in the wheel track, showing that the microtopography changes also in the wheel track.

Structural connectivity corresponded to direct measurement of runoff in the case of the

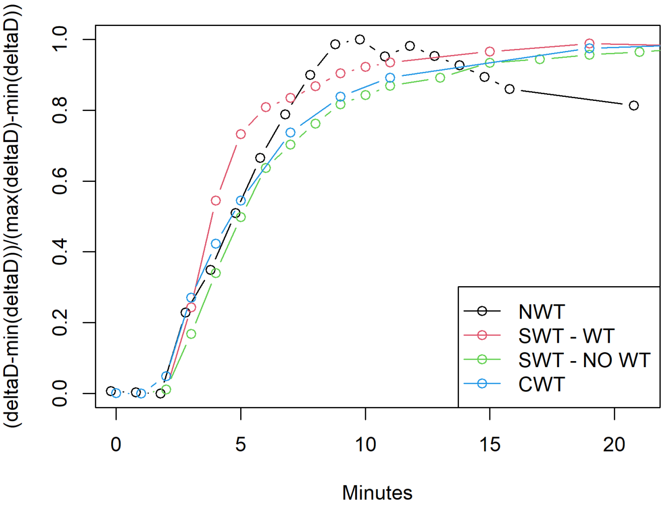

Figure 7.8: Mixing of deuterium pulse water with pre-pulse water at NWT, SWT, and CWT plot

before-rainfall soil surface conditions. NDD index increased in most cases for the after-rainfall soil surface conditions. This increase was associated with a decrease in structural connectivity, which is in contradiction to intuition and also to the literature. However, it is clear that the length of the flow pathways are larger at the CWT plot and shortest at SWT indicating larger average velocity of flow at the SWT plot and therefore increase in sediment transport in SWT plot. The flow accumulation algorithm showed changes in pathways while comparing the before- and after-rainfall soil surface conditions which corresponded with the direct measurements. It was concluded that while structural connectivity can show the inter plot changes (reorganization) of the soil surface, the temporal changes of the whole-plot connectivity were not examined well with this index.

Functional connectivity exhibited a similar behaviour to direct measurement of runoff and soil loss. The expected increase in connectivity after rainfall was captured with this index. The increase in connectivity is attributed to reduction of soil surface depression storage due to runoff and the kinematic energy of rainfall. The functional connectivity index may be used to evaluate the runoff in large-scale models. Typically, a cell in the larger-scale model releases runoff when a threshold value is reached. This is not true in nature, where the soil surface of several squared meters produces runoff even if not all of the soil surface depressions are filled. This behaviour can be mimicked with the functional connectivity presented in this study.

Chapter 8

Infiltration into tilled soil

8.1 Introduction

The work presented in this chapter is original research that has not yet been published in any peer-reviewed journal. Preliminary results were published during several conferences (e.g. Jeřábek et al., 2019).

The infiltration and transport processes in the soil are affected by the heterogeneity of the soil hydraulic properties (SHP). As shown in Jeřábek et al. (2017), the spatial heterogeneity of tilled topsoil is much higher compared to the subsoil heterogeneity in agricultural sites. Furthermore, the morphology of the subsoil layer may affect the generation of shallow subsurface runoff (Du et al., 2016; Ali et al., 2011). Effect such morphology on transport in cultivated soils was studied in Coquet et al. (2005a,b) or Filipović et al. (2018). In (Coquet et al., 2005b), the compacted layer introduced a lateral flow and a wheel track blocked infiltration. The lateral flow may be activated on the plough pan if a saturation zone is created on its surface, as observed in (Strouhal, 2016). In Filipović et al. (2018), the lateral flow was observed during limit periods in the year under specific field conditions. The thickness of the low-permeable horizon played an important role in the amount of lateral flow generated. The retention curve and the hydraulic conductivity curve were scaled to simulate the variability of the soil horizons Hammel et al. (1999). This approach could generate high and low flow velocity regions; however, the simulated tracer concentration corresponded to the measurements only to limited extent.

The objective of the following study was to investigate infiltration in soils affected by tillage and the presence of a wheel track and lateral flow as hypothesized in the conceptual model (Figure 1. Three distinct soil materials were identified: tilled topsoil (TOP), wheeled topsoil (WTOP), and subsoil (SUB). The morphology of the soil surface and subsoil was explicitly defined using photogrammetric methods. The soil hydraulic parameters were measured and estimated by inverse modeling with the 1D model, and the 2D model of the shallow part of the plot with a wheel track was used to investigate the fluxes in the shallow part of the soil profile and the effect of the morphology of the soil horizons.

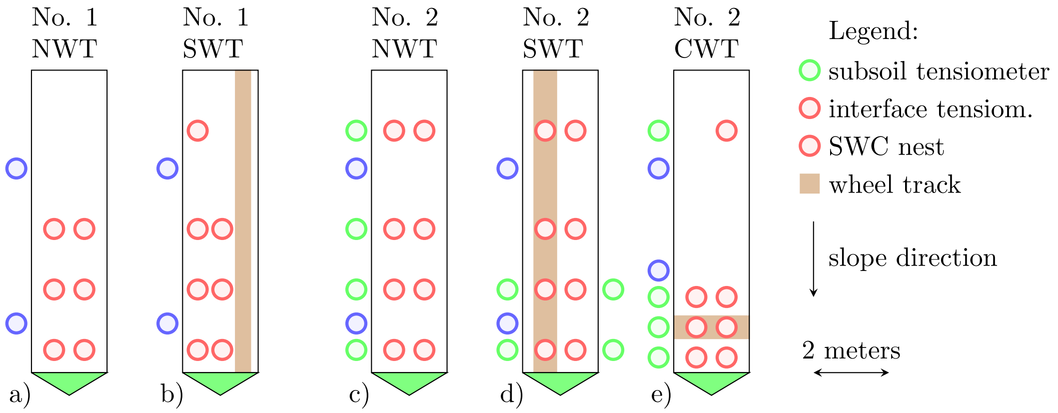

Figure 8.1: Schema of the measurement during both measuring campaigns

8.2 Material & Methods

8.2.1 Experimental setup

The artificial rainfall experiments were carried out during measuring campaigns at the Řisuty site as described in Section 6.3.1. The artificial rainfall experiment was described in sections 6.3.2 and 6.3.3. As shown above, the plot without the wheel track (NWT), slope wise wheel track plot (SWT) and contour lines wheel track plot (CWT) were investigated.

Infiltration, soil water potential (SWP), volumetric water content (VWC), and vertical flow were measured during campaigns. The schema of SWP and VWC measurements is shown in Figures 8.1 and 8.2. Specific depths and location of the probes in each plot are provided in the Appendix Table B.1. The measurement scheme differed between plots. For instance, probes were installed along with the whole plot to observe the infiltration over the plot not affected by the wheel track on the NWT plots (especially at the No. 2 campaign). In contrast, measurements were located closer to the wheel track in the case of the SWT and CWT plots to observe the effect of the wheel track.

Two VWC nests were installed in each plot using CS650 probes (Campbell Scientific Inc., Logan, UT). Each nest consisted of three probes installed: 5 cm below the surface, at a depth of 12 — 15 cm at the topsoil-subsoil interface, and at a depth of ca 25 — 30 cm at the subsoil (Figure 8.2).

All SWP probes (T8, Decagon Devices, Inc., USA) were installed on the interface between the tilled topsoil and the subsoil (a depth of approximately 12 - 15 cm) during campaign No. 1. During campaign No. 2, the measurement setup of the SWP probes was extended by deeper measurements (depth 35 – 45 cm) as shown in Figure 8.2. Generally, four positions along each plot were monitored for SWP. A pair of SWP probes were installed at each of those four positions in most cases. A pair was installed in the wheel track in case of CWT plot. One probe of the pair was installed in the wheel track in case of the SWT plot.

The vertical flow was sampled with zero-tension lysimeters. Each plot was equipped

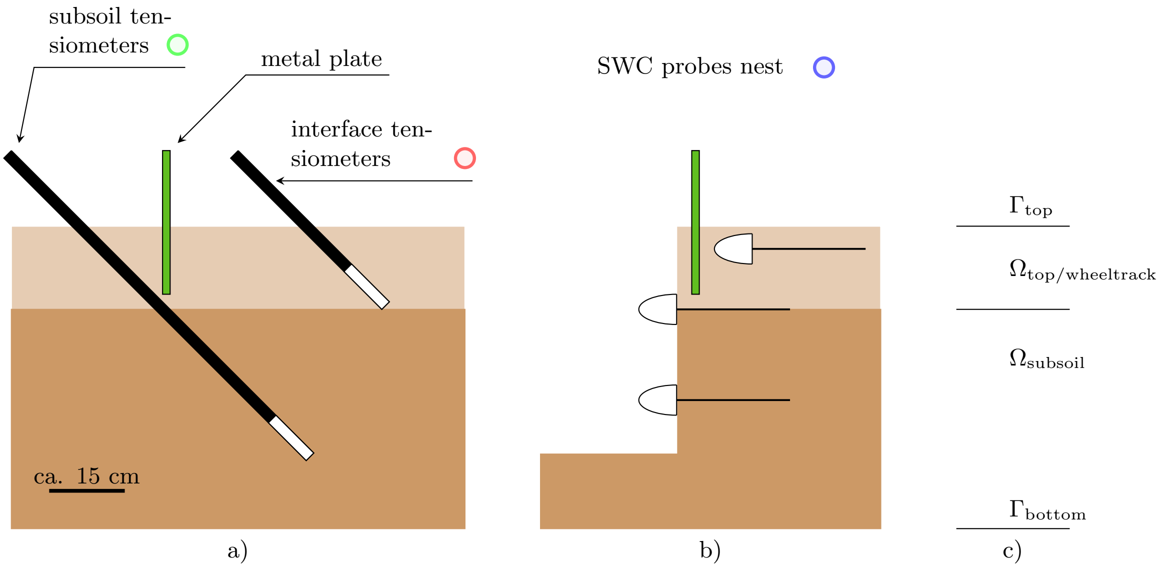

Figure 8.2: The position of a) the interface and subsoil tesiomters, b) the soil water content nest, and c) the schema of the boundary conditions and soil layers delineation used in for the numerical model

with a single or pair of lysimeters in the upper corner(s) of the plot. Lysimeters were inserted to a depth of approximately 12 cm; just above the compacted subsoil. Each lysimeter consisted of a metal plate (50x50 cm) with inclined sites to drain the water from the soil.

8.2.2 Soil hydraulic characteristics

Regular undisturbed soil samples (cylinder volume 100 - 140 ml) were taken from the TOP, WTOP and SUB. Seven samples were collected from each of the soil layers during the campaign No. 1. Nine and five samples were taken from the TOP and WTOP layer, respectively, during campaign No. 2. Additionally, three triplets of 250 ml cylinders were sampler in the WTOP and TOP and in the subsoil during campaign No. 2.

Regular samples were analyzed with the hydrostatic method using a sand tank and a pressure chamber aperture to obtain the soil water retention curve (SWRC). The RETC software (van Genuchten et al., 1991) was used to optimize the parameters of van Genuchten's SWRC. 250 ml samples were analyzed for saturated hydraulic conductivity (K_s) using the KSat© device (METER Group) and for the SWRC and unsaturated hydraulic conductivity curve using the evaporation method with the HYPROB© device (METER Group). The van Genuchten parameters were determined with the HYPROB-FIT software (Pertassek et al., 2015). Furthermore, field saturated hydraulic conductivity (K_{fs}) was measured using a dual-head automatic infiltrometer (SATURO© METER Group).

8.2.3 Modeling approach

The numerical model HYDRUS1D was used to study the infiltration process. The modeling of the infiltration into tilled soil was done in two steps:

Figure 8.3: Excavated subsoil with visible furrows

1. Inverse 1D modeling was used to obtain the effective SHPs.
2. The effect of the morphology of the topsoil-subsoil interface and the presence of a wheel track on the infiltration and lateral subsurface flow was studied using the 2D approach.

Only the CWT plot of the campaign No. 2 was used for the numerical investigation.

8.2.3.1 One-dimension: inverse modeling

VWC and SWP were monitored at several positions along the plot (Figure 8.1). Each position was considered as a 1D vertical profile for the purposes of the inverse modeling. The Marquardt-Levenberg parameter estimation approach built in HYDRUS1D modle (Šimunek et al., 2012) was used for the inverse modeling.

The inverse modeling approach followed the same procedure for each 1D profile:

1. The measured SWRC and K_s were used to estimate the initial parameters and to estimate the ranges of the parameters.
2. The measured SWP in two depths (and two soil layers) was used to optimize SWRC and K_s.
3. VWC data were used to obtain more realistic soil hydraulic parameters and to reduce uncertainty (combination of SWP and VWC data was shown to be successful in identifying unique parameter sets (Šimůnek and Van Genuchten, 1996)).
4. Multiple initial parameter estimation was used to reduce equifinality and the risk of finding a local minimum in the objective function (Šimunek et al., 2012).
5. The parameter ranges were adjusted to better fit the measured data if necessary.

The generic soil profile scheme with the approximate location of the probes is shown in Figure 8.2. The locations and depths of the probes during the experiments are shown in Tables B.1 and B.2.

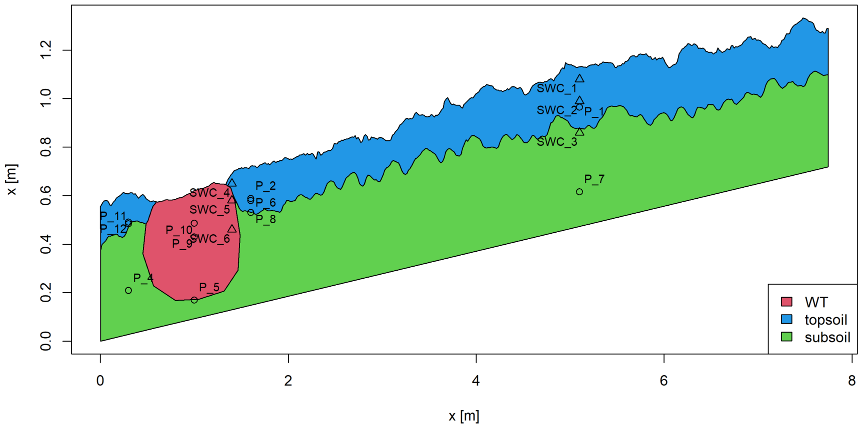

(a) With morphology

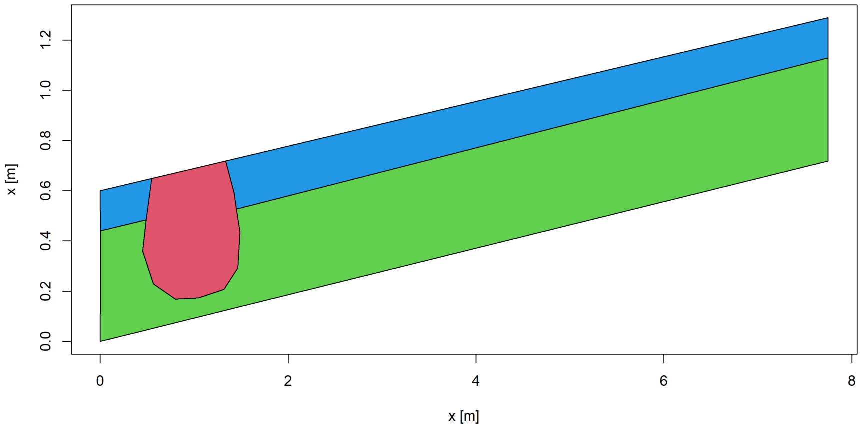

(b) Without morphology

Figure 8.4: Geometry of the three layers morphology at the CWT plot as used in HYDRUS2D model. The positions of tensiometers (○) and soil water content probes (△) are shown.

8.2.3.2 One-dimension: model setup

A soil profile was modeled at a depth of 70 cm. The modeled profile consisted of two soil layers (Figure 8.2c). The delineation between the topsoil and subsoil was at a depth of 15 to 17 cm (depending on the position along the plot). The soil layer Ω_1 represented the TOP and WTOP topsoil. The soil profile Ω_2 represented the SUB (Figure 8.2c). The atmospheric boundary condition (allowing surface runoff) was used in all cases at the upper boundary of the domain. The free drainage boundary condition was used at the bottom of the domain. The initial pressure was set at -850 cm according to the SWP measurement, although the pressure was probably lower in the field. The 1 cm increment was used for spatial discretization.

8.2.3.3 Two-dimension: soil layers morphology effect

To investigate the effect of the morphology of soil layers on water flow, the model with complex morphology (Figure 8.4a) was compared with a simplified geometry model without the morphology of the topsoil-subsoil interface (Figure 8.4b).

CWT plot of campaign No. 2 was modeled as a 2D cross section. The geometry of the soil surface was obtained from the DEM of the soil surface as described in Chapter 7. Additionally, the topsoil was uncovered in the vicinity of the CWT plot in order to obtain the DEM of the subsoil layer. The tillage created furrows on subsoil layer as shown in Figure 8.3. A 2D transect geometry was constructed from the topsoil and subsoil DEM as shown in Figure 8.4a. The depth of the wheel track zone was estimated based on the ERT images shown in chapter 6.3.

All boundaries, but the top boundary condition, were set as no flow boundary condition. The top boundary conditions were set as atmospheric boundary conditions with runoff allowed. A pressure of -850 hPa was used as the initial condition. The effective parameters obtained with the 1D inversion modeling were used for the three soil materials in the 2D model: TOP, WTOP, SUB.

8.3 Results & Discussion

8.3.1 The soil structure

Three distinct soil materials were identified in the tilled soil profile: wheeled topsoil (WTOP), unwheeled topsoil (TOP) and subsoil (SUB). Topsoil consists of loose soil material with no structure. Individual soil aggregates and small clods could be identified. The loose soil structure was created by the previous tillage. Measured topsoil dry bulk density was 1.31 ± 0.09 g/cm^3 and 1.19 ± 0.39 g/cm^3 during the campaigns No. 1 and No. 2 respectively. The SUB was not tilled and therefore the structure was relatively coherent. It was impossible to penetrate under dry conditions (Figure 6.10). The tillage operations created a distinct morphology, furrows, at the interface between the topsoil and the subsoil (Figure 8.3). The measured SUB dry bulk density was 1.77 ± 0.03 g/cm^3. Wheel track compaction firmed the soil and increased the dry bulk density to 1.40 ± 0.1 g/cm^3 and 1.35 ± 0.03 g/cm^3 during the campaign No. 1 and No. 2, respectively. The soil surface on the wheel track was lowered below the surrounding soil. ERT (Chapter 6.3) showed that the wheel track compaction propagated slightly to the subsoil.

8.3.2 Infiltration front approach

The initial soil water potential (SWP) and volumetric water content (VWC) were low. SWP was around -850 kPa, which is the close to the ceramic cup aeration limit. The initial topsoil VWC obtained with the gravimetric method exhibited values of 0.10 ± 0.01 $\mathrm{cm^3\ cm^{-3}}$ and 0.12 ± 0.015 $\mathrm{cm^3\ cm^{-3}}$ during the campaign No. 1 and No. 2 respectively.

The development of SWP during irrigation is shown in Figure 8.5. At the topsoil-subsoil interface, the SWP exhibited a sharp increase in the first 2 hours of irrigation (Figures 8.5a, 8.5b, 8.5c, 8.5e, and 8.5h). The increase was concentrated about an hour after the beginning of the irrigation during campaign No. 2 (Figures 8.5c, 8.5e, and 8.5h). The SWP in the subsoil layer also exhibited a rapid increase; however, this increase was less noticeable in time, especially during the campaign No. 2 (Figure 8.5g).

The increase in SWP did not coincide with the depth of the tensiometer installation.

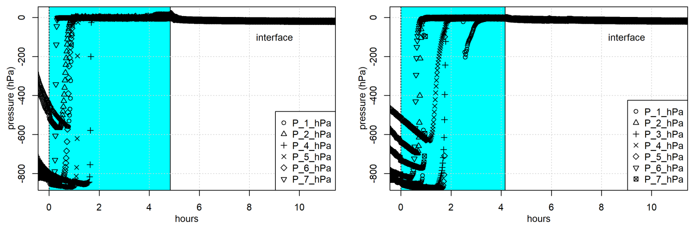

(a) Interface No. 1 NWT (b) Interface No. 1 SWT

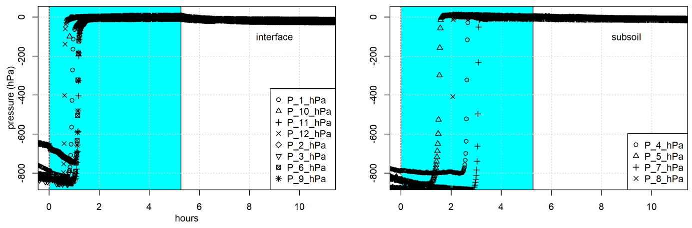

(c) interface No. 2 NWT (d) subsoil No. 2 NWT

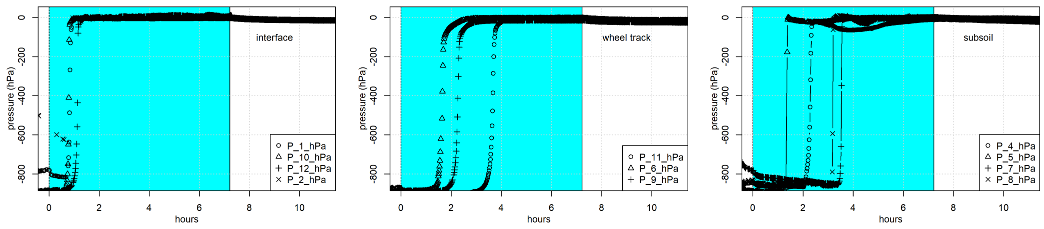

(e) interface No. 2 SWT (f) wheel track No. 2 SWT (g) subsoil No. 2 SWT

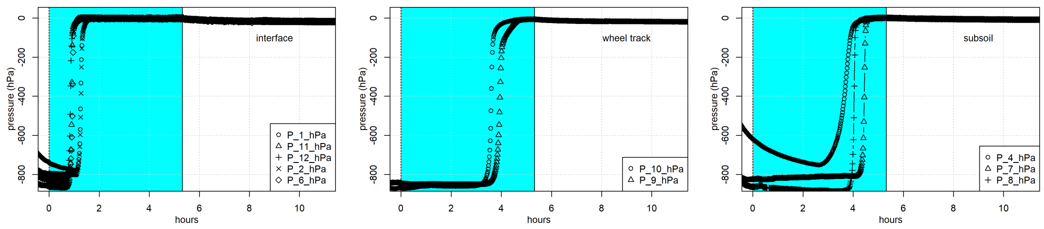

(h) interface No. 2 CWT (i) wheel track No. 2 CWT (j) subsoil No. 2 CWT

Figure 8.5: Soil water potential in the topsoil, wheeled topsoil, and subsoil during the artificial rainfall experiments. The blue area indicates the irrigation. The exact position of each tensiometer is given in Table B.1.

For instance, tensiometers P_5_hPa and P_8_hPa in Figure 8.5g were placed in similar depth (Table 8.1) while the SWP increase occurred approximately 2 hours apart. The same was applied to the SWP measured on the wheel track itself (Figures 8.5f, and 8.5i). SWP exhibited values close to zero after the infiltration front reached the measured depth, suggesting saturated or near-saturated soil conditions in all cases (Figure 8.5).

The lag time of the infiltration front arrival to each SWP measurement position is shown in Figure 8.6. The front arrival lag time did not correlated with the measuring depth for tensiometers in depth up to -20 cm. Below the depth of -20 cm, SWP exhibited delayed infiltration front arrival. However, a high variability was also clearly observed even for the deeper positions.

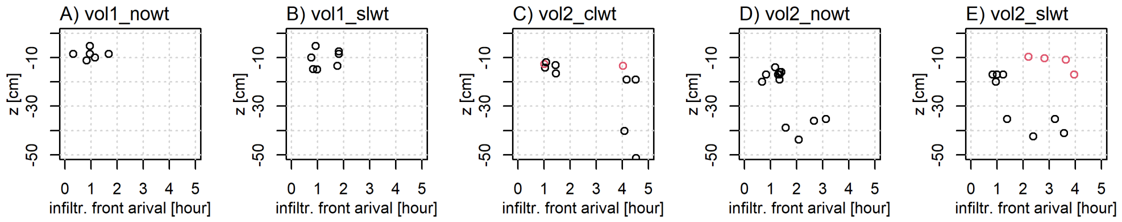

Figure 8.6: The estimation of infiltration front arrival time to the installation depth of the each tensionmeter for the plot NWT No. 1 A); SWT No. 1 B); NWT No. 2 C); SWT No. 2 D); CWT No. 3. Red color depicts the tensiometers installed in the wheel track.

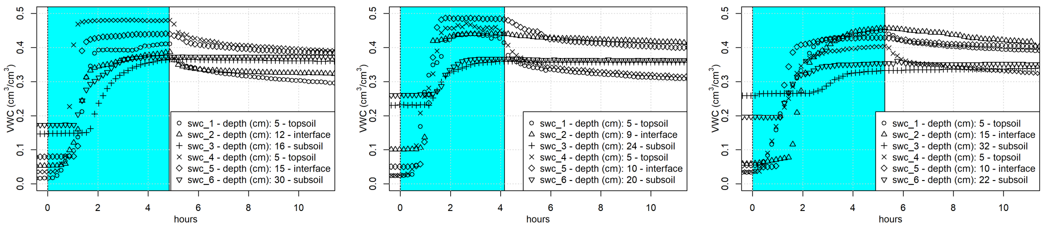

(a) No. 1 NWT (b) No. 1 SWT (c) No. 2 NWT

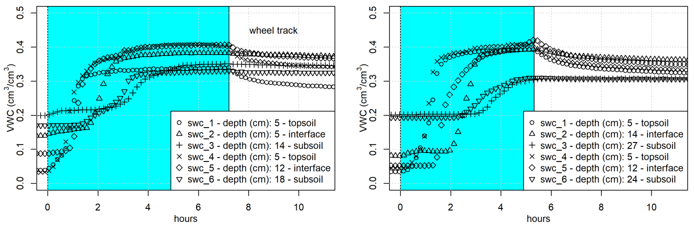

(d) No. 2 SWT (e) No. 2 CWT

Figure 8.7: Volumetric water content in all VWC nests during artificial rainfall experiments. The interface and subsoil probes were placed approximately bellow the wheel track during the campaign No. 2 (Figure 8.7d). The exact sensori position are shown in Tabla B.2.

The development of VWC during and after rainfall is shown in Figure 8.7. The increase in VWC was more gradual compared to SWP. This more gradual increase could have been caused by the larger measured volume of the CS650 probes used for the measurement. The initial VWC values were unrealistically high in the deepest probes. This could be a result of the probe calibration, which did not correspond to the site compacted soils; the soil samples and tensiometer reading indicated a very low water saturating.

VWC was constant in the SUB while the SWP started to decrease in all depths after the rainfall (Figure 8.5). This may suggest altered water retention characteristics of the subsoil compared to topsoil (e.g. higher bubbling pressure).

8.3.3 Vertical flow

The vertical flow in the soil was observed with zero-tension lysimeters inserted into the soil at the interface between topsoil and subsoil. Despite some erratic behaviour, the quasi-steady vertical flow was estimated to be approximately 5 mm / hour in the case of all plots as shown in Figure 8.8 (the rainfall intensity was set to 30 mm/hour). Despite some

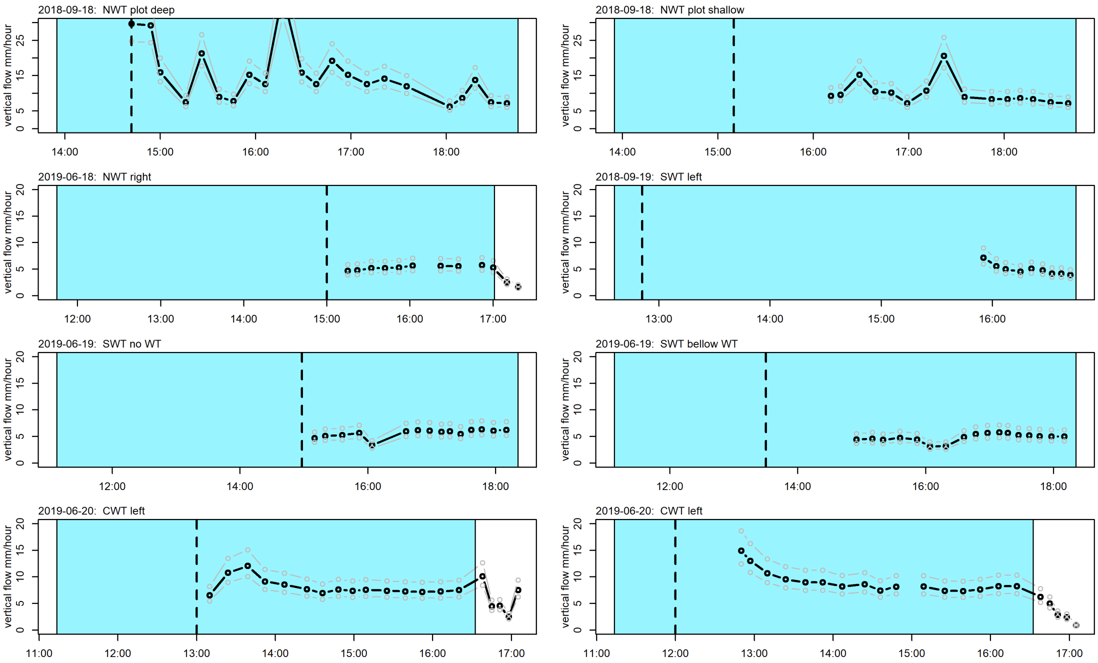

Figure 8.8: Vertical flow on plots measured with zero-tension lysimeters. The plot and position is indicated at the upper left corned of each plot. Blue area indicates the rainfall. The vertical dashed line indicates the vertical flow initiation. Since the active area of each lysimeter was uncertain, the grey lines indicate the situation where the lysimeter is inserted ± 5 cm in the soil; has larger or smaller active area.

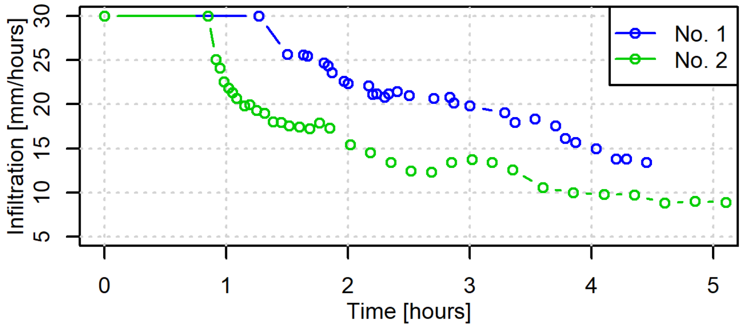

Figure 8.9: infiltration into the NWT plot (rainfall - runoff / plot ares)

similarities in the flow rate, the lag time for vertical flow initiation differed substantially between the experiments (indicated with a vertical dashed line in Figure 8.8).

The plot-average infiltration intensity was calculated as the difference between rainfall and runoff for the two NWT plots in Figure 8.9. Most notably, the infiltration did not reach a steady state in none of the plots. Also, the infiltration values were higher compared to the vertical flow measurement on the lysimeter (Figure 8.8). This discrepancy may indicate a lateral flow above the lysimeter or a lower intensity of rainfall above the lysimeter (Figure 8.9).

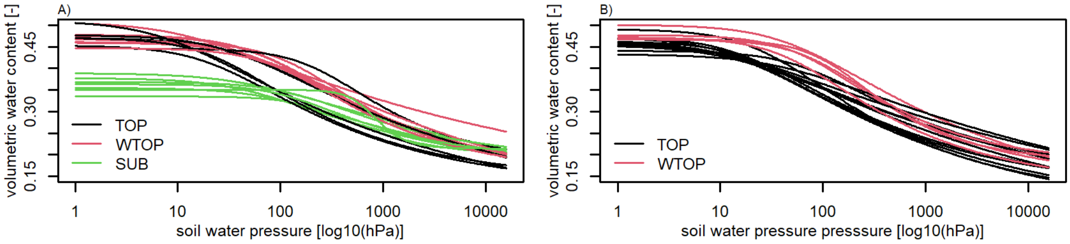

Figure 8.10: The soil water retention curve for the 3 examined soil layers in both campaigns

8.3.4 Measured soil hydraulic characteristics

The parameters of the van Genuchten soil water retention curve (SWRC), the saturated hydraulic conductivity K_s and the field saturated hydraulic conductivity K_{fs} are shown in Figures 8.10 and 8.10, and in Table 8.1.

The SUB parameters differed significantly from the TOP in terms of θ_s using the hydrostatic method. The differences between WTOP and TOP were more pronounced in the case of campaign No. 2 where θ_s, α and n parameters differed significantly. SUB exhibited the lowest values of the parameters α and n using the hydrostatic method; however, due to high variability, not significantly. The literature reported a decrease or constant value in the water content for less negative pressures and an increase in the water content for more negative pressures as a result of soil compaction (Alaoui et al., 2011). In presented measurements the θ_r increased due to compaction while the θ_s remained unchanged.

The evaporation method exhibited higher values and somehow random variation in θ_r and θ_s. The α parameter was the lowest for the WTOP and the n parameter did not increase above 1.3 which was in contrast to the hydrostatic method measurements. However, as shown by Bittelli and Flury (2009), the hydrostatic pressure method can lead to overestimation in VWC for lower pressures, which probably happened in the case of this study.

The saturated hydraulic conductivity K_s exhibited high variability depending on the method used (Table 8.1). In general, the falling head experiments exhibited the highest K_s due to macropore flow during saturated conditions. The evaporation method and the field measurements were on the same order of magnitude. However, the evaporation method exhibited the highest values in SUB which was most likely caused by fitting artifacts, as shown in Appendix B.2. The evaporation method exhibited uncertainties related to the dynamics nature of the measurement procedure and uneven pressure distribution in the soil sample; however, linearization was shown to produce only minor error (Peters and Durner, 2008). The saturated hydraulic conductivity should be decreasing due to soil compaction (Pagliai et al., 2003; Seehusen et al., 2019). This effect was also shown in the presented data regardless of the measurement method used. The decrease K_s was attributed to the decrease in macroporosity, the area of the largest pores, and porosity by (Kim et al., 2010).

Table 8.1: The fitted soil hydraulic parameters for the 3 soil layers. Letters indicate Tukey's honest significance test.

			Hydrostatic method				
camp.	soil layer	n	θ_r	θ_s	α	n	
			cm^3cm^{-3}	cm^3cm^{-3}	cm^{-1}	$-$	
No. 1	topsoil	7	$0.10^{a,*}$ $(0.05)^{**}$	0.47^a (0.02)	0.038^a (0.036)	1.27^a (0.12)	
	wheel tr.	7	0.11^a (0.05)	0.47^a (0.02)	0.023^a (0.027)	1.28^a (0.11)	
	subsoil	7	0.15^a (0.07)	0.36^b (0.02)	0.010^a (0.008)	1.64^a (0.78)	
No. 2	topsoil	9	0.05^a (0.05)	0.46^a (0.02)	0.050^a (0.020)	1.20^a (0.08)	
	wheel tr.	5	0.14^b (0.05)	0.48^a (0.01)	0.013^b (0.005)	1.41^b (0.15)	
			Evaporation method				
camp.	soil layer		θ_r	θ_s	α	n	K_s
			cm^3cm^{-3}	cm^3cm^{-3}	cm^{-1}	-	$cm\ day^{-1}$
No. 2	topsoil	1	0.001	0.37	0.041	1.21	4.57
	topsoil	1	0.05	0.46	0.057	1.18	7.42
	wheel tr.	1	0.001	0.38	0.005	1.26	0.37
	subsoil	1	0.11	0.44	0.035	1.29	9.62
	subsoil	1	0.001	0.41	0.049	1.16	30.3
			Faling head		Field ponding experiment		
camp.	soil layer	n	K_s		n	K_fs	
			$cm\ day^{-1}$			$cm\ day^{-1}$	
No. 1	topsoil	0	N/A		1	4.58 (N/A)	
	wheel tr.	0	N/A		3	0.50 (0.14)	
	subsoil	0	N/A		2	0.17 (0.001)	
No. 2	topsoil	24	177.0 (130.1)		0	N/A (N/A)	
	wheel tr.	20	3.77 (6.2)		3	0.26 (0.25)	
	subsoil	28	189.6 (63.4)		0	N/A (N/A)	

* indicate mean value and **; the standard deviation.

Table 8.2: Summary of the optimized paramters for each soil material for all plots

material		θ_r	θ_s	α (1/cm)	n	K_s (cm/day)
TOP	mean	0.06	0.44	0.028	1.40	6.36
	sd	0.02	0.02	0.010	0.16	2.95
WTOP	mean	0.11	0.41	0.015	1.43	0.42
	sd	0.07	0.06	0.014	0.28	0.37
SUB	mean	0.14	0.38	0.029	1.47	1.05
	sd	0.06	0.03	0.019	0.28	0.67

8.3.4.1 Optimized soil hydraulic properties

The average SHPs of the three main materials obtained with the optimization procedure are shown in Table 8.2. The optimized θ_r of all soil materials was comparable to the measured data (as shown in Table 8.1). θ_s exhibited similar measured and optimized values compared to campaign No. 1. θ_s and θ_r were negatively correlated between the plots that correspond to the literature (Alaoui et al., 2011) where a decrease in θ_s and an increase in θ_r was reported. The measured and optimized α exhibited the lowest values on the wheel track. However, the optimized and measured values of α were of similar order of magnitude. The optimized n resulted in a similar value for all soil materials (Table 8.2). Optimized K_s exhibited lower variation between materials compared to measurements. K_s was the highest in TOP and the lowest in WTOP. SUB K_s was between those values closer to WTOP soil K_s. This did not correspond to the falling head experiments and the evaporation method, where TOP and SUB exhibited similar values. Only the measured field K_s showed a similar order in the values to the optimized one.

8.3.5 Effect of soil layers morphology - 2D transects model

The average SHPs obtained with the 1D optimization were used in the 2D model (Figure 8.11 and Table 8.2) to explore. As it is shown in Figure 8.11, the modeled soil water pressure (SWP) coincided well with the measurements at the topsoil/subsoil interface. The model fits the timing of the sharp infiltration front. In SUB the SWP development was modeled poorly. The modeled SWP started to increase already after 2 hours of rainfall while the measured SWP started to react to rainfall after 3 hours. The SWP development in the wheel track was not modeled well in the 2d model, as well.

Similarly as in the SUB the model overestimates the velocity of the infiltration in the WTOP. As expected, the increase in VWC was not well modeled. The onset of the increase in VWC occurred sooner according to the model, similar to Coquet et al. (2005b). However, after rainfall, the model was able to mimic stable VWC in the subsoil while the topsoil was drained.

8.3.5.1 Influence of morphology on water dynamics in the soil

The development of the SWP and Darcian velocity for a flat top-soil-subsoil interface scenario is shown in Figure 8.12. Three important stages of runoff generation can be identified as:

1. The water infiltrates freely to the soil at the whole soil surface except the wheel track (Figure 8.12a). At this stage, water infiltrates vertically to the soil outside the wheel track 8.12b and overland flow is created on the wheel track.
2. The perched saturation area started to build up at the interface of the topsoil and subsoil at the upper part of the plot and bellow the wheel track (Figure 8.12c). Water flows into the wheel track due to pressure gradient and lateral flow occurred at the area of saturation (Figure 8.12d).
3. After about 2.5 hours the saturation is present at the whole topsoil layers (Figure 8.12e) and a lateral flow is initiated (Figure 8.12f). Saturation excess overland flow is created at TOP. The development of lateral flow depends on the sufficiently low K_s of the subsurface layer (Filipović et al., 2018).

The transect with the topsoil and topsoil-subsoil interface morphology is shown in Figure 8.13. The first stage coincided with the-without-morphology scenario shown in Figure 8.12; infiltration excess surface runoff presented in the wheel track Figures 8.13a and 8.13b. However, unlike in the-without-morphology case, the saturation started to develop in the vicinity of the wheel track (Figure 8.13c) and the flow direction was affected by the morphology of the interface (Figure 8.13d). In the last stage, the topsoil was saturated (Figure 8.13e), but (unlike the case of the no morphology scenario) the flow

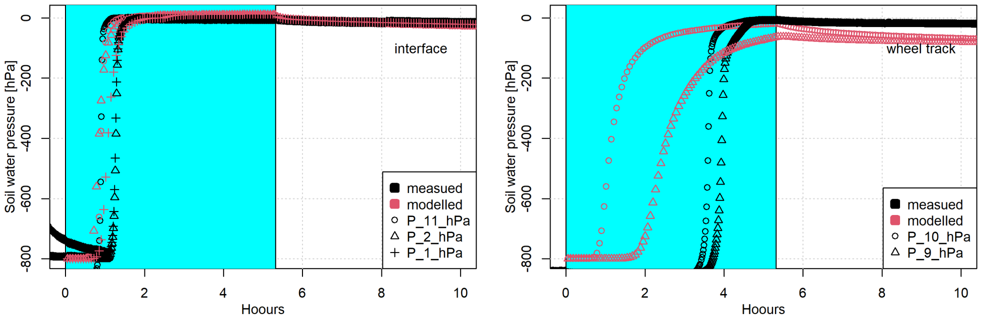

(a) Measured and modeled pressure head at the topsoil subsoil interface

(b) Measured and modeled pressure head in the wheel track

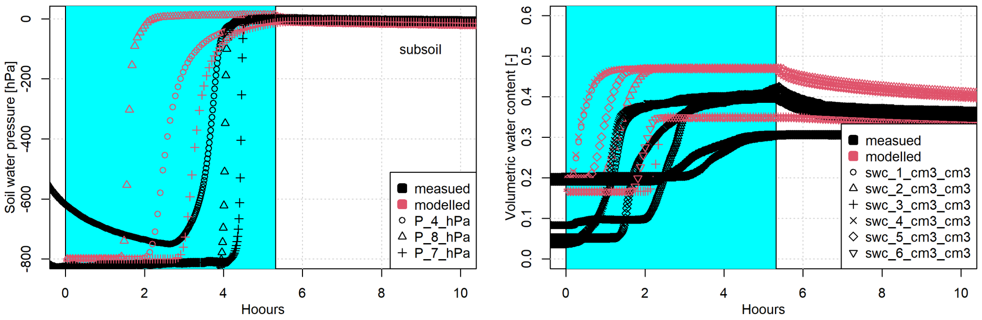

(c) Measured and modeled pressure head in the subsoil

(d) Measured and modeled volumetric water content

Figure 8.11: Measured and modeled pressure head and soil water content of the CWT plot using the average SHPs obtained with the inverse modeling

direction was controlled by the topsoil-subsoil morphology and the lateral movement was not identified (Figure 8.13f). As it is shown in Figure 8.13f, the flow is directed toward the "depression" in the topsoil-subsoil interface morphology.

The material averaged volumetric water content [1] (MAVWC) was analyzed for the three soil materials in Figure 8.14. MAVWC and net in/out flow in each of the materials did not change substantially between scenarios. It was clearly visible that the topsoil reached full saturation (porosity of topsoil was 0.47 in both scenarios) at around 2 hours (Figure 8.14a and 8.14b) of rainfall. The subsoil region starts to be saturated after about 1.25 hours. The wheel track gradually increases its MAVWC even after the rain has stopped, which was caused by suction into it due to pressure gradient. The latter effect was also visible with the ERT imaging presented in previous chapters.

---

[1] Material averaged volumetric water content is calculated as the ration between water volume in give soil material and the area of the given soil material.

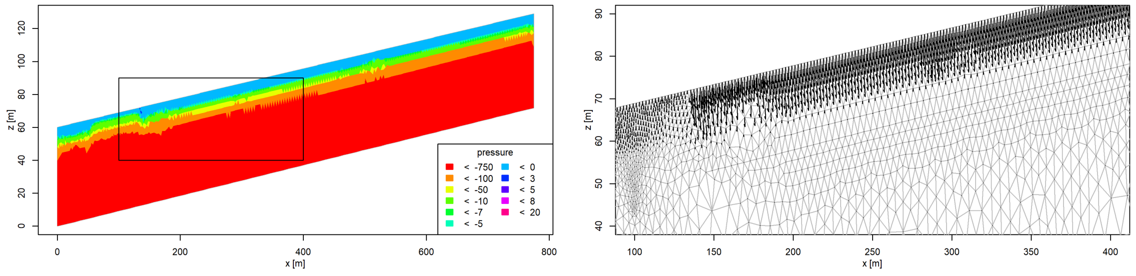

(a) Pressure head after 1 hour of rainfall

(b) Flow velocity after 1 hour of rainfall

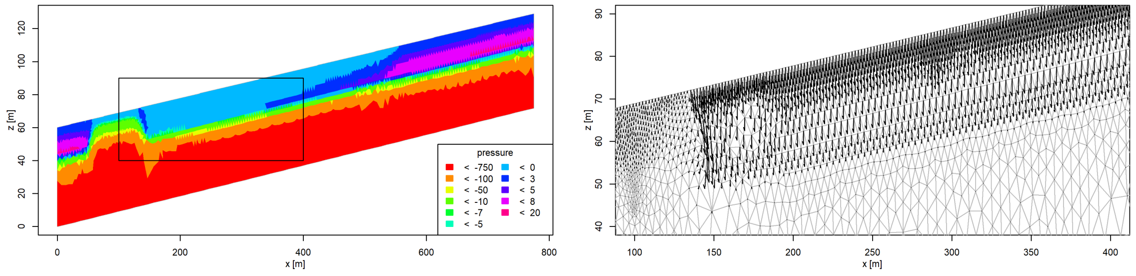

(c) Pressure head after 2 hour of rainfall

(d) Flow velocity after 2 hour of rainfall

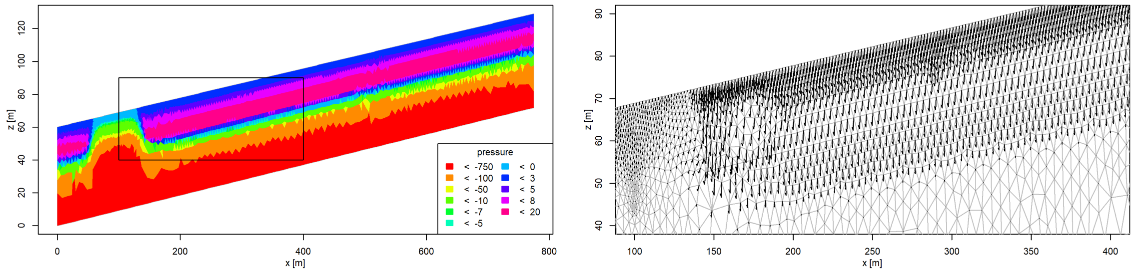

(e) Pressure head after 2.5 hour of rainfall

(f) Flow velocity after 2.5 hour of rainfall

Figure 8.12: Development of the flow regime at the transect with no morphology after 3 times. The rectangle in pressure head graphs shown the zoom region for the flow velocity vector graphs.

The net in/out flow between soil materials for with and without morphology scenario is shown in Figures 8.14c and 8.14d. Again, the flow between regions is similar in both scenarios; however, the exchange between regions is established more gradually in the case of the with-morphology scenario. This effect is attributed to the varying depths of the topsoil layers cased by the topsoil and topsoil-subsoil interface morphology.

8.3.5.2 Influence of morphology on soil water pressure

To show the effect of topsoil and topsoil-subsoil interface morphology six observation points were placed on the modeled transect as shown on Figure 8.15. Triplets of observation points were placed in depressions and on ridges of the interface in the model with morphology. These locations were selected because the saturation zone starts to develop there; as shown in Figure 8.13c. The observation points were placed at the corresponding locations in the model without morphology (Figure 8.15d).

The SWP development in the without-morphology model was almost identical in all

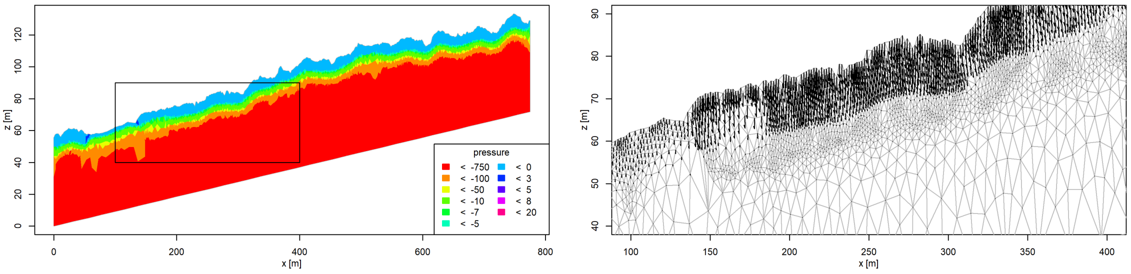

(a) Pressure head after 1 hour of rainfall

(b) Flow velocity after 1 hour of rainfall

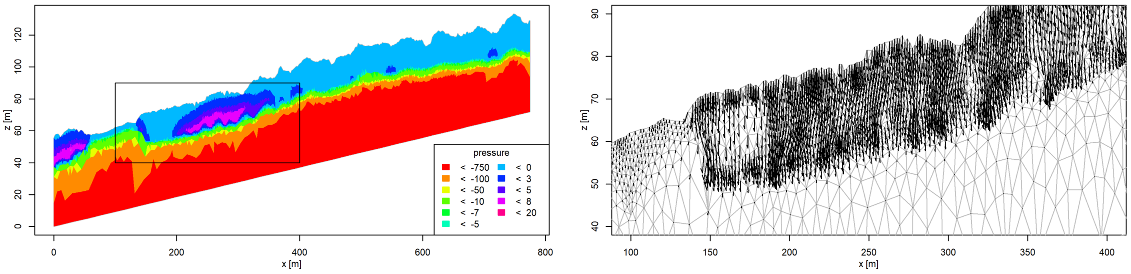

(c) Pressure head after 2 hour of rainfall

(d) Flow velocity after 2 hour of rainfall

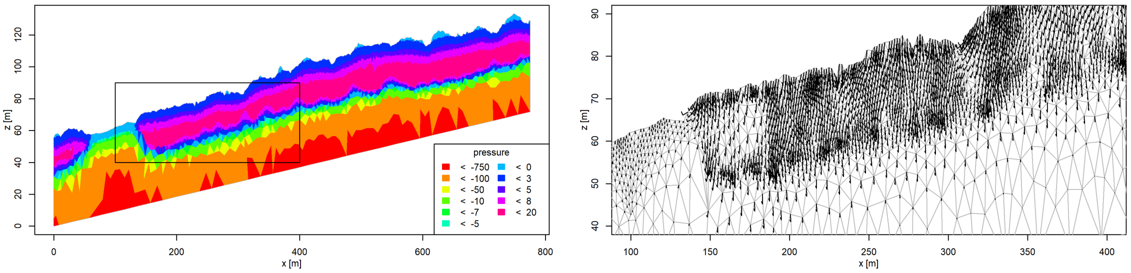

(e) Pressure head after 3 hour of rainfall

(f) Flow velocity after 3 hour of rainfall

Figure 8.13: Development of the flow regime at the transect with morphology at 3 times. The rectangle in pressure head graphs shown the zoom region for the flow velocity vector graphs.

observation points (Figure 8.15a). Under a detailed look, the SWP of the uppermost observation point started to develop slightly earlier compared to the other points (Figure 8.16. However, the time difference at the lower and upper observation points was about 0.2 hours.

The effect of morphology on SWP at the topsoil-subsoil interface was substantial (Figure 8.15c). Observation points at the ridges started to react much sooner to rainfall water. The earliest reaction was at the observation point located below the soil surface depression. The time difference between the earliest and latest increase in SWP was about one hour. This variation corresponded to the variation of the measured SWP as shown in Figures 8.5a, 8.5b, 8.5c, 8.5e, and 8.5h.

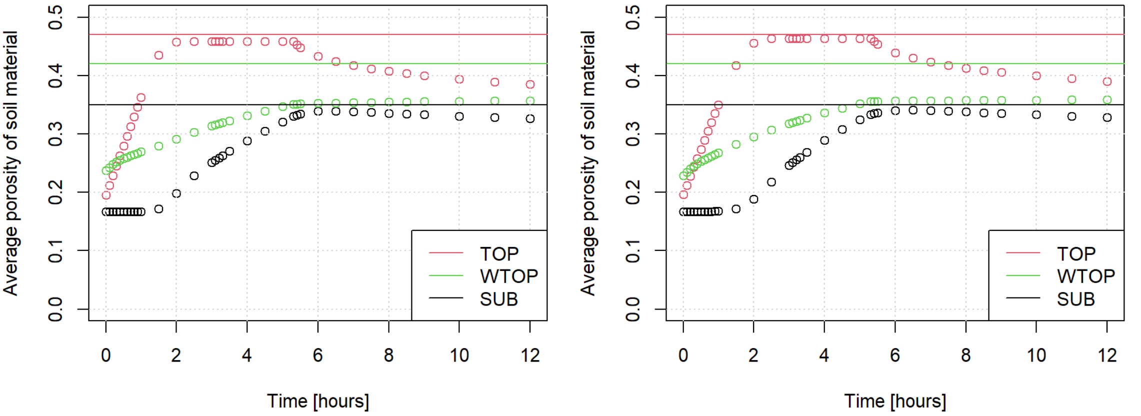

(a) Average VWC of 3 soil materials with no morphology

(b) Average VWC of 3 soil materials with morphology

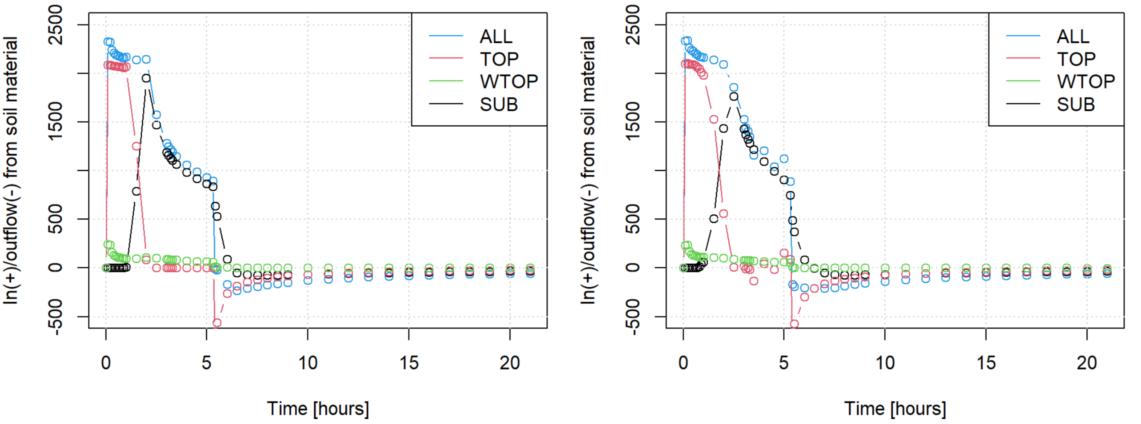

(c) Flow across of 3 soil materials with no morphology

(d) Flow across of 3 soil materials with morphology

Figure 8.14: Soil water balance variables of the 3 soil soil materials. Lines depicts porosity of the material.

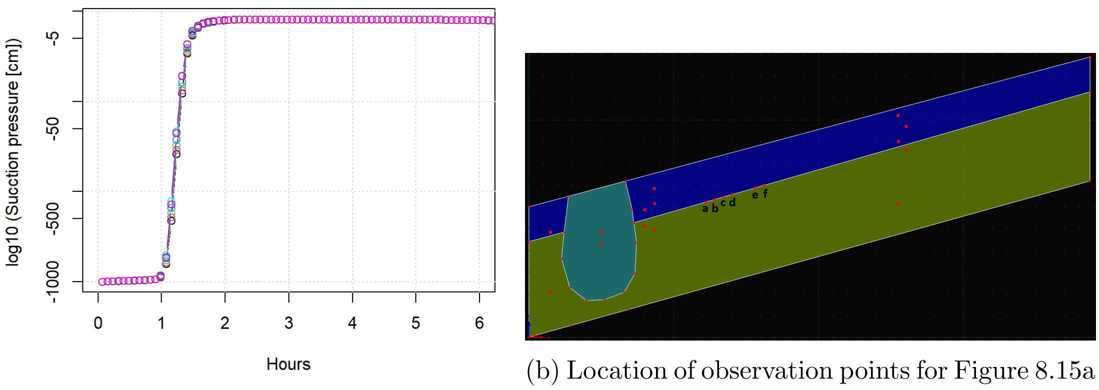

(a) Soil water pressure at the interface without morphology.

(b) Location of observation points for Figure 8.15a

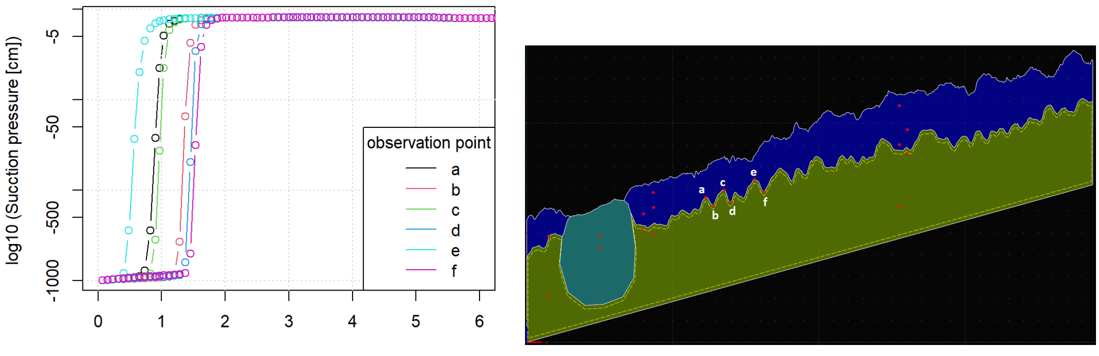

(c) Soil water pressure at the interface with morphology.

(d) Location of observation points for Figure 8.15c

Figure 8.15: Soil water potential development affected by the presence subsoil morphology

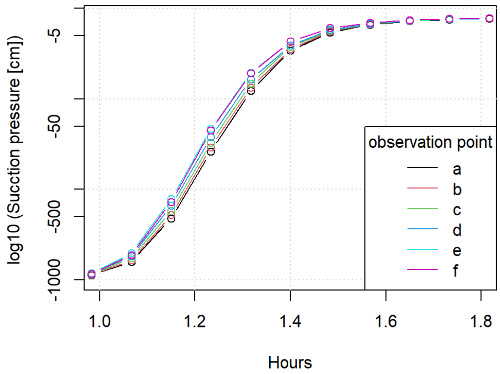

Figure 8.16: Detail of soil water pressure at the interface without morphology in Figure 8.15a

8.4 Key findings

This study investigated shallow water transport in tilled soil and the presence of wheel tracks with explicitly defined morphology of soil layers. First, three soil materials soil hydraulic properties (SHPs) were defined in terms of field and laboratory measurement methods. The measured parameters were used as a basis for the optimization of the SHPs.

The 2D model with and without morphology was constructed to explore the occurrence of lateral flow and the effect of subsurface morphology. The averaged optimized SHP exhibited only limited fitness with the measured soil water pressure and volumetric water content if in the 2D model.

It was shown that saturated conditions can be created on the top of the low-permeable subsoil layers. However, the morphology of the subsurface prevents lateral movement from developing. Water is directed rather in the depression in the subsoil morphology then laterally. Large temporal variability was observed in the lag time of the SWP increase during rainfall, which was clearly caused by the thickness of the topsoil layer, which is controlled by the topsoil and subsoil morphology.

Conclusions

The purpose of this thesis was to study the dominant effects that influence the processes of runoff generation in small agricultural catchments. The conceptual model of runoff generation was hypothesized prior to the investigation (Figures 1 and 3). The shallow part of the soil profile was monitored with electrical resistivity tomography and using fine-resolution digital elevation models. The effect of wheel tracks and soil layer stratification and morphology was further studied using the concept of hydrological connectivity to evaluate the validity of the conceptual model.

Based on the experimental and numerical analyses, the conceptual model was redefined as shown in Figure 8.17 and Figure 8.18. **Infiltration** is not affected by the morphology of the subsoil layer until the topsoil becomes saturated. The infiltration process is sensitive to the high variability of the soil physical properties. The intensity of infiltration decreases when the wetting front reaches the compacted subsoil. **Saturated subsurface lateral flow** can occur if the topsoil is saturated. However, it is strongly affected by the topsoil-subsoil interface morphology. Water flows towards the depressions in the interface rather than laterally downslope. Significantly lower hydraulic conductivity needs to be presented in the subsoil compared to the topsoil to generate the perched saturation zone. **Water routing via the wheel tracks** was observed during surface runoff conditions. The wheel track fills due to the infiltration excess mechanism and due to the inflow of water from the surface upslope. Runoff routing was shown to be strongly influenced by the orientation of the wheel tracks. When the contour line wheel track is filled, water overflows the wheel track and starts to contribute to surface runoff. According to the 2D numerical model, the **overland flow** is generated by the saturation excess mechanism outside the wheel track. However, the field experiment showed ponding soon after the beginning of rainfall (Figure 8.18). Water first started to fill the surface depressions in the soil microtopography. The water stored in the depressions initiated overland flow if connected. When overland flow is generated, the translocation of soil particles causes increased connectivity of the soil surface, and hence further increase of overland flow. Water **deep percolation** appears to be not affected by the soil surface morphology or by the topsoil - subsoil interface morphology.

The slope-wise wheel tracks affect the runoff at the small catchment scale. Due to its low infiltration capacity and depth of the wheel rut, water can be quickly transported to the bottom of the hillslope. With time, slope-wise wheel tracks transport more water and

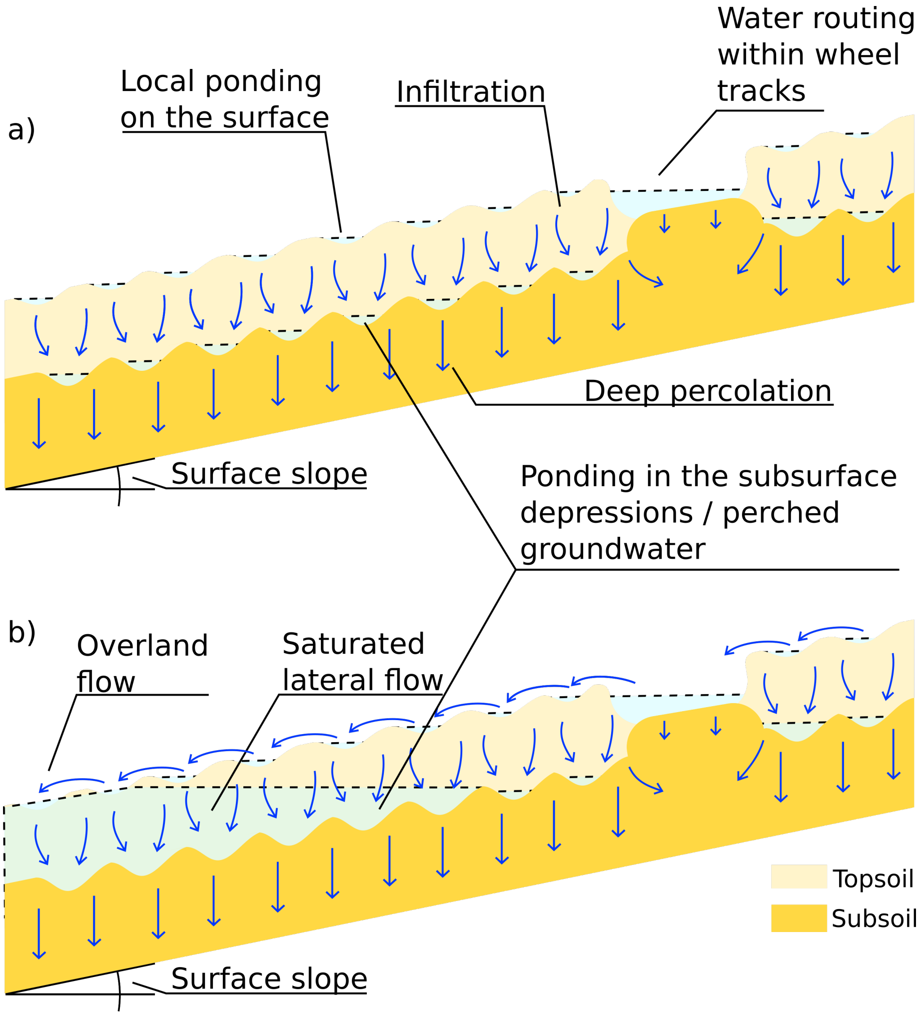

Figure 8.17: The redefined conceptual model is shown in Figures 1 and 3. a) Beginning of runoff generation; water starts to pond in the depressions on the soil surface and the wheel track. b) The surface runoff develops and the topsoil is fully saturated.

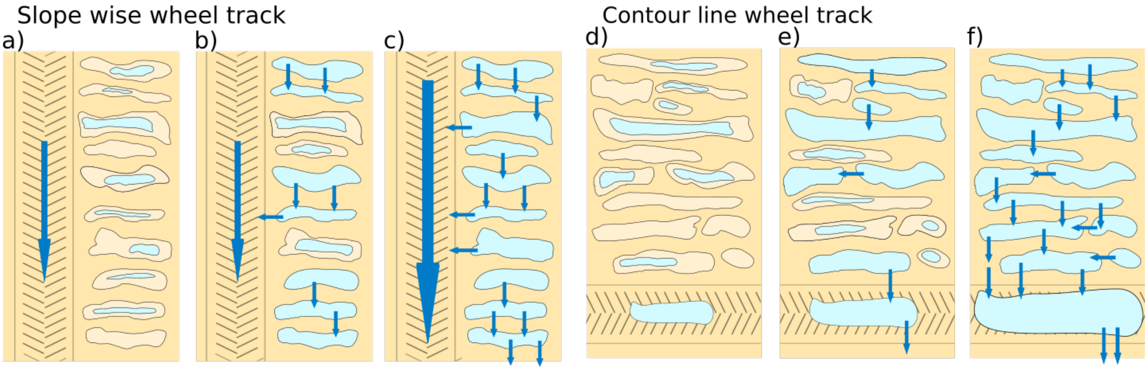

Figure 8.18: Conceptual model of overland flow generation with various wheel tracks orientations. a) - c) depict filling and spilling of soil surface depressions and the role of the wheel track in the case of the SWT plot. d) - f) depict filling and spilling of soil surface depressions and the role of the wheel track in the case of the CWT plot.

sediment due to a decrease in the roughness of the surface of the catchment soil and an increase in connectivity between the wheel track and the surrounding soil. Although the contour line wheel tracks decrease the overland flow, their effect is only temporary. The shallow subsurface lateral flow does not significantly affect runoff at the field scale and may occur under specific circumstances at the local scale. However, it can locally affect the distribution of nutrients or chemicals.

The most notable conclusions are as follows:

- Electrical resistivity tomography is a suitable tool for observing the compacted subsoil layer and the artefacts of wheel track compaction under topsoil.
- Slope-oriented wheel tracks increase surface runoff and hydrological connectivity of soil surface; recurring rainfall events further increase connectivity.
- Contour line oriented wheel tracks act as a barrier for overland flow and decrease the connectivity; however, while the wheel tracks are being filled with sediment, the connectivity increases with time.
- Infiltration excess overland flow occurs on wheel tracks, while saturation excess overland flow was identified in the surrounding soil, as was shown in the numerical model.
- Lateral subsurface flow is limited by the morphology of the subsoil layer and the contrasting soil hydraulic properties in the topsoil and subsoil.
- The spatial heterogeneity of the infiltration is mainly driven by the surface microrelief and morphology of the subsoil; hence, the thickness of the permeable topsoil.

8.5 Further advances

The results of the thesis bring partial advances in the research of rainfall-runoff processes and runoff routing over tilled soils. However, many open questions remain. The following topics are suggested for detailed study in the future.

- In addition to explicit soil morphology, semivariance of electrical resistivity can be used to explore spatially variable soil hydraulic properties for every soil depth.
- The development of the crust on the soil surface and the time variable soil hydraulic properties should be included in the analysis, as they affect the infiltration process and the hydraulic connectivity of the soil surface.
- Subsurface processes are coupled, and the used approach does not account for it. For example, uneven surface ponding may further affect the heterogeneity of infiltration, which is already affected by the thickness of soil layers.
- The concept of connectivity can be further tested on the hillslope and field scale because the length of the plot presented in Chapter 7 is a limitation.
- The concept of functional connectivity may be used to investigate the effect of wheel tracks on the catchment scale.

- The artificial rainfall experiment provides insight into the runoff generation mechanism; however, the behaviour of the transect under real long-term meteorological conditions should be investigated in the future.
- The morphology of the topsoil-subsoil interface may be different for various tillage practices and may affect the soil water balance similarly as different tillage practices (Jeřábek et al., 2021).
- The application of tracers can be considered to investigate the possible accumulation of nutrients or contaminants in the subsoil morphology depressions.

Bibliography

Abudeif, A. M. (2015). Integrated electrical tomography and hydro-chemical analysis for environmental assessment of El-Dair waste disposal site, west of Sohag city, Egypt. *Environmental Earth Sciences*, 74(7):5859–5874.

Ahuja, L., Fiedler, F., Dunn, G., Benjamin, J., and Garrison, A. (1998). Changes in soil water retention curves due to tillage and natural reconsolidation. *Soil Science Society of America Journal*, 62(5):1228–1233.

Alaoui, A., Lipiec, J., and Gerke, H. (2011). A review of the changes in the soil pore system due to soil deformation: A hydrodynamic perspective. *Soil and Tillage Research*, 115-116:1–15.

Ali, G. A., L'Heureux, C., Roy, A. G., Turmel, M.-C., and Courchesne, F. (2011). Linking spatial patterns of perched groundwater storage and stormflow generation processes in a headwater forested catchment. *Hydrological Processes*, 25(25):3843–3857.

Ali, G. A. and Roy, A. G. (2009). Revisiting hydrologic sampling strategies for an accurate assessment of hydrologic connectivity in humid temperate systems. *Geography Compass*, 3(1):350–374.

Anderson, M. G. and Burt, T. P. (1990). Process studies in hillslope hydrology. *Process studies in hillslope hydrology.*

Angermann, L., Jackisch, C., Allroggen, N., Sprenger, M., Zehe, E., Tronicke, J., Weiler, M., and Blume, T. (2017). Form and function in hillslope hydrology: characterization of subsurface flow based on response observations. *Hydrology and Earth System Sciences*, 21(7):3727–3748.

Ankeny, M. D., Kaspar, T. C., and Horton, R. (1990). Characterization of tillage and traffic effects on unconfined infiltration measurements. *Soil Science Society of America Journal*, 54(3):837–840.

Antoine, M., Javaux, M., and Bielders, C. (2009). What indicators can capture runoff-relevant connectivity properties of the micro-topography at the plot scale? *Advances in Water Resources*, 32(8):1297–1310.

Antoine, M., Javaux, M., and Bielders, C. L. (2011). Integrating subgrid connectivity properties of the micro-topography in distributed runoff models, at the interrill scale. *Journal of Hydrology*, 403(3-4):213–223.

Appels, W. M., Bogaart, P. W., and van der Zee, S. E. (2011). Influence of spatial variations of microtopography and infiltration on surface runoff and field scale hydrological connectivity. *Advances in Water Resources*, 34(2):303–313.

Appels, W. M., Bogaart, P. W., and van der Zee, S. E. (2016a). Surface runoff in flat terrain: How field topography and runoff generating processes control hydrological connectivity. *Journal of Hydrology*, 534(Supplement C):493 – 504.

Appels, W. M., Bogaart, P. W., and van der Zee, S. E. (2016b). Surface runoff in flat terrain: How field topography and runoff generating processes control hydrological connectivity. *Journal of Hydrology*, 534:493–504.

Archie, G. E. (1942). The electrical resistivity log as an aid in determining some reservoir characteristics. *Transactions of the AIME*, 146(01):54–62.

Augustin, K., Kuhwald, M., Brunotte, J., and Duttmann, R. (2020). Wheel load and wheel pass frequency as indicators for soil compaction risk: A four-year analysis of traffic intensity at field scale. *Geosciences (Switzerland)*, 10(8):1–15.

Bachmair, S. and Weiler, M. (2012). Hillslope characteristics as controls of subsurface flow variability. *Hydrology and Earth System Sciences*, 16(10):3699–3715.

Bachmair, S., Weiler, M., and Nützmann, G. (2009). Controls of land use and soil structure on water movement: Lessons for pollutant transfer through the unsaturated zone. *Journal of hydrology*, 369(3):241–252.

Bachmair, S., Weiler, M., and Troch, P. A. (2012). Intercomparing hillslope hydrological dynamics: Spatio-temporal variability and vegetation cover effects. *Water Resources Research*, 48(5):n/a–n/a. W05537.

Basher, L. and Ross, C. (2001). Role of wheel tracks in runoff generation and erosion under vegetable production on a clay loam soil at pukekohe, new zealand. *Soil and Tillage Research*, 62(3):117 – 130.

Basso, B., Amato, M., Bitella, G., Rossi, R., Kravchenko, A., M., L. S. L., Carvahlo, and Gomes, J. (2010). Two-dimensional spatial and temporal variation of soil physical properties in tillage systems using electrical resistivity tomography. *Agronomy Journal*, 102(2):440–449.

Bauer, T., Strauss, P., Grims, M., Kamptner, E., Mansberger, R., and Spiegel, H. (2015). Long-term agricultural management effects on surface roughness and consolidation of soils. *Soil and Tillage Research*, 151:28–38.

Bertolino, A. V., Fernandes, N. F., Miranda, J. P., Souza, A. P., Lopes, M. R., and Palmieri, F. (2010). Effects of plough pan development on surface hydrology and on soil physical properties in southeastern brazilian plateau. *Journal of Hydrology*, 393(12):94 – 104.

Besson, A., Cousin, I., Samouëlian, A., Boizard, H., and Richard, G. (2004). Structural heterogeneity of the soil tilled layer as characterized by 2d electrical resistivity surveying. *Soil and Tillage Research*, 79(2):239–249.

Beven, K. J. and Kirkby, M. J. (1979). A physically based, variable contributing area model of basin hydrology. *Hydrological Sciences Bulletin*, 24(1):43–69.

Bittelli, M. and Flury, M. (2009). Errors in Water Retention Curves Determined with Pressure Plates. *Soil Science Society of America Journal*, 73(5):1453–1460.

Blanco-Canqui, H. and Lal, R. (2007). Impacts of Long-Term Wheat Straw Management on Soil Hydraulic Properties under No-Tillage. *Soil Science Society of America Journal*, 71(4):1166–1173.

Blanco-Canqui, H., Lal, R., Post, W. M., Izaurralde, R. C., and Shipitalo, M. J. (2007). Soil hydraulic properties influenced by corn stover removal from no-till corn in Ohio. *Soil and Tillage Research*, 92(1-2):144–155.

Boizard, H., Richard, G., Roger-Estrade, J., Dürr, C., and Boiffin, J. (2002). Cumulative effects of cropping systems on the structure of the tilled layer in northern france. *Soil and Tillage Research*, 64(12):149 – 164.

Borselli, L., Cassi, P., and Torri, D. (2008). Prolegomena to sediment and flow connectivity in the landscape: A GIS and field numerical assessment. *Catena*, 75(3):268–277.

Bracken, L., Wainwright, J., Ali, G., Tetzlaff, D., Smith, M., Reaney, S., and Roy, A. (2013). Concepts of hydrological connectivity: research approaches, pathways and future agendas. *Earth-Science Reviews*, 119:17–34.

Bracken, L. J. and Croke, J. (2007). The concept of hydrological connectivity and its contribution to understanding runoff-dominated geomorphic systems. *Hydrological processes*, 21(13):1749–1763.

Brooks, R. and Corey, A. (1964). *Hydraulic Properties of Porous Media*. Colorado State University Hydrology Papers. Colorado State University.

Buckingham, E. (1907). Studies on the movement of soil moisture. *Bureau of Soil, USDA, Washington DC*, 38.

Castellini, M. and Ventrella, D. (2012). Impact of conventional and minimum tillage on soil hydraulic conductivity in typical cropping system in Southern Italy. *Soil and Tillage Research*, 124:47–56.

Celia, M. A., Bouloutas, E. T., and Zarba, R. L. (1990). A general mass-conservative numerical solution for the unsaturated flow equation. *Water resources research*, 26(7):1483–1496.

Chambers, J., Wilkinson, P., Uhlemann, S., Sorensen, J., Roberts, C., Newell, A., Ward, W., Binley, A., Williams, P., Gooddy, D., et al. (2014). Derivation of lowland riparian wetland deposit architecture using geophysical image analysis and interface detection. *Water Resources Research*, 50(7):5886–5905.

Chang, C. and Lindwall, C. W. (1992). Effects of tillage and crop rotation on physical properties of a loam soil. *Soil and Tillage Research*, 22(3-4):383–389.

Cheng, Q., Tao, M., Chen, X., and Binley, A. (2019). Evaluation of electrical resistivity tomography (ERT) for mapping the soil–rock interface in karstic environments. *Environmental Earth Sciences*, 78(15):1–14.

Childs, E. C. and Collis-George, N. (1950). The permeability of porous materials. *Proceedings of the Royal Society of London. Series A. Mathematical and Physical Sciences*, 201(1066):392–405.

Colangelo, G., Lapenna, V., Loperte, A., Perrone, A., and Telesca, L. (2008). 2D electrical resistivity tomographies for investigating recent activation landslides in Basilicata Region (Southern Italy). *Annals of Geophysics*, 51(1):275–285.

Colombi, T., Braun, S., Keller, T., and Walter, A. (2016). Artificial macropores attract crop roots and enhance plant productivity on compacted soils. *Science of The Total Environment*, pages –.

Coquet, Y., Coutadeur, C., Labat, C., Vachier, P., Van Genuchten, M., Roger-Estrade, J., and Šimůnek, J. (2005a). Water and solute transport in a cultivated silt loam soil– 1. field observations. *Vadose Zone Journal*, 4(3):573–586.

Coquet, Y., Šimůnek, J., Coutadeur, C., van Genuchten, M. T., Pot, V., and Roger-Estrade, J. (2005b). Water and solute transport in a cultivated silt loam soil– 2. numerical analysis. *Vadose Zone Journal*, 4(3):587–601.

Couturier, A., Daroussin, J., Darboux, F., Souchère, V., Le Bissonnais, Y., Cerdan, O., and King, D. (2013). Improvement of surface flow network prediction for the modeling of erosion processes in agricultural landscapes. *Geomorphology*, 183:120–129.

Dahlin, T. and Loke, M. (1997). Quasi-3d resistivity imaging-mapping of three dimensional structures using two dimensional dc resistivity techniques. In *3rd EEGS Meeting*.

Daraghmeh, O. A., Jensen, J. R., and Petersen, C. T. (2008). Near-saturated hydraulic properties in the surface layer of a sandy loam soil under conventional and reduced tillage. *Soil Sci. Soc. Am. J.*, 72:1728–1737.

Darboux, F., Davy, P., and Gascuel-Odoux, C. (2002a). Effect of depression storage capacity on overland-flow generation for rough horizontal surfaces: Water transfer distance and scaling. *Earth Surface Processes and Landforms*, 27(2):177–191.

Darboux, F., Davy, P., Gascuel-Odoux, C., and Huang, C. (2002b). Evolution of soil surface roughness and flowpath connectivity in overland flow experiments. *Catena*, 46(2-3):125–139.

Darcy, H. (1856). Les fontaines publiques de la ville de dijon ("the public fountains of the town of dijon"). *Dalmont, Paris.*

Dörner, J. and Horn, R. (2009). Direction-dependent behaviour of hydraulic and mechanical properties in structured soils under conventional and conservation tillage. *Soil and Tillage Research*, 102(2):225–232.

Dostál, T., Váška, J., and Vrána, K. (2000). SMODERP — A Simulation Model of Overland Flow and Erosion Processes. *Soil Erosion*, pages 135–161.

Du, E., Jackson, C. R., Klaus, J., McDonnell, J. J., Griffiths, N. A., Williamson, M. F., Greco, J. L., and Bitew, M. (2016). Interflow dynamics on a low relief forested hillslope: Lots of fill, little spill. *Journal of Hydrology*, 534:648–658.

Du, J., Xie, S., Xu, Y., yu Xu, C., and Singh, V. P. (2007). Development and testing of a simple physically-based distributed rainfall-runoff model for storm runoff simulation in humid forested basins. *Journal of Hydrology*, 336(3):334 – 346.

Dusek, J. and Vogel, T. (2014). Modeling subsurface hillslope runoff dominated by preferential flow: One- vs. two-dimensional approximation. *VADOSE ZONE JOURNAL*, 13.

Dušek, J., Vogel, T., Dohnal, M., and Gerke, H. H. (2012). Combining dual-continuum approach with diffusion wave model to include a preferential flow component in hillslope scale modeling of shallow subsurface runoff. *Advances in Water Resources*, 44:113 – 125.

Esteves, M., Faucher, X., Galle, S., and Vauclin, M. (2000). Overland flow and infiltration modelling for small plots during unsteady rain: numerical results versus observed values. *Journal of hydrology*, 228(3-4):265–282.

Evans, R. (2017). Factors controlling soil erosion and runoff and their impacts in the upper wissey catchment, norfolk, england: A ten year monitoring programme. *Earth Surface Processes and Landforms*, 42(14):2266–2279.

Filipović, V., Gerke, H. H., Filipović, L., and Sommer, M. (2018). Quantifying Subsurface Lateral Flow along Sloping Horizon Boundaries in Soil Profiles of a Hummocky Ground Moraine. *Vadose Zone Journal*, 17(1):170106.

Flury, M., Flühler, H., Jury, W. A., and Leuenberger, J. (1994). Susceptibility of soils to preferential flow of water: A field study. *Water resources research*, 30(7):1945–1954.

Freeze, R. A. (1971). Three-dimensional, transient, saturated-unsaturated flow in a groundwater basin. *Water Resources Research*, 7(2):347–366.

Freeze, R. A. (1972). Role of subsurface flow in generating surface runoff: 1. base flow contributions to channel flow. *Water Resources Research*, 8(3):609–623.

Frei, S., Lischeid, G., and Fleckenstein, J. (2010). Effects of micro-topography on surface–subsurface exchange and runoff generation in a virtual riparian wetland—a modeling study. *Advances in Water Resources*, 33(11):1388–1401.

Furman, A., Ferré, T., and Warrick, A. (2003). A sensitivity analysis of electrical resistivity tomography array types using analytical element modeling. *Vadose Zone Journal*, 2(3):416–423.

Germann, P. F. (1990). Preferential flow and the generation of runoff: 1. boundary layer flow theory. *Water Resources Research*, 26(12):3055–3063.

Głab, T. and Kulig, B. (2008). Effect of mulch and tillage system on soil porosity under wheat (Triticum aestivum). *Soil and Tillage Research*, 99(2):169–178.

Grayson, R. B., Western, A. W., Chiew, F. H. S., and Blöschl, G. (1997). Preferred states in spatial soil moisture patterns: Local and nonlocal controls. *Water Resources Research*, 33(12):2897–2908.

Hammel, K., Gross, J., Wessolek, G., and Roth, K. (1999). Two-dimensional simulation of bromide transport in a heterogeneous field soil with transient unsaturated flow. *European Journal of Soil Science*, 50(4):633–647.

Haruna, S. I., Anderson, S. H., Nkongolo, N. V., and Zaibon, S. (2018). Soil Hydraulic Properties: Influence of Tillage and Cover Crops. *Pedosphere*, 28(3):430–442.

Haskins, N. (2010). Book Review - A Field Guide to Geophysics in Archaeology. *Archae-*

ological Prospection, 62(December 2009):61–62.

Hassanizadeh, S. M. and Gray, W. G. (1987). High velocity flow in porous media. *Transport in porous media*, 2(6):521–531.

Hassanizadeh, S. M. and Gray, W. G. (1993). Thermodynamic basis of capillary pressure in porous media. *Water Resources Research*, 29(10):3389–3405.

Heathwaite, A. L., Quinn, P. F., and Hewett, C. J. (2005). Modelling and managing critical source areas of diffuse pollution from agricultural land using flow connectivity simulation. *Journal of Hydrology*, 304(1-4):446–461.

Hopp, L. and McDonnell, J. (2009). Connectivity at the hillslope scale: Identifying interactions between storm size, bedrock permeability, slope angle and soil depth. *Journal of Hydrology*, 376(3-4):378–391.

Hutson, J. and Cass, A. (1987). A retentivity function for use in soil–water simulation models. *European Journal of Soil Science*, 38(1):105–113.

Jackisch, C., Angermann, L., Allroggen, N., Sprenger, M., Blume, T., Tronicke, J., and Zehe, E. (2017). Form and function in hillslope hydrology: in situ imaging and characterization of flow-relevant structures. *Hydrology and Earth System Sciences*, 21(7):3749–3775.

Jeřábek, J., Zumr, D., and Dostál, T. (2017). Identifying the plough pan position on cultivated soils by measurements of electrical resistivity and penetration resistance. *Soil and Tillage Research*, 174:231–240.

Jeřábek, J., Zumr, D., Dostál, T., Tenreiro, T., Strauss, P., and VaverkováM.D. (2021). The effects of management practices and fires on soil water dynamics at three locations across europe. In *2021 IEEE International Workshop on Metrology for Agriculture and Forestry*, volume 175226, Como, IT. IEEE Instrumentation and Measurement Society.

Jeřábek, J., Zumr, D., Krása, J., and Dostál, T. (2018). Monitoring of runoff processes during an artificial rainfall on a freshly tilled soil. *TRANSPORT VODY, CHEMIKÁLIÍ A ENERGIE V SYSTÉME PÔDA-RASTLINA-ATMOSFÉRA*, 25:21–31.

Jeřábek, J., Zumr, D., Krása, J., and Dostál, T. (2019). Surface runoff and soil loss generation at an agricultural catchment with developed wheel-tracks. In *10th EGU Leonardo Conference: Global change, landscape ageing and the pulse of catchments*, Katlenburg-Lindau, DE. The European Geosciences Union (EGU).

Jeřábek, J., Zumr, D., Laburda, T., Kása, J., and Dostál, T. (2022). Soil surface connectivity of tilled soil with wheel tracks and its development under simulated rainfall. *Manuscript sumitted for publication.*

Jester, W. and Klik, A. (2005). Soil surface roughness measurement - Methods, applicability, and surface representation. *Catena*, 64(2-3):174–192.

Jeřábek, J. and Zumr, D. (2021). GEOPHYSICAL SURVEY AS A TOOL TO REVEAL SUBSURFACE STRATIFICATION AT A SMALL AGRICULTURAL HEADWATER CATCHMENT: A CASE STUDY. *Stavební obzor - Civil Engineering Journal*, 30(3).

Kašpar, M., Bližňák, V., Hulec, F., and Müller, M. (2021). High-resolution spatial analysis of the variability in the subdaily rainfall time structure. *Atmospheric Research*, 248:105202.

Katsvairo, T., Cox, W. J., and Van Es, H. (2002). Tillage and rotation effects on soil physical characteristics. *Agronomy Journal*, 94(2):299–304.

Kavka, P., Jeřábek, J., Kubínová, R., Pešek, O., Dufka, D., Marek, O., and Landa, M. (2020). Smoderp line. `https://smoderp.fsv.cvut.cz`. Software.

Kavka, P., Jeřábek, J., and Landa, M. (2022). Smoderp2d—sheet and rill runoff routine validation at three scale levels. *Water*, 14(3).

Kavka, P., Strouhal, L., Jáchymová, B., Krása, J., Báčová, M., Laburda, T., Dostál, T., Devátý, J., and Bauer, M. (2018). Double Size Fulljet Field Rainfall Simulator for Complex Interrill and Rill Erosion Studies. *Stavební obzor - Civil Engineering Journal*, 27(2):183–194.

Kim, H., Anderson, S., Motavalli, P., and Gantzer, C. (2010). Compaction effects on soil macropore geometry and related parameters for an arable field. *Geoderma*, 160(2):244 – 251.

Kmec, J., Fürst, T., Vodakand, R., and Šír, M. (2019). A semi-continuum model of saturation overshoot in one dimensional unsaturated porous media flow. *Scientific Reports*, 9:8390:1–12.

Kroulík, M., Kvíz, Z., Kumhála, F., Hůla, J., and Loch, T. (2011). Procedures of soil farming allowing reduction of compaction. *Precision Agriculture*, 12(3):317–333.

Laburda, T., Krasa, J., Zumr, D., Devátý, J., Vrána, M., Zambon, N., Johannsen, L., Klik, A., Strauss, P., and Dostál, T. (2021). Sfm-mvs photogrammetry for splash erosion monitoring under natural rainfall. *Earth Surface Processes and Landforms*, 46.

Lal, R. (1999). Long-term tillage and wheel traffic effects on soil quality for two central ohio soils. *Journal of Sustainable Agriculture*, 14(4):67–84.

Landa, M., Jeřábek, J., Pešek, O., and Kavka, P. (2019). SMODERP2D SOIL EROSION MODEL ENTERING AN OPEN SOURCE ERA with GPU-BASED PARALLELIZATION. *International Archives of the Photogrammetry, Remote Sensing and Spatial Information Sciences - ISPRS Archives*, 42(4/W14):143–149.

Lexartza-Artza, I. and Wainwright, J. (2009). Hydrological connectivity: linking concepts with practical implications. *Catena*, 79(2):146–152.

Li, T., Jeřábek, J., Zumr, D., Noreika, N., and Dostál, T. (2021). Assessing spatial soil moisture patterns at a small agricultural catchment. In *2021 IEEE International Workshop on Metrology for Agriculture and Forestry*, volume 175226, Como, IT. IEEE Instrumentation and Measurement Society.

Lindstrom, M. J., Voorhees, W. B., and Randall, G. W. (1981). Long-Term Tillage Effects on Interrow Runoff and Infiltration. *Soil Science Society of America Journal*, 45(5):945–948.

Lipiec, J., Horn, R., Pietrusiewicz, J., and Siczek, A. (2012). Effects of soil compaction on root elongation and anatomy of different cereal plant species. *Soil and Tillage Research*, 121:74 – 81.

Loke, M. H. (1999). Electrical imaging surveys for environmental and engineering studies. A practical guide to 2-D and 3-D surveys. (1999):59.

Loke, M. H. (2004). Tutorial : 2-d and 3-d electrical imaging surveys.

Luo, J., Zheng, Z., Li, T., and He, S. (2018). Assessing the impacts of microtopography on soil erosion under simulated rainfall, using a multifractal approach. *Hydrological Processes*, 32(16):2543–2556.

Molnar, D. and Julien, P. (2000). Grid-size effects on surface runoff modeling. *Journal of Hydrologic Engineering*, 5(1):8–16.

Mooney, S. and Nipattasuk, W. (2003). Quantification of the effects of soil compaction on water flow using dye tracers and image analysis. *Soil Use and Management*, 19(4):356–363.

Moramarco, T. and Singh, V. (2002). Accuracy of kinematic wave and diffusion wave for spatial-varying rainfall excess over a plane. *Hydrological processes*, 16(17):3419–3435.

Morrow, R. N. (1970). Physics and thermodynamics of capillary action in porous media. *Industrial & Engineering Chemistry*, 62.

Mualem, Y. (1976). A new model for predicting the hydraulic conductivity of unsaturated porous media. *Water Resources Research*, 12(3):513–522.

O'Callaghan, J. F. and Mark, D. M. (1984). The extraction of drainage networks from digital elevation data. *Computer Vision, Graphics, and Image Processing*, 28(3):323 – 344.

Onstad, C. A., Wolfe, M. L., Larson, C. L., and Slack, D. C. (1984). Tilled soil subsidence during repeated wetting.

Or, D., Keller, T., and Schlesinger, W. H. (2021). Natural and managed soil structure: On the fragile scaffolding for soil functioning. *Soil and Tillage Research*, 208(December 2020):104912.

Pagliai, M., Marsili, A., Servadio, P., Vignozzi, N., and Pellegrini, S. (2003). Changes in some physical properties of a clay soil in central italy following the passage of rubber tracked and wheeled tractors of medium power. *Soil and Tillage Research*, 73(12):119 – 129.

Pagliai, M., Vignozzi, N., and Pellegrini, S. (2004). Soil structure and the effect of management practices. *Soil and Tillage Research*, 79(2):131 – 143.

Palacky, G. J. (1988). 3. Resistivity Characteristics of Geologic Targets. In *Electromagnetic Methods in Applied Geophysics*, pages 52–129.

Peñuela, A., Darboux, F., Javaux, M., and Bielders, C. L. (2016). Evolution of overland flow connectivity in bare agricultural plots. *Earth Surface Processes and Landforms*, 41(11):1595–1613.

Pertassek, T., Peters, A., and Durner, W. (2015). HYPROP-FIT User's Manual. (V.3.0):66.

Peters, A. and Durner, W. (2008). Simplified evaporation method for determining soil hydraulic properties. *Journal of Hydrology*, 356(1-2):147–162.

Philip, J. (1957a). Numerical Solution of Equations of the Diffusion Type with Diffusivity Concentration-Dependent. II. *Australian Journal of Physics*, 10(1):29.

Philip, J. (1957b). The theory of infiltration: 1. the infiltration equation and its solution. *Soil science*, 83(5):345–358.

Pikul, M. F., Street, R. L., and Remson, I. (1974). A numerical model based on coupled one-dimensional richards and boussinesq equations. *Water Resources Research*, 10(2):295–302.

Pringle, C. M. (2003). What is hydrologic connectivity and why is it ecologically important? *Hydrol. Process.*, 17(13).

Prosdocimi, M., Burguet, M., Di Prima, S., Sofia, G., Terol, E., Rodrigo Comino, J., Cerdà, A., and Tarolli, P. (2017). Rainfall simulation and Structure-from-Motion photogrammetry for the analysis of soil water erosion in Mediterranean vineyards. *Science of the Total Environment*, 574:204–215.

Prunty, L. and Casey, F. X. M. (2002). Soil Water Retention Curve Description Using a Flexible Smooth Function. *Vadose Zone Journal*, 1(1):179–185.

Ren, L., Nest, T. V., Ruysschaert, G., D'Hose, T., and Cornelis, W. M. (2019). Short-term effects of cover crops and tillage methods on soil physical properties and maize growth in a sandy loam soil. *Soil and Tillage Research*, 192(April):76–86.

Richards, L. A. (1931). Capillary conduction of liquids in porous mediums. physics 1: 318-333. 1:318 – 333.

Rinderer, M., Ali, G., and Larsen, L. G. (2018). Assessing structural, functional and effective hydrologic connectivity with brain neuroscience methods: State-of-the-art and research directions. *Earth-Science Reviews*, 178:29–47.

Roth, K. (2006). *Soil Physics: Lecture Notes.*

Roulier, S., Angulo-Jaramillo, R., Bresson, L.-M., Auzet, A.-V., Gaudet, J.-P., and Bariac, T. (2002). Water transfer and mobile water content measurement in a cultivated crusted soil. *Soil science*, 167(3):201–210.

Ryken, N., Nest, T. V., Al-Barri, B., Blake, W., Taylor, A., Bodé, S., Ruysschaert, G., Boeckx, P., and Verdoodt, A. (2018a). Soil erosion rates under different tillage practices in central belgium: New perspectives from a combined approach of rainfall simulations and 7be measurements. *Soil and Tillage Research*, 179:29 – 37.

Ryken, N., Vanden Nest, T., Al-Barri, B., Blake, W., Taylor, A., Bodé, S., Ruysschaert, G., Boeckx, P., and Verdoodt, A. (2018b). Soil erosion rates under different tillage practices in central Belgium: New perspectives from a combined approach of rainfall simulations and7Be measurements. *Soil and Tillage Research*, 179(January):29–37.

Samouëlian, A., Cousin, I., Tabbagh, A., Bruand, A., and Richard, G. (2005). Electrical resistivity survey in soil science: a review. *Soil and Tillage Research*, 83(2):173 – 193.

Satriani, A., Loperte, A., Imbrenda, V., and Lapenna, V. (2012). Geoelectrical surveys for characterization of the coastal saltwater intrusion in metapontum forest reserve (Southern Italy). *International Journal of Geophysics*, 2012.

Scherrer, S. and Naef, F. (2003). A decision scheme to indicate dominant hydrological flow processes on temperate grassland. *Hydrological processes*, 17(2):391–401.

Schrott, L. and Sass, O. (2008). Application of field geophysics in geomorphology: Advances and limitations exemplified by case studies. *Geomorphology*, 93(1-2):55–73.

Schwen, A., Bodner, G., and Loiskandl, W. (2011). Time-variable soil hydraulic properties in near-surface soil water simulations for different tillage methods. *Agricultural Water Management*, 99(1):42–50.

Seehusen, T., Riggert, R., Fleige, H., Horn, R., and Riley, H. (2019). Soil compaction and stress propagation after different wheeling intensities on a silt soil in South-East Norway. *Acta Agriculturae Scandinavica Section B: Soil and Plant Science*, 69(4):343–355.

Seong, J. N., Hyunuk, A., Sanghyum, K., and Hyeonju, K. (2015). Simulation of soil moisture on a hillslope using multiple hydrologic models in comparison to field measurements. *Journal of Hydrology*, 523:342–355.

Silgram, M., Jackson, D., Bailey, A., Quinton, J., and Stevens, C. (2010). Hillslope scale surface runoff, sediment and nutrient losses associated with tramline wheelings. *Earth Surface Processes and Landforms*, 35(6):699–706.

Šimunek, J., van Genuchten, M. T., and Šejna, M. (2012). HYDRUS: Model use, calibration, and validation. *Transactions of the ASABE*, 55(4):1263–1274.

Šimůnek, J. and Van Genuchten, M. T. (1996). Estimating unsaturated soil hydraulic properties from tension disc infiltrometer data by numerical inversion. *Water Resources Research*, 32(9):2683–2696.

Singh, V. (1994). Accuracy of kinematic wave and diffusion wave approximations for space independent flows. *Hydrological Processes*, 8(1):45–62.

Sloan, P. G. and Moore, I. D. (1984). Modeling subsurface stormflow on steeply sloping forested watersheds. *Water Resources Research*, 20(12):1815–1822.

SMODERP2D development team (2017). *SMODERP2D - uživatelský manuál (in CZECH)*. CTU in Prague, https://storm.fsv.cvut.cz/cinnost-katedry/volne-stazitelne-vysledky/smoderp/?lang=en, Prague, Czechia.

Sokolowski, A. C., Prack McCormick, B., De Grazia, J., Wolski, J. E., Rodríguez, H. A., Rodríguez-Frers, E. P., Gagey, M. C., Debelis, S. P., Paladino, I. R., and Barrios, M. B. (2020). Tillage and no-tillage effects on physical and chemical properties of an Argiaquoll soil under long-term crop rotation in Buenos Aires, Argentina. *International Soil and Water Conservation Research*, 8(2):185–194.

Souchere, V., King, D., Daroussin, J., Papy, F., and Capillon, A. (1998). Effects of tillage on runoff directions: Consequences on runoff contributing area within agricultural catchments. *Journal of Hydrology*, 206(3-4):256–267.

Strouhal, L. (2016). Kvantifikace vlivu liniových opatření na povodňové odtoky (quantifying effect of linear measures on flood runoff).

Taconet, O. and Ciarletti, V. (2007). Estimating soil roughness indices on a ridge-and-furrow surface using stereo photogrammetry. *Soil and Tillage Research*, 93(1):64–76.

Takken, I., Govers, G., Steegen, A., Nachtergaele, J., and Guérif, J. (2001). The prediction of runoff flow directions on tilled fields. *Journal of Hydrology*, 248(1-4):1–13.

Tarboton, D. G. (2015). Terrain Analysis Using Digital Elevation Models (TauDEM).

Te Chow, V., Maidment, D., and Mays, L. (1988). *Applied Hydrology*. McGraw-Hill international editions. McGraw-Hill.

Topp, G. C. and Miller, E. E. (1966). Hysteretic Moisture Characteristics and Hydraulic Conductivities for Glass-Bead Media. *Soil Science Society of America Journal*, 30(2):156–162.

Tromp-van Meerveld, H. J. and McDonnell, J. J. (2006a). Threshold relations in subsurface stormflow: 1. a 147-storm analysis of the panola hillslope. *Water Resources Research*, 42(2):n/a–n/a. W02410.

Tromp-van Meerveld, H. J. and McDonnell, J. J. (2006b). Threshold relations in subsurface stormflow: 2. the fill and spill hypothesis. *Water Resources Research*, 42(2):n/a–n/a.

van Genuchten, M. T. (1980). A closed-form equation for predicting the hydraulic conductivity of unsaturated soils. *Soil Sci. Soc. Am J.*, 44:892 – 898.

van Genuchten, M. T., Leij, F. J., and Yates, S. R. (1991). The RETC code for quantifying the hydraulic functions of unsaturated soils.

van Genuchten, M. T. and Nielsen, D. (1985). On describing and predicting the hydraulic properties. 3(5):615–628.

Wang, T. P., Chen, C. C., Tong, L. T., Chang, P. Y., Chen, Y. C., Dong, T. H., Liu, H. C., Lin, C. P., Yang, K. H., Ho, C. J., and Cheng, S. N. (2015). Applying FDEM, ERT and GPR at a site with soil contamination: A case study. *Journal of Applied Geophysics*, 121:21–30.

Weiler, M. and McDonnell, J. (2004). Virtual experiments: a new approach for improving process conceptualization in hillslope hydrology. *Journal of Hydrology*, 285(1):3–18.

Weiler, M. and McDonnell, J. (2007). Conceptualizing lateral preferential flow and flow networks and simulating the effects on gauged and ungauged hillslopes. *Water Resources Research*, 43(3).

Weninger, T., Kamptner, E., Dostal, T., Spiegel, A., and Strauss, P. (2021). Detection of physical hazards in soil profiles using quantitative soil physical quality assessment in the Pannonian basin, Eastern Austria**. *International Agrophysics*, 34(4):463–471.

Withers, P. J. A., Hodgkinson, R. A., Bates, A., and Withers, C. M. (2006). Some effects of tramlines on surface runoff, sediment and phosphorus mobilization on an erosion-prone soil. *Soil Use and Management*, 22(3):245–255.

Yakirevich, A., Borisov, V., and Sorek, S. (1998). A quasi three-dimensional model for flow and transport in unsaturated and saturated zones: 1. implementation of the quasi two-dimensional case. *Advances in Water Resources*, 21(8):679–689.

Yang, J. and Chu, X. (2013). Quantification of the spatio-temporal variations in hydrologic connectivity of small-scale topographic surfaces under various rainfall conditions. *Journal of Hydrology*, 505:65–77.

Zhang, W. and Cundy, T. W. (1989). Modeling of two-dimensional overland flow. *Water Resources Research*, 25(9):2019–2035.

Zhao, L., Hou, R., Wu, F., and Keesstra, S. (2018). Effect of soil surface roughness on infiltration water, ponding and runoff on tilled soils under rainfall simulation experiments. *Soil and Tillage Research*, 179(June 2017):47–53.

Zhou, W., Beck, B. F., and Stephenson, J. B. (2000). Reliability of dipole-dipole electrical resistivity tomography for defining depth to bedrock in covered karst terranes. *Environmental Geology*, 39(7):760–766.

Zobeck, T. M. and Onstad, C. A. (1987). Tillage and rainfall effects on random roughness: A review. *Soil and Tillage Research*, 9(1):1–20.

Zuecco, G., Rinderer, M., Penna, D., Borga, M., and van Meerveld, H. (2019). Quantification of subsurface hydrologic connectivity in four headwater catchments using graph theory. *Science of The Total Environment*, 646:1265–1280.

Zumr, D., Dostál, T., and Devátý, J. (2015). Identification of prevailing storm runoff generation mechanisms in an intensively cultivated catchment. *Journal of Hydrology and Hydromechanics*, 63(3):246 – 254.

List of author's publications

The list of publications indexed in Web of Science or Scopus database. The first-author publications are listed first followed by publication in alphabetical order. The percentage at the end of each item indicates author's contribution based on `v3s.cvut.cz` database. The citation count is without self-citation (accessed on 27.7.2022). The h-index of the author is 3 (based on the Web of Science).

1. Jeřábek, J. and Zumr, D. (2021). Geophysical survey as a tool to reveal subsurface stratification at within a small agricultural headwater catchment: a case study. The Civil Engineering Journal, 30(3). (60 %)

2. Jeřábek, J., Zumr, D., Dostál, T., Tenreiro, T., Strauss, P., and M.D., V. (2021a). The effects of management practices and fires on soil water dynamics at three locations across europe. In 2021 IEEE International Workshop on Metrology for Agriculture and Forestry, Como, IT. IEEE Instrumentation and Measurement Society. (60 %)

3. Jeřábek, J., Rinderer, M., Gessler, A., and Weiler, M. (2020b). Xylem sap phosphorus sampling using microdialysis—a non-destructive high sampling frequency method tested under laboratory and field conditions. Tree Physiology, 40(11). (60 %)

4. Jeřábek, J., Zumr, D., and Dostál, T. (2017). Identifying the plough pan position on cultivated soils by measurements of electrical resistivity and penetration resistance. Soil & Tillage Research, 174. (60 %, **10 citations**)

5. Kavka, P., Jeřábek, J., and Landa, M. (2022). Smoderp2d—sheet and rill runoff routine validation at three scale levels. Water, 14(3). (30 %)

6. Landa, M., Jeřábek, J., Pešek, O., and Kavka, P. (2019b). Smoderp2d soil erosion model entering an open source era with gpu-based parallelization. In The International Archives of the Photogrammetry, Remote Sensing and Spatial Information Sciences, Göttingen, DE. Copernicus GmbH (Copernicus Publications). (15 %)

7. Li, T., Jeřábek, J., Noreika, N., Dostál, T., and Zumr, D. (2021a). An overview of hydrometeorological datasets from a small agricultural catchment (nučice) in the czech republic. Hydrological Processes, 35(2). (25 %)

8. Li, T., Jeřábek, J., Zumr, D., Noreika, N., and Dostál, T. (2021d). Assessing spatial soil moisture patterns at a small agricultural catchment. In 2021 IEEE International Workshop on Metrology for Agriculture and Forestry, Como, IT. IEEE Instrumentation and Measurement Society. (20 %)
9. Tenreiro T.R., Jeřábek J., Gómez J.A., Zumr D., Martínez G., García-Vila M., and Fereres E. (2022). Simulating water lateral inflow and its contribution to spatial variations of rainfed wheat yields. European Journal of Agronomy, 137. (25 %)
10. Zumr, D., Jeřábek, J., Klípa, V., Dohnal, M., and Sněhota, M. (2019b). Estimates of tillage and rainfall effects on unsaturated hydraulic conductivity in a small central european agricultural catchment. Water, 11(4). (15 %, **7 citations**)
11. Zumr, D., David, V., Jeřábek, J., Noreika, N., and Krása, J. (2020a). Monitoring of the soil moisture regime of an earth-filled dam by means of electrical resistance tomography, close range photogrammetry and thermal imaging. Environmental Earth Sciences, 79(12). (16 %, **3 citation**)
12. Zumr, D., Mützenberg, D., Neumann, M., Jeřábek, J., Laburda, T., Kavka, P., Johannsen, L., Zambon, N., Klik, A., Strauss, P., and Dostál, T. (2020f). Experimental setup for splash erosion monitoring—study of silty loam splash characteristics. SUSTAINABILITY, 12(1). (15 %, 6 citations)

The list of other authored and co-authored publications in alphabetical order is given. The list was generated on 27.7.2022 from the `v3s.cvut.cz` database (Scopus and WoS publications are shown above).

1. Dostál, T., Jeřábek, J., Li, T., and Zumr, D. (2019). Monitoring of runoff processes during an artificial rainfall on a freshly tilled soil. In EGU General Assembly 2019, volume vol. 21, Vienna, AT. European Geosciences Union.
2. Herbstritt, B., Jeřábek, J., Rinderer, M., Gessler, A., and Weiler, M. (2017). Investigating water and nutrient uptake by trees with in-situ measurements of water stable isotopes and phosphate in xylem. In Conference: EGU Leonardo - Water stable isotopes in the hydrological cycle, Freiburg, DE. Institute of Hydrology, Freiburg University.
3. Jáchymová, B., Křízek, P., Strouhal, L., Kavka, P., Jeřábek, J., Landa, M., Krása, J., Weyskrabová, L., šoul, M., and Císlerová, M. (2019a). Atlas hydrologie. Jáchymová, B., Křížek, P., Strouhal, L., Landa, M., Jeřábek, J., Krása, J., and Kavka, P. (2019b). Atlas hydrologie - moderní nástroj pro výpočet smyvu, odtoku a dimenzování prvků protierozní ochrany. In Vodní nádrže 2019, Brno, CZ. Povodí Moravy, s.p.
4. Jeřábek, J., Kavka, P., and Neumann, M. (2020a). Parameter space and sensitivity analysis of smoderp2d model using a set of artificial rainfall experiments. In Sborník Hydrologie, GIS a životní prostředí 2020, Praha, CZ. české vysoké učení technické v Praze.

5. Jeřábek, J., Rinderer, M., Weiler, M., and Gessler, A. (2019a). Novel use of microdialysis for high frequent phosphate sampling in xylemsap of beech trees. In EGU General Assembly 2019, volume vol. 21, Vienna, AT. European Geosciences Union.

6. Jeřábek, J. and Zumr, D. (2015). Non-invasive observation of the compacted plough pan layer and its effect on soil water regime. In AGU Fall Meeting Abstracts, Washington, US. American Geophysical Union.

7. Jeřábek, J. and Zumr, D. (2016a). Identifikace zhutnělé vrstvy na zemědělském povodí pomocí odporové tomografie. In GIS a životní prostředí 2016, Praha, CZ. česká technika nakladatelství čVUT, čVUT v Praze.

8. Jeřábek, J. and Zumr, D. (2016b). Non-invasive observation of the shallow soil profile stratification and its effect on soil water regime. In Geophysical Research Abstracts, Göttingen, DE. Copernicus GmbH.

9. Jeřábek, J. and Zumr, D. (2016c). Výsledky měření odporovou tomografií na zhutnělé zemědělské půdě. In Voda a krajina 2016, Praha, CZ. české vysoké učení technické v Praze, Fakulta stavební.

10. Jeřábek, J. and Zumr, D. (2018). Dominantní vlivy na odtok ze zemědělských povodí. In Sborník abstraktů konference Hydrologie, GIS a životní prostředí 2018, Praha, CZ. české vysoké učení technické v Praze.

11. Jeřábek, J., Zumr, D., Krása, J., and Dostál, T. (2018). Monitoring of runoff processes during an artificial rainfall on a freshly tilled soil. In TRANSPORT VODY, CHEMIKÁLIÍ A ENERGIE V SYSTéME PÔDA-RASTLINA-ATMOSFéRA, Bratislava, SK. Institute of Hydrology SAS.

12. Jeřábek, J., Zumr, D., Krása, J., and Dostál, T. (2019b). Formování odtoku na orné půdě runoff formation at a cultivated soil. In SBORNÍK ABSTRAKTů KONFERENCE HYDROLOGIE, GIS A žIVOTNÍ PROSTŘEDÍ 2019, 1, Praha, CZ. české vysoké učení technické v Praze.

13. Jeřábek, J., Zumr, D., Krása, J., and Dostál, T. (2019c). Surface runoff and soil loss generation at an agricultural catchment with developed wheel-tracks. In 10th EGU Leonardo Conference: Global change, landscape ageing and the pulse of catchments, Katlenburg-Lindau, DE. The European Geosciences Union (EGU).

14. Jeřábek, J., Zumr, D., Laburda, T., Krása, J., and Dostál, T. (2020c). Surface runoff connectivity during rainfall simulation experiments. In 2nd Workshop on soil physics and landscape hydrology, Praha, CZ. katedra hydromeliorací a krajinného inženýrství.

15. Jeřábek, J., Zumr, D., Li, T., Tenreiro, T., Strauss, P., and Dostál, T. (2021b). New infrastructure in nučice + agronomic operations affect swc dynamics. In 3rd Workshop on soil physics and landscape hydrology, Praha, CZ. Fakulta stavební.

16. Kavka, P., Jeřábek, J., Kubínová, R., Pešek, O., Dufka, D., Marek, O., and Landa, M. (2020a). Smoderp line.

17. Kavka, P., Jeřábek, J., and Strouhal, L. (2016). Numerical model smoderp. In AGU Fall meeting 2016, Baltimore, US. AGU.

18. Kavka, P., Jeřábek, J., and Vlasák, K. (2018). Development of the surface runoff-erosion model smoderp2d. In Geophysical Research Abstracts, Volume 18, Göttingen, DE. Copernicus Publications.

19. Kuráž, M., Holub, J., and Jeřábek, J. (2017). Numerical solution of the richards equation based catchment runoff model with dd-adaptivity algorithm and boussinesq equation estimator. Pollack Periodica, An International Journal for Engineering and Information Sciences.

20. Landa, M., Jeřábek, J., Kavka, P., and Jáchymová, B. (2019a). Could be hydrological model parameters inferred from a soil texture? In EGU General Assembly 2019, volume vol. 21, Vienna, AT. European Geosciences Union.

21. Li, T., Jeřábek, J., Noreika, N., Dostál, T., and Zumr, D. (2020a). Detailed temporal and spatial topsoil moisture content changes in a small agricultural catchment in the czech republic. In GEA (Geo Eco-Eco Agro) International Conference - Book of Abstracts, Podgorica, ME. GEA (Geo Eko-Eko Agro), University of Montenegro.

22. Li, T., Jeřábek, J., Noreika, N., Dostál, T., and Zumr, D. (2021b). The soil moisture dynamics at the nučice catchment. In 3rd Workshop on soil physics and landscape hydrology, Praha, CZ. Fakulta stavební.

23. Li, T., Jeřábek, J., Noreika, N., Dostál, T., and Zumr, D. (2021c). Spatial patterns of soil moisture in a small agricultural catchment in the czech republic. In Hydrologie, GIS a životní prostředí 2021, Praha, CZ. Fakulta stavební.

24. Li, T., Noreika, N., Jeřábek, J., Dostál, T., and Zumr, D. (2021e). Exploring hydrological processes at a small agricultural catchment in the czech republic. In EGU General Assembly 2021, Göttingen, DE. Copernicus Publications.

25. Li, T., Noreika, N., Jeřábek, J., and Zumr, D. (2020b). An overview of hydrometeorological datasets from a small agricultural catchment (nučice) in the czech republic. In Sborník Hydrologie, GIS a životní prostředí 2020, Praha, CZ. české vysoké učení technické v Praze.

26. Li, T., Noreika, N., Jeřábek, J., Zumr, D., Krása, J., and Dostál, T. (2020c). Investigating spatio-temporal variability of soil moisture in a small farmland: from point to catchment scale. In EGU General Assembly 2020, Göttingen, DE. Copernicus Publications.

27. Lolk Johannsen, L., Balenovic, N., Strauss, P., Dostál, T., Neumann, M., Jeřábek, J., Zumr, D., Arnaiz, M., Cochrane, T., and Klik, A. (2018). Investigation of rainfall

kinetic energy in central europe and new zealand. In EGU General Assembly 2018, volume Vol. 20, Munich, DE. European Geosciences Union.

28. Zumr, D., Devátý, J., Jeřábek, J., Neumann, M., Laburda, T., Dostál, T., Klik, A., and Strauss, P. (2017). Experimentální sledování deformace půdních agregátů při přívalové srážce. In HYDROLOGIE MALéHO POVODÍ 2017, Praha, CZ. Ústav pro hydrodynamiku AV čR, v. v. i.
29. Zumr, D. and Jeřábek, J. (2016). Prostorově distribuované monitorování objemové vlhkosti v kulturní krajině. In GIS a životní prostředí 2016, Praha, CZ. česká technika - nakladatelství čVUT, čVUT v Praze.
30. Zumr, D. and Jeřábek, J. (2019). The effect of wheel tracks on water and sediment runoff – results of the plot scale experiments. In 5th Biohydrology - Humans and Nature, Valencia, ES. University of Valencia.
31. Zumr, D., Jeřábek, J., Dohnal, M., and Sněhota, M. (2019a). Temporal changes in hydraulic conductivity of cultivated topsoil as a result of seasonal rainfall impacts. In 5th Biohydrology - Humans and Nature, Valencia, ES. University of Valencia.
32. Zumr, D., Jeřábek, J., and Dostál, T. (2016a). Observation of the dominant runoff pathways on inclined arable soils. In Proceedings of the WG and MC Connecteur Meeting, Negev, IL. Ben-Gurion University of the Negev.
33. Zumr, D., Jeřábek, J., Krása, J., and Dostál, T. (2020b). Plot-scale experiments to assess the effects of surface spatialheterogeneity on runoff and soil loss. In EGU General Assembly 2020, Göttingen, DE. Copernicus Publications.
34. Zumr, D., Jeřábek, J., and Li, T. (2020c). Foreseen potential of crns for better understanding of catchment runoff dynamic. In Proceedings of 6th international COSMOS workshop, Heidelberg, DE. University of Heidelberg.
35. Zumr, D., Jeřábek, J., Li, T., Klípa, V., Dohnal, M., and Sněhota, M. (2019c). Variability of topsoil unsaturated hydraulic conductivity as a result of seasonal rainfall impacts. In EGU General Assembly 2019, volume vol. 21, Vienna, AT. European Geosciences Union.
36. Zumr, D., Jeřábek, J., and Neumann, M., editors (2021a). 3rd Workshop on soil physics and landscape hydrology, Desná. Fakulta stavební.
37. Zumr, D., Jeřábek, J., and Strouhal, L. (2015a). Experimentální sledování formování odtoku na orné půdě. In Seminář Adolfa Patery 2015 Extrémní hydrologické jevy v povodích, Rok 2015, Praha, CZ. česká vědeckotechnická vodohospodářská společnost.
38. Zumr, D., Jeřábek, J., and Strouhal, L. (2015b). Predominant runoff components during heavy rainfall events on cultivated catchment. In AGU Fall Meeting Abstracts, Washington, US. American Geophysical Union.

39. Zumr, D., Jeřábek, J., Strouhal, L., and Dostál, T. (2015c). Surface and shallow subsurface runoff connectivity in a cultivated catchment. In 3rd Connecteur Meetings presentations, Durham.

40. Zumr, D., Jeřábek, J., Vláčilová, M., and Dostál, T. (2015d). Konektivita povrchového a podpovrchového odtoku z obdělávaného povodí. In GIS a životní prostředí 2015, 1. vydání, Týnec nad Sázavou.

41. Zumr, D., Kavka, P., Jeřábek, J., and Dostál, T. (2016b). Režim odtoku z intenzivně zemědělsky využívaných povodí. In Malá povodí jako trvalý zdroj informací, Praha, CZ. AV čR, Ústav pro hydrodynamiku.

42. Zumr, D., Kavka, P., Neumann, M., and Jeřábek, J., editors (2020d). 2nd Workshop on soil physics and landscape hydrology, Praha - Dejvice. katedra hydromeliorací a krajinného inženýrství.

43. Zumr, D., Li, T., and Jeřábek, J. (2020e). Cosmic rays neutron sensing as a tool to understand catchment water regime. In Sborník Hydrologie, GIS a životní prostředí 2020, Praha, CZ. české vysoké učení technické v Praze.

44. Zumr, D., Li, T., Jeřábek, J., Noreika, N., Laburda, T., Vrána, M., Winkler, J., and Vaverková, M. (2021b). Dynamics of topsoil properties after a fire: small scale straw burning experiment. In Proceedings of FES2021, Valencia, ES. University of Valencia.

45. Zumr, D., Vláčilová, M., Dostál, T., Jeřábek, J., and Sněhota, M. (2015e). Spatial variability of compacted subsoil depth: a combination of field observation, electrical resistivity tomography and x-ray computed tomography. In CONGRESS MATERIALS - 7th Congress of the European Society for Soil Conservation, Moscow.

46. Zumr, D., Vláčilová, M., Dostál, T., Jeřábek, J., Sobotková, M., and Sněhota, M. (2015f). Spatial analysis of subsoil compaction on cultivated land by means of penetrometry, electrical resistance tomography and x-ray computed tomography. In Geophysical Research Abstracts, Volume 17, (Memory stick), Göttingen, DE. Copernicus Publications.

List of Figures

1 Conceptual model of runoff generation on tilled soil with the presence of wheel tracks 2

2 Topsoil and subsoil soil water content dynamics along the hillslope 3

3 Concept of wheel track influence on the runoff. Figures (a), (b) and (c) show the detail process. Figure (d) show the overall impact on the runoff at catchment scale. 3

5.1 The example of electrode arrays for the ERT measurement (Loke, 1999) . . 26

6.1 Nučice catchment. The numbers denote the three fields parcels (Zumr et al., 2015). 34

6.2 ERT profiles shown at its real positions at the Nučice catchment 35

6.3 Location and orthophoto of the experimental Řisuty site on the left (orthophoto by Tomáš Laburda and Josef Krása). Experimental plot setting of campaign No. 1 and campaign No. 2 on the right (Jeřábek et al., 2022). 36

6.4 Transects measured at the NWT plot during the No. 1 campaign. Both transects were measured in the along the plot orientation. Left: electrical resistivity 17.75 hours after the rainfall. Right: electrical resistivity 22.92 hours after the rainfall. 38

6.5 Transects measured at the SWT plot during the No. 1 campaign. Left: transect measured in the along the plot orientation 16.42 hours after the rainfall. Right: transect measured in the perpendicular direction to the plot 27.67 hours after the rainfall. 38

6.6 Detail of the ERT transect measured at the SWT plot during the No. 1 campaign and excavated pit along the transect. 39

6.7 Transects measured at the NWT plot during the No. 2 campaign. All transects were measured in the perpendicular direction. Upper left: electrical resistivity measured 2.75 hours after the rainfall. Upper right: electrical resistivity measured 14.58 hours after the rainfall. Lower: electrical resistivity measured 25.08 hours after the rainfall. 39

6.8 Transects measured at the sWT plot during the No. 2 campaign. All transects were measured in the perpendicular direction. Left: electrical resistivity measured 3 hours after the rainfall. Right: electrical resistivity measured 14 hours after the rainfall. 40

6.9 Transect measured at the CWT plot during the No. 2 campaign. Transect measured in the along the plot orientation. Electrical resistivity measured 1.5 after the rainfall. 40

6.10 The mechanical penetration of the dry a), wet wheel track b) and wet non wheeled soil. 41

6.11 Correlation between normalized penetration resistance (p_{pr}) and electrical resistivity (ρ_e) (Jeřábek et al., 2017). 42

7.1 Diagram explaining the lengths of the normalized downslope distance index 45

7.2 Diagram explaining the shape and shifts of the functional connectivity index 45

7.3 Development of: A) the surface runoff, B) the sediment flow rate and C) the concentration of the suspended solids in time. The time is normalized to the duration of the experiment. 48

7.4 A) Bar plots of the random roughness for all wheel track configurations and for before- and after-rainfall soil surface conditions. B) Bar plots of the random roughness of the wheel track (in WT) and the surrounding soil surface (outside WT) on the SWT plot. 49

7.5 The histogram of NDD and the corresponding contribution area raster of the before-rainfall and after-rainfall surface conditions of: A) the NWT No. 1 plot, B) SWT No. 1 plot, C) NWT No. 2 plot, D) NWT No. 2 plot, and E) CWT No. 2 plot. Arrows in some of the flow accumulation rasters indicate the main flow direction. 50

7.6 Functional connectivity of A) before-rainfall situation and B) after-rainfall soil surface conditions 51

7.7 δD development in surface runoff and simulated rainfall on NWT plot (left), SWT plot (middle), and CWT plot (right) 51

7.8 Mixing of deuterium pulse water with pre-pulse water at NWT, SWT, and CWT plot 52

8.1 Schema of the measurement during both measuring campaigns 54

8.2 The position of a) the interface and subsoil tesiomters, b) the soil water content nest, and c) the schema of the boundary conditions and soil layers delineation used in for the numerical model 55

8.3 Excavated subsoil with visible furrows 56

8.4 Geometry of the three layers morphology at the CWT plot as used in HYDRUS2D model. The positions of tensiometers (○) and soil water content probes (△) are shown. 57

8.5 Soil water potential in the topsoil, wheeled topsoil, and subsoil during the artificial rainfall experiments. The blue area indicates the irrigation. The exact position of each tensiometer is given in Table B.1. 59

8.6 The estimation of infiltration front arrival time to the installation depth of the each tensionmeter for the plot NWT No. 1 A); SWT No. 1 B); NWT No. 2 C); SWT No. 2 D); CWT No. 3. Red color depicts the tensiometers installed in the wheel track. 60

8.7 Volumetric water content in all VWC nests during artificial rainfall experiments. The interface and subsoil probes were placed approximately bellow the wheel track during the campaign No. 2 (Figure 8.7d). The exact sensori position are shown in Tabla B.2. 60

8.8 Vertical flow on plots measured with zero-tension lysimeters. The plot and position is indicated at the upper left corned of each plot. Blue area indicates the rainfall. The vertical dashed line indicates the vertical flow initiation. Since the active area of each lysimeter was uncertain, the grey lines indicate the situation where the lysimeter is inserted ± 5 cm in the soil; has larger or smaller active area. 61

8.9 infiltration into the NWT plot (rainfall - runoff / plot ares) 61

8.10 The soil water retention curve for the 3 examined soil layers in both campaigns 62

8.11 Measured and modeled pressure head and soil water content of the CWT plot using the average SHPs obtained with the inverse modeling 65

8.12 Development of the flow regime at the transect with no morphology after 3 times. The rectangle in pressure head graphs shown the zoom region for the flow velocity vector graphs. 66

8.13 Development of the flow regime at the transect with morphology at 3 times. The rectangle in pressure head graphs shown the zoom region for the flow velocity vector graphs. 67

8.14 Soil water balance variables of the 3 soil soil materials. Lines depicts porosity of the material. 68

8.15 Soil water potential development affected by the presence subsoil morphology 69

8.16 Detail of soil water pressure at the interface without morphology in Figure 8.15a . . . 69

8.17 The redefined conceptual model is shown in Figures 1 and 3. a) Beginning of runoff generation; water starts to pond in the depressions on the soil surface and the wheel track. b) The surface runoff develops and the topsoil is fully saturated. . . . 72

8.18 Conceptual model of overland flow generation with various wheel tracks orientations. a) - c) depict filling and spilling of soil surface depressions and the role of the wheel track in the case of the SWT plot. d) - f) depict filling and spilling of soil surface depressions and the role of the wheel track in the case of the CWT plot. . . . 72

B.1 Diagram with the codes of the tensiometers location . . . 169

B.2 The measure (dots) and fitted (lines) retention curve and hydraulic conductivity obtained with the evaporation method. . . . 170

List of Tables

5.1 Typical electrical resistivity ρ_e of the subsurface materials (Palacky, 1988) . 26

6.1 Overview of ERT transects measurements performed after each artificial rainfall experiment. None to two repetitions were performed. ERT transect was either aligned along the plot (in downslope direction) or perpendicularly to the plot (in the contour line directions). 37

7.1 Soil hydraulic parameters of Loam soil used to calculate the functional connectivity with the SMODERP2D model (SMODERP2D development team, 2017) 47

8.1 The fitted soil hydraulic parameters for the 3 soil layers. Letters indicate Tukey's honest significance test. 63

8.2 Summary of the optimized paramters for each soil material for all plots . . 64

B.1 The locations of the SWC sensors used during both Řisuty experiments . . 171

B.2 Exact positions of the CS650 soil moisture probes during all experiment . . 172

Nomenclature

List of Abreviations

ARE	Artificial rainfall experiment
CFL	Courant–Friedrichs–Lewiho criterion
CWT	Contour line wheel track
DEM	Digital elevation model
ERT	Electrical resistivity tomography
IC	Index of connectivity (Borselli et al., 2008)
MAVWC	Material averaged volumetric water content
NDD	Normalized downslope distance (-)
NWT	No wheel track
RR	Random roughness
RSCf	Relative surface connection function Antoine et al. (2009)
SfM	Structure from Motion
SOC	Soil organic carbon
SWP	Soil water potential
SWRC	Soil water retention curve
SWT	Slope wise wheel track
VWC	Volumetric water potential

List of Symbols

Ψ	Total water potential (L)
ψ	Suction pressure (L)
ρ_e	Electrical resistivity (Ωm)
θ	Volumetric water content ($L^3.L^{-3}$)
α, n, m	Fitting parameters of van Genuchten soil water retention curve ($L^{-1}, -, -$)

a, m	Power law fitting parameters (−,−)
h	SWP or Surface water level (hPa or L)
L_d	Pathway length of flowing particle to the bottom of the plot (L)
L_s	Shortest length to the bottom of the plot (L)
q	Darcian flow or unit width overland flow ($L.t^{-1}$ or $L^2.t^{-1}$)
S	Sorptivity ($L.t^{-1/2}$)
S_{ox}, S_{oy}	Friction slope in x and y direction
S_{ox}, S_{oy}	Surface slope in x and y direction
u	Velocity in x direction ($L.t^{-1}$)
v	Velocity in y direction ($L.t^{-1}$)
w	Width of the flow section (L)
X, Y, b	Manning-Strickler formula fitting parameters (−,−,−)
$C(h)$	Water capacity $C(h) = \partial\theta/\partial h$ (L^{-1})
K_{fs}	Field saturated hydraulic conductivity ($L.t^{-1}$)
$K(h)$	Unsaturated hydraulic conductivity ($L.t^{-1}$)
K_r	Relative unsaturated hydraulic conductivity (−)
K_s	Saturated hydraulic conductivity ($L.t^{-1}$)
p_{pr}	Mechanical resistance (MPa)
θ_r	Residual volumetric water content ($L^3.L^{-3}$)
θ_s	Saturated volumetric water content ($L^3.L^{-3}$)

Appendix A

Collection of studies

Study 1: Geophysical survey as a tool to reveal subsurface stratification at within a small agricultural headwater catchment: a case study (Jeřábek and Zumr, 2021)
Study 2: Identifying the plough pan position on cultivated soils by measurements of electrical resistivity and penetration resistance (Jeřábek et al., 2017)
Study 3: Soil surface connectivity of tilled soil with wheel tracks and its development under simulated rainfall (Jeřábek et al., 2022)

Article no. 59

THE CIVIL ENGINEERING JOURNAL 3-2021

GEOPHYSICAL SURVEY AS A TOOL TO REVEAL SUBSURFACE STRATIFICATION AT WITHIN A SMALL AGRICULTURAL HEADWATER CATCHMENT: A CASE STUDY

Jakub Jeřábek and David Zumr

Czech Technical University in Prague, Faculty of Civil Engineering, The Department of Landscape Water Conservation, Prague, Thákurova 7/2077, 166 29, Praha 6 - Dejvice, Czech Republic*; e-mail: jakub.jerabek@fsv.cvut.cz*

ABSTRACT

Managers use the catchment as a basic spatial unit in landscape hydrology to estimate local water balance and manage water resources. The catchment drainage area is commonly delineated based on the surface topography, which is determined using a digital elevation model. Therefore, the surface outflow only is implicitly considered. However, a substantial portion of the rainfall water infiltrates and percolates through the soil profile towards the groundwater, where geological structures control the drainage area instead of the soil surface topography. The discrepancy between the surface topography-based and bedrock-based drainage area can cause larger discrepancies in water balance calculations. It this paper, we present the investigation of the subsurface media stratification within the headwater catchment, located in the central part of the Czech Republic using a geophysical survey method - electrical resistivity tomography (ERT). Results indicate that the complexity of the subsurface geological layers cannot be estimated solely from the land surface topography. Although the shallow layers follow the shape of the surface, the deeper layers do not. This finding has a strong implication on the water flow regime since it suggests that the deep drainage may follow different pathways and other preferential directions as compared to the water flow within the shallow subsurface.

KEYWORDS

Electrical resistivity tomography, Hydrology, Subsurface stratigraphy, Headwater catchment

INTRODUCTION

Catchment drainage area is a key concept in hydrology. It is defined by the catchment topographical boundaries which restrict the area from which all of the water flows to the common outlet. The catchment divide serves as a delineation between the adjacent catchments. Catchment drainage area also serves as a representative unit for water balance calculation. Water management is usually catchment-based as it is difficult to administrate the water resources within the landscape with politically designed boundaries where the water balance is not closed. The orographic divide is commonly used to delineate the catchment area. It is derived by means of topography (i.e. on a digital elevation model), therefore it is typically located at the ridge or a hilltop as is shown in Figure 1a. In some cases, the hydrogeological setting in the subsurface creates a low permeable geological layer in a way that the water which infiltrates towards this layer flows in opposite direction compared to the overlaying soil surface (Figure 1b). Knowledge about the subsurface stratification is important in order to be able to close or complete the water balance equation, since the water flow through the catchment orographic boundary may be affected by those layers [1]. However, the information about the subsurface settings at a catchment is not always available.

DOI 10.14311/CEJ.2021.03.0059

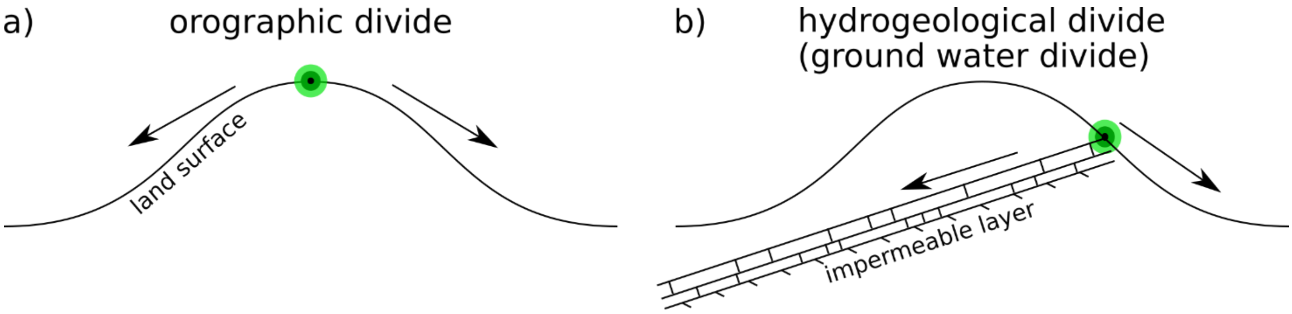

Fig. 1 – Difference between a) orographic and b) hydrogeological divide. Arrows indicate direction of the flowing water. Green dots indicate the divide.

Geophysical survey is a common option how to investigate the subsurface structures and the bedrock position. Number of geophysical techniques are available for practice and research purposes. The most common ones are: ground penetration radar, seismic refraction, magnetic methods, and electrical resistivity tomography [2]. Ground penetration radar (GPR), emits and detects electromagnetic pulses. The pulses are reflected from contrasted dialectical properties. Although GPR provides the best spatial resolution, it is not a suitable technique for materials with low contrast dielectric properties and in general for materials with lower el. resistivity than ca. 50 – 100 Ωm [2]. Seismic reflection uses geophones to detect a velocity of seismic waves introduced with sledgehammer (or earthquake). Although this method is well suited for bedrock detection and can reach deeper depths, it requires an increasing density of subsurface layers with depth. Magnetic methods are based on measuring of the magnetic properties (magnetic susceptibility) which reflect upon different concentrations of various ferromagnetic materials in the subsurface. Electrical resistivity tomography has shown to be a promising tool for its versatility and ease to obtain the field data. The depth ranges and spatial resolution can be easily set by the user. However, the technique requires good connection between the material and electrodes (principle explained bellow) and does not provide good results within a blocky subsurface structure [2].

In this study, we utilize the electrical resistivity tomography method (ERT), as described e.g. by Samouëlian et al. [3]. In principle, ERT can be used to detect the spatial distribution of electrical resistivity in the subsurface by introducing electrical current to the soil and detecting the resulting voltage of the subsurface media (more details are provided in the Methods section). Distinct soil layers or various rock materials, as well as soils of various water saturation, have different electrical resistivity [3], and therefore different subsurface structures can be detected and delineated.

ERT has been widely used in many fields of research and practical applications in various spatial scales, such as investigation of landslide to design protection measures (e.g. [4]), identification and delineation of soil contamination e.g. [5], [6], investigation of leachate from a landfill [7] or mixing of fresh and seawater in the coastal areas [8], [9]. ERT has been used to delineate individual soil layers above the bedrock [10] or even to study the shallow part of the soil profile (topsoil) where the tillage takes place [11], [12], and it is also commonly used in archaeology [13]. Furthermore, ERT has also been successfully used to identify the bedrock position in karst areas, where the heterogeneous bedrock (caused by uneven dissolution of the limestone) makes such a task very challenging [14], [15]. The representatives of the ERT method was successfully evaluated when compared with soil layers stratification observed in excavated trenches [14].

In this study we utilize electrical resistivity tomography (ERT) to observe and delineate subsurface structures and the bedrock, within a small agricultural headwater catchment. The main objective is to improve the understanding of the geological layering at the catchment in order to be able to assess movement of water e.g. via hydrological models [16].

METHODS

Study area

The study was performed at the experimental catchment Nučice which is located at the central part of the Czech Republic (Figure 2). The catchment area is 53 ha with a mean slope of 3.9%. The majority of the catchment is covered with arable land (96.4%). The soils are classified as Cambisols and Haplic Luvisols with sandy loam texture. The bedrock consists of layers of sandstone, siltstone and conglomerate from Carboniferous and Permian geological period (geological map CR, Figure 2). The Czech Geological Survey classifies the whole catchment area as "Alternating sandstone and claystone – permeability low to moderate". For more information about the catchment and instrumentation at the catchment we refer to [17].

The deep ground water level was observed at 355 m a.s.l. (57.7 m below ground surface) within a nearby borehole survey. The borehole survey was performed in the southern direction at a distance of 700 meters (m) from the west-south edge of the catchment. The borehole survey showed sandstone and conglomerate layers with thickness up to 10 meters.

The shallow groundwater level (GWL) of the quaternary alluvial aquifer was measured at two locations in the catchment (Figure 2). Generally, the shallow GWL dropped 3 m below the soil surface during prolonged dry periods in the summer. During heavy rain events GWL almost reached the surface. For most of the year the groundwater is between 2 and 3 m below the ground. The shallow and deep groundwater indicate a complex hydrogeological situation within the catchment, where the proposed ERT survey may help to understand the system.

There are 3 separated fields at the catchment: the top field (Figure 2) and bottom fields (fields 2 and 3 in Figure 2). The asphalt road separates the top and bottom fields. An ephemeral stream is located between the fields 2 and 3. The stream starts at the lowest part of the top field where outlet from tile drain is located. The tile drain then continues in thalweg to the other side of the field 1 where the main road is located near the catchment boundary.

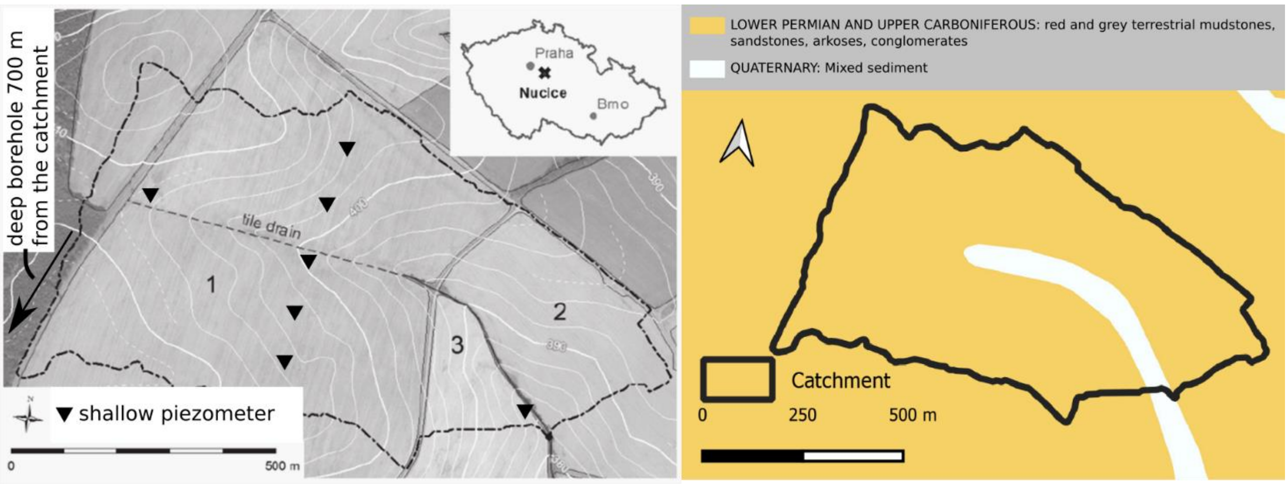

Fig. 2 - .The experimental catchment (left). The numbers stand for three different fields. Location of the shallow groundwater level monitoring and the location of borehole are indicated in the map. Geological map of the experimental catchment (right) © ČGS.

Soils and rocks of different composition and water saturation have distinct electrical properties. The electrical resistivity of the shallow soil layers (down to 1 meter from the surface) was measured at the same catchment by Jerabek et al. [11], the values ranged between 20 – 50 Ωm. The electrical resistivity of the sedimentary rocks is usually considerably higher, the literature reports values in a wide range of 10 – 10^4 Ωm order of magnitude [18], [19]. According to [20] the electrical resistivity of relevant media is shown in Table 1.

Tab. 1: overview of materials and their electrical resistivity (based on [20])

		electrical resistivity Ωm	
origin	material	from	to
shield un-weathered rocks	massive sulfides, graphite	0.01	10
	Igneous and metamorphic rocks	1000	100000
weathered layered		1	10000
glacial sediments	clays	3	100
	tills	30	3000
	gravel and sand	30	10000
sedimentary rocks	shales	50	300
	sandstone and conglomerate	50	10000
	lignite, coal	10	700
	dolomite, limestone	1000	100000
water, aquifers	salt water	0.3	1
	fresh water	2	100

Electrical resistivity tomography

The electrical resistivity tomography (ERT) survey consists of several steps. The so-called apparent electrical resistivity data is collected in the field. In this step, a number of electrodes are inserted into the soil surface along the line (in the case of a 2D profiling). An electrical field is introduced by a pair of electrodes (current electrodes) in the soil, while another pair of electrodes (potential electrodes) measures the voltage caused by the electrical field in the subsurface structure. Configuration of current and potential (voltage) electrodes, commonly called ERT array, exhibits varying horizontal or vertical spatial resolution, and sensitivity to the vertical (e.g. buried boulders) or horizontal (e.g. soil horizons or groundwater level) structures [3, 21]. Based on the geometry of the ERT array a hemisphere with a given apparent electrical resistivity is constructed.

The apparent electrical resistivity data collected has to be processed by inverse numerical modelling in order to obtain real electrical resistivity at a given location in the measured transect [22]. In the inversion procedure, the electrical resistivity is optimized based on the given ERT array and the apparent electrical resistivity data. In some cases, thousands of values need to be optimized which makes the process nontrivial and computationally intensive [22]. The numerical inversion also introduces a certain degree of uncertainty in the results and has to be considered during the data interpretation.

ERT survey design

Five independent ERT transects were performed within this study. An overview of the measured transects is shown in Table 2. Each of the ERT profiles consisted of several individual overlapping sub-transects which were merged before inversion. Most of the measurements were performed with the electrode spacing of 5 m, except the measurements BFC3 and TFC3 with 3 m electrode spacing. Location and orientation of each transect is shown in Figure 3. Two transects follow the thalweg and brook of the catchment, three transects cross the catchment perpendicularly to the catchment thalweg and the stream (Figure 3). There were three interceptions of the ERT transects; two in the field 1 and one in bottom fields 2 and 3.

Tab. 2: Overview of all measured ERT transects.

Date mm/yyyy	Measurement ID	Transect length [m]	Electrode spacing [m]	Location at the catchment – orientation
04/2012	BFC3	540	3	Bottom fields – cross
12/2016	TFC3	444	3	Top field – cross
08/2019	BFB5	395	5	Bottom fields – brook
10/2019	TFC5	620	5	Top field – cross
10/2019	TFT5	580	5	Top field – thalweg

Automatic resistivity system (ARES, GF Instruments, Brno, Czech Republic) was used to obtain the apparent resistivity data. Wenner-Schlumberger array was used for all the measurements. Res2DInv software was used for the data inversion to calculate the electrical resistivity profiles [22]. Total of 1233 (in case of BFB5) to 3161 (in case of BFC3) data points were inverted with the Res2DInv. The software reached the values of the absolute error between the measured end inverted data below 1.5% after 5 – 6 iterations. The robust inversion method (which is more suitable for layers detection) was used for all transects. The topography of each transect was extracted from the digital elevation model with 1 m spatial resolution.

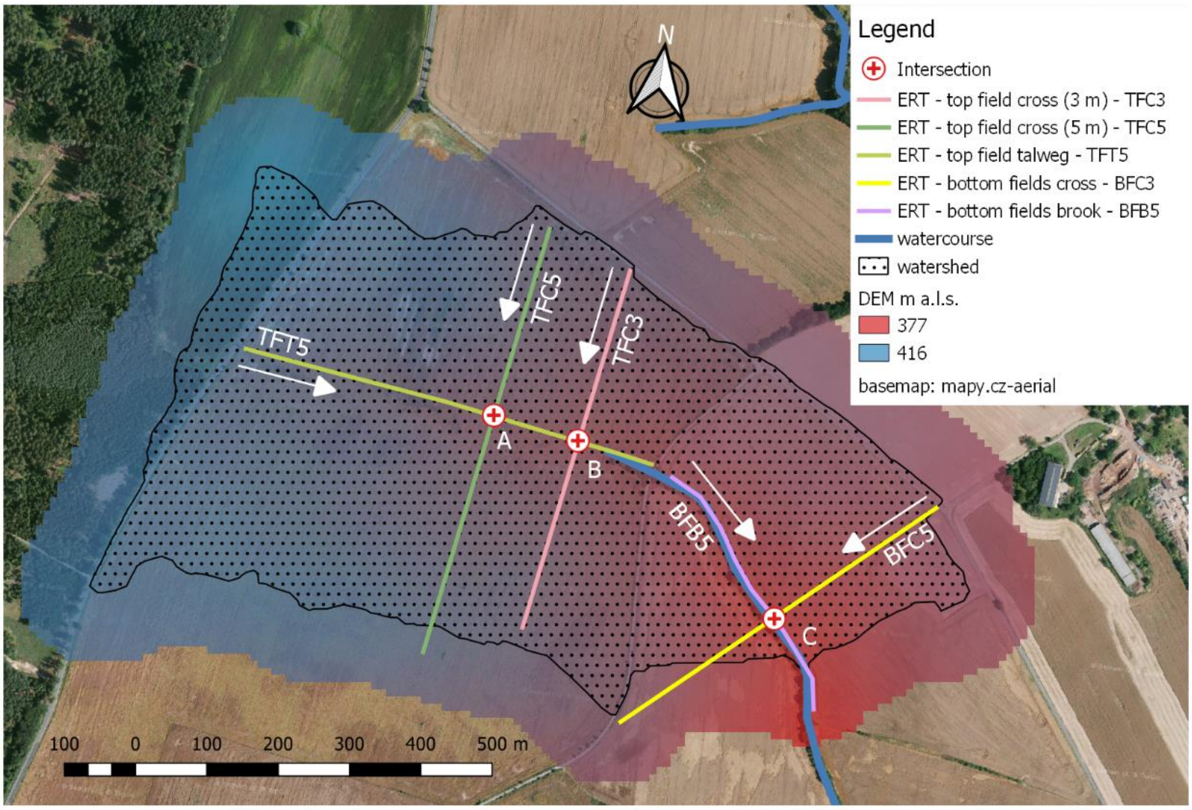

Fig. 3 - The location and intersections of the measured transects. Arrows indicate start and direction of each transect. Digital elevation model provided (C) ČÚZK.

RESULTS

ERT transects

All ERT profiles show electrical resistivity (ρ) in a range of 20 – 150 Ωm. The highest ρ was observed either in the layer located 4 to 6 m below the soil surface or in the deeper layer which is located 15 to 20 m below the soil surface. Soil layer of lower ρ (30 to 50 Ωm) is found in between these regions. Such a layering is clearly visible in the field 1 on transects TFT5, TFC5 and TFC3. Although the same pattern was observed in the bottom fields (field 2 and 3; transects BFB5 and BFC3) the alteration with the regions of different resistivity is less clear. Low electrical resistivity was also observed close to the surface in some cases. The resistivity variability of the upper soil layers (only few meters of a depth) could be attributed to varying soil properties which may differ in organic matter and clay content, and in the actual soil moisture conditions.

The thalweg (TFT5) and along-the-brook (BFB5) transects are both shown in Figure 4. Several spots with high electrical resistivity (ρ) are aligned in the depth of approximately 4 to 10 m. The bottom half of the profile also exhibits higher ρ at the transect TFT5. The area with high ρ was also observed within the BFB5 transect, which appears closer to the soil surface.

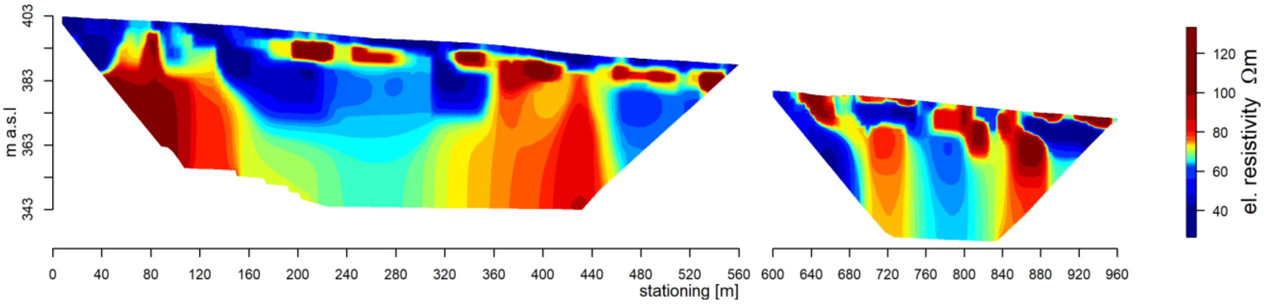

Fig. 4 – ERT transects TFT5 and BTB5 shown in single plot with elevation and stationing starting at the western boundary of the catchment.

The field 1 ERT transects were oriented in the orthogonal direction to the thalweg (TFC transects) and are as shown in Figure 5. Both transects exhibit lower electrical resistivity ρ near the soil surface. High ρ zone near the soil surface areas are restricted only to a limited part of both the transects. Both profiles also exhibit low ρ (below 50 Ωm) in the upper half of each transect. The bottom half of both these transects exhibited higher ρ. Both transects also exhibited the same pattern of the low and high ρ layers despite the different electrode spacing.

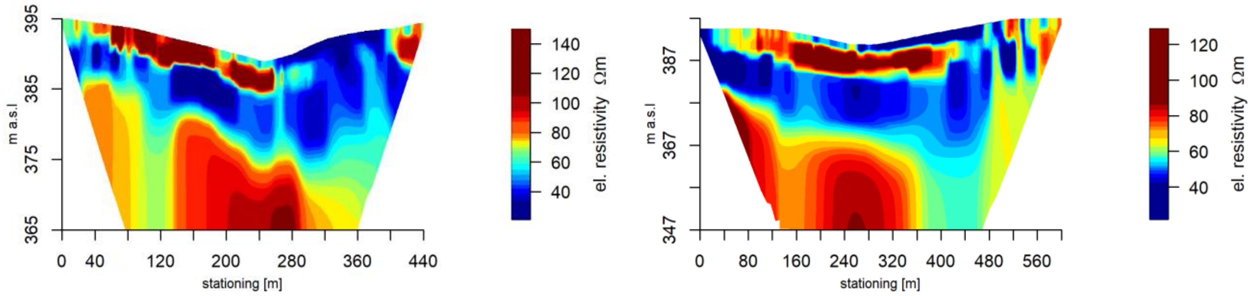

Fig. 5 – ERT transects TFC3 (left) and TFC5 (right).

The ERT profile in the orthogonal direction to the brook (BFC3) transecting the lower fields 2 and 3 is shown in Figure 6. The bottom of the valley is at the stationing of 260 m. The lower ρ was measured only in the shallow part of the field 2 (right hillslope in Figure 6). Below the field 3 (left hillslope in Figure 6) the low ρ layer reaches the depth of approximately 20 m below the soil surface.

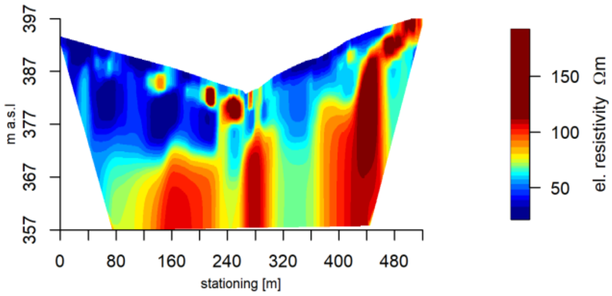

Fig. 6 – BFC3 ERT transects.

ERT transects intersections

The ERT transects were intersected at 3 locations (Figure 7). Intersections A and B were located in the field 1, the intersection C in the field 2 close to the valley. 1D graphs of electrical resistivity ρ with corresponding depth for the 3 intersections are shown in Figure 7. The intersection of transects TFT5 and TFC5 is shown in Figure 7 intersection A. The high ρ values near the soil surface are recognizable in the same depth at both the transects. Also, the second increase of ρ values which can be observed at an altitude of 375 m a.s.l. appeared at a similar depth. The ρ to depth graph of the intersection B (TFT5 and TFC3 ERT transects) exhibited difference in the onset of the shallower high ρ region (Figure 7 intersection B). The difference of the onset was about 2.5 m. The high ρ area which can be observed in the TFC3 profile at an altitude 370 m a.s.l. (approximately 15 m deep) did not appear in the TFT5 transects. Similar results were observed in the intersection of transects BFB5 and BFC3, where onset of the high ρ in near soil surface were also shifted (Figure 7 intersection C). The BFB5 transect exhibited oscillation of the electrical resistivity which could be caused by an error in the measurement or created as an artifact during the mathematical inversion.

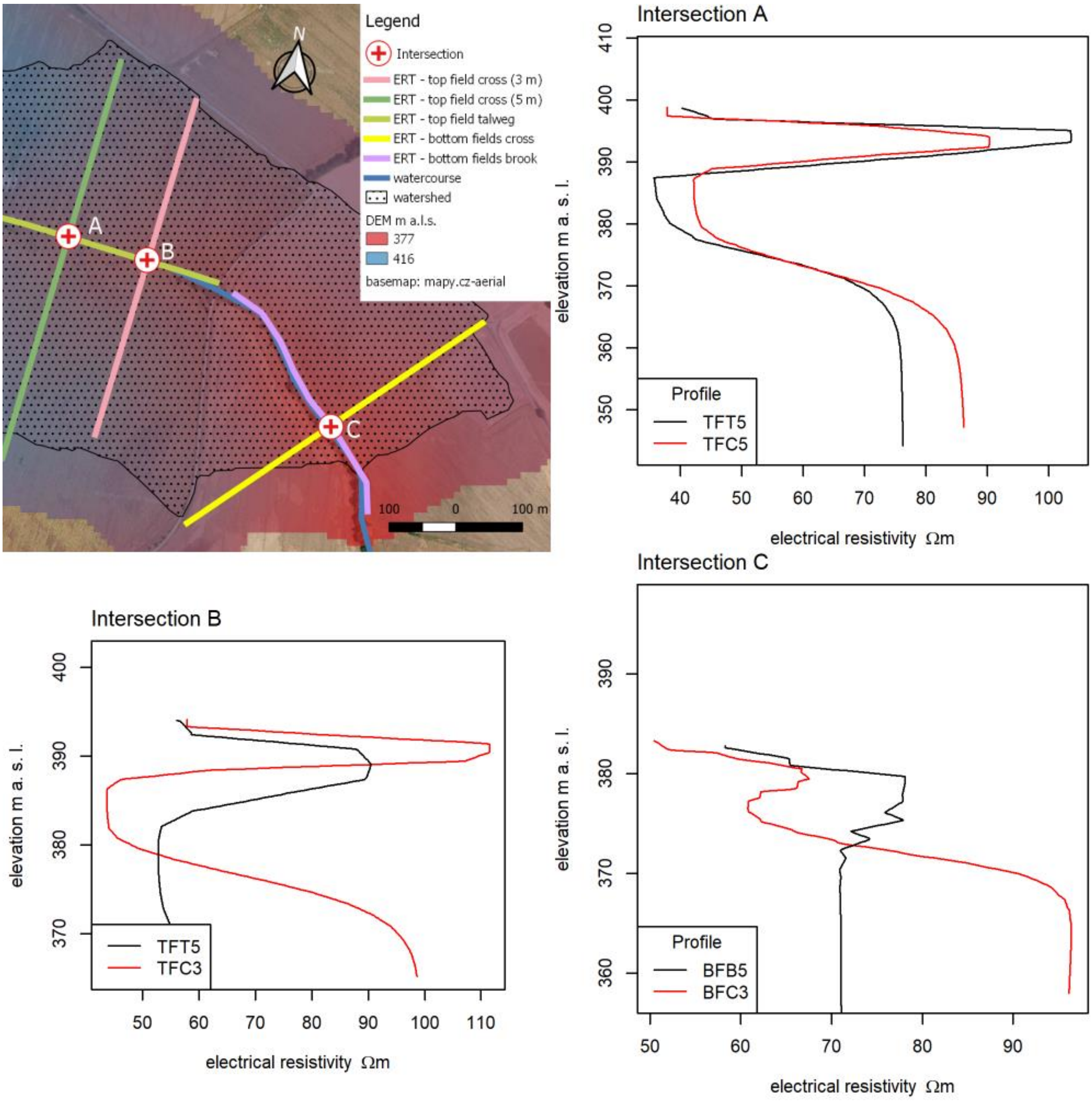

Fig. 7 – Map of intersections and comparison of ERT intersections: intersection A of transects TFT5 and TFC5, intersection B of transects TFT5 and TFC3, and intersection C of transects BFB5 and BFC3.

Hydraulic conductivity of the subsurface structures

Electrical resistivity transects were recalculated with the use of Archie's law [23] to hydraulic conductivity for investigating the hydrological behavior of the subsurface (Figure 8). A high conductive layer is presented at the transects TFC5 and TFC3 overlaid with multiple orders of magnitude lesser conductive layer, probably an aquitard. Presence of a confined aquifer can be hypothesized in this high conductive layer. However, no clear aquitards or aquifers are visible at the perpendicular transects TFT5 and BFB5 or the transect BFC5 at the bottom field. Shallow ground water levels (1 – 3 meter depth) which were recorded in the piezometers indicate an unconfined aquifer on the top of the low-conductivity layer which is visible few meters below the surface. The usage of Archie's law in this context has to be considered only as qualitative metrics, since we cannot distinguish amongst the various factors affecting the electrical resistivity changes (e.g. soil water content).

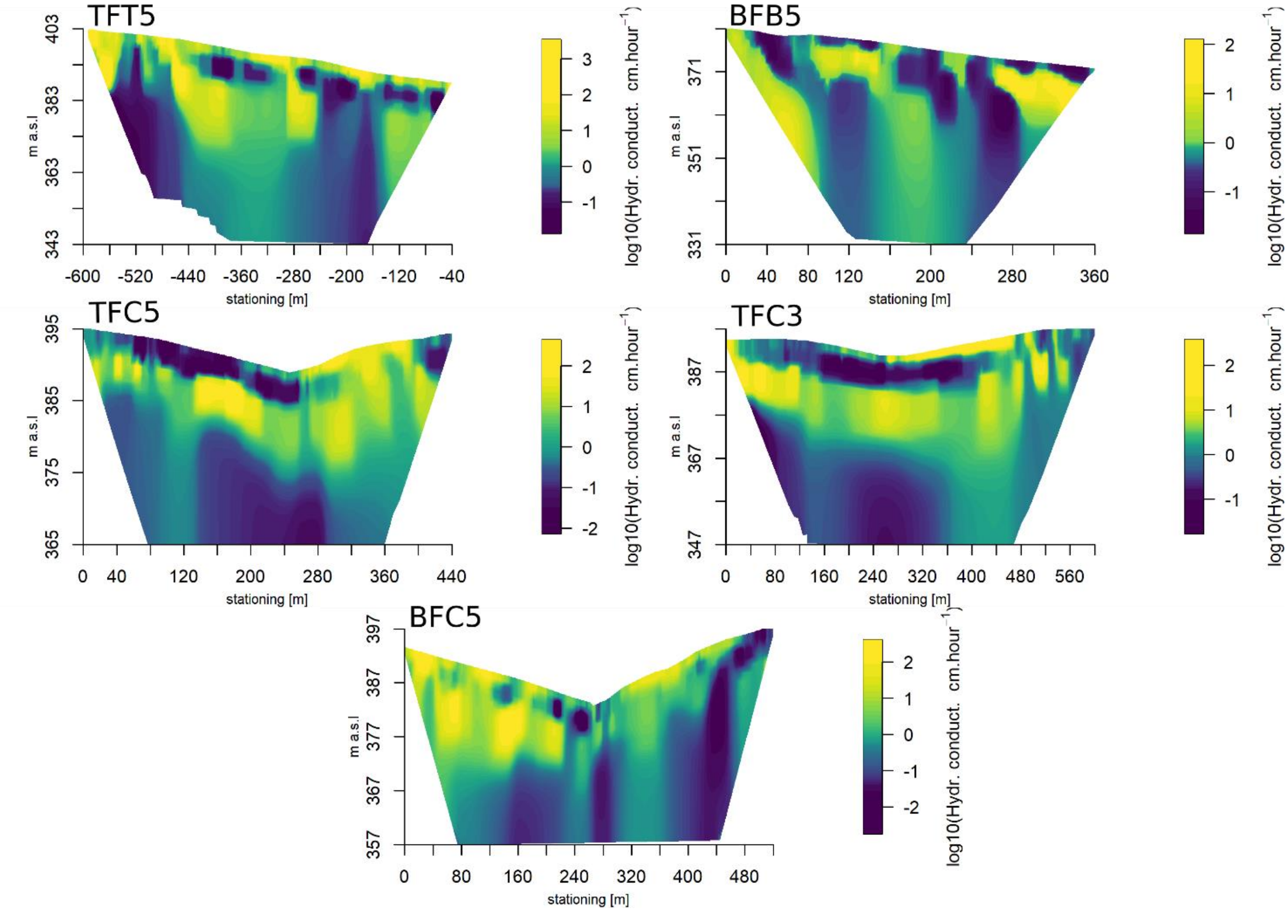

Fig. 8 -The hydraulic conductivity calculated with Archie's law for all the ERT transects.

DISCUSSION

ERT transects

Four distinct layers were distinguished in all ERT transects based on the electrical resistivity values. The layers are shown in Figure 9 (profile TFC5 is shown for illustration):

Layer L1: Low electrical resistivity (ρ) values up to 60 Ω m. Close to the surface - down to the depth of 1 – 2 meters. This layer is not continuous in some transects.

Layer H1: Higher ρ layer. All the transects exhibited areas of higher ρ (up to 150 Ω m) which are located below the layer L1 and reaches the depth of 5 – 10 meters below the soil surface. This layer is more developed at the field 1 compared to fields 2 and 3.

Layer L2: Low ρ layer. This layer exhibit varying thickness and ρ around 40 Ω m. The layer reaches depths down to 25 m below the soil surface.

Layer H2: The bottom of the measured profiles are formed by an area with higher ρ of values above 60 Ω m. Layer H2 is however very heterogeneous, locally reaching resistivity values above 150 Ω m at some transects. It also has to be noted that the ERT profiles exhibit a high degree of uncertainty and lower resolution in the deeper regions.

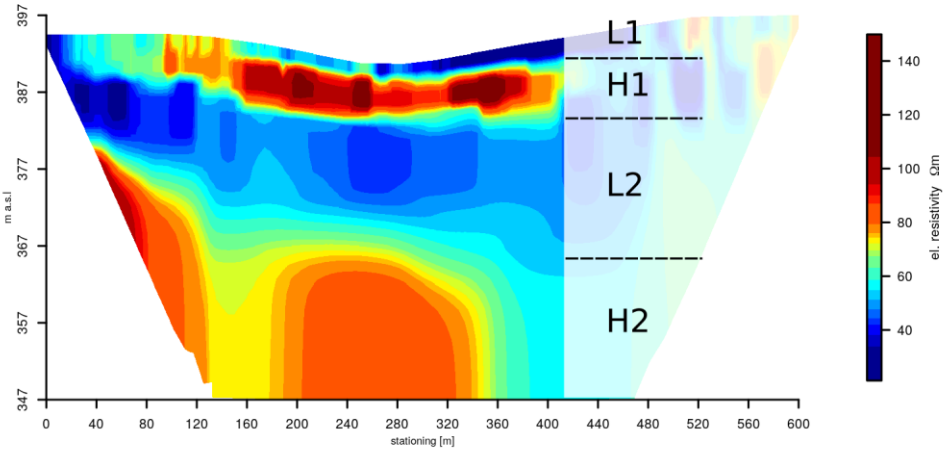

Fig. 9 - The profile TFC5 with clearly developed 4 distinct subsurface layers. Similar stratification is to some extend visible at all measured ERT transects. The TFC5 transect is used here as an example.

The layer L1 is not present in all transects as it is shown in Figure 10. However, in Jeřábek et al. [11], it was shown that the top 1 – 2 meters consist of soil material with ρ around 40 Ωm. The fact that the low ρ layer is not present in all profiles could also be caused by uncertainty in the measured resistivity closer to the surface. The median depth of investigation starts at 2.5 m and 1.55 m for the 5 and 3 m electrode spacing in case of the Wenner-Schlumberger array [18]. The H1 layer was presented mainly below the field 1. It was visible especially in the transects crossing the valley thalweg (TFC5 and TFC3). The ERT transect TFT5 exhibited H1 layer only within a limited area. A key property of the H1 layer is that its shape copies the topography of the surface (compared to the H2 layer as described later). The L2 layer, which is characteristic by its comparatively low resistivity, has a variable thickness and even reaches the soil surface at the BFC3 transect. The delineation between the layers L2 and H2 is not very sharp, as compared to the divide between layers H1 and L2. This may be caused by more gradual transition between geological layers, but also by artifact of inversion, which was not successful in recognizing areas below high ρ layers (such as H1 in this case) [18] . The interface, even though not very sharp, between L2 and H2 layers clearly declines in a southern direction, the inclination does not mirror the topography of the land surface.

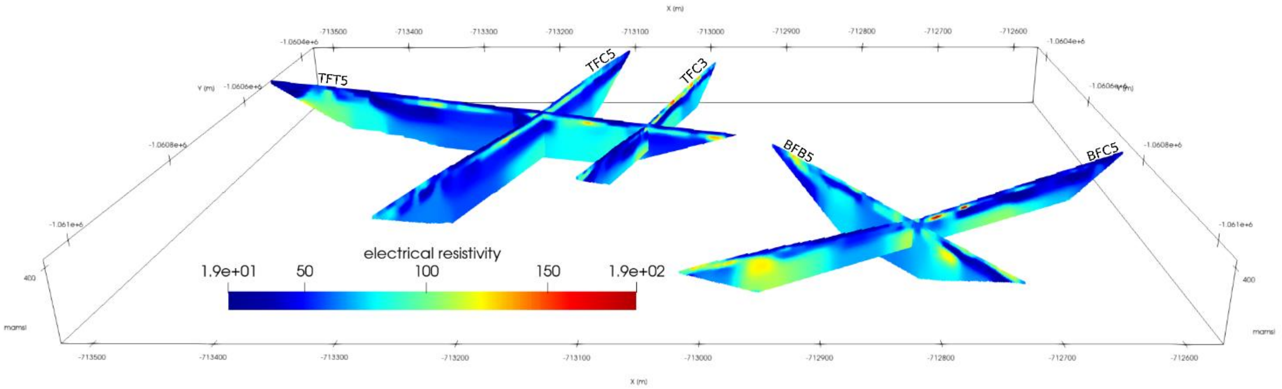

Fig. - 10. All ERT profiles shown at its real positions. Profiles coding is shown in the Figure.

The declination of the layer H2 differed for the area below field 1, and below fields 2 and 3. This difference indicates a large geological complexity in the area. At the same time, the electrical resistivity of the layers are not very different which suggest similarities within the geological layers.

The shallow and deep groundwater levels qualitatively correspond to the ERT measurements. The shallow GWL is likely positioned above the impermeable H1 layer while the deeper one above the H2 layer. The high electrical resistivity indicates rocks or less water-saturated areas. The low electrical resistivity in layers L1 and L2 may be caused by ions dissolved in the ground water. The deep GWL derived from the borehole data was observed deeper compared to the ERT. However, the borehole was located further from the catchment in the direction of thickening of the L2 layer. It is therefore possible that the less permeable H2 layer is even deeper at the location of the borehole.

ERT transects intersections

Intersections of the ERT profiles served as cross-validation of the highly qualitative measurement which the ERT is. The transects were measured under different topsoil moisture and vegetation conditions, which may have affected the results. Also, the 2D transects which are perpendicular to each other can capture the 3D structures differently. For instance, the presence of the brook may result in differences in the transects BFB5 and BFC3 and cause the discrepancies in the intersection C [24]. The highly variable geology of the catchment and inclinations of the subsurface layers may also manifest differently to the perpendicular cross-sections. The perpendicular transects B and C exhibited larger differences. Here the differences may be also caused by different electrode spacings, where one of the transects had electrode spacing 3 and the other 5 meters. Besides these factors ERT measurement loses its sensitivity with depth and suffer various artifacts due to inversion during data processing which may also have led to deviations between profiles [25].

CONCLUSION

In this paper, we present and discuss results of a geophysical survey performed at a small headwater agricultural catchment. The survey aimed to extend the knowledge about the subsurface stratification. This information helps to interpret the water transport in the catchment and can be used for setting up the hydrological models. Results indicated a complex geology within the area. The ERT identified at least four layers with distinct electrical resistivity. Interestingly, the shallow layers (approximately 5 m below surface) corresponded to the topography of the soil surface, however, the deeper layers interface did not. These results confirm the hypothesis that portion of the water which percolates into the deep horizon can be transported from the catchment through the flow paths which do not correspond to the drainage paths inferred from the digital elevation model. Also, the shape and declination of the deep layers are different in the upper and bottom parts of the catchment which indicates heterogeneous geological setting even in a relatively small area. Although the indirect ERT method is hard to interpret quantitatively, the information presented in the manuscript increase understanding of the water transport regime within the catchment.

ACKNOWLEDGEMENTS

We would like to thank Nina Noreika, Tailin Li, Tomáš Laburda and Jáchym Jeřábek for an assistance during the labor-intensive field surveys and to Saunak Sinha Ray for the proofreading. The field work, data analysis, and manuscript preparation were funded by the Horizon 2020 research and innovation program project 773903 - “Shui - Soil Hydrology research platform underpinning innovation to manage water scarcity in European and Chinese cropping systems,” funded by the European Union, and by the Grant Agency of the Czech Technical University in Prague project no. SGS20/157/OHK1/3T/11 - “Experimentání výzkum a modelování komplexních fyzikálních procesů v půdním prostředí”.

REFERENCES

[1] Beven, K. 2006. Searching for the Holy Grail of scientific hydrology: Q_t=(S, R, Δt)A as closure. Hydrology and Earth System Sciences. Vol. 10, No. 5, p. 609–618. DOI 10.5194/hess-10-609-2006.

[2] Schrott, L., Sass, O. 2008. Application of field geophysics in geomorphology: Advances and limitations exemplified by case studies. Geomorphology. Vol. 93, No. 1–2, p. 55–73.

DOI 10.1016/j.geomorph.2006.12.024.

[3] Samouëlian, A., Cousin, I., Tabbagh, A., Bruand, A., Samouëlian, A., Cousin, I., Tabbagh, A., Bruand, A., Electrical, G.R. 2006. Electrical resistivity survey in soil science : a review . To cite this version : HAL Id : hal-00023493. .

[4] Colangelo, G., Lapenna, V., Loperte, A., Perrone, A., Telesca, L. 2008. 2D electrical resistivity tomographies for investigating recent activation landslides in Basilicata Region (Southern Italy). Annals of Geophysics. Vol. 51, No. 1, p. 275–285. DOI 10.4401/ag-3048. ze se pouziva na landslide

[5] Abudeif, A.M. 2015. Integrated electrical tomography and hydro-chemical analysis for environmental assessment of El-Dair waste disposal site, west of Sohag city, Egypt. Environmental Earth Sciences. Vol. 74, No. 7, p. 5859–5874. DOI 10.1007/s12665-015-4610-5.

[6] Wang, T.P., Chen, C.C., Tong, L.T., Chang, P.Y., Chen, Y.C., Dong, T.H., Liu, H.C., Lin, C.P., Yang, K.H., Ho, C.J., Cheng, S.N. 2015. Applying FDEM, ERT and GPR at a site with soil contamination: A case study. Journal of Applied Geophysics. Vol. 121, p. 21–30. DOI 10.1016/j.jappgeo.2015.07.005.

[7] Audebert, M., Clément, R., Moreau, S., Duquennoi, C., Loisel, S., Touze-Foltz, N. 2016. Understanding leachate flow in municipal solid waste landfills by combining time-lapse ERT and subsurface flow modelling – Part I: Analysis of infiltration shape on two different waste deposit cells. Waste Management. Vol. 55, p. 165–175. DOI 10.1016/j.wasman.2016.04.006.

[8] Sherif, M., Mahmoudi, A. El, Garamoon, H., Kacimov, A., Akram, S., Ebraheem, A., Shetty, A. 2006. Geoelectrical and hydrogeochemical studies for delineating seawater intrusion in the outlet of Wadi Ham, UAE. Environmental Geology. Vol. 49, No. 4, p. 536–551. DOI 10.1007/s00254-005-0081-4.

[9] Satriani, A., Loperte, A., Imbrenda, V., Lapenna, V. 2012. Geoelectrical surveys for characterization of the coastal saltwater intrusion in metapontum forest reserve (Southern Italy). International Journal of Geophysics. Vol. 2012. DOI 10.1155/2012/238478.

[10] Chambers, JE , Wilkinson, PB , Uhlemann, S , Sorensen, JPR , Roberts, C , Newell, AJ , Ward, WOC , Binley, Andrew , Williams, PJ , Gooddy, DC, O. 2014. Derivation of lowland riparian wetland deposit architecture using geophysical image analysis and interface detection. Water Resources Research. DOI 10.1111/j.1752-1688.1969.tb04897.x. ze se pomic ert pokouseli rozdelit jednotlive vrstby (ne jen bedrock a soil profile)

[11] Jeřábek, J., Zumr, D., Dostál, T. 2017. Identifying the plough pan position on cultivated soils by measurements of electrical resistivity and penetration resistance. Soil and Tillage Research. Vol. 174, p. 231–240. DOI 10.1016/j.still.2017.07.008.

[12] Besson, A., Cousin, I., Samouëlian, A., Boizard, H., Richard, G. 2004. Structural heterogeneity of the soil tilled layer as characterized by 2D electrical resistivity surveying. Soil and Tillage Research. Vol. 79, No. 2 SPEC.ISS., p. 239–249. DOI 10.1016/j.still.2004.07.012.

[13] Haskins, N. 2010. Book Review - A Field Guide to Geophysics in Archaeology. Archaeological Prospection. Vol. 62, No. December 2009, p. 61–62. DOI 10.1002/arp.

[14] Zhou, W., Beck, B.F., Stephenson, J.B. 2000. Reliability of dipole-dipole electrical resistivity tomography for defining depth to bedrock in covered karst terranes. Environmental Geology. Vol. 39, No. 7, p. 760–766. DOI 10.1007/s002540050491.

[15] Cheng, Q., Tao, M., Chen, X., Binley, A. 2019. Evaluation of electrical resistivity tomography (ERT) for mapping the soil–rock interface in karstic environments. Environmental Earth Sciences. Vol. 78, No. 15, p. 1–14. DOI 10.1007/s12665-019-8440-8.

[16] Noreika, N., Li, T., Zumr, D., Krasa, J., Dostal, T., Srinivasan, R. 2020. Farm-scale biofuel crop adoption and its effects on in-basin water balance. Sustainability (Switzerland). Vol. 12, No. 24, p. 1–15. DOI 10.3390/su122410596.

[17] Li, T., Jeřábek, J., Noreika, N., Dostál, T., Zumr, D. 2021. An overview of hydrometeorological datasets from a small agricultural catchment (Nučice) in the Czech Republic. Hydrological Processes. DOI 10.1002/hyp.14042.

[18] Loke, M.H. 1999. Electrical imaging surveys for environmental and engineering studies. A practical guide to 2-D and 3-D surveys. . No. 1999, p. 59.

[19] Samouëlian, A., Cousin, I., Tabbagh, A., Bruand, A., Richard, G. 2005. Electrical resistivity survey in soil science: A review. Soil and Tillage Research. Vol. 83, No. 2, p. 173–193. DOI 10.1016/j.still.2004.10.004.

[20] Palacky, G.J. 3. Resistivity Characteristics of Geologic Targets. In : Electromagnetic Methods in Applied Geophysics. 1988. p. 52–129.

[21] Furman, A., Ferré, T.P.A., Warrick, A.W. 2003. A Sensitivity Analysis of Electrical Resistivity Tomography Array Types Using. Vadose Zone Journal. Vol. 2, p. 416–423.

[22] Loke, M.H. 1998. “Res2dInv.” Rapid 2D resistivity and IP inversion using the least-squares method.

User Manual, Austin Tex, Advanced Geoscience Inc.

[23] Archie, G.E. 1942. The electrical resistivity log as an aid in determining some reservoir characteristics. Transactions of the AIME. Vol. 146, No. 01, p. 54–62.

[24] Hung, Y.C., Lin, C.P., Lee, C.T., Weng, K.W. 2019. 3D and boundary effects on 2D electrical resistivity tomography. Applied Sciences (Switzerland). Vol. 9, No. 15. DOI 10.3390/app9152963.

[25] Loke, M.H. 2004. Tutorial: 2-d and 3-d electrical imaging surveys, Geotomo Software, Malaysia. . No. July, p. 136.

Soil & Tillage Research 174 (2017) 231–240

Contents lists available at ScienceDirect

Soil & Tillage Research

journal homepage: www.elsevier.com/locate/still

Identifying the plough pan position on cultivated soils by measurements of electrical resistivity and penetration resistance

Jakub Jeřábek*, David Zumr, Tomáš Dostál

Department of Irrigation, Drainage and Landscape Engineering, Faculty of Civil Engineering, Czech Technical University in Prague, Thákurova 7, 16629 Prague 6, Czech Republic

ARTICLE INFO

Keywords:
Electrical resistivity tomography (ERT)
Penetration resistance
Subsoil compaction

ABSTRACT

Long term tillage has led to soil profile degradation in many cultivated fields. The topsoil is disturbed by plowing. The movement of fine particles from the topsoil to the subsoil and direct pressure from agricultural machinery create an abrupt delineation in the form of a plough pan with very low permeability. The plough pan prevents water infiltrating deeper into the soil profile and reduces the water supply to the lower layers. The plough pan also has a negative effect on the root growth of the crop, leading to a reduced yield. In this paper we discuss the feasibility of using electrical resistivity tomography and penetrometry to identify the presence and the position of plough pans, and also their spatial uniformity, on two fields with different tillage depths. Electrical resistivity measurements were subjected to a comparison with soil physical characteristics, such as soil water content, porosity and bulk density. Standard statistical and geostatistical methods were used. Electrical resistivity tomography seems to be an attractive method that offers a faster and more efficient method than standard invasive soil sampling for obtaining continuous information about the plough pan. It has been shown that the position of a compacted layer within the soil profile can be identified reasonably well by combining electrical resistivity data and penetration resistance data. The semivariogram showed higher variation by orders of magnitude in the topsoil than in the subsoil. This suggests macroscopic homogeneity of the compacted layer formatted in the subsoil in two differently tilled fields. We conclude that a short span between the electrodes should be used (app 10 cm) in order to observe the shallow positioned plough pan clearly.

1. Introduction

Soil compaction, which may lead to the formation of a plough pan, is a well-recognized phenomenon in agricultural lands. Crop root degradation is one of the most dangerous effects of soil compaction. Roots are of reduced length (Lipiec et al., 2012) and there is reduced biomass (Colombi et al., 2016) in the compacted layer. Various effects can influence the degree of compaction in a field. Climatic or weather conditions, tillage system (Pagliai et al., 2004), the condition of the soil during harvesting (Boizard et al., 2002) and the machinery that is used (Pagliai et al., 2003) can lead to an increase or reduction in soil compaction. As a consequence, the hydraulic properties of the soil are affected. Ahuja et al. (1998), for example, showed how the water retention capacity of a field changes according to the tillage conditions. Dörner and Horn (2009) investigated of the isotropy/anisotropy of hydraulic conductivity in conventionally and conservationally tilled fields. Unlike conservationally tilled fields, conventionally tilled fields exhibited anisotropic conditions in the seedbed and in the plough pan.

A number of studies have investigated changes in the properties of porous media due to compaction. Bertolino et al. (2010) concluded that, in comparison with soils treated by minimum tillage, smaller and less connected pores occurred in the plough pan of conventionally tilled soil. Direct compaction due to the passage of traffic causes large differences in porosity (n) and differences in bulk density (ρ_{bd}) which leads to changes in the saturated hydraulic conductivity (Kim et al., 2010). However, the lower hydraulic conductivity of the plough pan is not necessarily the only reason. A significant decrease in hydraulic conductivity in combination with flow irregularity may also occur due the role of trapped air in the upper layer during infiltration (Císlerová et al., 1990; Sněhota et al., 2008). In contrast, Roulier et al. (2002) presented evidence of undisturbed bio-macropores in the plough pan, formed after soil cultivation or not yet disturbed e.g. by shrinkage, which allows water to flow through preferential pathways and to bypass the compacted plough pan. This consequently increased the overall hydraulic conductivity.

Changes of soil properties due to compaction lead to changes in the electrical properties of the soil. The changes in soil water content (θ), in the salinity of the water, in the clay fraction or in the bulk density lead

---

* Corresponding author.
E-mail address: jakub.jerabek@fsv.cvut.cz (J. Jeřábek).

http://dx.doi.org/10.1016/j.still.2017.07.008
Received 23 May 2016; Received in revised form 12 June 2017; Accepted 14 July 2017

to changes in the electrical resistivity (ρ) of the soil (e.g. Besson et al., 2004); Loke et al., 2013). The specific surface area of soil particles affects the resistivity because of an adsorbed water film on the soil particles (Revil et al., 2012), whereas the soil particles themselves (irrespective of size) and the soil air are often considered as an insulating material (e.g. Fukue et al., 1999). Macropores, cracks or voids and organic residues usually increase the electrical resistivity of the soil (Besson et al., 2013). Since the specific surface area of soil particles alters the electrical resistivity of the soil ρ, and it is affected by of soil compaction causing changes in the bulk density and in the structure of the soil, we assume that measurements of changes in ρ can provide information about the plough pan depth and homogeneity.

We used the electrical resistivity tomography (ERT) technique to obtain the position and the spatial uniformity of the plough pan. The study covered a series of 10 specific ERT transects. In general, this approach faces a few ambiguities. The electrical properties of soils, e.g. their electrical resistivity, are affected by several factors. It is problematic to recognize which factor is of major influence. Kowalczyk et al. (2014) conducted experiments with a sandy material in which it was shown that changes in electrical resistivity are caused by changes in bulk density, water content and total porosity. Similar results in field soils were observed by Besson et al. (2013), where the ERT data was influenced by the degree of water saturation. The bulk density was therefore tricky to determine. Organic carbon can also affect resistivity measurements, especially in the uppermost layer of the soil in agricultural land (Hadzick et al., 2011). When all quantities except the bulk densities are excluded, i.e. their effect is set as constant over a measured sample, the influence of bulk density is clearly present (Besson et al., 2004). In a study performed by Besson et al. (2004), 2D ERT measurements were compared with a visual inspection of the uncovered soil profile transect on an experimental plot. Although the resistivity was significantly lower in the plough pan, its exact position could not be determined. ERT did not detect the position of all clods in the topsoil. However, a clear negative relationship was found between electrical resistivity and bulk density for field soil samples. When the topsoil was less heterogeneous, it was less problematic to indicate the position of the plough pan.

Séger et al. (2009) presented a comparison of identifying topsoil features using 2D and 3D ERT. The 2D method was influenced by the hemisphere integration effect (Séger et al., 2009). The electrical current introduced to the ground by electrodes along a line introduces to the ground an electrical field that is hemispherical in shape. The records are therefore affected by lateral features to the side of the 2D line. Séger et al. (2009) showed that 3D measurements diminish the hemisphere integration effect, and enhance the sensitivity of the method to the structure of the topsoil. In qualitative terms, large clods, which occupied the whole depth of the topsoil (ca 30 cm), had the lowest resistivity; loose material had slightly higher resistivity, but smaller clods (∅ ca 5–10 cm) embedded in loose material had markedly higher resistivity. However, the position of the plough pan appeared only in the form of smoother changes in the horizontal 2D cross-sections of the 3D measurements. ERT and a penetration test were used by Basso et al. (2010). To assess the variations in soil resistivity in several differently tilled plots. They concluded that ERT can assist in identifying a compacted layer in the soil profile.

After a rain event, the infiltration capacity of the plough pan can be exceeded due to its low permeability. This causes the formation of lateral flow, (Coquet et al., 2005). Higher saturation above the plough pan affects data acquisition and makes the results more difficult to interpret. A detailed laboratory analysis of changes in the resistivity of different clays under variably saturated conditions was undertaken by Fukue et al. (1999). They measured abrupt changes in electrical resistivity at a certain saturation, at which the water film on the surface of a clay particle becomes connected, or ceases to be connected. The soil structure appeared to have a limited effect on the electrical resistivity (or conductivity) (Nadler, 1991). In many studies, the relationship between bulk density and electrical resistivity is assumed to be negative. However, some other studies have reached the opposite conclusion (e.g. Naderi-Boldaji et al., 2014). Electrical resistivity measurements of soil are also used in hydraulic conductivity assessments, (Mazáč et al., 1988), in soil classification based on resistivity distinctions between soil layers (Buvat et al., 2014) and in tracking distinct pedological volumes in a single soil layer (Séger et al., 2014).

The objective of our study is to assess the feasibility of using the ERT technique to determine the position of the plough pan, and its spatial uniformity and continuity. It is not our ambition to obtain the concrete physical properties of the soil layers. We utilize the sharp contrast in electrical properties between the topsoil and the subsoil caused by a combination of attributes such as organic matter content, clay particles, bulk density or current saturation to identify the divide. Data collection took place at two sites exposed to different tillage. From the agricultural, pedological, geological and climatological point of view, the two sites are representative of their region. The penetration resistance tests and the measurements of soil physical properties were collected in order to compile a data set for a comparative analysis. The results of the measurements are analyzed by means of standard statistical and geostatistical methods.

2. Material and methods

Our study consists of ERT measurements, penetration tests and measurements of the physical properties of soil core samples. We conducted four measurement campaigns. In each campaign, several ERT transects were measured. In selected ERT transects, three to five penetration tests were performed and soil core samples were collected at different depths. The penetration tests were performed to a depth of ca 65 cm. The soil core samples were taken at three to six depths, down to a depth of ca 50 cm. At least one set of core samples was taken from the top soil, and at least one was taken from the compacted layer if a plough pan was present. The penetration tests provided evidence of the presence and the position of a plough pan. The physical properties of the soil, namely soil bulk density, total porosity and water content, were evaluated to clarify the interpretation of the ERT data. The setup for typical ERT transect measurements, together with penetration tests and the collection of soil core samples is shown in Fig. 1. Each measurement campaign has its unique identifier (character A–D). The distribution of the measured transects (*T*) within the experimental catchment is depicted in Fig. 2. A summary of all measurements is shown in Table 1.

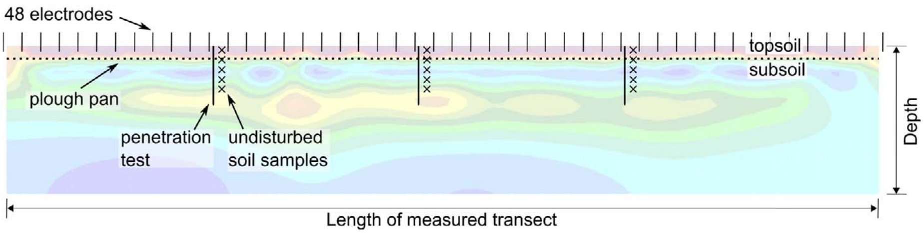

Fig. 1. Set up of ERT, penetration test and undisturbed soil sample sites at one ERT transect.

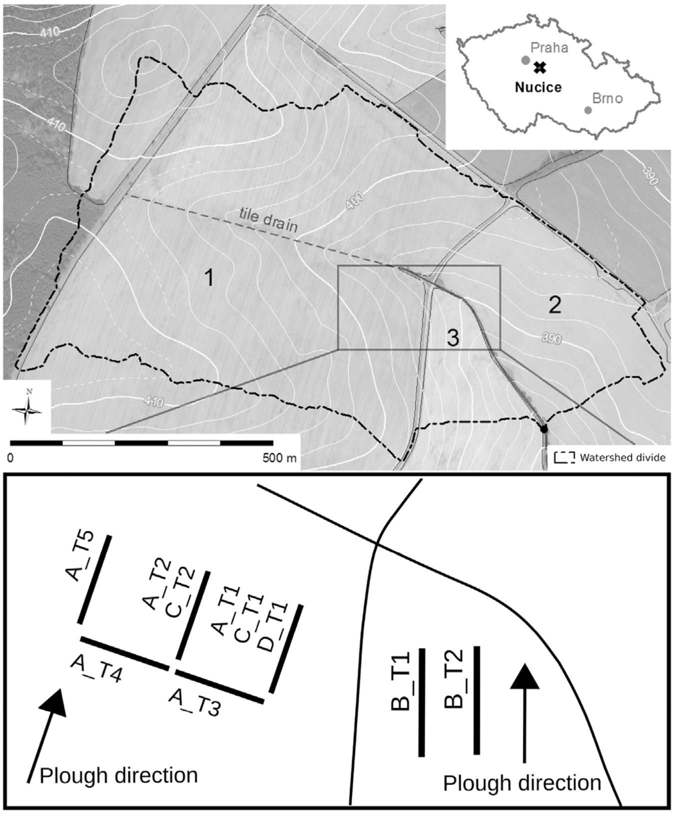

Fig. 2. The study site and the location of the experiment profiles; A–D denote the order in which the campaign was organized. The last digit denotes the order of the measurements undertaken in a transect identifier.

2.1. Study area

The study was performed in a small catchment located in the central part of the Czech Republic, 30 km south-east of Prague. The catchment, with a total area of 0.5 km^2, consists of three fields cultivated by two farmers.

The two largest fields (field 1 and 2 in Fig. 2) are exposed to conservation tillage. The crop in field 1 was white mustard (*Sinapis alba*) in season 2013 and winter wheat (*Triticum aestivum*) in seasons 2013–2014 and 2014–2015. After harvesting, a Horsch Joker 12 cultivator was used for stubble cultivation and a Horsch Tiger compact disk harrow was used for seedbed preparation. The farmer uses John Deere 9630T rubber tracked tractors. Cultivation is done to a depth of 10–12 cm, and seedbed preparation is done to a depth of 18 cm. After harvesting in October 2015, chisel plowing was done to a depth of 25–28 cm.

The smallest field (field 3 in Fig. 2) was treated by conventional tillage until 2012, after which conservation tillage was introduced. Deep plowing is done after harvesting in order to disturb the wheel tracks and the plough pan in field 3. In 2015, stubble cultivation was done to a depth of 8 cm using a Vaderstad Carrier CR 925-1225 cultivator. Deep plowing to a depth of 45 cm and seedbed preparation were done using a Vaderstad Topdown TD 300-900 cultivator. The farmer uses Vicon wheeled tractors with 1.2 bar wheel pressure. The crop in field 3 was winter wheat (*T. aestivum*) in the 2014–2015 season. The most important cultivation activities before each measurement are briefly presented in Table 1 .

Agricultural land covers 96.4% of the catchment area, with a mean slope of 3.9%. The soil is classified as Cambisols and Luvisols, with an Ap horizon between 0.1 and 0.2 m in depth and a B horizon beneath it. Both the topsoil and the subsoil were classified as a loamy soil, but there was a slightly higher clay content in the subsoil. The bedrock consists of conglomerates, sandstone and siltstone. The organic matter content is assumed to be homogeneous within the catchment. The mean annual precipitation is 630 mm, and the mean evapotranspiration is 500–550 mm. The mean annual temperature is 6 °C. Detailed information about the hydrology of the experimental site can be found in Zumr et al. (2015).

2.2. Electrical resistivity tomography

Electrical resistivity tomography (ERT) was used to determine the electrical resistivity (ρ) of the soil profile. The research was conducted using the ARES device, manufactured by GF Instruments (Czech Republic). Date of the 10 measurements are presented in Table 1 . After each measurement, the water content was determined (last column in Table 1). The measurements were made after the harvest, when the fields were bare. A dipole–dipole array with 48 electrodes was used for each transect. The electrodes were inserted to a depth of 2–4 cm, which coincided with the surface roughness. The spacing of the electrodes was 0.2 m for transects A and B, and 0.1 m for transects C and D. In transects A and B, the array parameter a was within an interval of a = 0.2–1.8. For transects C and D, array parameter a was within an interval of a = 0.1–0.9. For all transects, parameter n was between 1 and 4. A single measurement consisted of 1035 datum points and 45 depth levels.

The dipole–dipole array is weaker in capturing deep structures, but it is more sensitive in the shallowest part of the measured profile (Furman et al., 2003; Dahlin and Loke, 1997). It has higher horizontal sensitivity than other electrode arrays (Samouëlian et al., 2005), which we found convenient for capturing the heterogeneity of the plough pan. However, the dipole - dipole array has low sensitivity in deeper structures, which was taken into account during the inversion procedure.

To obtain the electrical resistivities, the datum points need to be inverted. In situ measurements offer the so-called apparent electrical resistivity. The apparent electrical resistivity represents the surficial effect of the introduced electrical field. A model of the apparent electrical resistivities based on an array geometry is fitted to the apparent electrical resistivities obtained in the field during the inversion procedure. The spatial distribution of the electrical resistivities serves as a set of model parameters (Loke, 2004).

Before inversion, data points which had, compared to adjacent data points, abnormal resistivity were filtered out to reduce the noisiness. Based on previous experiences, the abnormal resistivity is caused by weak connection between an electrode and a soil rather than on

Table 1
Overview of measurements and cultivation activities.

Date (D.M.Y.)	Transect	Penetrometry	Undisturbed core samples	Previous activity	Soil water cont.
2.10.2014	A_T1, A_T2, A_T3, A_T4, A_T5	Yes	Top soil only	12.8. cultivation depth 10–12 cm; 28.9. seeding preparation depth 18 cm	Wet θ_{top} = 0.29
27.10.2015	B_T1, B_T2	Yes	Yes	25.8. plowing 20 depth cm; 1.9. clover seeding	Wet θ_{top} = 0.34
20.11.2015	C_T1[a], C_T2[a]	At C_T1	Yes	28.10. chisel plowing 25–28 cm	Very wet θ_{top} = 0.39
30.3.2016	D_T1[a]	Yes	Yes	After winter with no agricultural activity	Wet θ_{top} = 0.29

[a] Electrode spacing = 0.1 m; θ_{top} topsoil volumetric water content [cm^3/cm^3].

properties of a soil material. The threshold error of the reciprocal measurements was set to 5%. The ratio of the removed noisy points varied between 0 and 4%. Due to the increased noisiness of the dipole–dipole array with depth (Furman et al., 2003; Dahlin and Loke, 1997), the number of layers was reduced to 10 for transects A and B and to 20 for transects C and D. The total number of computation blocks was reduced to 940 for transects A and B and to 1880 for transects C and D.

Typically 3–6 iterations were needed to bring the relative change in the subsequent RMS error below 1%. The maximum number of iterations was set to 7. In all cases, the desired results were reached before the 7th iteration. In most cases, the number of iterations was 3 or 4. A finite-elements mesh with triangular elements and one half of the space of the electrodes span was used. The smoothness constraint on the model resistivity values was used for transects B_T1 and B_T2. For field 3, a smoother transition between the topsoil and the subsoil was expected, as was also suggested by the profiles of the apparent electrical resistivities (as was discussed in Section 3.1). The robust inversion option was used for other transects measured in field 1 (transects A, C and D), where a sharper transition was expected between the soil and subsoil. The standard Gauss–Newton method was employed for the optimization.

2.3. Penetration resistance

We measured the penetration resistance (p_{pr}) in the subset of ERT profiles with spacing from 1 to 2 m along the profile. Eijkelkamp penetrologger agrisearch equipment (art. no. 06.15.01) was used. At each location, 5 consecutive penetration tests were performed to a depth of approximately 65 cm. The probing cone had a 30° top angle and a base area of 1.3 cm^2. The resolution of data points were 1 cm. The resulting p_{pr} profile at each location was obtained as the average of 5 depth measurements.

2.4. Soil core samples

At each p_{pr} measurement location, undisturbed soil samples were taken in metallic cylinders at various depths. One sample was always taken in the topsoil (the upper 20 cm of the profile). The number of samples in the subsoil depended on the time available during each campaign. The number varied between 2 and 5 in the subsoil. The volume of each cylinder was 137.4 cm^3. Gravimetric methods were used to obtain the bulk density ρ_{bd}, the total porosity n, and the volumetric water content θ. We used a displacement method to estimate porosity based on difference of fully saturated and dry masses of undisturbed samples with a known volume.

2.5. Statistics and geo-statistics

Semivariograms were used for the geostatistical analysis. The general semivariogram can be written as follows,

$$E\left[Y(s+\mathbf{h})-Y(s)\right]^2=\mathrm{Var}(Y(s+\mathbf{h})-Y(s))=2\gamma(\mathbf{h})$$

where $Y(s)$ is an observed variable at position s and $\mathbf{h}$ is the vector denoting the spatial shift of variable Y from position s. $2\gamma(\mathbf{h})$ is the variogram and $\gamma(\mathbf{h})$ is the semivariogram, and both are dependent only on $\mathbf{h}$, which is the relative distance between variable Y at positions s and $s+\mathbf{h}$ (Banerjee et al., 2014). Here, we want to point out the ambiguity of the last statement in relation to the use of semivariograms to analyze ERT data. The reason is that ρ obtained by ERT is position dependent. However, we assume that for shallow depths this fact can be neglected.

In our paper we use a binned empirical semivariogram. A binned empirical semivariogram is defined as

$$\gamma_{\mathrm{ij}}=\frac{1}{2N_{B_{\mathrm{ik}}}}\sum_{(k,j):(s_k-s_l)\in B_{\mathrm{ij}}}(Y(s_k)-Y(s_l))^2$$

where B_{ik} is a so-called bin which contains pairs of points with a certain relative distance, and $N_{B_{ik}}$ is the number of pairs in a bin.

The inverted electrical resistivity data was linearly interpolated before the semivariance analysis. The linear interpolation was based on triangles of adjacent datum points, which corresponds to the finite-element modeling used in the inversion procedure.

The simple linear regression Student's t-test was used to evaluate whether or not the penetration resistance p_{pr} measurement can serve as an explanatory variable for electrical conductivity σ (inverse electrical resistivity). We tested the hypotheses of zero slope a and zero intercept b in the linear formula $\sigma = ap_{pr} + b$.

3. Results

3.1. ERT transects

Some trends can be evaluated from the ERT transects (Figs. A8–A.10, for convenience displayed in Appendix A) together with information about the water content in the topsoil during the measurements (last column in Table 1).

The apparent electrical resistivity (ρ_{ap}) of the transects is displayed in the topmost panel in Figs. A8– A.10. For transects A_T5 and C_T1 (Figs. A8– A.10) ρ_{ap} is higher ($>$ 80 Ωm) in the upper 20 cm of the soil profile. The ρ_{ap} is generally lower below the first 20 cm of the profile for transects A_T5 and C_T1. Some areas of higher resistivities are scattered evenly over the profile below a depth of 20 cm ($\rho_{ap} \in \langle 40-50 \rangle$ Ωm) in these transects. This suggests a sharper transition between the topsoil and the subsoil. In transects A_T5 and C_T1 we therefore used the robust inversion model option, which better captures sharp resistivity transitions. Apparent electrical resistivity ρ_{ap} exhibits different patterns for transect B_T1 (Fig. A.9). The highest ρ_{ap} values are found in the topsoil but, in comparison with transects A_T5 and C_T1, the decrease of ρ_{ap} with depth is more gradual. For this reason, we used the standard smoothness-constrained inversion model.

The inverted electrical resistivity ρ (second panel in Figs. A8– A.10) has the highest value in the shallowest part of all profiles, and it shows the greatest variation (variability is not shown in Figs. A8– A.10 due to the colour scale). Deeper in the profile, ρ is lower than 60 Ωm in transects A_T5 and C_T1.

The third and fourth panels in Figs. A8– A.10 show the sensitivity and the uncertainty of the model. In the case of transects A_T5 and C_T1 (Figs. A8– A.10), the sensitivity of the model is greatest in the upper 30–40 cm of the profile, where the transition between topsoil and subsoil is located. In transect B_T1, higher sensitivity values are propagated deeper in the profile to a depth of ca 50 cm. The higher ρ patterns located at a depth of 60–70 cm in the central area of all transects exhibit lower sensitivity of the model. Therefore it is not possible to identify the central areas as a more conductive area or as an inversion artefact. In transect B_T1, the uncertainty of the model increases rapidly with depth. The uncertainty values are the highest in the position of the high ρ object located in the central part of transect B_T1 at a depth of 60–90 cm. The uncertainty of the model is difficult to interpret for transects A_T5 and C_T1 because a robust inversion model underestimates the uncertainty value (Loke, 2004). Scattered areas of higher uncertainty are located below the possible topsoil/subsoil transition (ca 30 cm) for transect A_T5 and for the upper 20–30 cm in transect C_T1.

The ERT measurements were also conducted under very dry conditions (the topsoil water content was 0.09 $\mathrm{cm}^3/\mathrm{cm}^3$). These data are not presented here, but the electrical resistivity results exhibited large errors due to these conditions, especially due to weak contact between the electrodes and the soil. The penetration test also performed poorly in this measurement. Although these results are not shown here, it

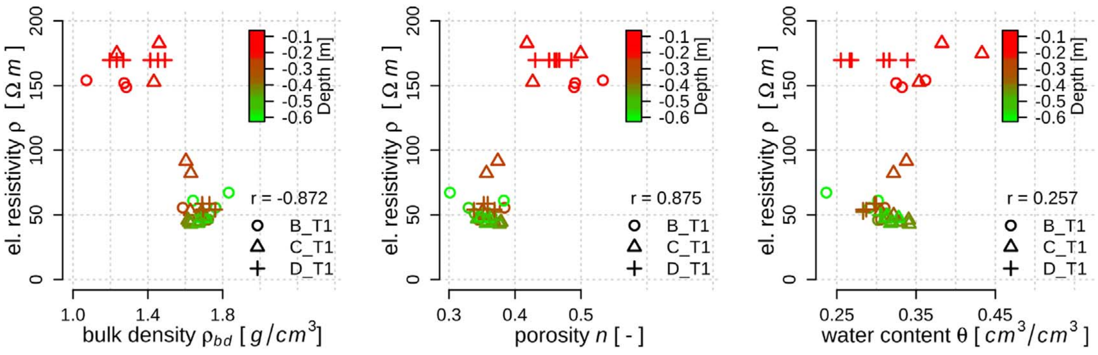

(a) (b) (c)

Fig. 3. Correlation between electrical resistivity (ρ) and the physical properties of soil samples ((a) bulk density (ρ_{bd}); (b) porosity (n); (c) volumetric water content (θ)); r stands for Pearson's correlation coefficient.

should be pointed out that moderate to high water content has to be reached in order to obtain reliable measurements of this type.

3.2. ERT and soil physical properties (ρ_{bd}, n, θ)

Fig. 3 shows the relationship between the electrical resistivity ρ and the physical properties of the soil. The relations between ρ and bulk density ρ_{bd} are displayed in Fig. 3a; porosity n is displayed in Fig. 3b and water content θ in Fig. 3c. The negative correlation between ρ and ρ_{bd} corresponds to findings published in the literature (Besson et al., 2004; Basso et al., 2010; Kowalczyk et al., 2014). The correlation between ρ and n is positive and it is also as expected. The correlation between ρ and θ depends on the antecedent weather conditions. Data from transect A_T are not shown due to missing physical properties data from the subsoil. The data points for all graphs in Fig. 3 form two clusters, one cluster of higher ρ (around 150 Ωm) and the second cluster of lower ρ (around 50 Ωm). Data points belonging to the higher ρ cluster are located in the topsoil. Data points belonging to the lower ρ cluster are located in the subsoil and in the plough pan. Two data clusters can be distinguished for ρ values and also for ρ_{bd} values (Fig. 3a). The same behavior applies for the ρ and n values in Fig. 3b. Two clusters can be distinguished only for ρ values in Fig. 3c.

3.3. ERT and the penetration resistance

In Fig. 4, we show the electrical resistivity ρ and penetration resistance p_{pr} results for four transects. The selected transects represent typical $\rho \propto p_{pr}$ behavior.

The ρ values were extracted from the 60 cm wide strip of ten measured transects, and correspond to the location of the p_{pr} measurements. The location of the p_{pr} measurement along each ERT transect is depicted in the legend of Fig. 4. Penetrometry allows the p_{pr} to be captured at a greater number of depths (obtaining finer observation resolution) than ERT. In Fig. 4, the p_{pr} are linearly approximated from the two closest ρ measurements. Since the recorded depths are rather dense in the penetrometry measurement, and because p_{pr} is already averaged over 5 consecutive measurements, the linear approximation seems to be justifiable.

Fig. 4 shows that p_{pr} and ρ are almost inversely symmetric. An increase in p_{pr} corresponds to a decrease in ρ. An abrupt increase in p_{pr} at a certain depth indicates the surface of a plough pan. When the cone of the penetrologger penetrates through the plough pan, p_{pr} remains constant or decreases slightly. According to the p_{pr} profiles in Fig. 4a, c and d, the plough pan emerges at a depth of 20 cm. In transect B_T2 (measured on field 3 where there is a different tillage regime) in Fig. 4b, a more compacted layer emerges at a depth of 30 cm. We assume that there is also decreased electrical resistivity in the plough pan for transects B_T2, C_T1 and D_T1. The lowest values of ρ were deeper than the corresponding high p_{pr} for transect A_T5. The other measurements indicated in Table 1 have a similar trend to transects B_T1, C_T1 or D_T1 (transect B_T2) similar to transect A_T5 (transects A_T1, A_T2, A_T3, A_T4).

When 10 cm electrode spacing was used (Fig. 4c, d), better symmetry between electrical resistivity ρ and penetration resistance p_{pr} was identified (field 1 in Fig. 2). Sufficient symmetry between ρ and p_{pr} was shown for electrode spacing of 20 cm in field 3 in Fig. 4b.

The correlation between normalized penetration resistance p_{pr} and electrical conductivity $\sigma(=1/\rho)$ for all penetrometry data are shown in Fig. 5. The scattering of the points increases with increasing p_{pr}. However, if a single transect is under consideration, the relationship appears to be almost linear, with a certain deflection above or below the 1:1 line. A Student's t-test of the simple linear regression analysis of slope a and intercept b of the fitted line $\sigma = ap_{pr} + b$ for each transect is displayed in Table 2 . In terms of the slope, the null hypothesis (the hypothesis that the slope is equal to zero) is not rejected only for transect A_T5. In terms of intercepts, the null hypothesis (the hypothesis that the intercept is zero) is rejected, with the exception of profiles A_T5 and D_T1.

3.4. Semivariograms of ERT results

The spatial soil heterogeneity of a particular layer can be assessed with the use of a semivariogram. Fig. 7a–d shows the semivariance of transects A_T5, B_T1, C_T1 and D_T1. The semivariance is shown only to half the depth of the measured ERT transects to zoom the topmost part of each transect. The semivariogram exhibits a rapid increase in semivariance in dependence on the increase in distance in the uppermost layer for all profiles. The increase in semivariance becomes more gradual below a depth of 20 cm in transects A_T5, C_T1 and D_T1. A one order of magnitude decrease in semivariance occurs up to the points at a distance of 2 m for C_T1 and D_T1. In the case of transect A_T5, the semivariance below a depth of 20 cm is lowered by 2 orders of magnitude in comparison with the layers above.

Similar behavior is observed for transect B_T1 in Fig. 7b. However, the semivariance increases more gradually even in the first 20 cm of the transect.

4. Discussion

ERT was used to measure the electrical resistivity ρ on agricultural soils. In general, these soils are submitted to intense cultivation of the topsoil. This causes a distinct nature of the soil structure, and as a result a distinct ρ is measured in the first tens of centimeters of the soil profile.

The correlation between ρ and the soil physical properties (in Fig. 3) exhibited two clusters. Higher bulk density ρ_{bd} and low porosity n data points correspond to lower electrical resistivity measurements ρ. These

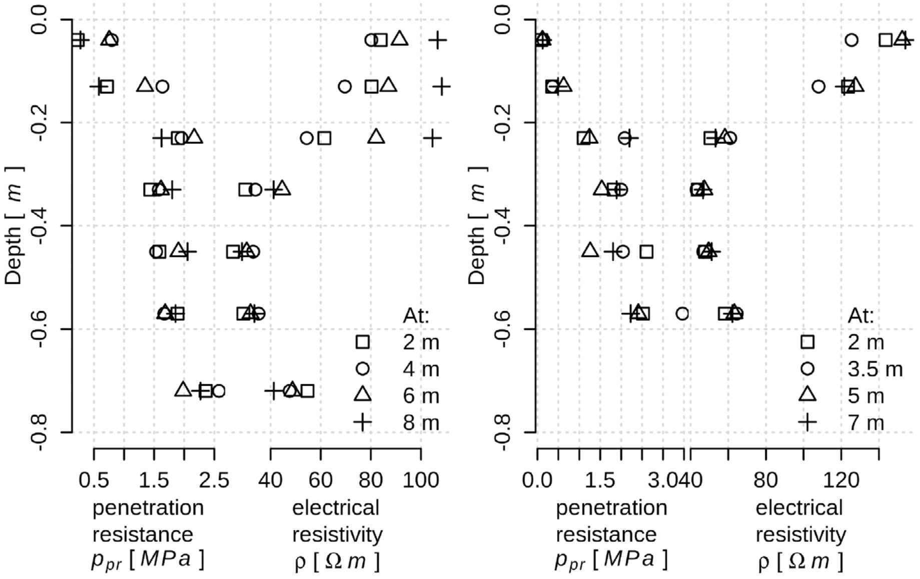

(a) A_T5

(b) B_T1

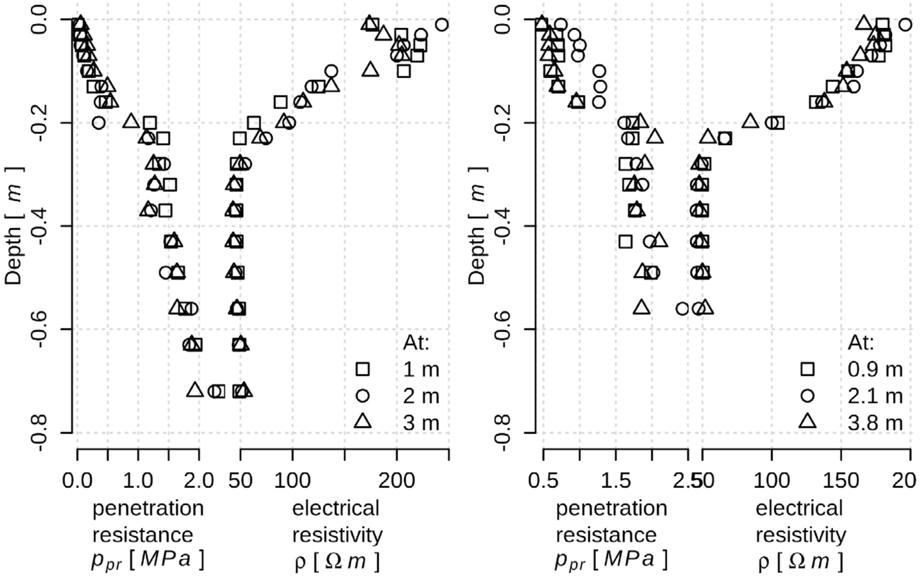

(c) C_T1

(d) D_T1

Fig. 4. A comparison between the penetration resistance measurements (p_{pr}) and the electrical resistivity (ρ) measurements within the selected transects.

data were collected from the subsoil where the plough pan is formed. Lower ρ_{bd} and higher n data points correspond to higher ρ and all these data were collected in the topsoil.

Besson et al. (2004) conducted a study where the soil samples were taken from a known (compacted or non-compacted) location within the topsoil and the corresponding ρ were compared. In their study, the decreasing relation between electrical resistivity and bulk density was less pronounced than in our results. Measurements taken from loose material exhibited high electrical resistivity ρ and low bulk density ρ_{bd} (Besson et al., 2004). Low ρ and high ρ_{bd} were measured in the samples taken from the compacted clods in Besson et al. (2004). This $\rho \propto \rho_{bd}$ relation corresponds to subsoil measurements in our research. This leads to the conclusion that the two distinct clusters of points in the $\rho \propto \rho_{bd}$ ($\sim n$) plot in Fig. 3a and b indicate the topsoil and the compacted plough pan, and that the data obtained by ERT reflect the changes in the physical properties of the soil.

The results for a comparison between electrical resistivity ρ and penetration resistance p_{pr} (Section 3.3) indicate an agreement between the quantities and the depth. We assume that p_{pr} reveals the real position of the plough pan. A comparison between electrical resistivity and penetration resistance for transects C_T1 and D_T1 indicated that the plough pan was at a depth of ca 20 cm, and the shapes of the two measured curves are inversely symmetric.

The ERT data was measured with shorter electrode spacing (10 cm, transects C_T1 and D_T1), which led to higher resolution of the electrical resistivity data. The measurements for profile B_T1 indicate that the plough pan is deeper in the soil profile due to deeper plowing. The peaks of the p_{pr} and ρ measurements are at a similar depth. Although the p_{pr} and ρ profiles are not perfectly inversely symmetric in all cases (A_T5; Fig. 4a), the depth of the lowest ρ values is very similar along the transects. In other words, the absolute depth of the plough pan is not clear in terms of ERT, but the relative change in the depth of the plough pan along the profile is reasonable in transect A_T5.

The correlations between penetration resistance p_{pr} and electrical

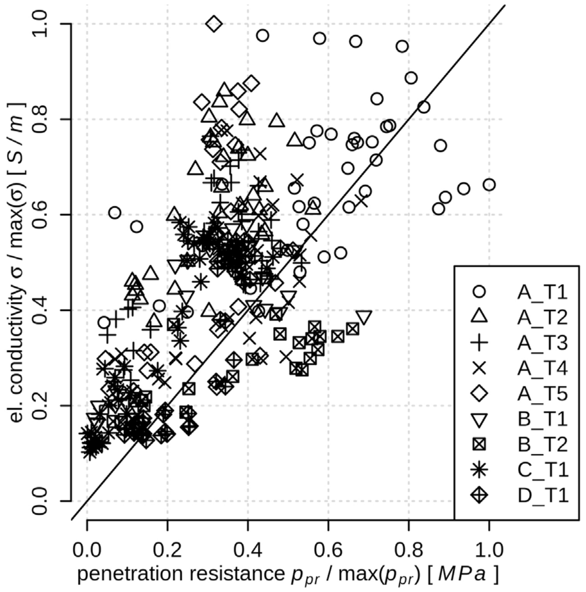

Fig. 5. Correlation between normalized penetration resistance (p_{pr}) and electrical conductivity (σ).

Table 2
Results of Student's *t*-test of the linear regression analysis; $\sigma = ap_{pr} + b$.

Transect	*b*	*a*	*P*-value *b*	*P*-value *a*
A_T1	0.471	0.371	< 0.001	< 0.001
A_T2	0.459	0.464	< 0.001	< 0.001
A_T3	0.409	0.445	< 0.001	< 0.001
A_T4	0.291	0.567	< 0.001	< 0.001
A_T5	0.256	0.469	0.032	0.012
B_T1	0.38	0.682	< 0.001	< 0.001
B_T2	0.429	0.501	< 0.001	< 0.001
C_T1	0.222	0.939	< 0.001	< 0.001
D_T1	−0.083	1.196	0.15	< 0.001

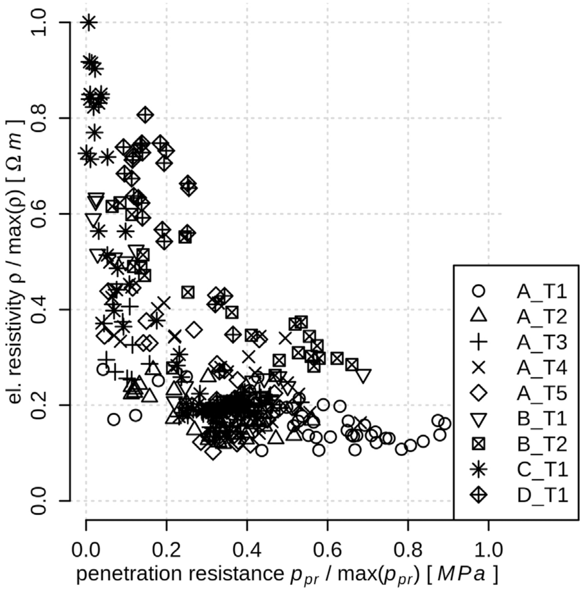

Fig. 6. Correlation between normalized penetration resistance (p_{pr}) and electrical resistivity (ρ).

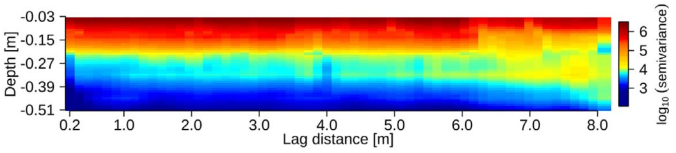

(a) Semivariogram of the electrical resistivity in transect A_T5

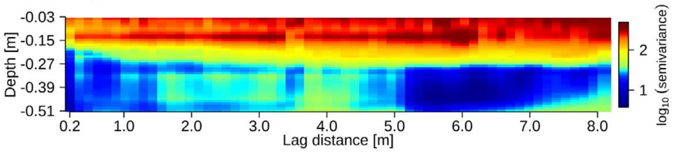

(b) Semivariogram of the electrical resistivity in transect B_T1

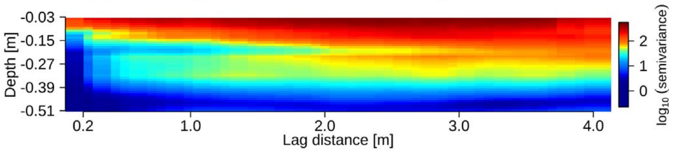

(c) Semivariogram of the electrical resistivity in transect C_T1

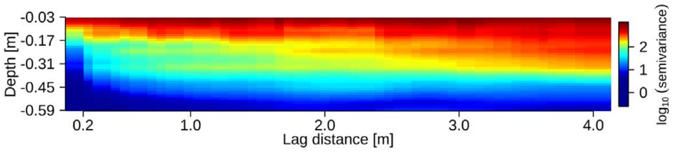

(d) Semivariogram of the electrical resistivity in transect D_T1

Fig. 7. Semivariograms of the electrical resistivity in transects A_T5, B_T1, C_T1 and D_T1. Figure represents the series of semivariograms in various depths (*Y*-axis). Each semivariogram was calculated separately for ca 1–2 cm thick slice of soil. The value of semivariance for every soil layer and the lag distance (*X*-axis) is represented by the colour scale. The lag distance is the spatial distance between pairs of datum points along each transect. The semivariance is shown in a logarithmic scale.

conductivity σ and between penetration resistance p_{pr} and electrical resistivity ρ shown in Figs. 5 and 6 exhibit visible trends. The Student's *t*-test of the linear regression slope and the intercept indicates that σ can serve as an explanatory variable for p_{pr} (and implicitly as a degree of compaction identifier). However, the intercept of the regression line differed from zero with a high level of significance. It may be in conflict with the physical meaning of this relationship. A zero p_{pr} is assumed to lead to zero σ when the porosity is equal to one. The inverse relation (Fig. 6) fulfills this assumption much better, since the asymptotic approach of ρ towards infinity at zero p_{pr} is observed. The relationship between p_{pr} and ρ is much stronger than has been suggested in the literature. In Basso et al. (2010), the correlation between p_{pr} and ρ was less significant; in Sudha et al. (2009) no correlation was shown; and in Naderi-Boldaji et al. (2014) the correlation was opposite to our findings and assumptions. However, different methods were used in the cited articles to assess the penetration resistance.

Electrical resistivity semivariograms provide evidence about the conformity or non-conformity of the soil layers. A decrease in semivariance in depth and distance indicates spatial uniformity of the subsoil. In Fig. 7a, c and d, a more gradual rise in semivariance along the distance emerges below the identified plough pan. This leads to the conclusion that the soil structure changes below a certain depth and becomes more homogeneous. Transect B_T1 in Fig. 7b, which was measured in a field that is more deeply plowed, exhibits a decrease in semivariance along the distance above the plough pan. Deeper plowing disturbed the compacted soil but keeps the soil relatively homogeneous. The decrease in the variability of the electrical resistivity was observed by Séger et al. (2009) with the use of 3D ERT, where the hemisphere effect is lower than for 2D measurements.

5. Conclusions

Measurements of electrical resistivity, mechanical penetration resistance and the physical properties of undisturbed soil samples were

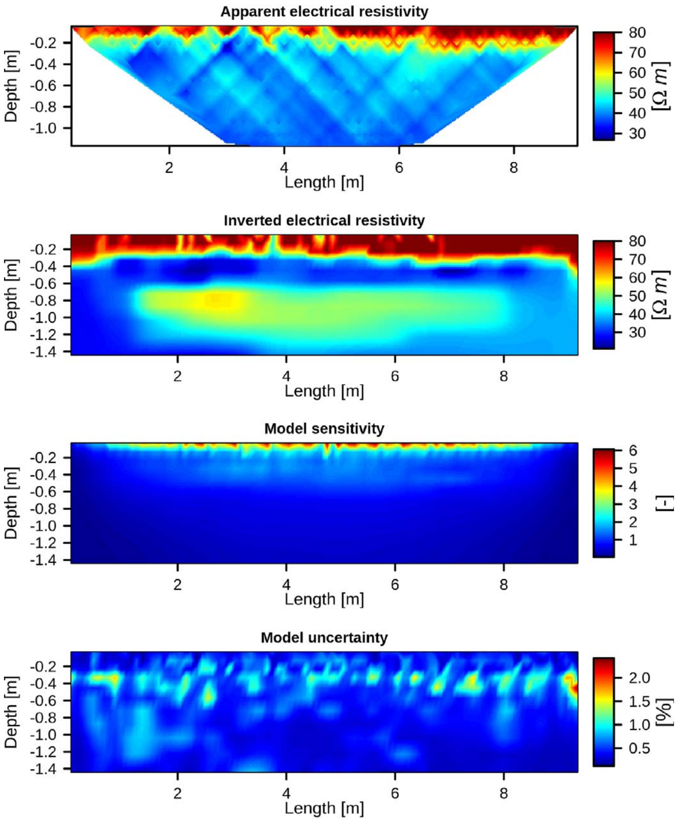

Fig. A.8. The results of the ERT transect A_T5; at the topmost panel are measured apparent electrical resistivities, at the second panel are depicted inverted electrical resistivities, at the third panel is the model sensitivity and at the bottommost panel is depicted the uncertainty of the model.

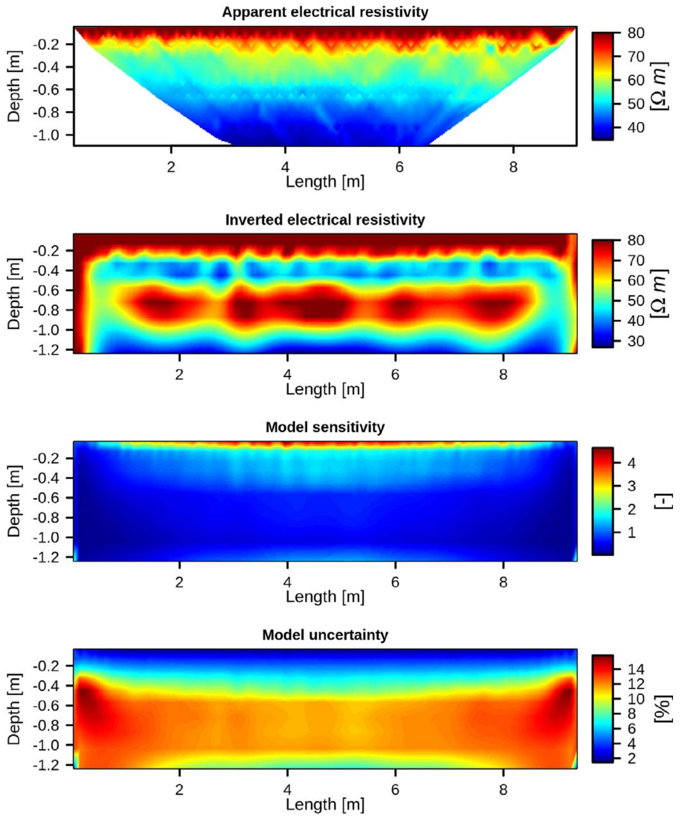

Fig. A.9. The results of the ERT transect B_T1; at the topmost panel are measured apparent electrical resistivities, at the second panel are depicted inverted electrical resistivities, at the third panel is the model sensitivity and at the bottommost panel is depicted the uncertainty of the model.

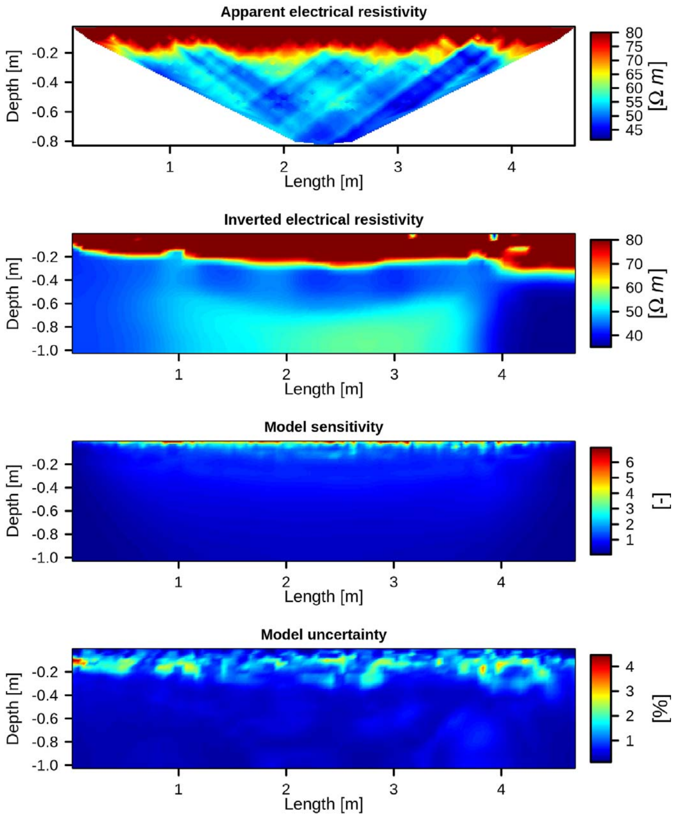

Fig. A.10. The results of the ERT transect C_T1; At the topmost panel are measured apparent electrical resistivities, at the second panel are depicted inverted electrical resistivities, at the third panel is the model sensitivity and at the bottommost panel is depicted the uncertainty of the model.

performed in order to assess the presence and the spatial uniformity of the plough pan along 10 transects in a small agricultural catchment in the central part of the Czech Republic. The measurements showed clearly that the plough pan is present in the soil profiles of the catchment in two distinctly tilled fields. According to the semivariance calculated from the electrical resistivity data, the plough pan exhibits a certain spatial variability, but the spatial variability of the topsoil is higher by one or two orders of magnitude. This leads to the conclusion that the plough pan is macroscopically uniform along the 2D transects.

We have demonstrated that the ERT technique is a useful tool for making a qualitative assessment of the spatial characteristics of the plough pan in cultivated fields. However, the success of this approach is dependent on the current saturation state of the soil, and on suitable electrode spacing according to the depth of the topsoil. Based on our findings, the water saturation should not be lower than field capacity. The electrode spacing is recommended to be approximately half of the expected depth of the plough pan. This is inhered from used ERT array.

Acknowledgements

The research presented here was performed within the framework of Czech Science Foundation postdoctoral project GP13-20388P, with support from a project supported by Czech Ministry of Agriculture grant no. QJ1230056, and with support from CTU internal project no. GS16/143/OHK1/2T/11.

Appendix A. ERT profiles

References

Ahuja, L., Fiedler, F., Dunn, G., Benjamin, J., Garrison, A., 1998. Changes in soil water retention curves due to tillage and natural reconsolidation. Soil Sci. Soc. Am. J. 62, 1228–1233.

Banerjee, S., Carlin, B.P., Gelfand, A.E., 2014. Hierarchical Modeling and Analysis for Spatial Data. CRC Press.

Basso, B., Amato, M., Bitella, G., Rossi, R., Kravchenko, A., Sartori, L., Carvahlo, L.M., Gomes, J., 2010. Two-dimensional spatial and temporal variation of soil physical properties in tillage systems using electrical resistivity tomography. Agron. J. 102, 440–449.

Bertolino, A.V., Fernandes, N.F., Miranda, J.P., Souza, A.P., Lopes, M.R., Palmieri, F., 2010. Effects of plough pan development on surface hydrology and on soil physical properties in southeastern Brazilian plateau. J. Hydrol. 393, 94–104.

Besson, A., Cousin, I., Samouëlian, A., Boizard, H., Richard, G., 2004. Structural heterogeneity of the soil tilled layer as characterized by 2d electrical resistivity surveying. Soil Tillage Res. 79, 239–249.

Besson, A., Sger, M., Giot, G., Cousin, I., 2013. Identifying the characteristic scales of soil structural recovery after compaction from three in-field methods of monitoring. Geoderma 204205, 130–139.

Boizard, H., Richard, G., Roger-Estrade, J., Dürr, C., Boiffin, J., 2002. Cumulative effects of cropping systems on the structure of the tilled layer in northern France. Soil Tillage Res. 64, 149–164.

Buvat, S., Thiesson, J., Michelin, J., Nicoullaud, B., Bourennane, H., Coquet, Y., Tabbagh, A., 2014. Multi-depth electrical resistivity survey for mapping soil units within two 3 ha plots. Geoderma 232234, 317–327.

Císlerová, M., Vogel, T., Simunek, J., 1990. Field-scale water and solute flux in soils. Birkhäuser Basel, Basel. The Infiltration-Outflow Experiment Used to Detect Flow Deviations. pp. 109–117.

Colombi, T., Braun, S., Keller, T., Walter, A., 2016. Artificial macropores attract crop roots and enhance plant productivity on compacted soils. Sci. Total Environ.

Coquet, Y., Coutadeur, C., Labat, C., Vachier, P., van Genuchten, M.T., Roger-Estrade, J., Šimåunek, J., 2005. Water and solute transport in a cultivated silt loam soil 1. Field observations. Vadose Zone J. 4, 573–586.

Dahlin, T., Loke, M., 1997. Quasi-3d resistivity imaging–mapping of three dimensional

structures using two dimensional dc resistivity techniques. 3rd EEGS Meeting.
Dörner, J., Horn, R., 2009. Direction-dependent behaviour of hydraulic and mechanical properties in structured soils under conventional and conservation tillage. Soil Tillage Res. 102, 225–232.
Fukue, M., Minato, T., Horibe, H., Taya, N., 1999. The micro-structures of clay given by resistivity measurements. Eng. Geol. 54, 43–53.
Furman, A., Ferré, T., Warrick, A., 2003. A sensitivity analysis of electrical resistivity tomography array types using analytical element modeling. Vadose Zone J. 2, 416–423.
Hadzick, Z., Guber, A., Pachepsky, Y., Hill, R., 2011. Pedotransfer functions in soil electrical resistivity estimation. Geoderma 164, 195–202.
Kim, H., Anderson, S., Motavalli, P., Gantzer, C., 2010. Compaction effects on soil macropore geometry and related parameters for an arable field. Geoderma 160, 244–251.
Kowalczyk, S., Maślakowski, M., Tucholka, P., 2014. Determination of the correlation between the electrical resistivity of non-cohesive soils and the degree of compaction. J. Appl. Geophys. 110, 43–50.
Lipiec, J., Horn, R., Pietrusiewicz, J., Siczek, A., 2012. Effects of soil compaction on root elongation and anatomy of different cereal plant species. Soil Tillage Res. 121, 74–81.
Loke, M., Chambers, J., Rucker, D., Kuras, O., Wilkinson, P., 2013. Recent developments in the direct-current geoelectrical imaging method. J. Appl. Geophys. 95, 135–156.
Loke, M.H., 2004. Tutorial: 2-D and 3-D Electrical Imaging Surveys.
Mazáč, O., Císlerová, M., Vogel, T., 1988. Application of geophysical methods in describing spatial variability of saturated hydraulic conductivity in the zone of aeration. J. Hydrol. 103, 117–126.
Naderi-Boldaji, M., Sharifi, A., Hemmat, A., Alimardani, R., Keller, T., 2014. Feasibility study on the potential of electrical conductivity sensor veris 3100 for field mapping of topsoil strength. Biosyst. Eng. 126, 1–11.
Nadler, A., 1991. Effect of soil structure on bulk soil electrical conductivity (ECa) using the TDR and 4P techniques. Soil Sci. 152, 199–203.
Pagliai, M., Marsili, A., Servadio, P., Vignozzi, N., Pellegrini, S., 2003. Changes in some physical properties of a clay soil in central Italy following the passage of rubber tracked and wheeled tractors of medium power. Soil Tillage Res. 73, 119–129.
Pagliai, M., Vignozzi, N., Pellegrini, S., 2004. Soil structure and the effect of management practices. Soil Tillage Res. 79, 131–143.
Revil, A., Karaoulis, M., Johnson, T., Kemna, A., 2012. Review: some low-frequency electrical methods for subsurface characterization and monitoring in hydrogeology. Hydrogeol. J. 20, 617–658.
Roulier, S., Angulo-Jaramillo, R., Bresson, L.M., Auzet, A.V., Gaudet, J.P., Bariac, T., 2002. Water transfer and mobile water content measurement in a cultivated crusted soil. Soil Sci. 167, 201–210.
Samouëlian, A., Cousin, I., Tabbagh, A., Bruand, A., Richard, G., 2005. Electrical resistivity survey in soil science: a review. Soil Tillage Res. 83, 173–193.
Séger, M., Cousin, I., Frison, A., Boizard, H., Richard, G., 2009. Characterisation of the structural heterogeneity of the soil tilled layer by using in situ 2D and 3D electrical resistivity measurements. Soil Tillage Res. 103, 387–398.
Séger, M., Guérin, R., Frison, A., Bourennane, H., Richard, G., Cousin, I., 2014. A 3d electrical resistivity tomography survey to characterise the structure of an albeluvic tonguing horizon composed of distinct elementary pedological volumes. Geoderma 219, 168–176.
Sněhota, M., Sobotková, M., Císlerová, M., 2008. Impact of the entrapped air on water flow and solute transport in heterogeneous soil: experimental set-up. J. Hydrol. Hydromech. 56, 247–256.
Sudha, K., Israil, M., Mittal, S., Rai, J., 2009. Soil characterization using electrical resistivity tomography and geotechnical investigations. J. Appl. Geophys. 67, 74–79.
Zumr, D., Dostál, T., Devaty, J., 2015. Identification of prevailing storm runoff generation mechanisms in an intensively cultivated catchment. J. Hydrol. Hydromech. 63, 246–254.

Soil surface connectivity of tilled soil with wheel tracks and its development under simulated rainfall

Jakub Jeřábek[a,]*, David Zumr[a], Tomáš Laburda[a], Josef Krása[a], Tomáš Dostál[a]

[a] Department of Landscape Water Conservation, Faculty of Civil Engineering, Czech Technical University in Prague, 16629 Prague, Czech Republic

* Corresponding author

e-mail: jakub.jerabek@fsv.cvut.cz

address: CTU in Prague, Faculty of Civil Engineering, The Department of Landscape Water Conservation, Thakurova 7, 166 29 Praha 6, Czech Republic

Abstract

Although wheel tracks cover only a small portion of the surface of agricultural fields, their effect on surface runoff and sediment transport is substantial. Wheel tracks change the microrelief of the soil surface, and influence how the surface is further altered by rainfall and runoff. This study presents a plot-scale microrelief analysis of a tilled surface with wheel tracks under simulated rainfall. Digital elevation models of the microrelief with 1 cm spatial resolution were obtained using the Structure from Motion method. The random roughness, the structural connectivity, and functional connectivity were calculated for before-rainfall and after-rainfall soil surface conditions. The experiments were carried out on inclined, freshly-tilled plots (8 m long, 2 m wide). The wheel tracks were created by four passages of machinery in the slope direction (SWT) and in the contour-line direction (CWT). The experiments were compared to reference plots without wheel tracks (NWT). The wheel tracks increase water and sediment connectivity if they are oriented in slope-wise direction. Microrelief analysis shows that SWT drains water from the surrounding soil. The soil surface adjacent to SWT can also become more connected with the wheel track, due to changes in microrelief introduced by rainfall and runoff. The calculated higher connectivity in the SWT plot corresponded to the measured increased sediment loads. This suggests faster overland flow and therefore shorter flow pathways on the soil surface microrelief. CWT leads to a decrease in the water and sediment connectivity compared to the NWT and SWT plots. Although the surface runoff can overflow the CWT, the network of flow paths results in decreased flow velocity and a slower sediment transport rate. However, the CWT effect is not permanent, and declines as the wheel tracks become silted with the deposited sediment. It is shown that detailed microrelief data provide relevant information for a study of the changes in flow routing in a tilled agricultural field with the presence of a wheel track. SWT accelerates the runoff and especially the sediment transport. During a rainfall event, the hydraulic connection between the wheel track and the surrounding soil increases dramatically. CWT reduces the surface runoff and also the sediment transport. In the long term, rainfall events and surface runoff alter the microrelief connectivity, causing the soil surface to be more hydraulically connected, irrespective of the wheel track orientation. This study demonstrates the effect of wheel tracks on water and sediment transport. The results draw attention to the importance of appropriate soil protection measures, as a bare unprotected surface microrelief exposed to rainfall leads to increased sediment connectivity.

Keyword: surface runoff, erosion, microrelief, connectivity, structure from motion, agricultural fields

1 INTRODUCTION

Surface runoff and sediment transport from arable land have a negative impact on soil quality (Boardman and Poesen, 2006), and this is nowadays the topic of international strategies such as the EU Soil Strategy for 2030 EC COM (2021) 699. Surface runoff and sediment transport also have negative off-site effects, such as damage to the infrastructure (Boardman et al., 2019), siltation of streams and water reservoirs (e.g. Krása et al., 2005), loss of nutrients from fields (e.g. Probst, 1985), and eutrophication of water bodies (e.g. Carpenter et al., 1998). Although water-driven nutrient transport can also occur in shallow groundwater flow (Outram et al., 2016) or sometimes via percolation through tile drainage systems (Deasy et al., 2008), surface runoff prevails in agricultural fields (e.g. Carpenter et al., 1998).

Direct wheel track compaction has been recognized as a cause of soil degradation, because compaction changes the physical and infiltration properties of soils (Lal 1999; Lindstrom et al. 1981). Topsoil saturated hydraulic conductivity may decrease up to fourfold int the upper soil horizon, mainly due to the decrease in macroporosity under direct compaction (e.g. Kim et al., 2010). The effect of compaction was observed mainly in the top 10 cm of the soil profile, where the proportion of elongated pores decreased rapidly (Pagliai et al., 2003). Compacted soil in wheel tracks also exhibits reduced near-saturated hydraulic conductivity due to the reduction in water-conducting pores (e.g. Ankeny et al., 1990; Seehusen et al., 2019; Pagliai et al., 2004; Daraghmeh et al., 2008). The decrease in porosity (and the increase in bulk density) is in fact an effect of rearrangements of the soil particles, which lead to an increased risk of runoff and erosion events.

GPS tracking shows that most parts of agricultural fields are crossed by a tractor at least once in the course of a single season, and some of the wheel tracks remain undisrupted on the soil surface until the harvest (Kroulík et al., 2011; Augustin et al., 2020). Wheel tracks act as preferential pathways for surface runoff and sediment transport, if they are oriented in the direction of the slope (Heathwaite et al., 2005; Silgram et al. 2010; Ryken et al. 2018), and they act as an obstacle if they are oriented in the contour-line direction (Heathwaite et al., 2005). Moreover, the flow direction introduced by the tillage exceeded the flow direction based on topography on 50% to 100% of the catchment area (Souchere et al. 1998; Takken et al. 2001; Couturier et al. 2013). Thus wheeltrack-induced compaction may affect runoff, sediment transport and therefore soil quality on the scale of whole parcels or fields.

Soil surface conditions (Leys et al., 2007) and soil surface microtopography are among key factors in the generation of surface runoff (e.g. Jester and Klik, 2005; Prosdocimi et al., 2017) The microtopography greatly influences runoff generation, since it affects whether and when the water from a local microrelief depression starts to contribute to runoff (Antoine et al., 2009). Due to the microtopography, the overland flow may become channeled, and may therefore gain higher velocity and initiate soil erosion (Chen et al., 2013; Gómez and Nearing, 2005). Infiltration is also affected by microtopography. Soil sealing in a microrelief depression may reduce infiltration, while higher soil water content may increase infiltration (Thompson et al., 2010).

Surface roughness is often used to characterize the conditions of the soil surface (Taconet and Ciarletti, 2008; Croft et al., 2013; Moreno et al., 2008; Luo et al., 2018). Surface roughness has been investigated to estimate surface depression storage (Onstad, 1984), to partition rainfall water into infiltration and surface runoff (Zhao et al., 2018), and to estimate runoff and sediment flow rates (Luo et al., 2018). The initial roughness affects the runoff and the development of rill flow (Gómez and Nearing, 2005). In addition, temporal changes in surface roughness have been observed due to the impact of raindrops (Zobeck and Onstad, 1987; Bauer et al., 2015), surface runoff (Zobeck and Onstad, 1987), or during infiltration (Onstad et al., 1984). Random roughness (RR) decreases in wheel tracks, but this effect is diminished when no-till management systems are used (Lindstorm et al., 1981).

The principle of hydrological connectivity is often used to explore the linkages of various water pools within the landscape (Pringle, 2003; Bracken et al., 2013). Hydrological connectivity can be divided into concepts of structural (topography-based) connectivity and functional (process-based) connectivity (Bracken et al., 2013), which have been utilized in several studies (Antoine et al., 2009; Angermann et al., 2017; Jackisch et al., 2017; Rinderer et al., 2018).

Structural connectivity was developed from DEM-based topographic indices. Some of the most popular indices are the topography-wetness index (Beven and Kirkby, 1979) and modifications to it (Stieglitz et al., 2003, Hjerdt et al., 2004). A combination of indices can also be used to identify the spill and fill runoff behavior on hillslopes (Hopp and McDonnell, 2009). Furthermore, the index of connectivity (IC) was developed to assess the connectivity of water flow and sediment within a landscape (Borselli et al., 2008). Although IC was initially created with a focus on steep Alpine valleys and alluvial fans, it has been successfully used to identify sediment source areas at submeter scales with a Digital Elevation Model (DEM) of 1 cm resolution (e.g. Prosdocimi et al., 2017).

Small-scale functional connectivity is often studied through observations of the temporal changes in the inter-(dis)connection between soil surface depressions (Darboux et al., 2002a, 2002b; Antoine et al., 2009) or roughness organization (Smith, 2014). Antoine et al. (2009) introduced the relative surface connection function (RSCf), which was a metric of surface depression connectivity. RSCf was then used in other studies to observe surface runoff connectivity (Antoine et al., 2011; Yang and Chu, 2013; Peñuela et al., 2016; Appels et al., 2011; Appels et al., 2016). RSCf expresses how much runoff is generated for a given fullness of the surface depressions storage (SDS), and therefore how well the surface depressions are hydraulically connected at each moment. In practical terms, the connectivity is assessed with a curve function relating the surface runoff and the actual filled surface depression storage. The gradient of the curve expresses how quickly the surface depressions are being connected and surface runoff is being generated. A large gradient indicates threshold behavior - the abrupt connection of a major surface storage to the outlet. A low gradient indicates a more complex surface, where e.g. multiple surface depressions need to be filled and connected with each other to produce runoff. A horizontal shift of the curve indicates an increase (or a decrease) in the surface depression storage during the experiment. According to Peñuela et al. (2016), the soil surface changes during a rainfall event and the subsequent response of the surface runoff are well explained by RSCf. Moreover, RSCf can be used to improve the simple stepwise surface retention parameter of large-scale hydrological models, as the runoff is usually observed before all depressions get filled (Antoine et al., 2009; Antoine et al., 2011; Peñuela et al., 2016).

As has been shown above, a vast amount of research has been done on analyzing the microrelief in terms of roughness or connectivity. However, there is a lack of studies on combinations of macro-features and micro-features, e.g. wheel tracks and the soil surface microrelief. In this study, we present a microrelief analysis of soil surfaces with the presence of wheel tracks, and we relate the analysis to direct measurements of the surface runoff and the sediment transport during a rainfall simulation. The goal is to better understand the dynamics of the initiation of surface runoff, soil erosion and rainfall-runoff-induced surface changes on a bare tilled soil. The Structure from Motion (SfM) photogrammetric method was used to capture the soil surface changes caused by rainfall and by surface runoff (Westoby et al., 2012), and to calculate the connectivity indices (Prosdocimi et al., 2017; Wolstenholme et al., 2020).

The specific objectives of our investigation are (1) to assess the changes in microtopography caused by a wheel track, and by rainfall and surface runoff, utilizing high-resolution microrelief DEMs and several indicators (surface roughness, structural and functional connectivity), and (2) to confront the observed changes in microrelief with the measured surface runoff and sediment transport on the plot scale.

2 MATERIALS AND METHODS

A series of artificial rainfall experiments were performed to study the effect of the presence and the orientation of wheel tracks on surface runoff and sediment transport. In general, we utilized two approaches: direct monitoring of surface runoff and sediment transport, and microrelief analysis utilizing random roughness and two connectivity indicators. In total, five experiments were performed in two independent experimental campaigns. The first experimental campaign was undertaken in September 2018 (referred to as campaign No. 1), and the second was undertaken in June 2019 (referred to as campaign No. 2). Two wheel-track orientations were examined: slope-wise direction (SWT) and contour-line direction (CWT). The experimental setup was complemented by reference experiments on plots with no wheel tracks (NWT), as shown in Figure 1.

2.1 LOCATION

The experiments were carried out on experimental plots located on an agricultural site ca 30 km to the north-west of Prague, Czech Republic, at coordinates 50°13'2.0"N, 14°1'2.2"E (Figure 1). The site is at an elevation of 310 – 315 m a.s.l. The annual mean temperature is 8°C, and the mean annual precipitation is 500 mm. The climate is characterized as humid continental. The site is located at the edge of larger fields, on which winter wheat and rapeseed were planted in both experimental years. The topsoil is classified as loam with 18.3% of clay, 33.8% of silt and 47.9% of sand. The soils are developed on sedimentary rocks consisting of claystone, sandstone and arkose, and are classified as Cambisols according to the World Reference Base for Soil Resources. The content of organic matter is in the range of 1.2 – 1.5 % in the topsoil.

2.2 EXPERIMENTAL PLOTS

All experimental plots had an inclination of approximately 10%, and were 8 m long and 2 m wide. The size of the plot was adopted from Kavka et al. (2018); the length of the plot is long enough to study the erosion process while preserving uniform rainfall distribution along the plot. the Each experimental plot was delineated by metal plates inserted ca 5 cm into the soil. The seedbed was prepared and the wheel tracks were created several days before the experiments. For both campaigns, no precipitation was recorded between the preparation of the topsoil and the experiments,.

2.2.1 **Campaign No. 1**

Campaign No. 1 was conducted on September 18th and 19th, 2018. The soil was stubble tilled to a depth of 12 - 15 cm using a stubble cultivator one day before the experiment (September 17th). The wheel tracks were created directly after cultivation by four passages of a New Holland T7.185 tractor and a trailed cultivator (in non-operational state; with two axles) driving in the uphill direction in the case of the SWT plot (Figure 1). Four passages were chosen in order to produce a representative wheel rut, without making an unrealistic number of passages. It has been shown that most compaction changes occur within the first 4 – 5 passages (Botta et al., 2009). The pressure in the tires of the tractor was 1.4 bar (front wheels) and 2.0 bar (rear wheels). The tire pressure of the stubble cultivator was 3.5 bar. The total weight of the machinery was 8.5 t (6 t for the tractor and 2.5 t for the stubble cultivator). The axle loads of the tractor were 2.8 t on the front axle and 3.2 t on the rear axle. The axle load of the stubble cultivator was 1.25 t. The maximum static ground pressure of a single tire was estimated using the *soilphysics* R package (de Lima et al., 2021) to be 201 kPa for the front axle of the tractor and 272 kPa for the rear axle, and 439 kPa for the stubble cultivator. The initial topsoil water conditions were very dry, with a volumetric water content of 0.10 ± 0.01 $cm^3\ cm^{-3}$. The topsoil bulk density was 1.31±0.09 $g\ cm^{-3}$. The topsoil bulk density of the soil in the wheel track was 1.40±0.1 $g\ cm^{-3}$. The mean wheel rut depth was 3.9±0.9 cm. During campaign No. 1 only the slope-wise WT was set.

2.2.2 **Campaign No. 2**

Experimental campaign No. 2 was conducted between July 18th and 20th, 2019. The vegetation cover (mainly *Atriplex, Galium Aparine* and common grasses) that had grown on the experimental plot location during the vegetation season was mulched on June 14th, 2019. Dry vegetation residues were manually removed from the soil surface. One day before the experiment, the topsoil was stubble tilled to a depth of 12 – 15 cm. The wheel tracks were prepared after stubble tillage with a New Holland T8040 tractor and a full 12 m^3 water tank trailer (with 4 wheels) driving 4 times in downhill direction (Figure 1). The tire pressure of the tractor was 1.4 bar (front wheels) and 1.6 bar (rear wheels). The pressure of each water tanker tire was 3.5 bar. The total weight of the machinery was about 22 t (8 t for New Holland T8040, 2 t for the water tank, and 12 t for the water). The axle load of the tractor was 3.8 t for the front axle and 4.2 t for the rear axle. The axle load of the water tank was approximately 7 t. The maximum static single tire ground pressure was estimated to be 206 kPa for the front wheels of the tractor, 236 kPa for the rear wheels of the tractor, and 455 kPa for the wheels of the water tank (also using the soil physics R package (de Lima et al., 2021)). The initial soil water conditions were very dry, with a volumetric water content around 0.13±0.02 $cm^3\ cm^{-3}$. The topsoil bulk density was 1.19±0.37 $g\ cm^{-3}$. The topsoil bulk density of the soil in the wheel track was 1.35±0.03 $g\ cm^{-3}$. The mean wheel rut depth at the SWT plot was 3.5±1.9 cm. Both slope direction and contour-line direction wheel tracks were set up for campaign No. 2.

2.3 SURFACE MICROTOPOGRAPHY OBSERVATION

The soil surface morphology was monitored by means of the Structure from Motion close-range photogrammetry method. Images for photogrammetry were taken before and after each experiment, using a Sony A6000 mirrorless camera with an APS-C size sensor with resolution of 24 Mpx and equipped with a standard Sony 16-50 mm zoom lens fixed on 16 mm. Each measurement consisted of approximately 40 – 60 images taken in two rows from a distance of 1.5 m.

Photogrammetry reference targets were installed on the perimeter of each plot at a mutual distance of 1 to 2 meters. The targets were inserted into the soil with 15 cm long screws, which held the targets in a steady position during the experiment. A small number of targets were also attached to the collection flume. The GPS positions of all targets were measured with vertical and horizontal accuracy of 15 mm. Images with geo-referenced targets were processed in Agisoft Photoscan Professional 1.4.2 build 6205 (Agisoft LLC). The output was an orthophoto and a digital elevation model (DEM) of the surface with a 1 mm ground sampling distance. 10 mm spatial resolution in x and y direction was used for all analyses. This resolution was optimized in order to maintain high detail in the analysis while providing reasonably low noise in the data and reasonable time for computation.

The DEMs were rotated to reorient the plots into the north direction in order to simplify further image processing (the coordinates are shown in Figure 1). The installed sensors, which partially covered the soil surface, were clipped off the images and the missing areas were linearly interpolated in the south-north direction. The raster cells on the sides of the plots were raised by 0.2 m to form a boundary for the drainage area, which was in reality maintained by metal sheets during the experiment. The raster was further resampled to 10 mm spatial resolution in order to reduce the noise of the initial point clouds and to decrease the size of the data for further processing and computation.

2.4 RAINFALL SIMULATION

Artificial rainfall with intensity of 27.4 ± 7.8 mm h^{-1} (measured with multiple totalizators throughout the simulation) and mean rainfall kinetic energy of 127 J m^{-2} h^{-1} (measured on site with a disdrometer) was set for all experiments. The target value of the rainfall was 30 mm h^{-1}, which is the 5-year return period rainfall at the location (Kašpar et al., 2021). The duration of the experiments varied between 290 minutes and 433 minutes. Funnels were installed at the bottom of each experimental plot to collect the surface runoff and sediment. For a detailed description of the simulator, see Kavka et al. (2018). On the SWT plots, two flumes were installed in order to separate the water flowing through the wheel track and the water flowing from the adjacent tilled soil surface (Figure 1). The runoff sampling interval was prolonged during the experiment, starting at 2.5 minutes and reaching 20 minutes when the runoff was approaching a steady state.

2.5 MICRORELIEF ANALYSIS

Roughness. The random roughness RR was calculated from the before- and after-rainfall DEMs for each plot. In addition, the wheel tracks and the adjacent tilled soil surface were analyzed separately for the SWT and CWT plots. The RR calculation was adopted according to Taconet and Ciarletti (2008).

The DEMs were leveled in order to exclude the plot slope from the RR calculation. Subsequently, RR was calculated as the standard deviation of the leveled pixel elevations:

$$RR = \sqrt{\frac{1}{(n-1)(m-1)} \sum_i^n \sum_j^m (Z_{i,j} - \bar{Z})^2} \quad (1)$$

where Z stands for detrended surface elevation and $\overline{Z}$ stands for the mean of the detrended surface elevation, *n* and *m* stand for the number of rows and columns in the rotated raster.

Structural connectivity analysis. The normalized downslope distance (NDD) was used to assess the structural connectivity. Our approach was inspired by the index of connectivity (Borselli et al., 2008), where the downslope distance is a part of the algorithm. The downslope distance algorithm provided by the TauDEM terrain analysis tool (Tarboton, 2013) was used to perform the analysis. As a result of the algorithm, a raster was created in which each cell contains a flow path length L_d to the bottom of the plot. At this stage, the downslope distance is dependent on the organization of the surface topography and the position of a given cell along the slope. To compensate the cell position along the plot, we normalized the pathway length L_d by the shortest length to the bottom of the plot L_s, as is shown in Figure 2. NDD is therefore calculated as

$$NDD = \frac{L_d}{L_s}. \quad (4)$$

The NDD expresses the bulk complexity of the surface topography from the perspective of the moving particle the trajectory of which is being tracked.

Functional connectivity analysis. Functional connectivity refers to a concept presented by Darboux et al. (2002b) and by Antoine et al. (2009), where a surface runoff model is used to assess the connectivity. For this task, we utilized the SMODERP2D[1] physically-based episodic distributed

---

[1] The model is provided in the public repository at the github online platform (github.com/storm-fsv-cvut/smoderp2d or on the web of the Department of Landscape Water Conservation, Faculty of Civil Engineering, CTU Prague (storm.fsv.cvut.cz/.../smoderp).

hydrological model (Dostál et al., 2000; Landa et al., 2019; Kavka et al., 2022). The results of the model were interpreted as the relationship between the runoff coefficient and the soil surface depressions storage. The interpretation of this relationship is shown in Figure 3.

The initial surface depression storage is calculated by subtracting sink-less[2] DEM from the original DEM. Sink-less DEM is calculated with the Fill tool of the spatial analysis extension of ESRI ArcMap 10.7 software. It was assumed that the plots have uniform soil hydraulic properties over the plot, which does not change in time. All plots were modeled with uniform rainfall intensity, which corresponded to the rainfall intensity used during the rainfall experiments. A more detailed description of the model and its infiltration and flow routing parameters is provided in Appendix Table 1.

2.6 LABORATORY ANALYSIS

The undisturbed soil samples were gravimetrically analyzed to obtain the initial soil water content and the bulk density. The sediment concentration in the runoff was obtained by filtering the sampled water. The paper filters with the trapped soil were oven-dried at 105°C to obtain the mass of the eroded soil.

2.7 STATISTICAL ANALYSIS

The significance of the wheel-track effect on surface runoff and sediment transport was analyzed using the Student t-test. In particular, the non-zero difference among the plots was tested. The test was performed with R software (R core team, 2018).

---

[2] Sinks in DEM are cells surrounded by cells with higher elevation. The sink-less DEM is a raster where such cells are artificially removed.

3 RESULTS

3.1 RANDOM ROUGHNESS

Random roughness (RR) is shown in Figure 4A for all experimental plots for before- and after-rainfall soil surface conditions. The RR of all the plots varies between 0.015 m and 0.045 m. The RR was larger in campaign No. 2 than in campaign No. 1 for all plots. A decline in roughness after rainfall was observed for all experiments, although the decrease in RR at the NWT plot in campaign No. 1 was only minor. The most pronounced drop in RR was observed for the NWT plot in campaign No. 1. The CWT plot exhibited the largest RR.

Figure 4B shows the random roughness RR in the wheel track (in-WT) and of the surrounding soil (out-WT) for the SWT plot. Similarly, in Figure 4A, the roughness decreased in all cases after the rainfall. The RR in Figure 4B shows a more pronounced decrease in campaign No. 1, especially in WT. Although a larger decrease was recorded, the overall roughness was lower in campaign No. 2. The decrease in RR was more pronounced between the campaigns than between the in-WT and the out-WT.

3.2 STRUCTURAL CONNECTIVITY

Histograms of the normalized downslope distance NDD with the before-rainfall and after-rainfall soil surface conditions, and the flow accumulation raster, are shown in Figure 5. NDD was used to assess the tortuosity of the downslope pathway, which serves as a measure of the structural connectivity. The flow accumulation rasters are displayed in order to diagnose the shifts in the NDD histograms.

The before-rainfall soil surface conditions of the CWT exhibited the highest NDD pixel count in the interval of 1.5 – 1.6. On the NTW plots, the highest NDD pixel count was observed in the interval 1.3 – 1.5 (Figure 5AC) plot during both campaigns. The SWT plots exhibited bimodal NDD distribution before the rainfall (Figure 5BD). The first peak in the pixel count of the histogram lay in the NDD interval of 1.1 - 1.2 for the first campaign and in the interval of 1.2 – 1.3 for the second campaign. The second peak was observed in the NDD intervals of 1.5 – 1.7 and 1.5 – 1.6 during the first and second campaigns.

The NDD pixel count increased in the interval 1.4 – 2 while it decreased in intervals 1-1.4 at the CWT plot after rainfall. After rainfall, the NWT plots exhibited an increase in the NDD pixel count, especially in intervals 1.5 – 1.6 and 1.4 – 1.6 for campaigns No. 1 and No. 2, respectively. The NDD pixel count showed a different change at the SWT plots during each campaign (Figure 5BD). The after-rainfall two-peak histogram became a single peak histogram due to the higher NDD values in intervals 1.3 – 1.5 and 1.7 – 2.0 during campaign No. 1. However, two peaks in the NDD histogram were preserved after the rainfall during campaign No. 2 - although the first peak shifted into the NDD interval 1.3 – 1.4.

The flow accumulation showed the main pathways and their complexity (Figure 5). Two peaks of the before-rainfall NDD histogram at the SWT No. 2 plot clearly correspond to two main flow pathways identified in the flow accumulation raster; one in wheel tracks and one in the surrounding soil surface (Figure 5B). The same situation applied for the SWT plot for the before-rainfall conditions, as shown in Figure 5D. The flow accumulation in campaign No. 1 showed that the flow paths were diverted from the tilled surface into the wheel track, which corresponds to a shift from unimodal to bimodal distribution in the NDD histograms. Two main flow paths were preserved in the after-rainfall conditions in campaign No. 2, which again corresponded to bimodal NDD after-rainfall distribution. The NDD changes in the NWT plot could not be explained by a visual inspection of the flow accumulation raster. On the CWT plot (Figure 5E), a change in the flow path can be observed in the lower right corner, which was disconnected from the upper right corner of the plot after the rainfall and was shifted to the left part of the plot.

3.3 FUNCTIONAL CONNECTIVITY

The functional connectivity for before-rainfall and after-rainfall surface conditions is shown in Figure 4. CWT plot No. 2 exhibited the largest storage capacity for the before-rainfall conditions (Figure 4A), and SWT exhibited the lowest storage capacity during both campaigns (Figure 4AB). NWT exhibited almost identical curves for the before-rainfall conditions during both campaigns (Figure 4A), however the curves deviated from each other for the after-rainfall conditions. The depression storage capacity was smaller for the after-rainfall conditions than for the before-rainfall conditions, with the exception of reference plot NWT in campaign No. 1, where the storage capacities remained very similar.

For the before-rainfall conditions, the SWT plots of both campaigns and NWT plot No. 2 exhibited a sharp increase in the runoff coefficient when a certain threshold was reached (Figure 4A). For NWT plot No. 1 and NWT plot No. 2, this increase occurred later, when more of the surface depression storage (SDS) was filled. This effect was most pronounced for the CWT plot, where the runoff coefficient increased more gradually while the SDS was being filled.

Threshold behavior was observed to some extent in all the experiments. Only a small portion of SDS had to be filled before runoff was initiated on the SWT plots in both before- and after-rainfall surface conditions. Up to 0.2 mm of SDS had to be filled at the NWT plots before the rainfall soil surface conditions initiated runoff. Interestingly, the CWT plot started to contribute to runoff for smaller filled SDS than the NWT plots for before-rainfall soil surface conditions (Figure 4A), but the increase in runoff was more gradual on the CWT plot, as described above.

3.4 RUNOFF AND SEDIMENT TRANSPORT

A summary of the direct measurements of surface runoff and sediment transport is shown in Table 1. The duration of the experiments differed, and therefore the total rainfall depth and the total rainfall kinetic also differed. The largest rainfall amount was received by SWT plot No. 2, and the smallest rainfall amount was received by SWT plot No. 1. During campaign No. 1, surface runoff from the SWT plot occurred only in the wheel track, while the surrounding tilled soil exhibited no runoff at the bottom of the plot. The surface runoff from the SWT plot during campaign No. 2 was drained through both parts of the plot – the wheel track and the surrounding tilled surface. However, the runoff from the surrounding tilled surface exhibited a much longer time lag (102 minutes), an almost 7.5 times lower cumulative runoff, and a 31.3 times lower total soil loss compared to the wheel track (see Table 1). No evidence of rill erosion was observed.

The runoff and the sediment flow development differed among the wheel track variants, as shown in Figure 7 and Table 2A. Neither the surface runoff nor the sediment flow rate reached steady rates during the experiments. Similar values were reached on the SWT plots and on the NWT plot of the second campaign; however, the time lag was different (Figure 7A). The NWT plots during campaign No. 2 exhibited significantly higher surface runoff when the lag time was excluded from the analysis (Table 2). NWT plot No. 1 exhibited similar behavior as the CWT plot in campaign No. 2, apart from the runoff time lag.

The sediment flow rate (Figure 7B) varied during the experiments. The SWT plots exhibited significantly greater sediment flow rates than the other plots, with the peak at about one third of the duration of the experiment (Table 2B). The rising limb of the sediment mass plot increased more gradually during campaign No. 1 than during campaign No. 2. The sediment flow rate on the NWT plots exhibited similar behavior during both campaigns, with the exception of the time lag. The sediment flow rate was significantly higher during campaign No. 1 (Table 2B). The curves of the sediment flow rate on both NWT plots were generally flat, which contrasts with the surface runoff, where the rate increased throughout the experiment. The CWT plot showed the smallest surface runoff (Table 2A) and the slowest increase in surface runoff (Figure 7A). The surface runoff increased throughout the experiment, while the sediment flow stabilized at a constant value (Figure 7B). All experiments where the sediment flow reached a quasi-steady value exhibited a decrease in the concentration of the suspended sediment, see Figure 7C.

4 DISCUSSION

4.1 EFFECT OF THE WHEEL TRACK ON CONNECTIVITY

The presence of a wheel track can be recognized by the structural connectivity. The greatest structural connectivity was observed on both SWT plots, while the lowest structural connectivity was observed on the CWT plot. The reference NWT plot exhibited medium values of structural connectivity. These findings indicate more prolonged paths of water and sediment on the CWT plot than on the NWT and SWT plots. As a consequence, water moves more slowly along the plot. This results in a decreased erosion rate. The two peaks of NDD in the SWT plots indicate that the higher connectivity is caused solely by the wheel track.

While structural connectivity expresses the connectivity among individual surface micro-depressions, functional connectivity indicates the connectivity between the soil surface and the outlet. As expected, functional connectivity showed that the SWT plots exhibited the highest connectivity, while the CWT plots exhibited the lowest connectivity. According to Antoine et al. (2009) the functional connectivity distinguished well between the microrelief composed of isolated craters and the microrelief composed of well-connected “valleys”. This suggests that the CWT surface contains more distinct depressions than the NWT and SWT plots. The SWT plot, on the other hand, consists of better-connected pathways. Ultimately, the soil flattened by the wheel tracks (the tire patterns are smaller than the roughness of the surrounding soil) creates well-connected pathways and therefore increases the connectivity.

In all cases in our study, the tillage was in the direction of the contour lines . In the case of the SWT plot, this created an unusual situation of contour tillage and slope wheel tracks, which however can occur with conventional soil tillage technology or on headlands (Kroulík et al., 2011). The number of passages affects the depth of the wheel rut. It has been shown that the first few passages have the most significant effect, and that the wheel rut depth becomes less reduced after 5 passages (Botta et al., 2009). Also, the soil moisture conditions while for all the passages play a significant role. However, due to the low soil water content at the beginning of both campaigns we would not expect substantial deepening of the wheel track if more passages were performed. The shape and the pattern of the surface depressions would also vary for different tillage types (Tarolli et al., 2019).

4.2 IMPACT OF RAINFALL AND RUNOFF ON CONNECTIVITY

The surface runoff evolution mechanism is shown in Figure 8. The surface runoff was formed by consecutive filling and spilling of water from the surface depressions. Once water reaches the wheel track it cannot return to the surrounding soil, and is preferentially transported downwards on the SWT plot. This contrasts with the CWT orientation, which acts as a large surface depression that releases runoff only when full. During runoff, the soil surface depressions gradually become filled with the mobilized sediment. This was observed during the experiment, and is also indicated by the decrease in RR and by the changes in soil surface storage after rainfall. This kind of behavior has been reported in the literature (Zobeck and Onstad, 1987; Withers et al., 2006; Peñuela et al., 2016).

When a surface depression is overtopped, a small neck is eroded at the boundary of the depression, accelerating both the runoff and the sediment transport. In the experiment, no rill flow developed (similarly to Helming et al., 1998). Small necks acted as short bypasses connecting the depressions with each other and with the wheel track. Although this effect was clear during the experiment, it could only be observed qualitatively in the flow accumulation raster on the CWT plots, where several flow paths from the wheel tracks emerged after rainfall (Figure 5).

The random roughness decreased due to the mechanical impact of the rain drops and the subsequent consolidation of the surface, which flattened the ridges formed by the tillage (Bauer et al., 2015; Zobeck and Onstad, 1987; Laburda et al., 2021). It has been shown in the literature that the surface roughness decreases exponentially with increasing rainfall amount or with rainfall kinetic energy (Zobeck and Onstad, 1987). This exponential relationship was shown to be consistent among multiple tillage systems (Guzha, 2004). However, simulated rainfall usually has an unnatural raindrop distribution, and the relation between random roughness and kinetic energy may therefore be altered. In this study, the same rainfall intensity and the same rainfall simulator – and therefore the same drop size distribution - was used. Only the rainfall depth (and the kinetic energy) differed among individual experiments. However, the extent to which the RR decreased did not coincide with the total rainfall depth.

The surface runoff also detached soil particles from ridges, and some of the particles later settled into the surface depressions. This led to decreasing surface roughness (Figure 4) and to decreasing depression storage capacity (Figure 6). Smoothing of the surface is clearly visible during all experiments, irrespective of the presence or the orientation of the wheel track. The roughness also decreased in the wheel track (Figure 4), which confirms that there are both soil erosion and soil deposition in the compacted wheel tracks, as has also been reported by (Basher and Ross, 2001). This suggests that the wheel tracks also contribute to the overall changes in connectivity. Soil swelling may also affect the surface changes. However, it is hard to distinguish between soil swelling and consolidation, even if high temporal resolution microrelief data are available (Eltner et al., 2017).

After the rainfall, the structural connectivity decreased at all plots. This non-intuitive surface development was most pronounced on the CWT plot (Figure 5E). The before-rainfall soil surface structures created only by tillage and by the passage of the tractor exhibited clear flow paths oriented downslope (arrows in Figure 5E). The impact of rainfall and runoff may create new flow paths via soil erosion, causing the water pathways to increase in length. The structural connectivity provides valuable information when observing surface changes within the plot. This was most visible on the SWT plots, where the flux between wheel track and surrounding soil was identified. Even when the wheel track is initially disconnected from the surrounding soil, the rainfall and runoff may form a connection. In this study, this happened in one of the SWT scenarios. This contrasting behavior may have been caused by the different tire tread for campaigns 1 and 2, since the passage of the tractor was in opposite directions and was followed by the trailed cultivator. The rainfall depth was higher during campaign No. 2 (when the two flow paths remained unchanged), and the wheel rut was slightly shallower during the second campaign. Two reasons can be put forward for the different outcome possibly affecting the NDD: (i) the different tire tread pattern, and (ii) the different lowering of the wheel track below the surrounding soil surface. Both of these effects potentially made the runoff more prone to create flow paths towards the wheel tracks (as seen in Figure 5B). These flow paths influenced the reorganization of the soil surrounding the wheel tracks.

An increase in connectivity and a decrease in soil surface storage capacity was observed in the functional connectivity for all plots. The surface storage capacity was observed to decrease after successive rainfall events, as has also been shown by Darboux et al. (2002a). However, the decrease in surface storage capacity cannot alone explain the increase in connectivity. A crucial factor is the spatial organization and the connectivity of the depressions. Similar trends were also observed by Peñuela et al. (2016) under natural rainfall. The storage depression capacity decreased rapidly after rainfall started, whereas the shift in the connectivity threshold first rose and then in some cases decreased (Peñuela et al., 2016).

The role of a wheel track in increased functional connectivity (unlike in the case of structural connectivity) is not shown explicitly. SWT plot No. 1 exhibited higher functional connectivity than SWT plot No. 2 in both before-rainfall and after-rainfall soil surface conditions. However, a connection between the wheel track and the surrounding soil may not always be created, even after a substantial rainfall.

4.3 COMPARISON BETWEEN CONNECTIVITY INDICES AND DIRECT MEASUREMENTS

The direct measurements of runoff and sediment flow were in agreement with both functional connectivity and structural connectivity. Both the runoff amount and the sediment transport followed the order SWT > NWT > CWT. Differences between the plots were more pronounced when comparing the sediment fluxes than when comparing the runoff. This is most likely caused by the flow velocity in the wheel track, which increased the carrying capacity of the water. Wheel-track compaction in the direction of the slope increased the runoff coefficient and the sediment transport across all studied tillage systems, Ryken et al. (2018). The direction of a passing tractor (upslope or downslope) and of course the initial moisture conditions alter the surface runoff and the transport of sediments (Withers et al., 2006). An accumulation of eroded soil was observed in wider wheel tracks, while narrower wheel tracks exhibited greater transport capacity due to the acceleration of the surface runoff (Eltner et al., 2017). This indicates the importance of the flow velocity.

The same behavior (SWT > NWT > CWT order in surface runoff and sediment transport) was observed with structural and functional surface connectivity for the before-rainfall soil surface conditions.

The structural connectivity agreed in terms of the connection of the wheel track and the surrounding soil, as shown on the SWT plot (Figure 5BD). The bi-modal to uni-modal shift of the NDD distribution corresponded to the SWT measurement, where runoff and sediment transport only occurred in the wheel track (Table 1). The NDD distribution during campaign No. 2 remained bimodal for before-rainfall and after-rainfall soil surface conditions. This corresponded to the direct measurements, where the runoff was active on both halves of the plot. No effect of different tire treads could be observed in the functional connectivity analysis.

The SWC and NWT plots exhibited similar maximum runoff in direct monitoring, and also similar functional connectivity during campaign No. 2 (Figures 6 and 7). The NWT in campaign No. 2 even exhibited significantly higher runoff compared to all other plots if the lag time was not taken into consideration in the analysis (Table 2). This was caused by the rapid increase in runoff after it started – after some time, the runoff reached values similar to those on both SWT plots (Figure 7). This increase may have been caused by the sudden connection of a few larger puddles to the outlet. The effect of the prolonged time lag in the NWT plot was not shown by functional connectivity. However, the largest time lag observed in the NWT plot during campaign No. 1 was well reproduced for the after-rainfall situation, in agreement with functional connectivity. The largest sediment flow rate occurred during campaign No. 2, but it was not reproduced by functional connectivity. However, functional connectivity was based on the model where erosion was not implemented, and correspondence with the sediment transport was therefore not to be expected.

4.4 COMPARISON OF STRUCTURAL AND FUNCTIONAL CONNECTIVITY METRICS

Structural connectivity allows the soil surface to be observed in greater detail. This index was able to identify multiple major flow paths which reached the bottom of the plot (via identification of uni-modal or bimodal distribution). Structural connectivity in combination with the flow accumulation algorithm was able to assess which part of the plot was connected to /disconnected from the drainage flow paths – i.e. the inter-plot connectivity. In contrast to the functional connectivity, the structural connectivity did not incorporate soil surface depressions in the analysis, since sink-less REM was used to generate the data. Functional connectivity takes the dynamics of the processes into consideration. The changes in surface depression storage can therefore be incorporated. Although the functional connectivity used in this study does not require physically-based derivation of the parameters or any calibration or validation procedure, additional information about soil properties and rainfall data are needed in order to derive the functional connectivity. In addition, it is much more time demanding to run an overland flow model in 10 mm raster resolution than to compute the structural connectivity.

5 CONCLUSION

Surface runoff, sediment transport and hydrological connectivity have been analyzed on freshly-tilled topsoil with wheel tracks by means of microrelief DEM indices. Two wheel-track orientations were studied: slope-wise direction (SWT) and contour lines-wise direction (CWT). The experimental setup was supplemented by a reference plot with no wheel track (NWT). The experimental plots were subjected to artificial rainfall, and DEMs were obtained using the Structure from Motion method -

before rainfall and after rainfall. The surface microrelief was assessed with random roughness, and two measures of connectivity were compared with direct runoff monitoring of surface runoff and sediment transport.

The slope-wise wheel tracks (SWT) increased the sediment and the hydraulic connectivity of the surface . The wheel track itself exhibited high structural connectivity and low roughness when oriented slope-wise. This led to an increase in runoff and sediment transport. The soil surface adjacent to SWT is connected to the wheel track only to some extent, as shown by the direct measurements. The plot with a contour line wheel track (CWT) exhibited even higher roughness and lower connectivity than the plot without wheel tracks. A temporal decrease in random roughness and in soil surface storage was observed on all plots as the effect of the kinetic energy of the rainfall and runoff. The surface became more connected during the rainfall, as shown via the functional connectivity metric.

The microtopography affects the water and sediment routing on the soil surface. The wheel tracks, depending on orientation, increase or decrease the water and sediment fluxes during runoff events. The effect of SWT after a rainfall-runoff event is pronounced, since it becomes more connected to the surrounding soil. On the other hand, the effect of CWT decreases in time, as it becomes filled with deposited sediment. The emergent connection of SWT to the surrounding soil needs to be further studied – however, our study has shown that microrelief analysis may be used to identify this process. The conditions under which the CWT effect is diminished also need to be further studied. Sudden connection of parts of fields previously disconnected by CWT increases the runoff and the risk of erosion. Since the rainfall and runoff process increases the functional connectivity regardless of the wheel track presence or orientation the importance of soil surface treatments is stressed.

The outcomes of this study may be used for large-scale modeling of arable lands, where a single computation cell of the large-scale model can be represented by the experimental plot in this study. The direct link to such models can be found in random roughness (RR) and functional connectivity. Different RR can be assigned to cells based on the orientation of the wheel tracks in the cells. However, this usage of RR may be misleading, since the wheel track is a physical feature in the model cell rather than the roughness of the soil surface. Functional connectivity can be used to represent the surface retention of the cell, as suggested by (Antoine et al., 2009; Antoine et al., 2011; Peñuela et al., 2016). In this case, different functional connectivity will represent the cells in the model with or without wheel tracks, as well as the orientation of the wheel tracks. This application has the potential to improve runoff generation modeling studies. However, further study is required to determine usability.

6 ACKNOWLEDGMENTS

We would like to give our thanks to Tomas Brunner and Anna Zeiser from BAW Petzenkirchen and to Nasrin Haacke from TU Berlin, to students of CTU in Prague Julie Winterová, Tomáš Najman, Jan-František Kubát, and to our colleagues Barbora Jáchymová, Adam Tejkl, Jakub Stašek, Nina Noreika, Tailin Li, Petr Koudelka, Petr Kavka, Vaclav David and others for their help with preparing the experimental plots and for their hard field work during the experiments. We would also like to thank Hanka Donátová for conducting the lab analyses and Michal Sněhota and Martin Šanda for providing the necessary equipment. We thank Robin Healey for correcting the language.

7 FUNDING SOURCES

This research was supported by Horizon 2020 research and innovation program project no 773903 under the title “Shui - Soil Hydrology research platform underpinning innovation to manage water scarcity in European and Chinese cropping systems”, by Ministry of Education, Youth and Sports of the Czech Republic project no. LTAUSA19019 “Connectivity of sediment transport within intensively-used rural catchments”, and by Ministry of Agriculture of the Czech Republic project no. QK1920224 ”Ways of soil erosion protection on the farm level after glyphosate ban”. Additional support from Grant Agency of the Czech Technical University in Prague project no. SGS20/156/OHK1/3T/11 “Monitoring, experiments, and mathematical modelling of rainfall runoff and soil erosion processes” is aso gratefully acknowledged.

8 REFERENCES

Angermann, L., Jackisch, C., Allroggen, N., Sprenger, M., Zehe, E., Tronicke, J., Weiler, M., Blume, T., 2017. Form and function in hillslope hydrology: Characterization of subsurface flow based on response observations. Hydrol. Earth Syst. Sci. 21, 3727–3748. https://doi.org/10.5194/hess-21-3727-2017

Ankeny, M. D., Kaspar, T. C., Horton, R.,1990. Characterization of tillage and traffic effects on unconfined infiltration measurements. Soil Science Society of America Journal, 54(3), 837–840. https://doi.org/10.2136/sssaj1990.03615995005400030037x

Antoine, M., Javaux, M., Bielders, C., 2009. What indicators can capture runoff-relevant connectivity properties of the micro-topography at the plot scale? Advances in Water Resources, 32(8), 1297–1310. https://doi.org/10.1016/j.advwatres.2009.05.006

Antoine, M., Javaux, M., Bielders, C.L., 2011. Integrating subgrid connectivity properties of the micro-topography in distributed runoff models, at the interrill scale. J. Hydrol. 403, 213–223. https://doi.org/10.1016/j.jhydrol.2011.03.027

Appels, W.M., Bogaart, P.W., van der Zee, S.E.A.T.M., 2011. Influence of spatial variations of microtopography and infiltration on surface runoff and field scale hydrological connectivity. Adv. Water Resour. 34, 303–313. https://doi.org/10.1016/j.advwatres.2010.12.003

Appels, W.M., Bogaart, P.W., van der Zee, S.E.A.T.M., 2016. Surface runoff in flat terrain: How field topography and runoff generating processes control hydrological connectivity. J. Hydrol. 534, 493–504. https://doi.org/10.1016/j.jhydrol.2016.01.021

Augustin, K., Kuhwald, M., Brunotte, J., Duttmann, R., 2020. Wheel load and wheel pass frequency as indicators for soil compaction risk: A four-year analysis of traffic intensity at field scale. Geosci. 10, 1–15. https://doi.org/10.3390/geosciences10080292

Basher, L. R., Ross, C. W., 2001. Role of wheel tracks in runoff generation and erosion under vegetable production on a clay loam soil at Pukekohe, New Zealand. Soil and Tillage Research, 62(3–4), 117–130. https://doi.org/10.1016/S0167-1987(01)00220-3

Bauer, T., Strauss, P., Grims, M., Kamptner, E., Mansberger, R., Spiegel, H. ,2015. Long-term agricultural management effects on surface roughness and consolidation of soils. Soil and Tillage Research, 151, 28–38. https://doi.org/10.1016/j.still.2015.01.017

Beven, K., and Kirkby, M. J., 1979. A physically based, variable contributing area model of basin hydrology/un modèle à base physique de zone d'appel variable de l'hydrologie du bassin versant. Hydrological Sciences Journal, 24(1):43–69.

Boardman, J. and Poesen, J., 2006. Soil Erosion in Europe, Soil Erosion in Europe: Major Processes, Causes and Consequences. John Wiley & Sons, Ltd, Chichester, UK. https://doi.org/10.1002/0470859202

Boardman, J., Vandaele, K., Evans, R., Foster, I.D.L., 2019. Off-site impacts of soil erosion and runoff: Why connectivity is more important than erosion rates. Soil Use Manag. 35, 245–256. https://doi.org/10.1111/sum.12496

Borselli, L., Cassi, P., Torri, D., 2008. Prolegomena to sediment and flow connectivity in the landscape: A GIS and field numerical assessment. Catena, 75(3), 268–277. https://doi.org/10.1016/j.catena.2008.07.006

Botta, G.F., Becerra, A.T., Tourn, F.B., 2009. Effect of the number of tractor passes on soil rut depth and compaction in two tillage regimes. Soil Tillage Res. 103, 381–386. https://doi.org/10.1016/j.still.2008.12.002

Bracken, L. J., Wainwright, J., Ali, G. A., Tetzlaff, D., Smith, M. W., Reaney, S. M., Roy, A. G., 2013. Concepts of hydrological connectivity: Research approaches, Pathways and future agendas. Earth-Science Reviews, 119, 17–34. https://doi.org/10.1016/j.earscirev.2013.02.001

Carpenter, S.R., Caraco, N.F., Correll, D.L., Howarth, R.W., Sharpley, A.N., Smith, V.H., 1998. Nonpoint pollution of surface waters with phosphorus and nitrogen. Ecol. Appl. 8, 559–568. https://doi.org/10.1890/1051-0761(1998)008[0559:NPOSWW]2.0.CO;2

Chen, L., Sela, S., Svoray, T., Assouline, S., 2013. The role of soil-surface sealing, microtopography, and vegetation patches in rainfall-runoff processes in semiarid areas. Water Resour. Res. 49, 5585–5599. https://doi.org/10.1002/wrcr.20360

Couturier, A., Daroussin, J., Darboux, F., Souchère, V., Le Bissonnais, Y., Cerdan, O., King, D., (2013. Improvement of surface flow network prediction for the modeling of erosion processes in agricultural landscapes. Geomorphology, 183, 120–129. https://doi.org/10.1016/j.geomorph.2012.07.025

Croft, H., Anderson, K., Brazier, R.E., Kuhn, N.J., 2013. Modeling fine-scale soil surface structure using geostatistics. Water Resour. Res. 49, 1858–1870. https://doi.org/10.1002/wrcr.20172

Daraghmeh, O.A., Jensen, J.R., Petersen, C.T., 2008. Near-Saturated Hydraulic Properties in the Surface Layer of a Sandy Loam Soil under Conventional and Reduced Tillage. Soil Sci. Soc. Am. J. 72, 1728. https://doi.org/10.2136/sssaj2007.0292

de Lima, R. P., da Silva, A. R., & da Silva, Á. P., 2021. soilphysics: An R package for simulation of soil compaction induced by agricultural field traffic. Soil and Tillage Research, 206, 104824. https://doi.org/10.1016/j.still.2020.104824

Darboux, F., Davy, P., Gascuel-Odoux, C., Huang, C., 2002a. Evolution of soil surface roughness and flowpath connectivity in overland flow experiments. Catena, 46(2–3), 125–139. https://doi.org/10.1016/S0341-8162(01)00162-X

Darboux, F., Davy, P., Gascuel-Odoux, C., 2002b. Effect of depression storage capacity on overland-flow generation for rough horizontal surfaces: Water transfer distance and scaling. Earth Surface Processes and Landforms, 27(2), 177–191. https://doi.org/10.1002/esp.312

Dostál, T., Váška, J., Vrána, K., 2000. SMODERP — A Simulation Model of Overland Flow and Erosion Processes. Soil Eros. 135–161. https://doi.org/10.1007/978-3-662-04295-3_8

Deasy, C., Brazier, R.E., Heathwaite, A.L., Hodgkinson, R., 2009. Pathways of runoff and sediment transfer in small agricultural catchments. Hydrol. Process. 23, 1349–1358. https://doi.org/10.1002/hyp.7257

Eltner, A., Kaiser, A., Abellan, A., Schindewolf, M., 2017. Time lapse structure-from-motion photogrammetry for continuous geomorphic monitoring. Earth Surf. Process. Landforms 42, 2240–2253. https://doi.org/10.1002/esp.4178

European Commission, 2021. COMMUNICATION FROM THE COMMISSION TO THE EUROPEAN PARLIAMENT, THE COUNCIL, THE EUROPEAN ECONOMIC AND SOCIAL COMMITTEE AND THE COMMITTEE OF THE REGIONS EU Soil Strategy for 2030 Reaping the benefits of healthy soils for people, food, nature and climate, COM(2021) 699 final, CELEX number: 52021DC0699.

Gómez, J.A., Nearing, M.A., 2005. Runoff and sediment losses from rough and smooth soil surfaces in a laboratory experiment. Catena 59, 253–266. https://doi.org/10.1016/j.catena.2004.09.008

Guzha, A.C., 2004. Effects of tillage on soil microrelief, surface depression storage and soil water storage. Soil Tillage Res. 76, 105–114. https://doi.org/10.1016/j.still.2003.09.002

Heathwaite, A. L., Quinn, P. F., Hewett, C. J. M., 2005. Modelling and managing critical source areas of diffuse pollution from agricultural land using flow connectivity simulation. Journal of Hydrology, 304(1–4), 446–461. https://doi.org/10.1016/j.jhydrol.2004.07.043

Hjerdt, K. N., McDonnell, J. J., Seibert, J., & Rodhe, A., 2004. A new topographic index to quantify downslope controls on local drainage. Water Resources Research, 40(5), 1–6. https://doi.org/10.1029/2004WR003130

Hopp, L., and McDonnell, J. J., 2009. Connectivity at the hillslope scale: Identifying interactions between storm size, bedrock permeability, slope angle and soil depth. Journal of Hydrology, 376(3–4), 378–391. https://doi.org/10.1016/j.jhydrol.2009.07.047

Jackisch, C., Angermann, L., Allroggen, N., Sprenger, M., Blume, T., Tronicke, J., Zehe, E., 2017. Form and function in hillslope hydrology: In situ imaging and characterization of flow-relevant structures. Hydrol. Earth Syst. Sci. 21, 3749–3775. https://doi.org/10.5194/hess-21-3749-2017

Jester, W., Klik, A., 2005. Soil surface roughness measurement - Methods, applicability, and surface representation. Catena 64, 174–192. https://doi.org/10.1016/j.catena.2005.08.005

Kašpar, M., Bližňák, V., Hulec, F., Müller, M., 2021. High-resolution spatial analysis of the variability in the subdaily rainfall time structure. Atmos. Res. 248. https://doi.org/10.1016/j.atmosres.2020.105202

Kavka, P., Strouhal, L., Jáchymová, B., Krása, J., Báčová, M., Laburda, T., Dostál, T., Devátý, J., Bauer, M., 2018. Double Size Fulljet Field Rainfall Simulator for Complex Interrill and Rill Erosion Studies. Stavební Obz. - Civ. Eng. J. 27, 183–194. https://doi.org/10.14311/cej.2018.02.0015

Krása, J., Dostal, T., Van Rompaey, A., Vaska, J., Vrana, K., 2005. Reservoirs' siltation measurements and sediment transport assessment in the Czech Republic, the Vrchlice catchment study. Catena 64, 348–362. https://doi.org/10.1016/j.catena.2005.08.015

Kroulík, M., Kvíz, Z., Kumhála, F., Hůla, J., Loch, T., 2011. Procedures of soil farming allowing reduction of compaction. Precis. Agric. 12, 317–333. https://doi.org/10.1007/s11119-010-9206-1

Laburda, T., Krása, J., Zumr, D., Devátý, J., Vrána, M., Zambon, N., Johannsen, L. L., Klik, A., Strauss, P., & Dostál, T. (2021). SfM-MVS Photogrammetry for Splash Erosion Monitoring under Natural Rainfall. Earth Surface Processes and Landforms, 46(5), 1067–1082. https://doi.org/10.1002/esp.5087

Lal, R. (1999). Long-term tillage and wheel traffic effects on soil quality for two central Ohio soils. Journal of Sustainable Agriculture, 14(4), 67–84. https://doi.org/10.1300/J064v14n04_07

Landa, M., Jeřábek, J., Pešek, O., Kavka, P., 2019. SMODERP2D SOIL EROSION MODEL ENTERING AN OPEN SOURCE ERA with GPU-BASED PARALLELIZATION. Int. Arch. Photogramm. Remote Sens. Spat. Inf. Sci. - ISPRS Arch. 42, 143–149. https://doi.org/10.5194/isprs-archives-XLII-4-W14-143-2019

Leys, A., Govers, G., Gillijns, K. and Poesen, J.: Conservation tillage on loamy soils: Explaining the variability in interrill runoff and erosion reduction, Eur. J. Soil Sci., 58(6), 1425–1436, https://doi:10.1111/j.1365-2389.2007.00947.x, 2007.

Luo, J., Zheng, Z., Li, T., He, S., 2018. Assessing the impacts of microtopography on soil erosion under simulated rainfall, using a multifractal approach. Hydrol. Process. 32, 2543–2556. https://doi.org/10.1002/hyp.13170

Lindstrom, M. J., Voorhees, W. B., & Randall, G. W. (1981). Long-Term Tillage Effects on Interrow Runoff and Infiltration. Soil Science Society of America Journal, 45(5), 945–948. https://doi.org/10.2136/sssaj1981.03615995004500050025x

Martin, Y., Valeo, C., Tait, M., 2008. Centimetre-scale digital representations of terrain and impacts on depression storage and runoff. Catena 75, 223–233. https://doi.org/10.1016/j.catena.2008.07.005

Moreno, R.G., Álvarez, M.C.D., Alonso, A.T., Barrington, S., Requejo, A.S., 2008. Tillage and soil type effects on soil surface roughness at semiarid climatic conditions. Soil Tillage Res. 98, 35–44. https://doi.org/10.1016/j.still.2007.10.006

Onstad, C.A., 1984. Depressional storage on tilled soil surfaces. Trans. - Am. Soc. Agric. Eng. https://doi.org/10.13031/2013.32861

Onstad, C.A., Wolfe, M.L., Larson, C.L., Slack, D.C., 1984. Tilled soil subsidence during repeated wetting. Trans. - Am. Soc. Agric. Eng. https://doi.org/10.13031/2013.32862

Outram, F.N., Cooper, R.J., Sünnenberg, G., Hiscock, K.M., Lovett, A.A., 2016. Antecedent conditions, hydrological connectivity and anthropogenic inputs: Factors affecting nitrate and phosphorus transfers to agricultural headwater streams. Sci. Total Environ. 545–546, 184–199. https://doi.org/10.1016/j.scitotenv.2015.12.025

Pagliai, M., Marsili, A., Servadio, P., Vignozzi, N., Pellegrini, S., 2003. Changes in some physical properties of a clay soil in Central Italy following the passage of rubber tracked and wheeled tractors of medium power. Soil Tillage Res. 73, 119–129. https://doi.org/10.1016/S0167-1987(03)00105-3

Peñuela, A., Darboux, F., Javaux, M., Bielders, C.L., 2016. Evolution of overland flow connectivity in bare agricultural plots. Earth Surf. Process. Landforms 41, 1595–1613. https://doi.org/10.1002/esp.3938

Philip, J.R., 1957. The theory of infiltration: 1. The infiltration equation and its solution. Soil Sci. 83, 345–357. https://doi.org/10.1097/00010694-195705000-00002

Pringle, C., 2003. What is hydrologic connectivity and why is it ecologically important? Hydrol. Process. 17, 2685–2689. https://doi.org/10.1002/hyp.5145

Probst, J. L., 1985. Nitrogen and phosphorus exportation in the Garonne Basin (France). Journal of Hydrology, 76(3–4), 281–305. https://doi.org/10.1016/0022-1694(85)90138-6

Prosdocimi, M., Burguet, M., Di Prima, S., Sofia, G., Terol, E., Rodrigo Comino, J., Cerdà, A., Tarolli, P., 2017. Rainfall simulation and Structure-from-Motion photogrammetry for the analysis of soil water erosion in Mediterranean vineyards. Sci. Total Environ. 574, 204–215. https://doi.org/10.1016/j.scitotenv.2016.09.036

R Core Team. (2018). R: A Language and Environment for Statistical Computing. https://www.r-project.org/

Rinderer, M., Ali, G., Larsen, L.G., 2018. Assessing structural, functional and effective hydrologic connectivity with brain neuroscience methods: State-of-the-art and research directions. Earth-Science Rev. 178, 29–47. https://doi.org/10.1016/j.earscirev.2018.01.009

Ryken, N., Vanden Nest, T., Al-Barri, B., Blake, W., Taylor, A., Bodé, S., Ruysschaert,G., Boeckx, P., Verdoodt, A., 2018. Soil erosion rates under different tillage practices in central Belgium: New perspectives from a combined approach of rainfall simulations and 7 Be measurements. Soil and Tillage Research, 179(January), 29–37. https://doi.org/10.1016/j.still.2018.01.010

Seehusen, T., Riggert, R., Fleige, H., Horn, R., Riley, H., 2019. Soil compaction and stress propagation after different wheeling intensities on a silt soil in South-East Norway, Acta Agric. Scand. Sect. B Soil Plant Sci., 69(4), 343–355, https://doi:10.1080/09064710.2019.1576762

Silgram, M., Jackson, D. R., Bailey, A., Quinton, J., Stevens, C., 2010). Hillslope scale surface runoff, sediment and nutrient losses associated with tramline wheelings. Earth Surface Processes and Landforms, 35(6), 699–706. https://doi.org/10.1002/esp.1894

Smith, M.W., 2014. Roughness in the Earth Sciences. Earth-Science Rev. 136, 202–225. https://doi.org/10.1016/j.earscirev.2014.05.016

Souchere, V., King, D., Daroussin, J., Papy, F., Capillon, A., 1998. Effects of tillage on runoff directions: Consequences on runoff contributing area within agricultural catchments. Journal of Hydrology, 206(3–4), 256–267. https://doi.org/10.1016/S0022-1694(98)00103-6

Stieglitz, M., Shaman, J., McNamara, J., Engel, V., Shanley, J., Kling, G. W., 2003. An approach to understanding hydrologic connectivity on the hillslope and the implications for nutrient transport. Global Biogeochemical Cycles, 17(4), n/a-n/a. https://doi.org/10.1029/2003gb002041

Taconet, O., Ciarletti, V. ,2007. Estimating soil roughness indices on a ridge-and-furrow surface using stereo photogrammetry. Soil and Tillage Research, 93(1), 64–76. https://doi.org/10.1016/j.still.2006.03.018

Takken, I., Govers, G., Steegen, A., Nachtergaele, J., & Guérif, J., 2001. The prediction of runoff flow directions on tilled fields. Journal of Hydrology, 248(1–4), 1–13. https://doi.org/10.1016/S0022-1694(01)00360-2

Tarboton, D.G., 2015. Taudem 5, Terrain Analysis Using Digital Elevation Models [Online]. Available from http://hydrology.usu.edu/taudem/taudem5/.

Tarolli, P., Cavalli, M., & Masin, R. (2019). High-resolution morphologic characterization of conservation agriculture. Catena, 172(July 2018), 846–856. https://doi.org/10.1016/j.catena.2018.08.026

Thompson, S.E., Katul, G.G., Porporato, A., 2010. Role of microtopography in rainfall-runoff partitioning: An analysis using idealized geometry. Water Resour. Res. 46, 1–11. https://doi.org/10.1029/2009wr008835

Westoby, M.J., Brasington, J., Glasser, N.F., Hambrey, M.J., Reynolds, J.M., 2012. “Structure-from-Motion” photogrammetry: A low-cost, effective tool for geoscience applications. Geomorphology 179, 300–314. https://doi.org/10.1016/j.geomorph.2012.08.021

Withers, P. J. A., Hodgkinson, R. A., Bates, A., & Withers, C. M., 2006. Some effects of tramlines on surface runoff, sediment and phosphorus mobilization on an erosion-prone soil. Soil Use and Management, 22(3), 245–255. https://doi.org/10.1111/j.1475-2743.2006.00034.x

Wolstenholme, J.M., Smith, M.W., Baird, A.J., Sim, T.G., 2020. A new approach for measuring surface hydrological connectivity. Hydrol. Process. 34, 538–552. https://doi.org/10.1002/hyp.13602

Yang, J., Chu, X., 2013. Quantification of the spatio-temporal variations in hydrologic connectivity of small-scale topographic surfaces under various rainfall conditions. J. Hydrol. 505, 65–77. https://doi.org/10.1016/j.jhydrol.2013.09.013

Zobeck, T.M., Onstad, C.A., 1987. Tillage and rainfall effects on random roughness: A review. Soil Tillage Res. 9, 1–20. https://doi.org/10.1016/0167-1987(87)90047-X

Zhao, L., Hou, R., Wu, F., & Keesstra, S. (2018). Effect of soil surface roughness on infiltration water, ponding and runoff on tilled soils under rainfall simulation experiments. Soil and Tillage Research, 179(June 2017), 47–53. https://doi.org/10.1016/j.still.2018.01.009

APPENDIX 1

SMODERP2D model parametrization

Table A1. The soil hydraulic parameters of a Loam soil used to calculate the functional connectivity with the SMODERP2D model

LIST OF FIGURES

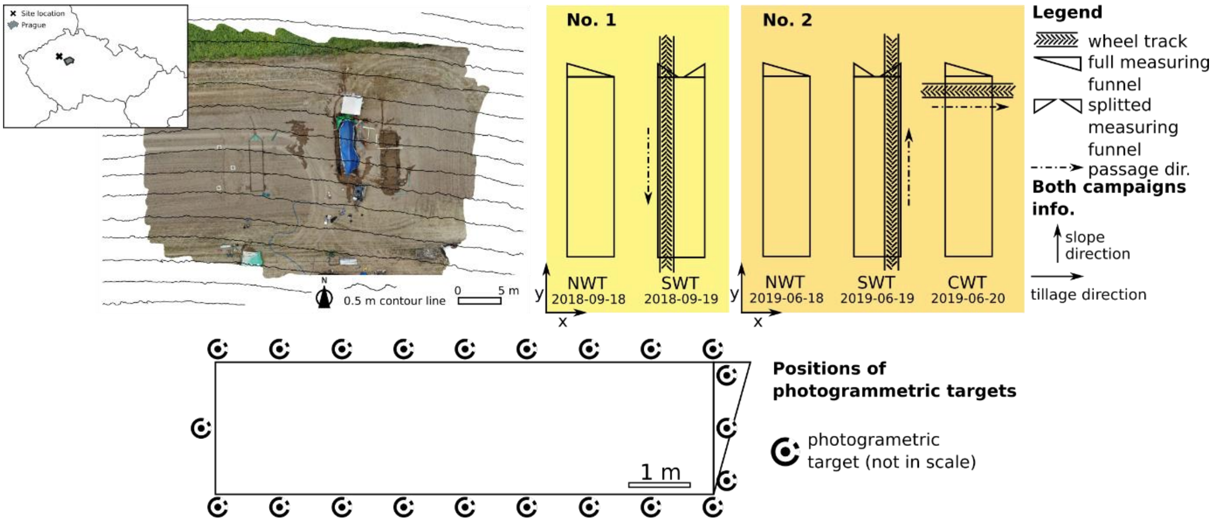

Figure 1. Location and an orthophoto of the experimental site on the top left. Experimental plot setting of campaign No. 1 and campaign No. 2 on the right. The schema of the photogrammetric measurement at the bottom.

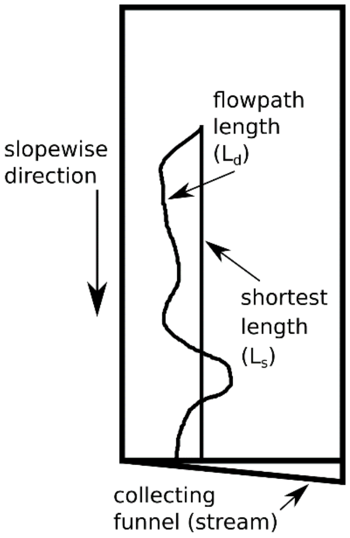

Figure 2. An explanatory diagram of the normalized downslope distance NDD. NDD is the ratio between the flowpath length calculated using a downslope distance algorithm – the flowpath length from a given raster cell to the bottom of the plot (to the collection funnel) and the shortest geometrical distance between the raster cell and the collection funnel.

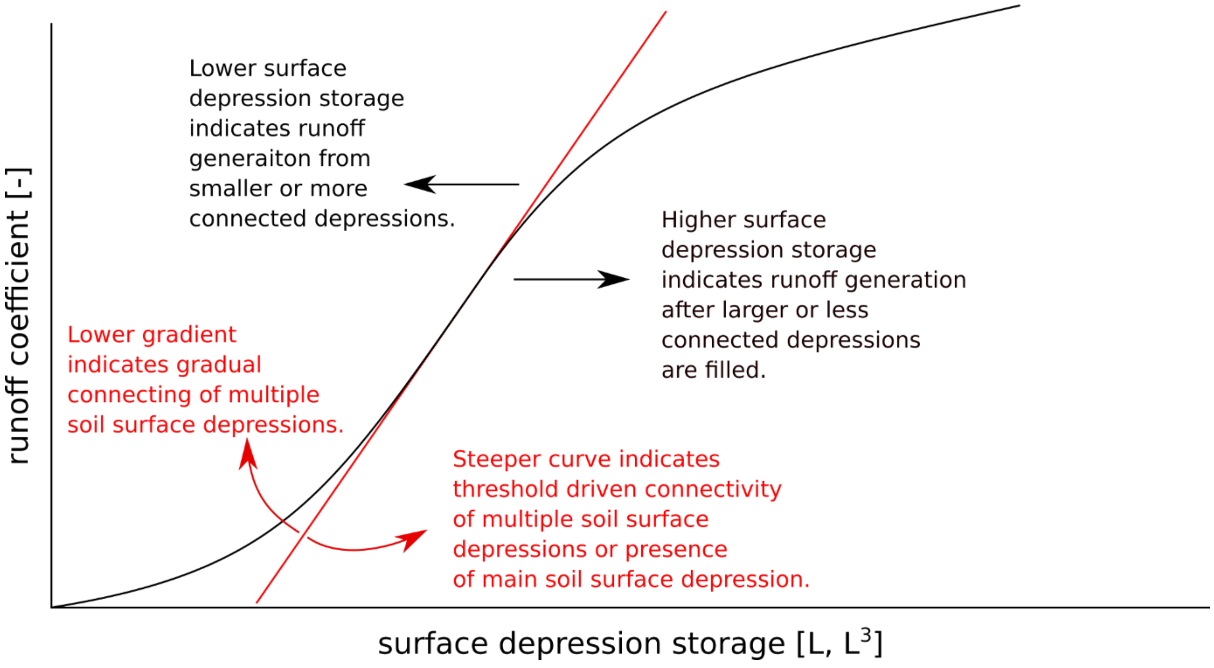

Figure 3. An example of the runoff coefficient to soil surface storage relationship – functional connectivity. Black arrows and text explain the horizontal shift of the curve. The red line indicates the gradient of the example curve. Red arrows and text explain the meaning of the gradient shift.

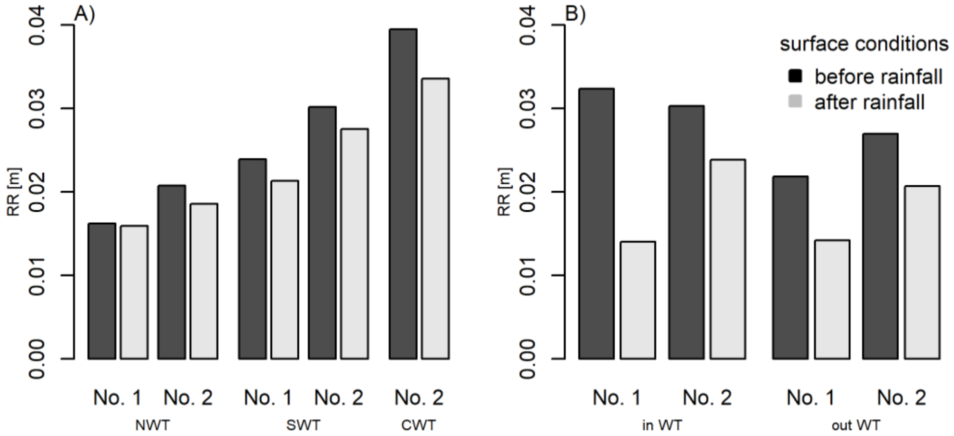

Figure 4. A) Bar plots of the random roughness for slope-wise and counter slope-wise wheel track orientation, and the no wheel track plot for before-rainfall and after-rainfall soil surface conditions. B) Bar plots of the random roughness of the wheel track (in WT) and the surrounding soil surface (outside WT) on the SWT plots of both campaigns.

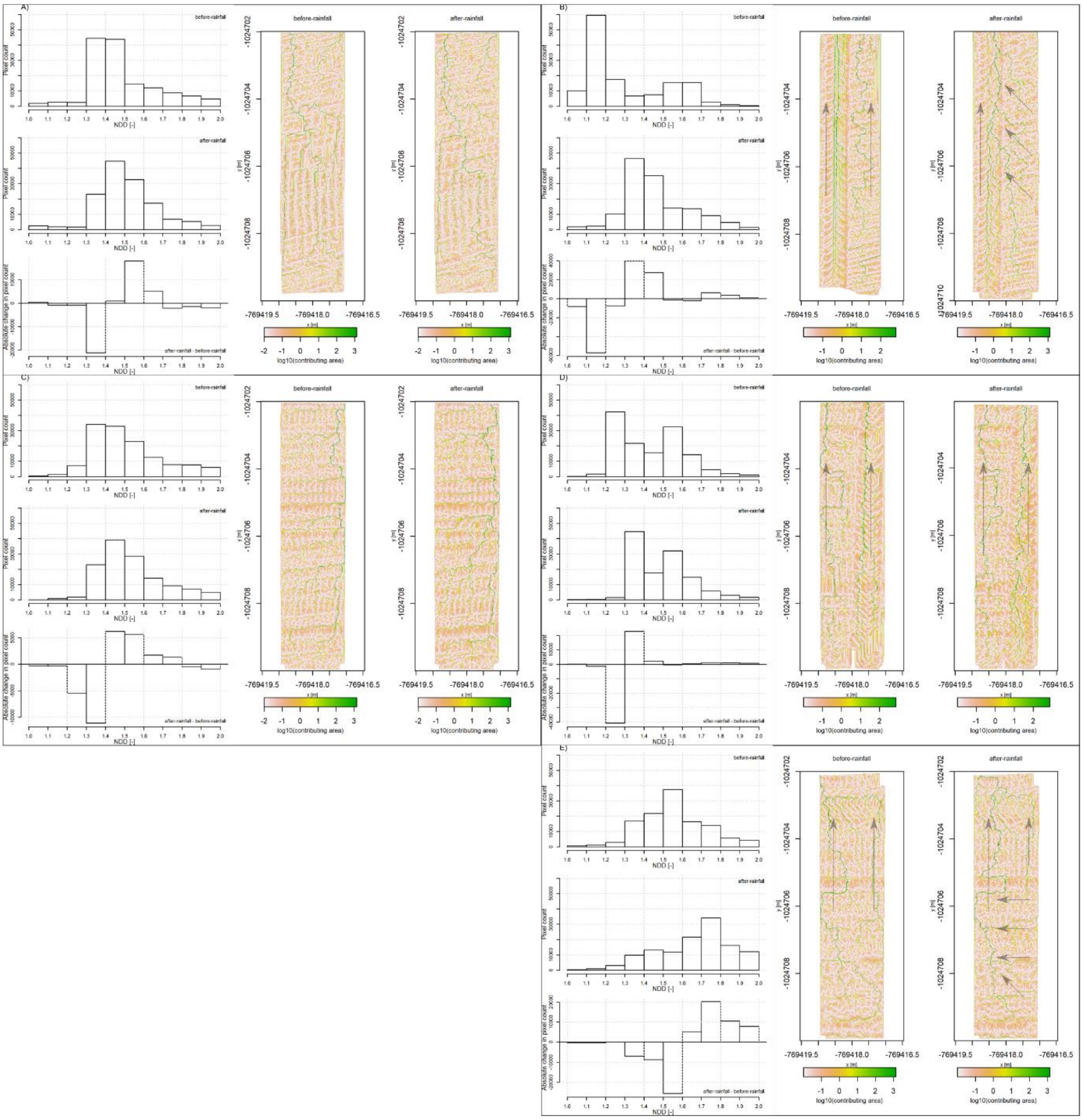

Figure 5. The histogram of NDD and the corresponding contribution area raster of the before-rainfall and after-rainfall surface conditions of: A) NWT No. 1 plot, B) SWT No. 1 plot, C) NWT No. 2 plot, D) NWT No. 2 plot, and E) CWT No. 2 plot. The difference between the before-rainfall histogram and the after-rainfall histogram is shown below the corresponding histograms to indicate the increase/decrease in the normalized downslope distance in each interval of the histogram. The arrows in some of the flow accumulation rasters indicate the main flow direction and are described in the manuscript text.

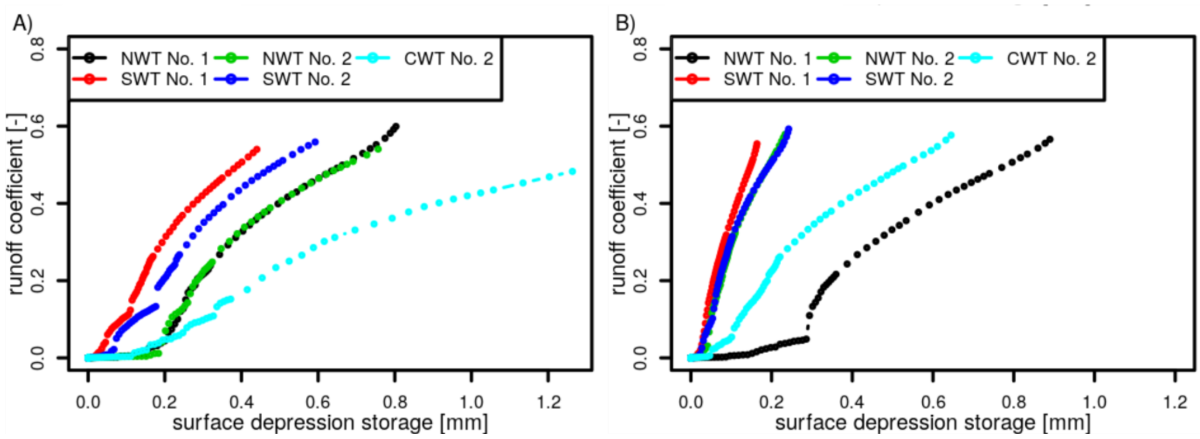

Figure 6. Functional connectivity as the relation between the runoff coefficient and the filled soil surface storage of A) the before-rainfall situation, and B) the after-rainfall situation of all plots.

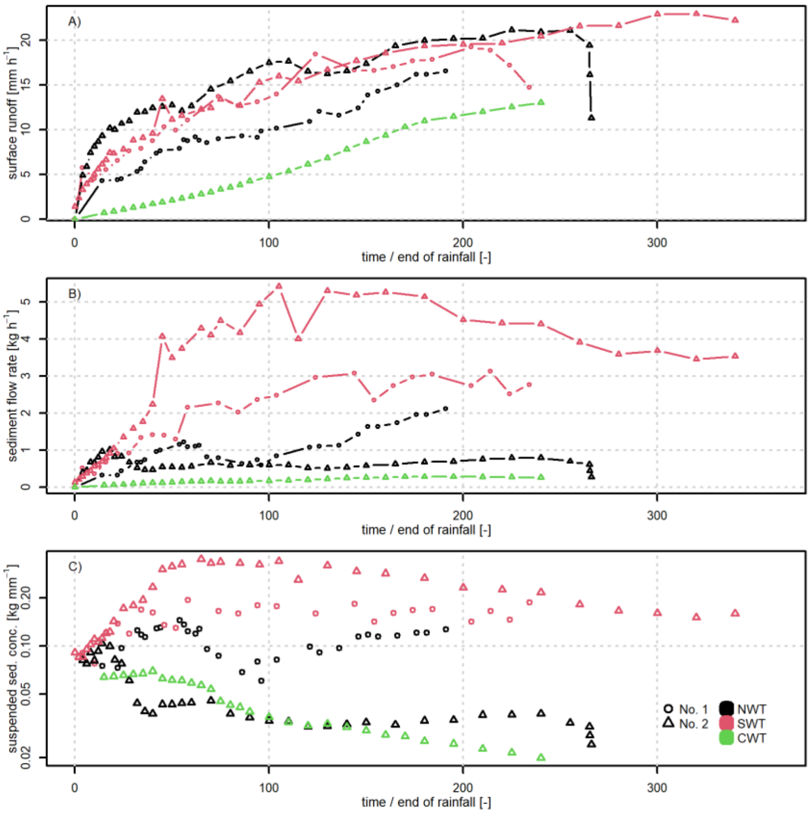

Figure 7. Development of: A) the surface runoff, B) the sediment flow rate and C) the concentration of the suspended solids in time. The runoff time lag is excluded from the graphs; therefore, all graphs start at a common zero time on the vertical axes.

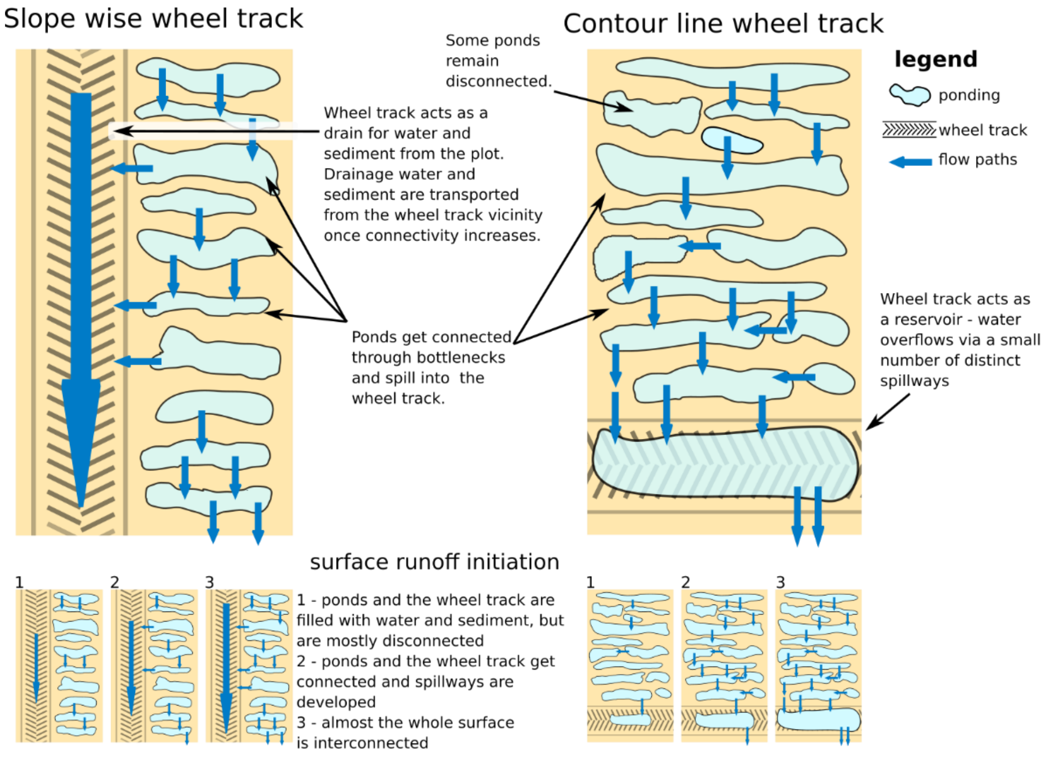

Figure 8. Runoff development visually observed during the rainfall simulation at the SWT and CWT experimental plot. The lower bar plots show the development of the connectivity of the soil surface depressions.

List of Tables

Table 1. Summary of experiments. Single values are presented. SWT – slope wise wheel track; CWT - contour line wheel track; NWT - no wheel track. At the SWT plot, the runoff was collected from a wheel track and from the surrounding soil, separately (shown in gray).

campaign	No. 1	No. 1	No. 1	No. 2	No. 2	No. 2	No. 2
plot setting	NWT	SWT	SWT	NWT	SWT	SWT	CWT
collected below WT	no	no	yes	no	no	yes	yes
date	9/18/2018	9/19/2018	9/19/2018	6/18/2019	6/19/2019	6/19/2019	6/20/2019
rainfall duration [min]	290	249	249	316	433	433	319
rainfall depth [mm]	145	124.5	124.5	158	216.5	216.5	159.5
runoff time lag [min]	76	no runoff	15	51	102	22	32.5
max. runoff [mm/hour]	22.7	no runoff	25.4	25	2.8	21.6	14.4
cumulative runoff [mm]	31	no runoff	54.7	73.5	8.5	88.5	26.1
runoff coefficient [%]	21.3	no runoff	45	46.5	3.9	40.9	16.4
total soil loss [g m^{-2}]	204	no runoff	550	175	38	1360	48

Table 2. The difference of: A) the surface runoff from the plots since the beginning of runoff; B) the sediment flow rate at the plots since the beginning of runoff. The Student t test was used, to test if the difference between the two plots is greater than 0. Red color indicates that the plot in the column exhibited significantly higher (α = 0.05) values than the plot in the row. Green color indicates a non-significant difference.

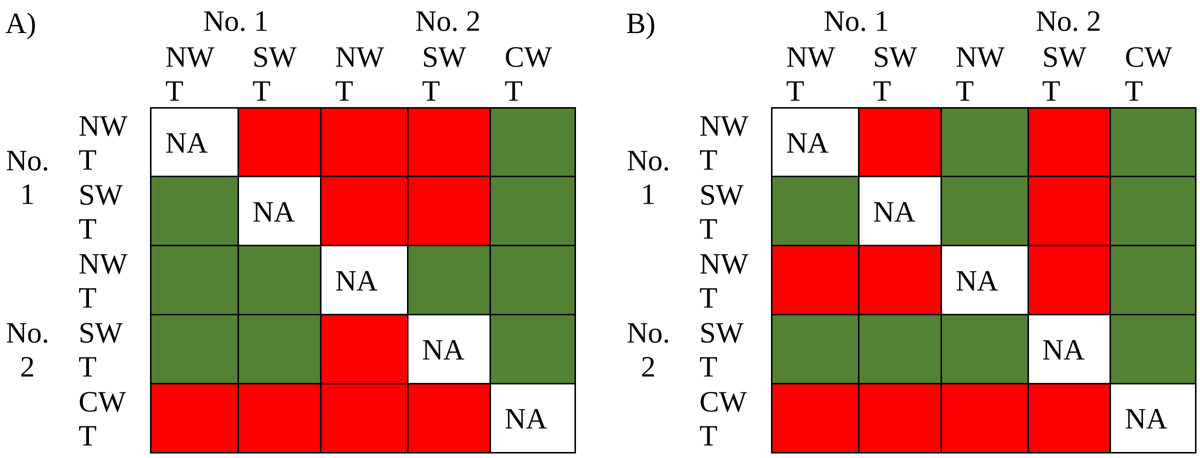

A)

		No. 1		No. 2		
		NWT	SWT	NWT	SWT	CWT
No. 1	NWT	NA	🟥	🟥	🟥	🟩
	SWT	🟩	NA	🟥	🟥	🟩
No. 2	NWT	🟩	🟩	NA	🟩	🟩
	SWT	🟩	🟩	🟥	NA	🟩
	CWT	🟥	🟥	🟥	🟥	NA

B)

		No. 1		No. 2		
		NWT	SWT	NWT	SWT	CWT
No. 1	NWT	NA	🟥	🟩	🟥	🟩
	SWT	🟩	NA	🟩	🟥	🟩
No. 2	NWT	🟥	🟥	NA	🟥	🟩
	SWT	🟩	🟩	🟩	NA	🟩
	CWT	🟥	🟥	🟥	🟥	NA

Table A1. The soil hydraulic parameters of Loam soil used to calculate the functional connectivity with the SMODERP2D model.

parameter name	parameter value
saturated hydraulic conductivity Ks [m s-1]	1.67E-06
sorptivity S [m s^{1/2}]	1.39E-04
shallow water flow eq. parameter b [-]	1.73
shallow water flow eq. parameter X [-]	10.08
shallow water flow eq. parameter Y [-]	0.56

Appendix B

Supplementary data for results section

```
      -----------
     |           |
D4.1 | T4.1 T4.2 | D4.2
     |           |
     |           |
D3.1 | T3.1 T3.2 | D3.2
     |           |
     |           |
D2.1 | T2.1 T2.2 | D2.2
     |           |
D1.1 | T1.1 T1.2 | D1.2
     |___________|
      \         /
        \     /
          \ /
```

Figure B.1: Diagram with the codes of the tensiometers location

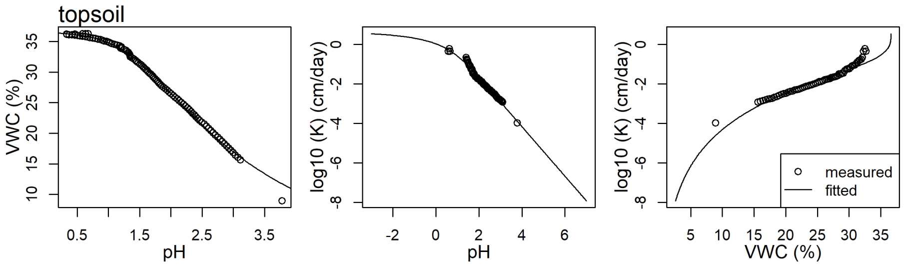

(a) Topsoil

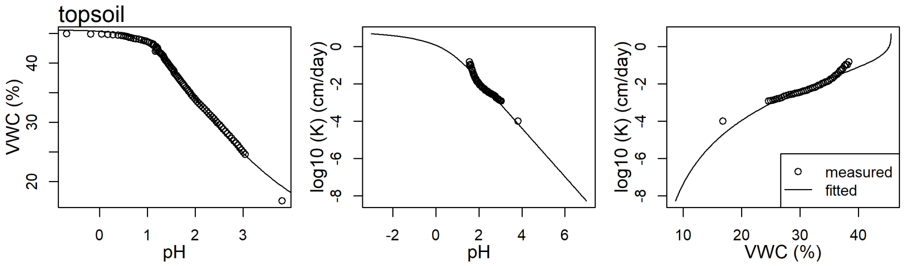

(b) Topsoil

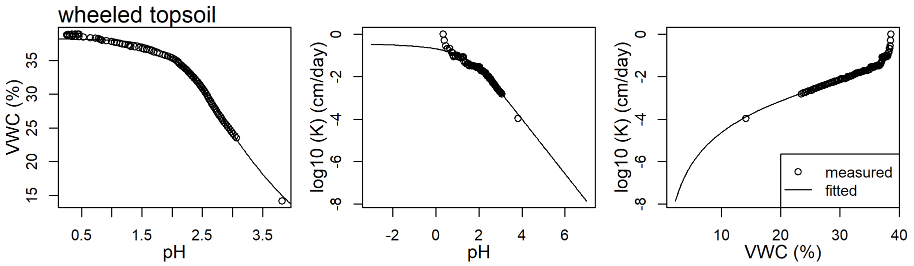

(c) Wheel track

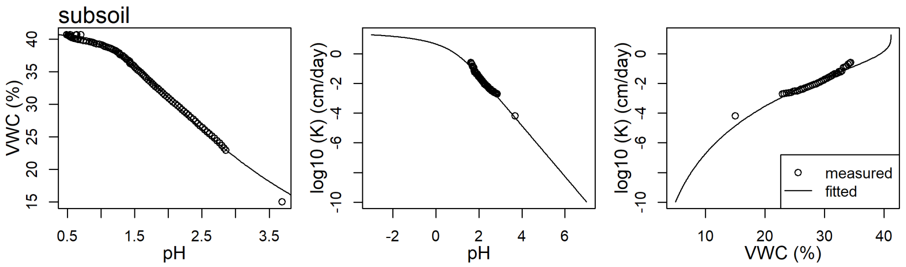

(d) Subsoil

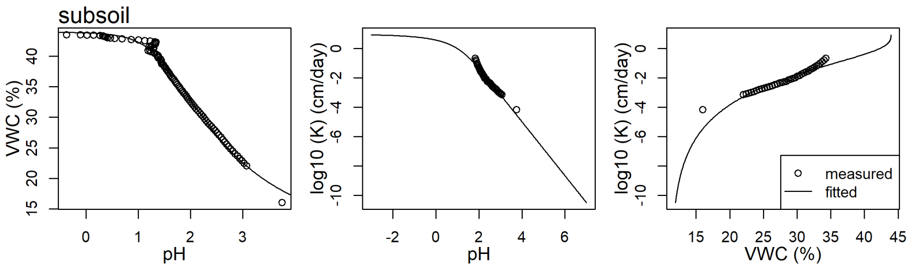

(e) Subsoil

Figure B.2: The measure (dots) and fitted (lines) retention curve and hydraulic conductivity obtained with the evaporation method.

Table B.1: The locations of the SWC sensors used during both Řisuty experiments

campaign id	tensio. id	tensio. id orig.	position*	z (cm)	y (cm)	x (cm)	in wheel track
vol1_noWT	P_1_hPa	M1	T3.1	5.1	4	38	FALSE
vol1_noWT	P_2_hPa	M3	T3.2	11.1	4	77	FALSE
vol1_noWT	P_4_hPa	nuc2	T1.1	8.5	1	41	FALSE
vol1_noWT	P_5_hPa	nuc3	T1.2	10	1	77	FALSE
vol1_noWT	P_7_hPa	VE	T2.1	8.5	1.9	87	FALSE
vol1_noWT	P_6_hPa	VE6	T2.2	8.5	1.9	44	FALSE
vol1_slWT	P_1_hPa	M1	T3.1	5.2	4	21	FALSE
vol1_slWT	P_2_hPa	M3	T3.2	14.7	4	64	FALSE
vol1_slWT	P_3_hPa	M4	T4.1	8.5	7	36	FALSE
vol1_slWT	P_4_hPa	nuc2	T1.1	7.5	1	20	FALSE
vol1_slWT	P_5_hPa	nuc3	T1.2	13.4	1	70	FALSE
vol1_slWT	P_7_hPa	VE	T2.1	14.8	1.9	61	FALSE
vol1_slWT	P_6_hPa	VE6	T2.2	9.9	1.9	25	FALSE
vol2_noWT	P_1_hPa	6384	T4.2	14	7	NA	FALSE
vol2_noWT	P_2_hPa	6382	T3.2	16	4	NA	FALSE
vol2_noWT	P_3_hPa	6383	T4.1	19	7	NA	FALSE
vol2_noWT	P_4_hPa	4319	D1.1	36.	0.8	NA	FALSE
vol2_noWT	P_5_hPa	4333	D2.1	38.9	1.8	NA	FALSE
vol2_noWT	P_6_hPa	4122	T3.1	17	4	NA	FALSE
vol2_noWT	P_7_hPa	4138	D4.1	35.3	7	NA	FALSE
vol2_noWT	P_8_hPa	4331	D3.1	43.8	4	NA	FALSE
vol2_noWT	P_9_hPa	3661	T2.1	16	1.8	NA	FALSE
vol2_noWT	P_10_hPa	3662	T2.2	17	1.8	NA	FALSE
vol2_noWT	P_11_hPa	4123	T1.1	17	0.8	NA	FALSE
vol2_noWT	P_12_hPa	4124	T1.2	20	0.8	NA	FALSE
vol2_slWT	P_1_hPa	6384	T4.2	17	7	NA	FALSE
vol2_slWT	P_2_hPa	6382	T3.2	20	4.8	NA	FALSE
vol2_slWT	P_3_hPa	6383	T4.1	10.9	7	NA	TRUE
vol2_slWT	P_4_hPa	4319	D1.1	42.4	1.1	NA	FALSE
vol2_slWT	P_5_hPa	4333	D1.2	35.4	1.1	NA	FALSE
vol2_slWT	P_6_hPa	4122	T3.1	9.6	4.8	NA	TRUE
vol2_slWT	P_7_hPa	4138	D2.2	41.1	3.8	NA	FALSE
vol2_slWT	P_8_hPa	4331	D2.1	35.3	3.8	NA	FALSE
vol2_slWT	P_9_hPa	3661	T2.1	10.2	2.2	NA	TRUE
vol2_slWT	P_10_hPa	3662	T2.2	17	2.2	NA	FALSE
vol2_slWT	P_11_hPa	4123	T1.1	17	1.1	NA	TRUE
vol2_slWT	P_12_hPa	4124	T1.2	17	1.1	NA	FALSE
vol2_clWT	P_1_hPa	6384	T4.2	16.5	5.1	NA	FALSE
vol2_clWT	P_2_hPa	6382	T3.2	13.2	1.6	NA	FALSE
vol2_clWT	P_3_hPa	6383	NA	NA	NA	NA	FALSE
vol2_clWT	P_4_hPa	4319	D1.1	40.1	0.3	NA	FALSE
vol2_clWT	P_5_hPa	4333	D2.1	45.1	1	NA	FALSE
vol2_clWT	P_6_hPa	4122	T3.1	14.1	1.6	NA	FALSE
vol2_clWT	P_7_hPa	4138	D4.1	51.4	5.1	NA	FALSE
vol2_clWT	P_8_hPa	4331	D3.1	19.0	1.6	NA	FALSE
vol2_clWT	P_9_hPa	3661	T2.1	19.1	1	NA	TRUE
vol2_clWT	P_10_hPa	3662	T2.2	13.4	1	NA	TRUE
vol2_clWT	P_11_hPa	4123	T1.1	12.6	0.3	NA	FALSE
vol2_clWT	P_12_hPa	4124	T1.2	11.9	0.3	NA	FALSE

* The explanation of the position code is in the figure B.1.

Table B.2: Exact positions of the CS650 soil moisture probes during all experiment

probe id	ems id orig.	Date	campaign id	z (cm)	y (cm)
swc_1_cm3_cm3	FDR1	2018-09-18	vol1_noWT	5	440
swc_2_cm3_cm3	FDR2	2018-09-18	vol1_noWT	12	440
swc_3_cm3_cm3	FDR3	2018-09-18	vol1_noWT	16	440
swc_4_cm3_cm3	FDR4	2018-09-18	vol1_noWT	5	150
swc_5_cm3_cm3	FDR5	2018-09-18	vol1_noWT	15	150
swc_6_cm3_cm3	FDR6	2018-09-18	vol1_noWT	30	150
swc_1_cm3_cm3	FDR1	2018-06-19	vol1_slWT	5	450
swc_2_cm3_cm3	FDR2	2018-06-19	vol1_slWT	9	450
swc_3_cm3_cm3	FDR3	2018-06-19	vol1_slWT	24	450
swc_4_cm3_cm3	FDR4	2018-06-19	vol1_slWT	5	150
swc_5_cm3_cm3	FDR5	2018-06-19	vol1_slWT	10	150
swc_6_cm3_cm3	FDR6	2018-06-19	vol1_slWT	20	150
swc_1_cm3_cm3	FDR1	2019-09-18	vol2_noWT	5	500
swc_2_cm3_cm3	FDR2	2019-09-18	vol2_noWT	15	500
swc_3_cm3_cm3	FDR3	2019-09-18	vol2_noWT	32	500
swc_4_cm3_cm3	FDR4	2019-09-18	vol2_noWT	5	145
swc_5_cm3_cm3	FDR5	2019-09-18	vol2_noWT	10	145
swc_6_cm3_cm3	FDR6	2019-09-18	vol2_noWT	22	145
swc_1_cm3_cm3	FDR1	2019-09-19	vol2_slWT	5	480
swc_2_cm3_cm3	FDR2	2019-09-19	vol2_slWT	5	480
swc_3_cm3_cm3	FDR3	2019-09-19	vol2_slWT	14	480
swc_4_cm3_cm3	FDR4	2019-09-19	vol2_slWT	5	220
swc_5_cm3_cm3	FDR5	2019-09-19	vol2_slWT	12	220
swc_6_cm3_cm3	FDR6	2019-09-19	vol2_slWT	18	220
swc_1_cm3_cm3	FDR1	2019-09-20	vol2_clWT	5	510
swc_2_cm3_cm3	FDR2	2019-09-20	vol2_clWT	14	510
swc_3_cm3_cm3	FDR3	2019-09-20	vol2_clWT	27	510
swc_4_cm3_cm3	FDR4	2019-09-20	vol2_clWT	5	140
swc_5_cm3_cm3	FDR5	2019-09-20	vol2_clWT	12	140
swc_6_cm3_cm3	FDR6	2019-09-20	vol2_clWT	24	140